

**Reconstruction of past climate variability during Marine Isotope
Stage 3 and the Holocene using speleothems:
Special emphasis on the application of the Sr isotope system**

Dissertation zur Erlangung des Grades „Doktor rerum naturalium (Dr. rer. nat.)“ der
Fachbereiche:

- 08 – Physik, Mathematik und Informatik
- 09 – Chemie, Pharmazie und Geowissenschaften,
- 10 - Biologie,
- Universitätsmedizin

der Johannes Gutenberg-Universität.

vorgelegt von

Michael Weber

geb. 12.03.1990

in Koblenz

Max Planck Graduate Center mit der Johannes Gutenberg-Universität Mainz

Angefertigt am Institut für Geowissenschaften

Mainz, 27. Mai 2019

Dekan:

1. Gutachter:

2. Gutachter:

Tag der mündlichen Prüfung: 15.08.2019

Eidesstattliche Erklärung

I hereby declare that I wrote the dissertation submitted without any unauthorized external assistance and used only sources acknowledged in the work. All textual passages which are appropriated verbatim or paraphrased from published and unpublished texts as well as all information obtained from oral sources are duly indicated and listed in accordance with bibliographical rules. In carrying out this research, I complied with the rules of standard scientific practice as formulated in the statutes of Johannes Gutenberg University Mainz to insure standard scientific practice.

.....

Michael Weber

Mainz, 27.05.2019

Zusammenfassung

Durch ihr Potential Klima- und Umweltbedingungen aller Kontinente und Klimazonen zu rekonstruieren, sind Speläotheme zu wichtigen Paläoklimaarchiven geworden, die mit der Uran-Ungleichgewichtsdatierung präzise datiert werden können. Damit können unabhängige Altersmodelle für die Paläoklimarekonstruktion mit Hilfe von $\delta^{13}\text{C}$, $\delta^{18}\text{O}$ und Spurenelementen erstellt werden. Neben diesen Proxies werden Sr Isotope zunehmend für Speläotheme angewandt. Das Sr Isotopensystem wird dabei sowohl zur Rekonstruktion von hydrologischen Prozessen im Karst genutzt, als auch um Veränderungen in den Verwitterungsprozessen innerhalb der Bodenzone zu rekonstruieren.

Strontiumisotope werden traditionell mit Thermal Ionisation Mass Spectrometry (TIMS) gemessen, was die chemische Abtrennung von Sr mit einem Ionen-Chromatographie Harz voraussetzt und eine lange Messdauer erfordert. Fortschritte in Laserablation (LA) und Multikollektor-ICP-Massenspektrometrie (MC-ICP-MS) erlauben die Kopplung dieser Techniken, um Sr Isotope in verschiedenen Materialien *in-situ*, ohne chemische Abtrennung zu messen. Die zusätzliche Verringerung der Messdauer erlaubt zudem einen höheren Probendurchsatz. Im Rahmen dieser Arbeit wurde die LA-MC-ICP-MS Analyse von Sr Isotopen für Speläotheme angewandt. Neben Speläothemen wurden Karbonat- und Phosphat-Referenzmaterialien (RMs) sowie Bioapatite analysiert, was das große Potenzial der Methodik zeigt. Da RMs die Grundlage für verlässliche Analysen darstellen, wurde die Verfügbarkeit von Sr Isotopie Daten von geeigneten RMs im Rahmen dieser Arbeit verbessert. Neben acht Karbonat- und Phosphat-RMs wurde ein maßgefertigtes mikroanalytisches Karbonat-RM charakterisiert, um die analytische Präzision und Genauigkeit für zukünftige *in-situ* Messungen von Karbonatproben mit wenig Sr, z.B. Speläotheme, zu verbessern.

Das Potential der Sr Isotope wurde bei einer Multi-Proxy Paläoklimarekonstruktion einer einzigartigen Speläothemprobe aus der Bunkerhöhle (Bu2) verdeutlicht. Der Stalagmit Bu2 zeigt zwei abgegrenzte Wachstumsphasen im Marinen Isotopenstadium 3, was bisher als zu kalt und trocken für Speläothemwachstum in Mitteleuropa galt. Die Analyse von stabilen Isotopen, Spurenelementen und Sr Isotopen zeigt, dass sich Mitteleuropa in einem warmen und humiden Klimazustand befand, welcher Speläothemwachstum und Bodenbildung begünstigte. Außerdem wurde gezeigt, dass die erste Wachstumsphase deutlich feuchter war, wie die zweite Phase.

Um die Aussagekraft einer einzelnen Stalagmiten -Isotopenkurve zu beurteilen, wurden stabile Isotope, Spurenelemente und Sr Isotope von vier Holozänen Proben aus der Hüttenbläterschachthöhle analysiert. Der Datensatz wurde mit der nahegelegenen Bunkerhöhle verglichen und zeigte deutliche Unterschiede in den stabilen Isotopen. Während des frühen Holozäns wurden vergleichbare Trends in beiden Höhlen festgestellt, allerdings zeigen die jüngsten 7 – 6 ka signifikante Unterschiede, besonders für $\delta^{13}\text{C}$. Die zusätzliche Analyse von Spurenelementen und Sr Isotopen zeigte, dass diese Unterschiede durch zunehmende Isotopen-Ungleichgewichtsfractionierung in der Hüttenbläterschachthöhle zustande kommen, ausgelöst durch verlangsamte Tropfraten. Paläoklimarekonstruktionen basierend auf einer einzelnen Speläothemprobe sollten daher immer als Multi-Proxy-Ansatz erfolgen.

Abstract

Speleothems are increasingly used as palaeoclimate archives due to their potential to reveal climatic and environmental patterns for all continental areas and climate zones. They can be precisely dated using the U-series disequilibrium method, allowing for the constraint of independent age depth models for proxy records, such as $\delta^{13}\text{C}$, $\delta^{18}\text{O}$ and trace elements to reconstruct palaeoclimate variability. Additionally, Sr isotopes have been increasingly applied to speleothem samples in the recent years. The Sr isotope system is used to investigate hydrological processes in the karst, as well as differences in the weathering of soil components.

Strontium isotopes have traditionally been analysed by thermal ionisation mass spectrometry (TIMS), which requires chemical separation of Sr using ion-chromatographic resins and suffer from long measurement times. Progress in laser ablation systems (LA) and multi-collector inductively plasma mass spectrometry (MC-ICP-MS) have recently allowed the combination of these two techniques to measure Sr isotopes in several materials *in-situ* without any chemical separation. Furthermore, sample throughput is significantly increased with this method due to reduced analysis time. In the framework of this thesis, the LA-MC-ICP-MS technique was adapted for the Sr isotope analysis of speleothems. Since this technique has numerous potential applications besides speleothems, numerous carbonate and phosphate reference materials, as well as bioapatite samples were analysed. In order to improve the data availability of suitable reference materials, which are a basic requirement for reliable analyses, eight different reference materials have been analysed for Sr isotopes. Furthermore, a customised carbonate microanalytical reference material was characterised, improving the analytical precision and accuracy for further *in-situ* measurements of low-Sr carbonate samples, such as speleothems.

The analysis of a unique speleothem sample from Bunker Cave (Bu2) demonstrates the potential of Sr isotopes in a multi-proxy palaeoclimate reconstruction. Stalagmite Bu2 revealed two distinctive growth phases during the early Marine Isotope Stage 3, which has been often argued to be too cold and dry to enable speleothem growth in Central Europe. Based on the analysis of stable isotopes, trace elements and Sr isotopes, we were able to show that Central Europe was in a warm and humid climate state during this time, allowing speleothems to grow and soil to form. In addition, we show that these two growth phases differed significantly from each other, with the early phase being much more humid.

To evaluate the significance of a single stalagmite stable isotope record, four Holocene speleothem samples from the Hüttenbläuserschachthöhle (HBSH) were analysed for stable isotopes, trace elements and Sr isotopes. The resulting dataset was compared to the nearby Bunker Cave and revealed significant differences in the stable isotope record. While similar trends were observed in the early Holocene in both cave systems, the most recent 7 – 6 ka revealed significant differences, especially in the $\delta^{13}\text{C}$ record. Based on the additional analyses of trace elements and Sr isotopes, it was possible to attribute these differences to increased disequilibrium isotope fractionation in HBSH. Therefore, speleothem palaeoclimate records based on a single sample should be handled with care and a multi-proxy approach should be applied to enable trustworthy conclusions.

Acknowledgements

Table of Contents

Eidesstattliche Erklärung	III
Zusammenfassung	V
Abstract	VII
Acknowledgements	IX
Table of Contents	X
Commonly used abbreviations	XV
List of Figures	XVI
List of Tables	XXIII
Chapter 1: Introduction	1
Chapter 2: Basics	4
2.1 Speleothem formation	4
2.2 Dating of speleothem samples	6
2.3 Stable isotopes and trace elements	9
2.4 Strontium isotopes	13
2.4.1 The global Sr cycle	13
2.4.2 Strontium isotopes in speleothems	14
2.4.3 Application of LA-MC-ICP-MS for Sr isotopes	16
Chapter 3: Manuscript I: Sr isotope analysis of speleothems by LA-MC-ICP-MS: high temporal resolution and fast data acquisition	19
3.1 Abstract	20
3.2 Introduction	20
3.3 Speleothem samples	22
3.4 Materials and methods	22
3.4.1 Analytical setup	24
3.4.2 Reference materials	25
3.4.3 Laser ablation sampling method	26
3.5 Correction procedure for LA-MC-ICP-MS	27
3.5.1 Background correction	28
3.5.2 Rare-earth elements (REE)	28
3.5.3 Molecular interferences	29
3.5.4 Mass bias	30
3.5.5 Interference of Rb	30
3.5.6 Data processing	31
3.6 Results	31
3.6.1 Influence of tuning parameters on the $^{87}\text{Sr}/^{86}\text{Sr}$ ratio	32

3.6.2 Tests with reference materials.....	32
3.6.2.1 Nanosecond LA-MC-ICP-MS	32
3.6.2.2 Femtosecond LA-MC-ICP-MS	33
3.6.3 Speleothem GP5	34
3.6.4 Speleothem MAW-4	37
3.7 Discussion	38
3.7.1 Line scan versus spot analysis	38
3.7.2 Nanosecond versus femtosecond laser systems.....	39
3.7.3 Tuning parameters and suitable reference materials	40
3.7.4 Standard Bracketing	42
3.7.5 LA-MC-ICP-MS of Sr isotopes on speleothem samples	42
3.8 Conclusions.....	44
3.9 Acknowledgements	44
3.10 Supplement	45
Chapter 4: Manuscript II: Calcium Carbonate and Phosphate Reference Materials for Monitoring Bulk and Microanalytical Determination of Sr Isotopes	53
4.1 Abstract	54
4.2 Introduction.....	54
4.3 Reference materials	55
4.4 Analytical techniques	56
4.4.1 Column chemistry.....	57
4.4.2 Solution MC-ICP-MS	58
4.4.3 Laser ablation systems	58
4.4.4 LA-MC-ICP-MS analysis.....	59
4.5 Results	61
4.6 Discussion	64
4.7 Conclusions.....	66
4.8 Acknowledgements	67
4.9 Supplement	68
Chapter 5: Manuscript III: NanoSr – A new carbonate microanalytical reference material for <i>in-situ</i> Sr isotope analysis	81
5.1 Abstract	82
5.2 Introduction.....	82
5.3 Material	83
5.4 Analytical techniques	84
5.4.1 Element mass fractions	85
5.4.1.1 Electron Microprobe	85

5.4.1.2 Solution ICP-MS	85
5.4.1.3 LA-ICP-MS	85
5.4.2 Strontium isotopes	87
5.4.2.1 TIMS	87
5.4.2.2 MC-ICP-MS	87
5.4.2.3 LA-MC-ICP-MS	88
5.5 Results	89
5.5.1 Calcium mass fractions	89
5.5.2 Mass fractions of Sr and potential interfering elements	91
5.5.3 Trace element imaging	93
5.5.4 Solution Sr isotope analyses	94
5.5.5 Laser ablation Sr isotope analyses	95
5.6 Discussion	96
5.6.1 Element mass fraction	96
5.6.2 Strontium isotope composition	97
5.6.3 Availability of NanoSr	99
5.7 Conclusions	99
5.8 Acknowledgements	99
5.9 Supplement	100
Chapter 6: Manuscript IV: Evidence of warm and humid interstadials in central Europe during early MIS 3 revealed by a multi-proxy speleothem record	111
6.1 Abstract	112
6.2 Introduction	112
6.3 Site and sample description	114
6.3.1 Bunker Cave	114
6.3.2 Stalagmite Bu2	114
6.4 Methods	115
6.4.1 ²³⁰ Th/U-dating	115
6.4.2 Trace element analysis	116
6.4.3 Stable isotope analysis	117
6.4.4 Strontium isotope analysis	117
6.5 Results	119
6.5.1 ²³⁰ Th/U-dating	119
6.5.2 Trace elements and stable isotopes	121
6.5.3 Strontium isotopes	122
6.6 Discussion	123

6.6.1 Timing of growth phases	123
6.6.2 Bu2 stable isotope data	125
6.6.3 Palaeoclimate implications.....	128
6.7 Conclusions.....	132
6.8 Acknowledgements	132
6.9 Supplement	133
6.9.1 Discussion of Bu2 $\delta^{18}\text{O}$ values	142
Chapter 7: Manuscript V: A comparison of Holocene speleothem proxy records from Germany: Spatial variability of site-specific effects?	143
7.1 Abstract	144
7.2 Introduction.....	144
7.3 Site and sample description	146
7.3.1 Hüttenbläuserschachthöhle	146
7.3.2 Speleothem samples	147
7.4 Analytical methods.....	148
7.4.1 $^{230}\text{Th}/\text{U}$ -dating.....	148
7.4.2 Stable isotope analysis	148
7.4.3 Trace element analyses	149
7.4.4 Strontium isotope analyses	150
7.5 Results	150
7.5.1 $^{230}\text{Th}/\text{U}$ -dating.....	150
7.5.2 Trace elements	151
7.5.3 Stable isotopes	154
7.5.3.1 Processing of stable isotope data for regression analysis.....	155
7.5.4 Strontium isotopes	156
7.6 Discussion	157
7.6.1 Growth phases.....	157
7.6.2 Proxy data.....	158
7.6.2.1 Stable oxygen isotopes.....	159
7.6.2.2 Stable carbon isotopes	159
7.6.2.3 Trace elements	161
7.6.2.4 Strontium isotopes	163
7.6.3 Within cave correlation of HBSH and Bunker Cave.....	164
7.6.4 Inter-cave correlation between HBSH and Bunker Cave.....	165
7.6.5 Implications for speleothem based palaeoclimate reconstructions	167
7.7 Conclusion	168

7.8 Acknowledgements	169
7.9 Supplement	170
Chapter 8: Outlook	175
Chapter 9: Conclusions	178
Chapter 10: References	180
Appendix.....	201

Commonly used abbreviations

D/O: Dansgaard-Oeschger

EPMA: electron probe microanalysis

Ga: “giga-annum”, i.e. billion years

GICC05: Greenland Ice Core Chronology 2005

GSJ: Geological Survey of Japan

H5: Heinrich 5

ICP-MS: inductively coupled plasma mass spectrometry

IRD: ice-rafted debris

IRMS: isotope ratio mass spectrometer

ka: “kilo-annum”, i.e. thousand years

LA: laser ablation

ns/fs LA: nanosecond/femtosecond laser ablation

MC-ICP-MS. multi-collector inductively coupled plasma mass spectrometry

MIS: Marine Isotope Stage

MRM: microanalytical reference material

NIST: National Institute for technology

PCP: prior calcite precipitation

REE: rare earth element

RM: reference material

RSF: relative sensitivity factor

SD: standard deviation

SE: standard error

SIMS: secondary ion mass spectrometry

(ID-)TIMS: (isotope dilution) thermal ionisation mass spectrometry

USGS: United States Geological Survey

$\mu\text{m/a}$: μm per year

List of Figures

Fig. 2.1: Schematic overview of a typical karst system with a carbonate host rock and overlying soil and vegetation cover. Dissolution of the carbonate host rock is induced due to the generation of carbonic acid in the soil zone (Eq. 2.I). As a consequence, the Calcium carbonate (CaCO_3) of the host rock is dissolved (Eq. 2.II) and $\text{Ca}^{2+}_{(\text{aq})}$ -ions are transported via drip water inside the cave system. Equation 3.III describes the precipitation of CaCO_3 , caused by degassing of CO_2 in the cave atmosphere. Modified after Fairchild et al. (2006).

Fig. 2.2: Schematic drawing of the ^{238}U , ^{235}U and ^{232}Th decay chains (modified after Bourdon et al., 2003). Blue boxes indicate nuclides which are used for the ^{230}Th -dating of speleothems. Green boxes represent the final and stable Pb isotopes, depending on the decay chain. The greyscale reflects the half-lives of each nuclide, the darker the colour, the longer the half-life. All half-lives are indicated in the bottom of the boxes. ^{210}Pb is tagged in orange, and is used as alternative dating technique for young speleothem samples, using the ^{210}Pb -excess method. Red arrows indicate α -decay, while dark blue arrows indicate β -decay.

Fig 2.3: The secular Sr isotope curve for seawater $^{87}\text{Sr}/^{86}\text{Sr}$ variations in the Phanerozoic. Single measurements are obtained from marine carbonate sediments, evaporites and fossils, representing the value of the ocean. The shaded area around the curve is the estimated uncertainty obtained by Banner (2004). Results are normalized to a $^{87}\text{Sr}/^{86}\text{Sr}$ value of 0.710248 for NIST 987 (McArthur et al., 2001). Q = Quaternary, PG = Paleogene, Pre-C. = Precambrian. Modified after Burke et al. (1982) and Banner (2004).

Fig.3.1: [A] Sampling approach for speleothem GP5. The red rectangle indicates the sampling section, blue lines show the LA-MC-ICP-MS line scan positions. The spot analyses were performed near the right end of the third line scan as indicated by the blue spots. [B] Sampling approach for speleothem MAW-4. The red rectangle indicates the sampling section. Line scan and spot analyses are similarly indicated as in [A]. All line lengths, widths and distances are on scale.

Fig. 3.2: $^{87}\text{Sr}/^{86}\text{Sr}$ ratios obtained on reference solution NIST SRM 987. The orange line represents the literature value of $^{87}\text{Sr}/^{86}\text{Sr} = 0.71034 \pm 0.00026$ (GeoReM, Jochum et al., 2005), the shading in bright orange shows the 2 SE. The large fluctuations in the Sr isotope ratio are caused by changes in the settings of the source and transfer lenses of the Nu Plasma MC-ICP-MS, marked by the black arrows. Black diamonds represent measurements with the original lens settings, while blue (red) diamonds represent measurements with a 10 V increase (decrease) in lens voltage in comparison to the original lens setting.

Fig. 3.3: Influence of the different correction steps on the $^{87}\text{Sr}/^{86}\text{Sr}$ ratio of Jct-1 (black diamonds), MAW-4 (squares) and GP5 (triangles). Note that all results are mass bias corrected.

Fig. 3.4: $^{87}\text{Sr}/^{86}\text{Sr}$ ratios of reference material Jct-1 obtained during different days, showing the tuning influence during the first measurements. The orange line represents the reference value of Jct-1 of $^{87}\text{Sr}/^{86}\text{Sr} = 0.70917 \pm 0.00001$ (Weber et al., 2018b), the shading in bright orange corresponds to its 2 SE. Dashed vertical lines separate different days of measurements.

Fig. 3.5: $^{87}\text{Sr}/^{86}\text{Sr}$ ratios of reference materials JcP-1 and MACS-3 obtained by fs-LA-MC-ICP-MS. The red line represents the literature value of MACS-3 of $^{87}\text{Sr}/^{86}\text{Sr} = 0.7075532 \pm 0.0000037$ (Jochum et al., 2011a), the blue line shows the literature value of JcP-1 of $^{87}\text{Sr}/^{86}\text{Sr} = 0.70916 \pm 0.00002$ (Ohno and Hirata, 2007), with its 2 SE shown as bright blue shading. The uncertainty range for the reference value of MACS-3 is too small to be visible in the figure. Note that sample MACS-3-8 was strongly affected by very variable ^{84}Kr intensities during the blank measurement and probably during the sample measurement as well.

Fig. 3.6: [A] $^{87}\text{Sr}/^{86}\text{Sr}$ ratios are plotted against the distance from top of speleothem GP5. Line scan measurements affected by low signal intensities are marked red. [B] $^{87}\text{Sr}/^{86}\text{Sr}$ ratios of speleothem MAW-4 against distance from top [mm] for the line scan as well as the spot analyses. For better visualization of the error bars, spot analyses data were shifted to the right by 0.05 mm.

Fig. 3.7: Scatter plot of ^{88}Sr intensity vs. $^{87}\text{Sr}/^{86}\text{Sr}$ 2 SE. The dependency of the $^{87}\text{Sr}/^{86}\text{Sr}$ 2 SE on the ^{88}Sr intensity is shown for the line scan measurements of Jct-1, *Glycimeris* sp., GP5 and MAW-4.

Fig. 3.8: Black diamonds show the raw results of the $^{87}\text{Sr}/^{86}\text{Sr}$ LA-MC-ICP-MS line scan measurements performed using Jct-1 as a reference material and a sample. Corrected $^{87}\text{Sr}/^{86}\text{Sr}$ ratios of Jct-1 are shown as red diamonds. Note that the uncertainties increased in comparison to the raw data due to correction via the reference material. The orange line represents the reference value of Jct-1 of 0.70917 ± 0.00001 (Weber et al., 2018b).

Fig. A4.1: Comparison of $^{87}\text{Sr}/^{86}\text{Sr}$ ratios of different measurement techniques and literature values for four selected RMs. Top left: JcP-1; Top right: Jct-1; Bottom left: MACS-3; Bottom right: MAPS-4. ns = nanosecond, referring to NWR UP-213; fs = femtosecond, referring to NWR Femto200. * Note that for clarity, only the ns-LA-MC-ICP-MS of the Nu setups for Jct-1 are shown. For a comparison of the $^{87}\text{Sr}/^{86}\text{Sr}$ ratios of ns-LA-MC-ICP-MS of Jct-1 between Nu and Neptune, see Table 4.3.

Fig. A4.2: Raw data for one measurement of JcP-1 (JcP-1-45) to demonstrate the measurement configuration used in this study. For details in cup configuration, see Table 4.2.

Fig. A4.3: Raw data for one measurement of MACS-1 (MACS-1-5) to demonstrate the measurement configuration used in this study. For details in cup configuration, see Table 4.2.

Fig. A4.4: Raw data for one measurement of MAPS-4 (MAPS-4-21) to demonstrate the measurement configuration used in this study. For details in cup configuration, see Table 4.2.

Fig. A4.5: Raw data for one measurement of MAPS-5 (MAPS-5-6) to demonstrate the measurement configuration used in this study. For details in cup configuration, see Table 4.2.

Fig. 5.1: [A] Top view of a pressed nanopowder pellet with a diameter of 13 mm and a thickness of ca. 2 mm. [B] Backscattered electron (BSE) image of the edge of the compacted nanopowder pellet. [C] Top view of the compacted nanopowder pellet as secondary electron image (SEI). [D] Top view of the compacted nanopowder pellet showing darker and brighter areas in the BSE-image. [E] BSE image of the compacted nanopowder pellet with a magnification of 1300, showing the compaction of the nanopowder and the small pore spaces below the μm -range.

Fig. 5.2: Solution-based ICP-MS results for the mass fractions of Sr (black square, top graph) and Yb (red square), Er (purple star), Dy (blue diamond) and Rb (orange circle, bottom graph) for digestion of six samples. The blue line represents the average mass fraction of Sr ($494.9 \pm 51.4 \mu\text{g/g}$, $n = 6$) with the respective 2 SD uncertainties expressed as red lines. All uncertainties in the bottom panel are 2 SD.

Fig. 5.3: LA-ICP-MS results obtained in different laboratories. In total, seven different nanopowder pellets were analysed. [A] Strontium and Rb mass fractions obtained at the Institute of Geosciences, Mainz ($n = 72$, pellet 1 – 6). [B] Strontium and Rb mass fractions obtained at the CIGS, Modena ($n = 5$, pellet 7). [C] Strontium and Rb mass fractions obtained at MPIC, Mainz by spot ($n = 72$, pellet 1 – 6) and [D] line scan analyses ($n = 18$, pellet 1). The blue line represents the average mass fractions for Sr and Rb with the respective 2 SD uncertainties expressed as red lines. All uncertainties of single measurements are 1 SD.

Fig. 5.4: Elemental distribution for Sr (top left), Rb (bottom left), Mg (top right) and Ba (bottom right) of the pressed nanopowder pellet (pellet 9) obtained with the MapIT! software (Sforna and Lugli, 2017). The upper half of the nanopowder pellet was analysed. The length of the x-axis is 13 mm (diameter of the pellet) and the y-distance 6.6 mm for each image obtained.

Fig. 5.5: [A] MC-ICP-MS data from CIGS ($n = 19$). [B] MC-ICP-MS data from MPIC ($n = 21$). Black squares represent the $^{87}\text{Sr}/^{86}\text{Sr}$ and $^{84}\text{Sr}/^{86}\text{Sr}$ ratios, respectively, of the individual measurements. Blue lines show the average ratios with the corresponding 2 SD uncertainties as red lines. The grey square represents the results from the pressed nanopowder pellet, which was dissolved for solution analysis.

Fig. 5.6: Laser ablation MC-ICP-MS data obtained at the MPIC, Mainz [A] (pellets 1 – 6), and the CIGS [B] (pellet 7). The $^{87}\text{Sr}/^{86}\text{Sr}$ as well as the $^{84}\text{Sr}/^{86}\text{Sr}$ ratio of the individual measurements (black squares) are shown as well as the average ratio (blue line) and the respective 2 SD uncertainties (red lines).

Fig. 6.1: Map showing north-western parts of Europe with the location of MIS 3 climate records from Bunker Cave [A, this study], Crag Cave [B, Fankhauser et al. (2016)], Grotte des Puits de Pierra-la-Treiche [C, Pons-Branchu et al. (2010)], Villars Cave [D, Genty et al. (2003)], Hölloch Cave [E,

Moseley et al. (2014)], Klee gruben Cave [F, Spötl et al. (2006)] and the Eifel maar lakes [G, Sirocko et al. (2016)].

Fig. 6.2: Slab of speleothem Bu2 showing petrographic features and sampling details. Sample locations for $^{230}\text{Th}/\text{U}$ -dating are presented in supplementary Table A6.1.

Fig. 6.3: Age-depth relationship for stalagmite Bu2. Black points show the MC-ICP-MS ^{230}Th -ages, blue points highlight the two ages measured by TIMS (supplementary Table A6.1). The green line represents the age model calculated by StalAge (Scholz and Hoffmann, 2011), while red lines show the corresponding age-uncertainties (95% confidence interval). The vertical black line marks the hiatus between the two growth phases and was guided by the abrupt change in Y mass fraction (see section 6.5.2).

Fig. 6.4: Mass fractions of Mg, Sr and Y (high resolution data shown by grey lines) as well as $\delta^{18}\text{O}_{\text{slc}}$ (blue) and $\delta^{13}\text{C}$ (red) values of speleothem Bu2 shown versus distance from top (DFT). Note that the $\delta^{13}\text{C}$ axis is inverted. A hiatus was identified at 139.3 mm DFT. The spike in Mg and Y at 280 – 282 mm DFT is due to a detrital layer (see Fig. 6.2).

Fig. 6.5: [A] $^{87}\text{Sr}/^{86}\text{Sr}$ ratios of the host rock (blue circle), soil horizon A (orange diamond) and soil horizon C (green diamond) at Bunker Cave compared to stalagmite Bu2 values (black squares). [B] Close-up of Bu2 $^{87}\text{Sr}/^{86}\text{Sr}$ ratios during MIS 3 (black squares). The mean value is shown as a black line for each phase with the red box indicating the 1 SD. MIS 3 phase 1 shows generally higher $^{87}\text{Sr}/^{86}\text{Sr}$ ratios than MIS 3 phase 2. The soil samples show much more radiogenic $^{87}\text{Sr}/^{86}\text{Sr}$ ratios than the host rock and the speleothem. All measurement uncertainties are 2 SE.

Fig. 6.6: Comparison of growth phases of different MIS 3 speleothems in Europe with the NGRIP $\delta^{18}\text{O}$ and the marine MD99-2331 records. [A] NGRIP $\delta^{18}\text{O}$ record (Svensson et al., 2008). [B] Abundance of the foraminifera *Neogloboquadrina pachyderma* (orange) and the number of IRD per gram of sediment (black) in marine core MD99-2331 (Sánchez Goñi et al., 2013). Heinrich event 5 is marked in the figure (grey box) based on these data. [C] $^{230}\text{Th}/\text{U}$ -ages of the NALPS record (Moseley et al., 2014). [D] $^{230}\text{Th}/\text{U}$ -ages from Crag Cave (Fankhauser et al., 2016). [E] $^{230}\text{Th}/\text{U}$ -ages of stalagmites Vil-stm27 (red diamond, Genty et al., 2010), Vil-stm9 (purple stars, Genty et al., 2010) and Vil-stm14 (grey circles, Wainer et al., 2009) from Villars Cave. [F] $^{230}\text{Th}/\text{U}$ -ages from Bunker Cave stalagmite Bu2 (this study) [G] Growth phases based on the age-depth model (green line) with the respective age uncertainties gives at 95 % confidence levels (red triangles) of Bu2 (this study).

Fig. 6.7: Speleothem Bu2 $\delta^{13}\text{C}$ (red) and $\delta^{18}\text{O}_{\text{slc}}$ (blue) record plotted against age. Also shown are the $\delta^{13}\text{C}$ and $\delta^{18}\text{O}$ values from modern calcite precipitated on watch glasses (Riechelmann, 2010) placed under a drip site (TS 7) close to the Bu2 drip site and the Holocene section of Bu2 (Fohlmeister et al., 2012). Note that the $\delta^{13}\text{C}$ axis is inverted.

Fig. 6.8: Comparison of the Bu2 multi-proxy record with other MIS 3 climate records. Yellow boxes show the timing of D/O-events 12 and 11. [A] NGRIP $\delta^{18}\text{O}$ record (Svensson et al., 2008). [B] Abundance of the foraminifera *Neogloboquadrina pachyderma* (orange) and the number of IRD per gram of sediment (black) in marine core MD99-2331 (Sánchez Goñi et al., 2013). Heinrich 5 event is marked in the figure (grey box) based on these data. [C] NALPS oxygen isotope record from alpine speleothem samples (Moseley et al., 2014). [D] Villars Cave stable carbon isotope records, Vil-stm9 (purple), Vil-stm14 (grey), Vil-stm27 (red, Genty et al., 2003; Genty et al., 2010; Wainer et al., 2009) [E] Percentage of *Poaceae*-pollen in drill core DE3 from the Eifel, Germany (Sirocko et al., 2016). [F] Percentage of *Picea*-pollen in drill core DE3 from the Eifel, Germany (Sirocko et al., 2016). [G] Sr isotope data of Bu2. [H] Mg mass fraction of Bu2. [I] $\delta^{13}\text{C}$ values of Bu2. Note inverted axis for Mg mass fractions and $\delta^{13}\text{C}$ values. [J] Growth rate of Bu2.

Fig. A6.1: Effect of the sea-level correction on the $\delta^{18}\text{O}$ values of Speleothem Bu2, based on the correction factor of Duplessy et al. (2007) and the sea-level reconstruction of Bates et al. (2014b) and Bates et al. (2014a).

Fig. A6.2: Growth rate of Bu2 against DFT, based on the age-depth model constructed with StalAge (Scholz and Hoffmann, 2011).

Fig. A6.3: Comparison of the age-depth relationships of four different European speleothems that cover MIS 3. Black closed squares are the ^{230}Th -ages from Bu2 (this study). ^{230}Th -ages from speleothems from Villars Cave are illustrated by red diamonds (Vil-stm27, Genty et al., 2010), grey circles (Vil-stm14, Wainer et al., 2009) and purple stars (Vil-stm-9, Genty et al., 2010). In general, there are only few data points between 48 and 50 ka, showing the inhabiting influence of the Heinrich 5 cold event on speleothem growth in Europe. Bu2 stopped growing completely, while the Vil-stm14 stalagmite showed a significantly diminished growth rate. Vil-stm27 started to grow at this time around 48.5 ka and shows rapid growth between 47 and 44 ka.

Fig. A6.4: Thin section of Bu2 between 63 and 101 mm DFT showing the hiatus between the Holocene and MIS 3 at 76 mm DFT. Around 100 mm DFT, no hiatus is visible.

Fig. A6.5: Thin section of Bu2 between 123 and 151mm DFT showing the hiatus between the two MIS 3 growth phases at 139 mm DFT.

Fig. A6.6: $^{230}\text{Th}/\text{U}$ dating results and stable isotope data of Bu2 plotted against DFT.

Fig. A6.7: Increase in U at the detrital layer (see Fig. 6.2) suggesting post-depositional mobilization of U probably resulting in an apparently too young age for sample Bu2-29 (see supplementary Table A6.1 and section 6.5.1 in the manuscript).

Fig. 7.1: Geological map of the cave area with Hüttenbläuserschachthöhle and Bunker Cave indicated in the Middle/Upper Devonian limestone. Weather station (WS) Hagen-Fley is indicated in the north-western part of the map. Modified after Riechelmann et al. (2011).

Fig. 7.2: Overview of HBSH samples HBSH-1, HBSH-3, HBSH-4, and HBSH-5 (left to right). For samples HBSH-1 and HBSH-5, only the upper parts covering the Holocene were investigated. For HBSH-3 and HBSH-4, the major parts cover the Holocene.

Fig. 7.3: Age-depth relationship for stalagmites HBSH-1 (black), HBSH-3 (green), HBSH-4 (red) and HBSH-5 (blue) resulting from U-series dating. Measurements performed with the Neptune Plus MC-ICP-MS at the Institut of Geosciences are marked with an asterisk or a diamond, respectively. The coloured squares/diamonds represent the resulting ^{230}Th -ages with their respective 2 SE uncertainties. Please note that some of the measurement uncertainties are smaller than the square/diamond indicating the resulting age and are therefore not visible in the figure. Detailed uncertainties are given in Table 7.1. The green lines represent the age model calculated by StalAge (Scholz and Hoffmann, 2011) with the red lines representing the corresponding age uncertainties on a 95% confidence level for each sample. For the ages before the onset of the Holocene in stalagmites HBSH-3 and HBSH-4, no age model was calculated.

Fig. 7.4: [A] $\delta^{13}\text{C}$ and [B] $\delta^{18}\text{O}$ values for stalagmites HBSH-1 (black), HBSH-3 (green), HBSH-4 (red) and HBSH-5 (blue) based on the age-depth model. Please note the inverted axis for $\delta^{13}\text{C}$.

Fig. 7.5: [A] $\delta^{13}\text{C}$ and [B] $\delta^{18}\text{O}$ values averaged by a centennial mean for stalagmites HBSH-1 (black), HBSH-3 (green), HBSH-4 (red) and HBSH-5 (blue). Please note the inverted axis for $\delta^{13}\text{C}$.

Fig. 7.6: Strontium isotope results for HBSH-3 (green), HBSH-4 (red) and HBSH-5 (blue). In addition, Sr isotope values from the host rock and overlying soil at the nearby Bunker Cave (Weber et al., 2018a) are shown (see section 7.6.2.4 for details).

Fig. 7.7: Correlation matrix for stable carbon and oxygen isotopes and trace elements of stalagmite HBSH-3 during the early [A] and late [B] phase of the Holocene.

Fig. 7.8: $\delta^{18}\text{O}$ and $\delta^{13}\text{C}$ correlation matrix for [A] the four HBSH stalagmites, as well as the two HBSH stacks and [B] the four Holocene Bu stalagmites (Fohlmeister et al., 2012), as well as the two Bu stacks.

Fig. 7.9: Correlation matrix for [A] $\delta^{18}\text{O}$ of the four Bu (Fohlmeister et al., 2012) and HBSH stalagmites, as well as the two HBSH and Bu stacks and [B] $\delta^{13}\text{C}$ of the four Bu (Fohlmeister et al., 2012) and HBSH stalagmites, as well as the two HBSH and Bu stacks.

Fig. 7.10: Scaled stable isotope stacks for [A] $\delta^{18}\text{O}$ of Bunker Cave [B] $\delta^{18}\text{O}$ of HBSH [C] $\delta^{13}\text{C}$ of Bunker Cave and [D] $\delta^{13}\text{C}$ of HBSH. For all stacks, the replication indicates the number of individual stable isotope measurements averaged for the centennial mean for the specific time interval. Please note that the axes for $\delta^{13}\text{C}$ are inverted to match with the plots shown in Fig. 7.4 and 7.5.

Fig. A7.1: Trace element records of P, Ba, Sr and Mg obtained from HBSH-1.

Fig. A7.2: Trace element records of P, Ba, Sr and Mg obtained from HBSH-3.

Fig. A7.3: Trace element records of P, Ba, Sr and Mg obtained from HBSH-5.

Fig. A7.4: Growth rates for speleothem samples HBSH-1, HBSH-3, HBSH-4, HBSH-5. Please note the break in the y-axis.

Fig. A7.5: Correlation matrix for stable isotopes and trace elements of HBSH-5.

Fig. A7.6: Correlation matrix for stable isotopes and trace elements of HBSH-3.

Fig. A7.7: Correlation matrix for stable isotopes and trace elements of HBSH-1.

Fig. 8.1: Stable carbon (top) and Sr isotope (bottom) data obtained from stalagmite HBSH-1 from Hüttenbläuserschachthöhle. Both proxies show a similar trend on the longer time scales, covering almost the entire MIS 5. The similar pattern observed in both isotope systems suggests that the underlying mechanisms driving both proxies must be the same or closely linked, potentially related to soil development and changes in weathering above the cave.

Fig. 8.2: Transect through an unaltered (black) and altered (red) dental cube consisting of enamel and dentin (EDJ = enamel dentin junction) for $^{87}\text{Sr}/^{86}\text{Sr}$ (straight line) and $^{84}\text{Sr}/^{86}\text{Sr}$ (dashed line). The unaltered sample shows constant $^{87}\text{Sr}/^{86}\text{Sr}$ ratios throughout the whole sample, without any significant changes between enamel and dentin. The invariant $^{84}\text{Sr}/^{86}\text{Sr}$ ratio is also constant for the whole sample. In contrast, the altered sample, which was placed in a ^{86}Sr -enriched solution at 90°C for 63 days shows a significant decrease in $^{87}\text{Sr}/^{86}\text{Sr}$, as well as $^{84}\text{Sr}/^{86}\text{Sr}$ in the outer rim of the enamel and the whole dentin. Only the inner part of the enamel shows pristine $^{87}\text{Sr}/^{86}\text{Sr}$ and $^{84}\text{Sr}/^{86}\text{Sr}$ ratios, with the other parts being highly overprinted.

List of Tables

Table 3.1: Nu Plasma collector block assignments used for *in-situ* LA-MC-ICP-MS Sr isotope analysis of speleothems. Collectors H1, H2, H4, Ax and L1 – L5 are Faraday cups, IC-1 is an ion counter.

Table 3.2: Results of the line scan and spot analysis from speleothem samples GP5 and MAW-4. The alignment of the different cups is presented with the corresponding signal intensities. For most sample layers, three runs were performed. For these samples, the mean of all runs is shown.

Table 3.3: Operating parameters of the Nu Plasma MC-ICP-MS and the two laser ablation systems.

Table A3.1: Results of the solution measurements of reference solution NIST SRM 987 for solution MC-ICP-MS and reference material Jct-1 for LA-MC-ICP-MS.

Table A3.2: Raw $^{87}\text{Sr}/^{86}\text{Sr}$ measurements for each line scan and spot measurement of GP5.

Table A3.3: Raw $^{87}\text{Sr}/^{86}\text{Sr}$ measurements for each line scan and spot measurement of MAW-4.

Table 4.1: Operating parameters of the Neptune and Nu-Plasma MC-ICP-MS systems and the NWR UP-213 and NWR Femto200 laser ablation systems. Note that the NWR UP-213 operating parameters here are those used for the coupling to the Nu-MC-ICP-MS. A short summary of operating parameters for the coupling to the Neptune are described in the analytical section in the text.

Table 4.2: Cup configuration for Nu Plasma and Neptune MC-ICP-MS and possible interferences during analysis.

Table 4.3: $^{87}\text{Sr}/^{86}\text{Sr}$ results of carbonate and phosphate RMs in the literature and this study in comparison. Compiled $^{87}\text{Sr}/^{86}\text{Sr}$ ratios are divided into reference (Ref) and information (Inf) values.

Table 4.4: Test portion masses and Sr content of carbonate and phosphate RMs for different measurement techniques.

Table A4.1: Results for ns-LA-MC-ICP-MS measurements of RM Jct-1.

Table A4.2: Results for fs-LA-MC-ICP-MS measurements of RM Jct-1.

Table A4.3: Results for ns-LA-MC-ICP-MS measurements of RM Jcp-1.

Table A4.4: Results for fs-LA-MC-ICP-MS measurements of RM Jcp-1.

Table A4.5: Results for ns-LA-MC-ICP-MS measurements of RM MACS-1.

Table A4.6: Results for ns-LA-MC-ICP-MS measurements of RM MACS-3.

Table A4.7: Results for fs-LA-MC-ICP-MS measurements of RM MACS-3.

Table A4.8: Results for ns-LA-MC-ICP-MS measurements of RM MAPS-4.

Table A4.9: Results for fs-LA-MC-ICP-MS measurements of RM MAPS-4.

Table A4.10: Results for ns-LA-MC-ICP-MS measurements of RM MAPS-5.

Table A4.11: Results for ns-LA-MC-ICP-MS measurements of RM NIST SRM 1400.

Table A4.12: Results for ns-LA-MC-ICP-MS measurements of RM NIST SRM 1486.

Table A4.13: Monitoring of Dy as potential interference on mass 82 during LA-MC-ICP-MS.

Table A4.14: Results for solution MC-ICP-MS measurements of RMs analysed in this study.

Table 5.1: Operational parameters for the different (LA-MC-)ICP-MS systems used during this study.

Table 5.2: Mass fractions of Mg, Rb, Sr, Ba, Dy, Er and Yb, as well as respective test portion mass for the different analytical techniques. Typical RSF (relative sensitivity factor) values for carbonate reference materials used during data acquisition usually agree within 10% uncertainty with the GeoReM values (Jochum et al., 2005) for all presented elements (supplementary Tables A5.1 and A5.2). 1 = Institute of Geosciences, Mainz; 2 = CIGS, Modena; 3 = MPIC, Mainz; NA = not available, b.d.l. = below detection limit.

Table 5.3: $^{87}\text{Sr}/^{86}\text{Sr}$ and $^{84}\text{Sr}/^{86}\text{Sr}$ ratios for the different analytical techniques with the respective test portion masses of the measurements. The resulting $^{87}\text{Sr}/^{86}\text{Sr}$ ratio for NanoSr is the mean of all solution-based measurements. *The test portion mass for the solution based analyses take the total amount of samples material into account, which was dissolved and homogenized for each aliquot. The actual Sr amount used for the measurements are usually much smaller, i.e. 100 ng for TIMS and 50 – 500 ng for MC-ICP-MS, depending on the analysis time and used mass fraction for analysis. All uncertainties are given as 2 SD. In addition, we provide the mean $^{87}\text{Sr}/^{86}\text{Sr}$ ratio based on a 95 % confidence level (CL). 1 = MPIC, Mainz, 2 = CIGS, Modena; NA = not available.

Table A5.1: Quality control materials from the LA-ICP-MS measurements at the Max Planck Institute for Chemistry, Mainz.

Table A5.2: Quality control materials from the LA-ICP-MS measurements at the Institute of Geosciences, Mainz.

Table A5.3: LA-ICP-MS spot analyses of NanoSr at the Institute of Geosciences, Mainz.

Table A5.4: LA-ICP-MS spot analyses at the Max Planck Institute for Chemistry, Mainz.

Table A5.5: LA-ICP-MS line scan analyses at Max Planck Institute for Chemistry, Mainz.

Table A5.6: LA-ICP-MS spot analyses at Centro Interdipartimentale Grandi Strumenti, University of Modena and Reggio Emilia.

Table A5.7: ICP-MS analyses at Centro Interdipartimentale Grandi Strumenti, University of Modena and Reggio Emilia.

Table A5.8: MC-ICP-MS analyses at Centro Interdipartimentale Grandi Strumenti, University of Modena and Reggio Emilia.

Table A5.9: MC-ICP-MS analyses at Max Planck Institute for Chemistry, Mainz.

Table A5.10: LA-MC-ICP-MS analyses at Centro Interdipartimentale Grandi Strumenti, University of Modena and Reggio Emilia.

Table A5.11: LA-MC-ICP-MS analyses at Max Planck Institute for Chemistry, Mainz.

Table A5.12: TIMS analyses at Max Planck Institute for Chemistry, Mainz.

Table A5.13: EPMA analyses at Institute of Geosciences, Mainz.

Table A6.1: Uranium and Th mass fractions, activity ratios and ^{230}Th -ages for stalagmite sample Bu2. All uncertainties are quoted as 2 SE. Samples marked with an asterisk were analysed by TIMS, all other samples by MC-ICP-MS. Ages are given in thousand years (ka) before 2017. All activity ratios and ages were corrected for detrital contamination, using a $^{232}\text{Th}/^{238}\text{U}$ mass ratio of 3.8, calculated from the average Th and U mass fractions of tonalities which are believed to be representative for the bulk continental crust (Wedepohl, 1995), assuming an uncertainty of 50 % and ^{230}Th , ^{234}U and ^{238}U in secular equilibrium for the detritus. Activity ratios were calculated using the half-lives from Cheng et al. (2000). Sample BU-2-29 was not used for the age model and is therefore presented in italic (see section 6.5.2).

Table A6.2: Quality control materials from the LA-ICP-MS measurements at the Institute of Geosciences, Johannes Gutenberg University Mainz.

Table A6.3: Operational parameters for LA-ICP-MS measurements at the Goethe University Frankfurt and the Johannes Gutenberg University Mainz.

Table 7.1: Uranium and Th mass fractions, activity ratios and ^{230}Th -ages for Holocene stalagmites from Hüttenbläuserschachthöhle. All uncertainties are quoted as 2 SE. All activity ratios and ages were corrected for detrital contamination, using a $^{232}\text{Th}/^{238}\text{U}$ mass ratio of 3.8 ± 1.9 , calculated from the average Th and U mass fractions of tonalities which are believed to be representative for the bulk continental crust (Wedepohl, 1995). We assumed ^{230}Th , ^{234}U and ^{238}U to be in secular equilibrium for the detritus. Activity ratios were calculated using the half-lives from Cheng et al. (2000). All measurements highlighted with an asterisk have been measured at the Institute of Geosciences with a Neptune Plus MC-ICP-MS. Sample HBSH-1 has been analysed at the School of Geographical Sciences, Bristol. BDL = below detection limit; NA = not available due to ^{232}Th mass fractions below detection limit.

Chapter 1: Introduction

During the past decades, speleothems became an important archive for terrestrial palaeoclimate reconstruction. Although dependent on karst areas, they are found worldwide in a variety of climatic zones, from the arctic to the tropics, as well as at different altitudes (Fairchild and Baker, 2012). One of their main advantages relative to other palaeoclimate archives, is their potential for very precise dating using U-series disequilibrium methods (Richards and Dorale, 2003; Scholz and Hoffmann, 2008). In addition, the analysis of stable isotope values of carbon ($\delta^{13}\text{C}$) and oxygen ($\delta^{18}\text{O}$) are established methods for deciphering past climate variability in high resolution and on long time scales, often as a continuous record (e.g. Cheng et al., 2016; Fairchild et al., 2006; Lachniet, 2009; McDermott, 2004; Wang et al., 2001). In addition, trace element mass fractions and ratios have been widely used to further constrain the palaeoclimate reconstructions based on speleothems (e.g. Fairchild et al., 2000; Fairchild and Treble, 2009; Verheyden et al., 2000; Wassenburg et al., 2012).

While most studies are based on the combination of stable carbon and oxygen isotopes, potentially combined with trace elements, several other proxies have been applied to speleothems in recent times. Strontium isotopes are one promising proxy in speleothem science, due to their independence from stable carbon and oxygen isotopes and their direct relationship with the dripwater entering the cave (Fairchild and Baker, 2012). In most cases, the radiogenic $^{87}\text{Sr}/^{86}\text{Sr}$ ratio is used to reconstruct past hydrological changes in the epikarst, as well as changes in aeolian dust incorporation in the overlying soil (e.g. Banner et al., 1994; Banner et al., 1996; Frumkin and Stein, 2004). Although the stable Sr isotope value $\delta^{88}\text{Sr}$ has been used to derive further information about processes in the soil (Halicz et al., 2008), it has not been widely applied to speleothems.

Initially, the analysis of Sr isotopes was restricted to thermal ionisation mass spectrometry (TIMS), which requires chemical separation prior to analysis and elongated analysis times for each sample (Platzner, 1985). The development of multi-collector inductively coupled plasma mass spectrometry (MC-ICP-MS) coupled to a laser ablation (LA) system (Wieser and Schwieters, 2005), allowed for dramatic reduction in the required analysis time. Furthermore, the use of *in-situ* laser ablation techniques does not require chemical separation prior to analysis.

This thesis deals with the application of Sr isotopes to a variety of speleothem samples and their use as palaeoclimatic and environmental proxies. *In-situ* analysis of Sr isotopes by LA-MC-ICP-MS was successfully applied to speleothem samples and further tested and improved by using suitable reference materials with different matrices. All measurement techniques for Sr isotopes described above (TIMS and (LA-)MC-ICP-MS) were used in this thesis research allowing for evaluation and direct comparison of the accuracy and precision of the different techniques. After careful quality assurance of the different techniques, Sr isotopes were analysed in multiple speleothem samples. The Sr isotopes were used to study Marine Isotope Stage (MIS) 3 and the Holocene and enabled a deeper understanding of the underlying processes affecting speleothem formation.

The initial requirement for successfully measuring Sr isotopes was the establishment of the analytical technique. Manuscript I (chapter 3) deals with the development of the *in-situ* methodology at the Max Planck Institute for Chemistry, Mainz, using a Nu Plasma MC-ICP-MS. The instrument was coupled to a CETAC Aridus desolvator system to establish the analytical procedure. Afterwards, the mass spectrometer was coupled to a conventional nanosecond (ns) laser ablation system, as well as a state-of-the-art femtosecond (fs) laser ablation system to highlight the robustness of the method, using different carbonate reference materials. The final step was the application of the LA-MC-ICP-MS methodology on two different aragonitic speleothem samples from India and Morocco and comparison of the results of spot and line scan analyses.

Measurements performed with *in-situ* techniques, such as LA-MC-ICP-MS, relies on the quality and choice of a suitable reference material for the sample of interest. Therefore, manuscript II (chapter 4) deals with the systematic investigation of suitable reference materials for Sr isotope analysis by laser ablation. In total, eight different reference materials (four carbonates and four phosphates) were analysed by solution based and ns-/fs-laser ablation MC-ICP-MS at different laboratories. The results obtained by solution techniques were in agreement with literature data (if available). However, some of the laser ablation results for reference materials with low Sr mass fraction and high mass fractions of Rare Earth Elements (REEs) showed significantly biased $^{87}\text{Sr}/^{86}\text{Sr}$ ratios. This indicates the importance of suitable reference materials for successful analysis of carbonate and phosphate (e.g. bones and teeth) samples for Sr isotope analysis by LA-MC-ICP-MS.

Most of the widely available carbonate reference materials have a high Sr mass fraction, since they often are processed marine carbonates. However, speleothems usually have a much lower Sr mass fraction than marine carbonates. Therefore, the quality control and correction of Sr isotope measurements of low Sr carbonates by LA-MC-ICP-MS should be performed with a reference material with a similar Sr mass fraction. In manuscript III (chapter 5), a new synthetic nanopowder carbonate reference materials (NanoSr) is presented, in which Sr mass fraction was customised to match the demands for a low Sr reference material. Since a new reference material needs to be very precisely characterized, different analytical techniques have been performed at different laboratories. Analyses included the determination of the Ca mass fraction by electron probe micro analysis (EPMA), as well as the determination of trace element mass fractions, both using solution and laser ablation ICP-MS. To determine the most accurate and precise Sr isotope ratios, TIMS analysis were performed for the reference material. In addition, Sr isotopes have been determined by MC-ICP-MS in two laboratories to support the results obtained by TIMS. The final proof-of-concept was established by performed LA-MC-ICP-MS Sr isotope analyses in two laboratories, which yielded identical $^{87}\text{Sr}/^{86}\text{Sr}$ ratios as the solution-based techniques, proving micro-homogeneity of the material for *in-situ* Sr isotope analysis.

In contrast to methodological development and validation, manuscript IV (chapter 6) deals with the reconstruction of past climate variability during the Marine Isotope Stage (MIS) 3 in Central Europe. A

unique speleothem sample from Bunker Cave, which grew during the early phase of MIS 3, was analysed using a multi-proxy approach, including stable isotope, trace element and Sr isotope analysis. Uranium-series dating revealed two growth phases, separated by a hiatus, potentially related to the Heinrich 5 event. While the first growth phase was characterised by a fast growth rate and warm and humid conditions, the second growth phase showed a significantly declined growth rate and much drier conditions. However, since speleothem growth in Central Europe is usually sparse during MIS 3, these two growth phases are exceptional and indicate much more humid conditions during this time than previously believed. Unfortunately, this record is only based on a single speleothem sample from Bunker Cave, covering the MIS 3, which required the multi-proxy approach to verify the palaeoclimate interpretation.

To assess the significance of a single speleothem record, several samples from the same cave need to be analysed and systematically compared. Manuscript V (chapter 7) deals with four Holocene speleothem samples from Hüttenbläuserschachthöhle (HBSH). The stable isotope of these speleothems were analysed, as well as trace elements and Sr isotopes. In general, the four speleothem samples show similar trends in their stable isotope records. However, a significant transition is visible between 7 – 6 ka, wherein $\delta^{13}\text{C}$ values becoming progressively more positive. This transition is also visible in the trace element record, as well as in the Sr isotopes. Based on correlations of the trace elements and stable isotopes, it was possible to validate this transition. As the younger phase is characterised by a much slower growth rate in all speleothem samples, as well as a progressive increase in $\delta^{13}\text{C}$ and $\delta^{18}\text{O}$, an increased disequilibrium isotope fractionation is assumed to mainly influence the younger part of the records. Due to the close proximity (<1 km) of HBSH to the intensively studied Bunker Cave, the Holocene stable isotope records of both caves have been compared. While the early Holocene shows similar trends in both caves, the $\delta^{13}\text{C}$ values diverge in the younger half of the Holocene. This pattern is attributed to the assumed disequilibrium isotope fractionation in HBSH, overprinting the climatic and environmental signal. These results clearly show, that climate interpretations based on a single speleothem, or even a single cave, can be biased by cave effects, which overprint the climatic signals. Thus, a multi-proxy approach (e.g. analysis of trace elements, Sr isotopes, ...) is strongly encouraged to validate the obtained stable isotope dataset.

Chapter 2: Basics

For the understanding of palaeoclimatic forcing on speleothems, some basic knowledge about speleothem formation and the proxy incorporation is necessary. To provide those basics, the following paragraphs will guide through different aspects of speleothem science and the analytical methodology.

2.1 Speleothem formation

Speleothems naturally occur in karstic environments all over the world. They grow inside of cavities in carbonate host rocks, which act as an aquifer and ensure the transport of liquid water inside the cave (Ford and Williams, 2013). Speleothems mainly consist of calcium carbonate (CaCO_3), usually in form of calcite and/or aragonite. Typical carbonate rocks in which stalagmites develop are limestones (CaCO_3) and dolomites ($\text{CaMg}(\text{CO}_3)_2$), resulting in differences in speleothem geochemistry. Due to their growth in a protected environment over time spans ranging from hundreds to several ten- to hundred thousands or even million of years, they contain valuable information about Earth's climate history. Most studies using speleothem samples deal with stalagmites, building up from the cave floor. However, some studies focus on flowstones, forming from a thin layer of water on cave walls and floors (Fairchild and Baker, 2012). To reconstruct past climate variability using speleothems, the formation processes need to be understood to draw conclusions about various influencing factors during growth. In general, there are five main factors influencing speleothem growth and geochemistry: the atmosphere, the vegetation and soil above the cave, the karstic aquifer, primary speleothem crystal growth and secondary alteration (Fairchild et al., 2006).

Speleothem formation is coupled to dissolution and precipitation of carbonate material. Meteoric water precipitates above the cave system and enters the soil. The high partial pressure of carbon dioxide ($p\text{CO}_2$) in the soil in comparison to the atmosphere, i.e. due to root transpiration and microbial activity, leads to the formation of carbonic acid (Fig 2.1, Eq. 2.I) which dissolves the carbonate in the host rock (Fig 2.1, Eq. 2.II). The seepage water in the karst ultimately enters a cavity with lower $p\text{CO}_2$ values than in the soil and epikarst. After dripping from the ceiling of the cave (potentially forming a stalactite), the water drips down on top of a stalagmite. A thin layer of solution (approximately 0.1 mm) is formed, excess CO_2 degasses within seconds from the saturated solution (Hansen et al., 2013) and speleothem formation is induced (Fig. 2.1, Eq. 2.III; Fairchild et al., 2006; Fairchild and Baker, 2012). Precipitation can also occur prior to the deposition in the cave, which is called prior calcite precipitation (PCP). This effect can cause reduced super-saturation and might be identified by a characteristic evolution of the chemical composition, e.g. increasing Mg/Ca or Sr/Ca ratios, of the water and ultimately in the speleothem (Fairchild and Baker, 2012).

The resulting growth rate of stalagmites can cover different magnitudes. Stalagmites growing in humid and warm climates can grow at a rate of several hundreds of μm per year ($\mu\text{m}/\text{a}$, see speleothem MAW-

4 in section 3.3) or even more. In contrast, speleothems in cold or temperate climate zones grow more slowly and can additionally show large variations in growth rate (see speleothem Bu2 in section 6.5.1 and speleothems from Hüttenbläuserschachthöhle in section 7.5.1). In general, a typical growth rate for speleothems in cool temperate regions might be less than 100 $\mu\text{m/a}$ (Fairchild and Baker, 2012). However, speleothem growth is not always continuous and can stop due to different reasons. Growth cessation results in a hiatus, which either indicates a deterioration in climatic conditions or a change in local processes within the aquifer, causing a shift in drip location (Fairchild et al., 2006; Fairchild and Baker, 2012).

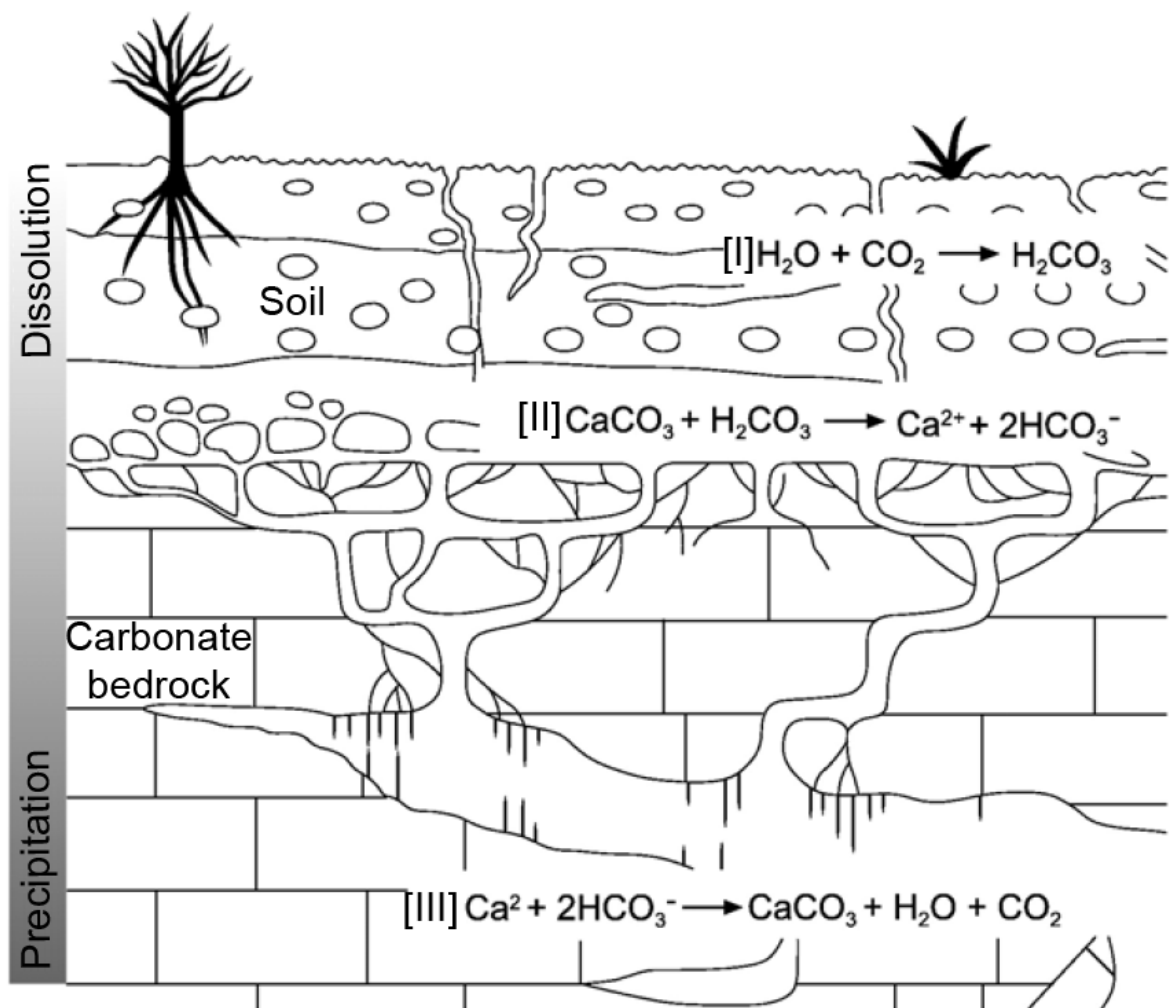


Fig. 2.1: Schematic overview of a typical karst system with carbonate host rock, overlying soil and vegetation cover. Dissolution of the carbonate host rock is induced by the carbonic acid in the soil zone (Eq. 2.I). As a consequence, the Calcium carbonate (CaCO_3) of the host rock is dissolved (Eq. 2.II) and $\text{Ca}^{2+}_{(\text{aq})}$ -ions are transported via drip water inside the cave system. Equation 2.III describes the precipitation of CaCO_3 , caused by degassing of CO_2 in the cave atmosphere. Modified after Fairchild et al. (2006).

2.2 Dating of speleothem samples

One of the major advantages of speleothems in comparison to other palaeoclimate archives is their precise age control. Nowadays, the most often applied dating technique for speleothem samples is the U-series disequilibrium method (Richards and Dorale, 2003; Scholz and Hoffmann, 2008). While initial U-series dating was performed using alpha spectrometry, the development of TIMS improved the precision of ^{230}Th -dating significantly. A further step towards modern-day applications of U-series dating of speleothems was the development of MC-ICP-MS (Wieser and Schwieters, 2005), with reduced sample size and improved analytical precision. However, all methods require chemical separation of U and Th using an ion-exchange resin prior to analysis (Hoffmann, 2008).

Uranium-series dating is based on the radioactive decay of the radionuclides ^{238}U , ^{235}U and ^{232}Th , all of which have a long half-life and, in each case, finally decay into a different stable isotope of Pb (Fig. 2.2). To date samples using these isotopes, the natural state of radioactive equilibrium (e.g. in the carbonate host rock) needs to be disturbed. Natural processes fractionating the nuclides and causing a disequilibrium, can disturb the activity between the daughter and parent isotope. By returning to the equilibrium state, it is possible to quantify the timing of fractionation and therefore the timing of speleothem deposition (Bourdon et al., 2003; Scholz and Hoffmann, 2008). Due to different geochemical behaviours of U and Th, elemental fractionation is induced in the cave system. On the one hand, U mainly exists as uranyl ion $(\text{UO}_2)^{2+}$ or several uranyl carbonate forms at the Earth's surface. Therefore, it is highly soluble in water and will be ultimately incorporated in the mineral lattice of a speleothem during CaCO_3 precipitation. Uranium mass fraction in speleothems ranges from nearly zero to even more than 100 $\mu\text{g/g}$ (Ford and Williams, 2013). On the other hand, Th is almost insoluble in water (Ivanovich and Harmon, 1992) and particle reactive, i.e. absorbed onto particles and therefore not available for the seepage and drip water in the karst system. Thus, Th is not incorporated in speleothem samples during deposition, resulting in an initial disequilibrium of U and Th and allowing the application of the ^{230}Th -dating technique.

However, prerequisites for the dating of speleothem samples using U-series disequilibrium methods include some basic assumptions:

- 1) No post-depositional diagenesis, resulting in a closed system;
- 2) No initial ^{230}Th incorporation into the speleothem during deposition, resulting in $(^{230}\text{Th}/^{238}\text{U}) = 0$;
- 3) No detrital ^{230}Th , ^{234}U and ^{238}U .

Due to the protected cave environment, the first assumption is usually true for most speleothem samples. Nevertheless, if there is any loss or addition of isotopes within the decay chain, the obtained ages will be erroneous and probably not in stratigraphic order. This can be caused by several factors. It is possible, for example that the U-series system was not closed for the entire formation time of the speleothem, i.e.

dissolution and re-precipitation of speleothem calcite has occurred after deposition. This is only possible when corrosive water is dripping on top of the stalagmite. Different scenarios resulting in corrosive waters are described in Scholz et al. (2014). Uranium can be either lost or added during those phases, resulting in deviating ($^{230}\text{Th}/^{238}\text{U}$) ratios. Thorium, however, is unlikely to be added or lost during open system behaviour due to its insolubility in water. Post-depositional U loss results in elevated ($^{230}\text{Th}/^{238}\text{U}$) ratios and will result in apparently older ^{230}Th -ages. In contrast, post-depositional U gain will result in lower ($^{230}\text{Th}/^{238}\text{U}$) ratios and therefore the obtained ages will appear to be too young (see section 6.5.1, Table A6.1 and Scholz et al., 2014). The second assumption is not always fulfilled, since several speleothem samples incorporate detrital ^{232}Th and therefore a detrital component of ^{230}Th . Unfortunately, there is no universal ($^{230}\text{Th}/^{232}\text{Th}$) ratio, resulting in different correction techniques for detrital Th, e.g. by using an estimation of the initial isotopic composition of the detrital material (Wedepohl, 1995). ^{230}Th ages must be rejected if significant Th contamination cannot be excluded or corrected. The third assumption is a general assumption for the U-series disequilibrium method. If this assumption is not fulfilled, i.e. due to large diagenetic alteration, the whole decay chain becomes disturbed, resulting in an open system, hampering the ^{230}Th -dating method.

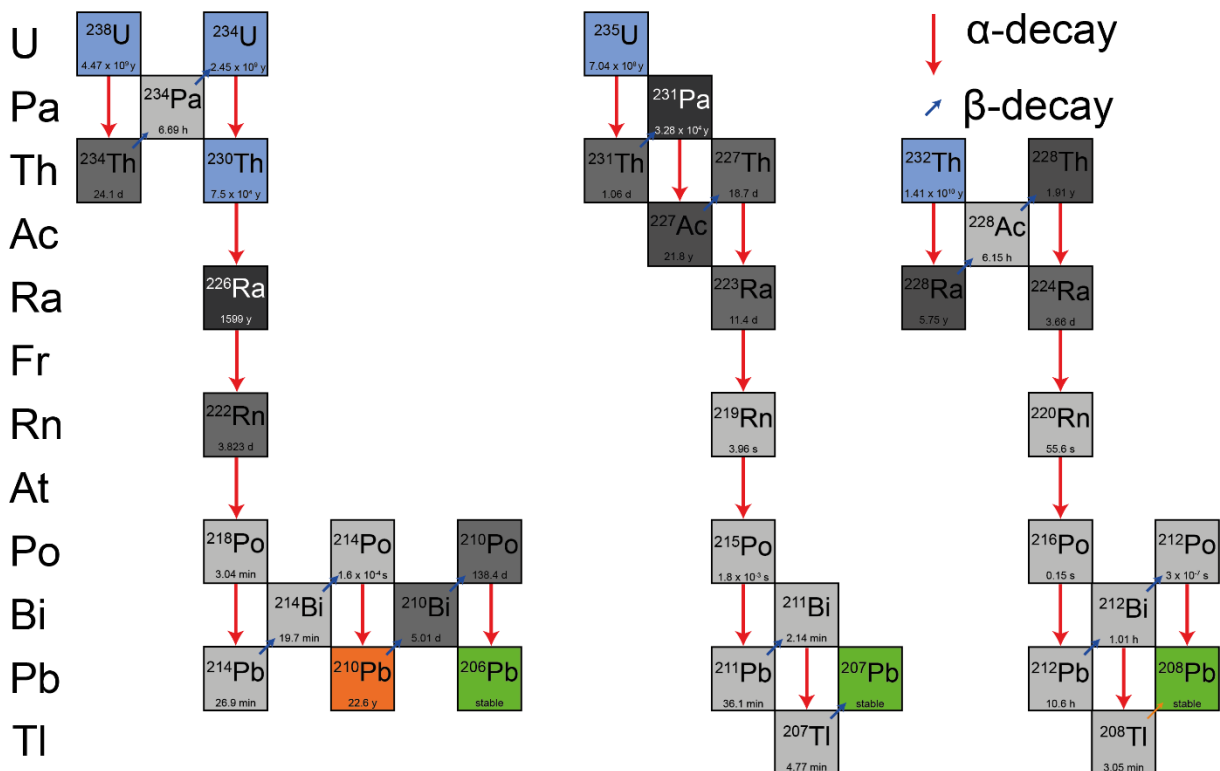


Fig. 2.2: Schematic drawing of the ^{238}U , ^{235}U and ^{232}Th decay chains (modified after Bourdon et al. 2003). Blue boxes indicate nuclides which are used for the ^{230}Th -dating of speleothems. Green boxes represent the final and stable Pb isotopes, depending on the decay chain. The greyscale reflects the half-lives of each nuclide, the darker the colour, the longer the half-life. All half-lives are indicated in the

bottom of the boxes. ^{210}Pb is tagged in orange, and is used as alternative dating technique for young speleothem samples, using the ^{210}Pb -excess method. Red arrows indicate α -decay, while dark blue arrows indicate β -decay.

In order to calculate ages using U-series dating, it is necessary to calculate both the ($^{230}\text{Th}/^{238}\text{U}$) as well as the ($^{234}\text{U}/^{238}\text{U}$) ratio. Isotope fractionation between ^{234}U and ^{238}U is caused by the α -recoil effect. During α -decay of ^{238}U to ^{234}U , a He nucleus is emitted and causes a displacement in the mineral lattice and the ^{234}U can be more easily removed subsequently. This effect usually causes higher $^{234}\text{U}/^{238}\text{U}$ ratios of ground water than expected from the equilibrium value. However, the ($^{234}\text{U}/^{238}\text{U}$) of the drip water can have two influencing factors, the age of the host rock and the water residence time within the host rock. A long residence time results in high ($^{234}\text{U}/^{238}\text{U}$) ratios, while during periods of fast percolating water, the ($^{234}\text{U}/^{238}\text{U}$) ratio should be close to secular equilibrium (Scholz and Hoffmann, 2008). Since the initial ($^{234}\text{U}/^{238}\text{U}$) ratio is not necessary for the age calculation, the application of ^{230}Th -dating is not affected by this process. Instead, the faster decay of ^{234}U (half-life = 2.45×10^5 a) in contrast to ^{238}U (half-life = 4.47×10^9 a) results in a decrease of ($^{234}\text{U}/^{238}\text{U}$) with increasing age and can therefore be used to calculate an age together with the ($^{230}\text{Th}/^{238}\text{U}$) ratio up to an age range of 600 ka before reaching secular equilibrium.

After calculating the individual ages of speleothem sub-samples, it is necessary to construct an age-distance model to generate a proxy time series. Since proxy records are usually in a much higher spatial resolution in comparison to the samples for the age determination (see also section 2.3), this step is necessary to construct a robust climate reconstruction with reliable ages. The simplest method is the linear point-to-point interpolation (e.g. McDermott et al., 1999), however, there are several models and algorithms available in the literature to calculate age-distance models (Breitenbach et al., 2012; Drysdale et al., 2004; Genty et al., 2006; Ramsey, 2008; Scholz and Hoffmann, 2011; Spötl et al., 2006). For this thesis, all age data was processed with the algorithm StalAge (Scholz and Hoffmann, 2011). This algorithm calculates the age model based on a Monte-Carlo simulation, always fitting straight lines to three data points. Major outliers are accounted for and age inversions are prevented by using an iterative procedure to increase the uncertainty of minor outliers, resulting in a final age model with 95% confidence intervals. The resolution of the age-distance model can be adjusted by the user to match the spatial resolution of the proxy data. Therefore, constructing an age model based on the ^{230}Th -dating is the final step of applying the U-series disequilibrium dating for speleothem samples.

Besides U-series dating, some other dating techniques have been applied for speleothem samples and a selection of methods will be discussed shortly in the following. Very young speleothem samples (only few decades old or younger) are often hard to date with U-series dating, especially if they have a low U-content. Due to the young age, only a small fraction of the initially incorporated ^{234}U has been decayed

to ^{230}Th within the ^{238}U decay series, limiting the application using even state-of-the-art MC-ICP-MS techniques. Radiocarbon (^{14}C) dating of speleothems is usually hampered by the highly variable dead carbon fraction of speleothem samples in the range of 5 – 40% (Genty and Massault, 1999; Genty et al., 1999; Genty et al., 2001) and the variability over time. However, due to atmospheric nuclear bomb testing in the 1960s, the so-called “bomb-peak”, which created a spike in atmospheric ^{14}C , is detectable in speleothem samples via vegetation and soil, leading to a significant increase in ^{14}C in speleothems after the 1960s. This information can be used to demonstrate modern deposition of speleothem calcite and to determine the transfer rate of carbon from the surface to the stalagmite (Genty and Massault, 1999; Genty et al., 1999).

A second approach to detect and estimate recent speleothem growth within the last 100 years is the ^{210}Pb excess method (Baskaran and Iliffe, 1993; Baskaran, 2012). The ^{210}Pb is part of the ^{238}U decay series and the radiogenic daughter (with some very short-lived isotopes in between) of ^{222}Rn with a half-life of 22.3 a. ^{222}Rn is highly concentrated in groundwater and will ultimately enter the cave as part of the seepage water and drip from the cave’s ceiling on top of the stalagmite. ^{210}Pb is then produced at a constant rate by the decay of ^{222}Rn (half-life = 3.8 d) and incorporated in the crystal lattice during CaCO_3 precipitation. Therefore, young speleothem samples (< 100 a) should be dateable by the ^{210}Pb excess method. The ^{210}Pb mass fraction decreases exponentially with depth from the outer surface and enables us to determine the age of speleothems (Baskaran and Iliffe, 1993).

While the dating techniques mentioned above have a maximum age limitation (i.e. resulting from reaching secular equilibrium for U-Th or the complete decay of the parent nuclide for ^{14}C), the U-Pb dating method has no upper limit and can, theoretically, be applied to samples older than approximately 100 ka (Richards et al., 1998). However, application of U-Pb dating to speleothems has several prerequisites, which have to be considered. Speleothems usually have a very low mass fraction of Pb, making the measurement challenging and MC-ICP-MS analysis the technique of choice. Ideal speleothem samples have a high U mass fraction and no “common Pb” (Richards et al., 1998; Woodhead et al., 2006). “Common Pb” is the variable initial Pb, which is usually unknown and hampers the application of U-Pb dating. This Pb is likely from the same source as detrital Th, i.e. organic matter, and making clean samples with low detrital Th (and therefore also detrital Pb) suitable for this dating technique (Fairchild and Baker, 2012).

2.3 Stable isotopes and trace elements

Palaeoclimate reconstructions using speleothems are usually based on a multi-proxy approach, using different geochemical proxies. The most commonly used proxies for speleothems are the stable oxygen ($\delta^{18}\text{O}$) and stable carbon ($\delta^{13}\text{C}$) isotopes. These proxies can be obtained in high spatial resolution (tens to hundreds of μm -range), where sampling is commonly performed using a MicroMill device and

measurements are performed with an isotope ratio mass spectrometer (IRMS). Stable isotope values are expressed in delta (δ) notation (e.g. Mook and De Vries, 2000; Sharp, 2007), here exemplary for $\delta^{18}\text{O}$:

$$\delta^{18}\text{O} = \left(\frac{{}^{18}\text{O}/{}^{16}\text{O}_{\text{sample}} - {}^{18}\text{O}/{}^{16}\text{O}_{\text{reference material}}}{{}^{18}\text{O}/{}^{16}\text{O}_{\text{reference material}}} \right) \quad (\text{Eq. 2.IV})$$

The reference material for carbonates is Vienna Pee Dee Belemnite (V-PDB; Craig, 1957) and for water samples Vienna Standard Mean Ocean Water (V-SMOW; Craig, 1961). Both reference materials' $\delta^{18}\text{O}$ values are defined as 0 ‰.

The $\delta^{18}\text{O}$ value of speleothem carbonate under equilibrium conditions is influenced by only two variables, the cave temperature and the $\delta^{18}\text{O}$ value of the drip water. However, in nature a number of processes occurring in the atmosphere, the soil and the karst, as well as inside the cave, can force disequilibrium. Thus, the fractionation between drip water and speleothem calcite is still a matter of debate (e.g. Hansen et al., 2019; Hendy, 1971; Kim and O'Neil, 1997; Kim et al., 2007). Moreover, the processes affecting the $\delta^{18}\text{O}$ value in the hydrological cycle are complex, not only in the cave system, but also on a global scale (see Lachniet, 2009 for a full review).

In general, the initial $\delta^{18}\text{O}$ value in the hydrological cycle is controlled by the $\delta^{18}\text{O}$ value of the water source, i.e. the ocean, which varies depending on salinity, evaporation, precipitation, sea ice melt, freshwater influence and global circulation patterns, both in ocean and atmosphere. Therefore, the $\delta^{18}\text{O}$ value of the ocean is not only spatially, but also temporally variable, i.e. on glacial/interglacial time scales. In general, evaporation of ocean water results in lower $\delta^{18}\text{O}$ values in the resulting atmospheric vapour, due to equilibrium, as well as kinetic fractionation. When precipitation from the atmospheric vapour occurs, the condensation of vapour to liquid occurs in equilibrium, where ^{18}O is preferentially incorporated into the liquid phase. Therefore, the remaining $\delta^{18}\text{O}$ value of the vapour will decrease with time due to the removal of ^{18}O into the rain. This continuous process of progressive condensation and decreasing $\delta^{18}\text{O}$ values of precipitation can be described by a Rayleigh distillation process, which itself is temperature dependent. Variations in $\delta^{18}\text{O}$ values of precipitation are therefore primary related to latitude, altitude and moisture source and result in spatially coherent variations over the whole globe (Bowen and Wilkinson, 2002; Bowen, 2008). Moreover, several local factors can alter the $\delta^{18}\text{O}$ value of precipitation, such as local temperature, altitude, distance from the sea, source effect, as well as increased rainfall amounts during single precipitation events (Lachniet, 2009).

Altogether, the local $\delta^{18}\text{O}$ value of the meteoric water can be highly variable. In addition to this large-scale variability, local processes in the cave system can also influence the $\delta^{18}\text{O}$ values. While the soil water $\delta^{18}\text{O}$ is mostly similar to the $\delta^{18}\text{O}$ value of precipitation, evaporation causes an increase in $\delta^{18}\text{O}$ of soil moisture. In contrast, large precipitation events will decrease the $\delta^{18}\text{O}$ value in the soil water. After passing the soil zone, the water enters the epikarst area, where dissolution of carbonate host rock occurs (see Fig. 2.1). In the epikarst, different pathways are possible, either as diffusive seepage flow or as

conduit flow (see also section 6.6), following different fractures and fissures, potentially affecting $\delta^{18}\text{O}$ values. After leaving the epikarst area, the water enters the cave interior as drip water from the ceiling of the cave. The $\delta^{18}\text{O}$ value of the drip water is typically a function of the mixture of precipitation $\delta^{18}\text{O}$ and the processes occurring in soil zone and epikarst (Mattey et al., 2008; Perrin et al., 2003). The resulting $\delta^{18}\text{O}$ value of the speleothem carbonate can be further influenced by the humidity in the cave and the residence time on the stalagmite surface, as well as the fractionation between the drip water and the carbonate phase, which can either occur in equilibrium or as kinetic isotope fractionation (Dreybrodt, 2008; Dreybrodt and Scholz, 2011; Dreybrodt et al., 2016; Hansen et al., 2019; Hendy, 1971; Lachniet, 2009; Mühlinghaus et al., 2009; Scholz et al., 2009). In general, the $\delta^{18}\text{O}$ values represent a complex interplay between different influencing factors. Climatic interpretations are often hampered by the factors described above and might be challenging, e.g. for speleothems from Central Europe (Mischel et al., 2017b; Scholz et al., 2012; Weber et al., 2018a). For other climate regimes, the $\delta^{18}\text{O}$ values can provide valuable information on past climate patterns, moisture source and the condition of the atmospheric circulation (Cheng et al., 2016; Fairchild et al., 2006; Genty et al., 2003; Lachniet, 2009; McDermott, 2004; Moseley et al., 2014; Wang et al., 2001; Wassenburg et al., 2016a).

The stable carbon isotope ($\delta^{13}\text{C}$) values of speleothems are referred to reference material V-PDB, which is set as 0 ‰, similar to V-SMOW for $\delta^{18}\text{O}$. Speleothem $\delta^{13}\text{C}$ values are mainly influenced by the DIC (dissolved inorganic carbon) of the soil water. Due to the pH values in karst areas (neutral to slightly basic), carbon is usually dissolved as bicarbonate ion (HCO_3^-) and soil water isotope chemistry is dominated by the bicarbonate- CO_2 fractionation, where CO_2 originates mainly from the vegetation. In an open-system model, the dissolved species in the soil water reflects the isotopic composition of soil CO_2 due to continuous equilibration between these two reservoirs, without an isotopic influence of the host rock. In contrast, a closed-system model includes the isotopic imprint of the host rock and percolating water becomes isolated from soil CO_2 (Hendy, 1971). However, natural systems are often at least partially open (see section 2.2 for U-Th-dating), resulting in a natural variability of the $\delta^{13}\text{C}$ values of speleothem calcite. For arid regions, changes in speleothem $\delta^{13}\text{C}$ values can reflect changes between a C3 and C4 vegetation above the cave, where more negative $\delta^{13}\text{C}$ values are associated with C3 plants and vice versa. For temperate regions, more positive $\delta^{13}\text{C}$ values can be obtained in speleothems, even if there is no C4 vegetation above the cave. This is possible due to several reasons. An increased drip interval can enhance disequilibrium fractionation on the stalagmite surface, resulting in increasing $\delta^{13}\text{C}$ values (Deininger et al., 2012; Mühlinghaus et al., 2009; Scholz et al., 2009). A further mechanism is the increase in host rock derived C (more positive $\delta^{13}\text{C}$ values) and a reduced soil CO_2 production (Cerling, 1984). In general, the $\delta^{13}\text{C}$ values are less influenced by direct climate patterns in comparison to $\delta^{18}\text{O}$ values, since they represent changes above the cave, which occur on longer time scales (changes in vegetation vs. changes in meteoric $\delta^{18}\text{O}$).

Trace elements have been established as an important palaeoclimate proxy in recent years, although they are not as often applied as stable isotope analyses. The complex cave environment causes a great variety in potential trace element sources and compositions, not only in temporal, but also in spatial terms. Therefore, the reconstruction of forcing factors enables the researcher to further understand the cave environment. One major advantage of trace element analysis is the high spatial resolution of the obtained dataset. Commonly, trace elements in speleothems are analysed by LA-ICP-MS, enabling a spatial resolution of several tens of μm , even allowing to reconstruct seasonal changes, depending on the growth rate of the stalagmite (see section 2.1). Trace elements are incorporated in the carbonate crystal lattice, usually in exchange with the Ca^{2+} -ion (especially true for Sr, Ba and Mg) and depending on the mass fraction of the drip water. Other elements may be incorporated by different mechanisms, such as fine detrital particles or small-sized colloids (e.g. Al, Y, P; Fairchild and Treble, 2009). The drip water composition itself reflects a mixture of different sources, such as soil components, the host rock, atmospheric deposition and vegetation. Details of trace element incorporation relies on several factors and is discussed in detail in the literature (see for example (Fairchild et al., 2000; Fairchild et al., 2006; Fairchild and Treble, 2009; Finch et al., 2001; Wassenburg et al., 2012; Wassenburg et al., 2016b)). One major application of trace elements is the identification of prior calcite precipitation (PCP) in cave environments (Fairchild et al., 2000; Fairchild and Treble, 2009). The term PCP describes precipitation of calcite before the precipitation on the stalagmite surface occurs, potentially affecting the observed trace element mass fractions. In this case, Ca^{2+} -ions are preferentially precipitated, causing a decrease of Ca in the solution and an increase in trace element mass fraction in the speleothem in relation to Ca, i.e. a strong enrichment in Mg and/or Sr in the speleothem calcite, as well as Mg – Sr covariations (McMillan et al., 2005). PCP can also cause a rise in $\delta^{13}\text{C}$ values, which makes a combined approach of stable isotopes and trace element analysis desirable. Magnesium is among the most intensively studied of trace elements and can provide insights into palaeohydrology, i.e. the effective rainfall (Tooth and Fairchild, 2003; Weber et al., 2018a). However, trends in trace element mass fraction can largely depend on the cave system. Therefore, a general trend of increasing/decreasing mass fraction relative to a specific climatic signal is not possible. For one manuscript in the framework of this thesis, Mg was used as indicator for changes in precipitation during the Marine Isotope Stage (MIS) 3 for Bunker Cave, Germany. In this case study, increased Mg mass fractions were associated with dry conditions due to an increased residence time and the preferential dissolution of Mg-rich dolomite in the host rock (see chapter 6 and (Weber et al., 2018a)). Besides palaeohydrological reconstructions, detrital trace elements (e.g. Y, P, Al) can help to locate growth hiatuses in speleothem records. Detrital components are usually incorporated at the end of a growth period and accumulate on the speleothem surface. When speleothem growth re-initiates, the new layers of calcite will grow on top of the detrital layer and it is possible to date the hiatus by obtaining the age of the closest possible layer below the detrital layer (see chapter 6). Due to the high resolution and the low test portion mass, trace element analysis by LA-ICP-MS is today

a widely applied approach to acquire deeper knowledge about processes in cave environments and should be included in multi-proxy speleothem records whenever possible.

2.4 Strontium isotopes

Strontium has four naturally occurring isotopes. Three of them are stable (^{84}Sr , ^{86}Sr and ^{88}Sr), while ^{87}Sr is a radiogenic isotope, which is produced by the decay of the radioactive parent isotope ^{87}Rb with a half-life of 48.8 Ga (Banner, 2004). Due to this decay, the Sr isotope composition of a material changes continuously over time. Therefore, the isotope ratio of interest in the Sr isotope system is $^{87}\text{Sr}/^{86}\text{Sr}$. This ratio in the target material depends on the time passed since the closure of the system and the initial Rb/Sr ratio.

2.4.1 The global Sr cycle

Today, the reconstruction of variability in the Sr isotope system is applied with great success to several scientific fields, such as petrology, archaeology, anthropology, ecology, palaeoclimatology, food science and forensics (Balter et al., 2012; Burke et al., 1982; Copeland et al., 2010; Durante et al., 2015; Hoogewerff et al., 2001; Kelly et al., 2005; Lewis et al., 2017; Lugli et al., 2017a; Lugli et al., 2017b; McCulloch and Wasserburg, 1978; Müller and Anczkiewicz, 2016; Outridge et al., 2002; Starinsky et al., 1983; Stewart et al., 2001; Weber et al., 2018a; Woodhead et al., 2005; Wortham et al., 2017). One basic Sr isotope application is the secular Sr isotope curve of Burke et al. (1982), where temporal changes of seawater Sr isotope ratios during the Phanerozoic are reconstructed based on measurements of marine carbonate sediments, evaporites and fossils (Fig. 2.3). While the Sr isotope evolution during the Phanerozoic is quite precisely known, the Precambrian Sr isotope evolution is largely unknown. The Precambrian period usually lacks pristine carbonate samples and obtained data from igneous and metamorphic samples represent the Sr isotope signature of the Earth's crust and mantle. Meteorites originating from the formation of the Earth yield very low $^{87}\text{Sr}/^{86}\text{Sr}$ ratios of ~ 0.699 , reflecting the chemical composition of the early Earth. Strontium isotopes in the Earth's upper mantle slowly increased over time due to the radiogenic decay of ^{87}Rb to present-day $^{87}\text{Sr}/^{86}\text{Sr}$ resulting in values of ~ 0.703 (Banner, 2004). This value is still much less radiogenic than modern ocean Sr isotope composition. Therefore, another process must be responsible for the more radiogenic $^{87}\text{Sr}/^{86}\text{Sr}$ ratio of the modern ocean. Differentiation of Earth's crust via partial melting and crystal fractionation processes were the major driver, producing magmas with high Rb/Sr ratios. Due to the increased total number of decays per time of ^{87}Rb , the resulting $^{87}\text{Sr}/^{86}\text{Sr}$ ratio increased with time. Today, Earth's crust is highly heterogeneous with magmatic, sedimentary and metamorphic rock types representing a wide range of $^{87}\text{Sr}/^{86}\text{Sr}$ ratios. During the Phanerozoic, the $^{87}\text{Sr}/^{86}\text{Sr}$ ratio reflects different inputs from mantle and crust derived sources. These changes can have different origins and time scales. Montañez et al. (2000)

concluded that the marine $^{87}\text{Sr}/^{86}\text{Sr}$ record is mainly influenced by continental erosion and that the Cambrian high $^{87}\text{Sr}/^{86}\text{Sr}$ ratio was caused by an enhanced sediment flux consisting of Sr with highly radiogenic $^{87}\text{Sr}/^{86}\text{Sr}$ ratios due to the uplift and weathering of metamorphic rocks formed during the Brasiliano-Pan African orogeny. Shorter fluctuations, such as the constant increase in $^{87}\text{Sr}/^{86}\text{Sr}$ since the Paleogene, are a consequence of increased weathering rates of radiogenic rocks, such as those from the Himalayan-Tibetan uplift (Harris, 1995). In addition, enhanced weathering due to glaciation can affect the oceanic Sr composition as well (Armstrong, 1971; Miller et al., 1991; Zachos et al., 1999). Most likely, all those different processes will act together and can be further influenced by changes in the speed of sea-floor volcanism (Mead and Hodell, 1995).

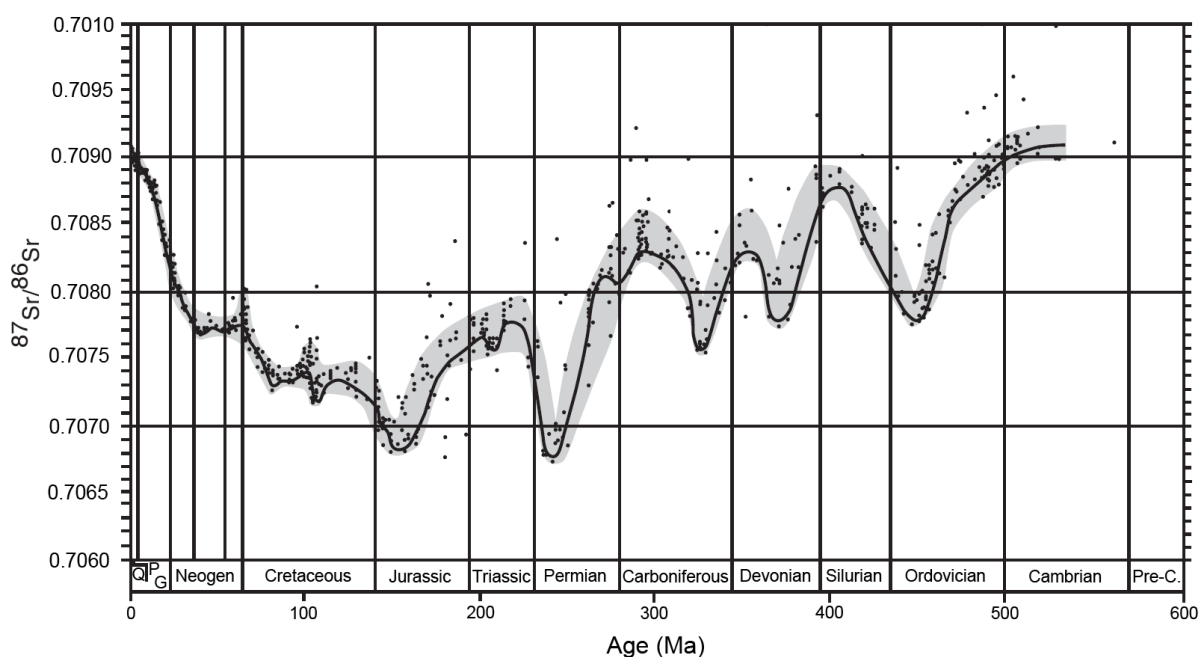


Fig. 2.3: The secular Sr isotope curve for seawater $^{87}\text{Sr}/^{86}\text{Sr}$ variations in the Phanerozoic. Single measurements are obtained from marine carbonate sediments, evaporites and fossils, representing the value of the ocean. The shaded area around the curve is the estimated uncertainty obtained by Banner (2004). Results are normalized to a $^{87}\text{Sr}/^{86}\text{Sr}$ value of 0.710248 for NIST 987 (McArthur et al., 2001). Q = Quaternary, PG = Paleogene, Pre-C. = Precambrian. Modified after Burke et al. (1982) and Banner (2004).

2.4.2 Strontium isotopes in speleothems

Strontium is one of the most commonly investigated trace elements in speleothems and is incorporated into speleothems when replacing the Ca^{2+} -ion in the carbonate crystal lattice, due to similar chemical behaviour. The main source of Sr in speleothems is the host rock. This implies that the Sr isotope signature of the speleothem should be quite similar to the host rock, since no isotopic fractionation of

the $^{87}\text{Sr}/^{86}\text{Sr}$ ratio occurs during dissolution and precipitation of Sr (Fairchild and Baker, 2012). Some studies, however, showed that the stable Sr isotope value ($\delta^{88}\text{Sr}$) can be affected during these processes, providing insights into the processes in the soil environment (Halicz et al., 2008) and that the fractionation during precipitation is also temperature dependent (Fietzke and Eisenhauer, 2006). Besides the host rock, external sources with varying Sr isotope signatures can additionally contribute to the Sr signal in the cave environment and ultimately in the speleothem. Potential external sources can vary significantly in their $^{87}\text{Sr}/^{86}\text{Sr}$ ratios, due to their different origins. The overlying soil can show a significantly different Sr isotope signature and can additionally be influenced by atmospheric inputs, such as dust or sea spray in coastal areas.

Strontium isotopes have been applied to speleothems since the 1990s. The first study was performed on a stalagmite sample from Avshalom Cave, Israel, by TIMS (Avigour et al., 1990). These authors observed that the obtained $^{87}\text{Sr}/^{86}\text{Sr}$ ratio of the speleothem was higher than the assumed ratio for the host rock and concluded that the increased ratio was caused by the influence of the local rainwater with a more radiogenic $^{87}\text{Sr}/^{86}\text{Sr}$ ratio. Since then, Sr isotopes have been applied for different purposes in the speleothem sciences. A study by Banner et al. (1996) revealed that the Sr isotope composition of a speleothem sample from Barbados showed similar high-resolution fluctuations when compared to the groundwater. They developed a model, which implies that low $^{87}\text{Sr}/^{86}\text{Sr}$ in the speleothem documents periods of relatively high rainfall rates, while high $^{87}\text{Sr}/^{86}\text{Sr}$ values represent periods of low rainfall rates. In addition, Sr isotopes can be used to reconstruct rainfall and water residence time in the host rock (Verheyden et al., 2000; Weber et al., 2018a; Wortham et al., 2017). In those studies, the $^{87}\text{Sr}/^{86}\text{Sr}$ ratios of the speleothems are more radiogenic than that of the respective host rock, indicating an external source with an increased radiogenic fingerprint. Depending on the rainfall and water residence time, the input of the radiogenic source varies with time.

Besides hydrology, external sources can also be responsible for variations in Sr isotope signals in speleothems. Goede et al. (1998) found two distinct end-members of Sr isotopes in a Tasmanian speleothem and reconstructed the Sr isotope signature of the limestone host rock and the value of a seawater related source, i.e. sea-spray. A similar mechanism was found for speleothems from Soreq Cave, Israel (Ayalon et al., 1999; Bar-Matthews et al., 1999), where intermediate $^{87}\text{Sr}/^{86}\text{Sr}$ ratios were determined, varying between the Sr isotope signature of the host rock and the sea spray. Relative proportions of the two main sources depend on the climate state, i.e. during deglaciation the host rock signal was increased due to enhanced rainfall and weathering. In coastal areas, the input of sea-spray can significantly influence the $^{87}\text{Sr}/^{86}\text{Sr}$ ratios of speleothems. This is especially true on glacial-interglacial time scales. A study from South Africa (Fisher et al., 2010) reconstructed the paleo-shoreline for the past 350 ka based on the input of sea-spray in speleothems and tufa deposits. Strontium isotopes can also help to improve the understanding of stalagmite geochemistry, i.e. to correct for the external

source of Sr and solely reconstructing the bedrock-derived Sr for further investigation in Sr trace element partitioning (Belli et al., 2017).

In general, radiogenic Sr isotopes have a broad application in speleothem science, not only for palaeoclimate aspects. The main challenge is to reconstruct the Sr isotope composition of each potential source and to estimate the respective contribution. For the carbonate host rock, the Sr isotope signature can be estimated by the depositional age due to the precipitation from the ocean in equilibrium (Burke et al., 1982). Modern sea-spray Sr isotope values are also known from the modern-day ocean value of 0.70917 ± 0.00001 (McArthur et al., 2012). However, aeolian derived dust can vary dramatically, not only due to different sources, but also due to different compositions. In addition, the mixing behavior between the external Sr and the host rock derived Sr can vary with different climatic conditions, i.e. temperature and rainfall patterns, forcing mineral phases to weather differently (Capo et al., 1998; Stewart et al., 1998).

2.4.3 Application of LA-MC-ICP-MS for Sr isotopes

The analysis of Sr isotopes was initially performed by TIMS (Platzner, 1985), where a chemical separation of Sr from other matrix elements was essential and mainly used to date rocks by using the Rb/Sr system (McCulloch and Wasserburg, 1978). Analyses by TIMS provide high precision and accuracy but are time consuming (several hours for each Sr isotope measurement) and have therefore a limited sample throughput. Due to the development of MC-ICP-MS systems (Wieser and Schwieters, 2005), the measurement time per sample was dramatically reduced (tens of minutes), with comparable precision. Still, the chemical separation of Sr was necessary. By coupling the MC-ICP-MS system with a laser ablation system, several advantages were achieved. Instead of bulk samples, the sample location could now be chosen in high spatial resolution using the laser ablation system. Additionally, no chemical procedure was necessary prior to analysis and measurement time was reduced (less than five minutes per sample) while measurement precision was only slightly affected. Accuracy of the analyses can be assured by several strategies, i.e. by standard bracketing using suitable reference materials during analysis (Irrgeher et al., 2016; Weber et al., 2017; Weber et al., 2018b) and monitoring of the naturally invariant $^{84}\text{Sr}/^{86}\text{Sr}$ ratio (Kimura et al., 2013; Müller and Anczkiewicz, 2016), providing reliable Sr isotope results using this technique.

The initial attempts to measure Sr isotopes by LA-MC-ICP-MS were performed by Christensen et al. (1995) on a modern gastropod shell. Results yielded a value of 0.70918 ± 0.00002 for the shell, which is indistinguishable from the Sr isotope signature of the modern ocean of 0.70917 ± 0.00001 (McArthur et al., 2012). This pioneering study showed, that the analysis of Sr isotopes in carbonate materials by LA-MC-ICP-MS is able to reproduce the results comparable to results obtained by TIMS and solution-based MC-ICP-MS Sr isotope analysis. Further experiments comparing solution based and LA-MC-

ICP-MS measurements of Sr isotopes were performed by Ehrlich et al. (2001) for carbonate samples, supporting previous results. After these initial successes, several studies focusing on the technical development of the methodology followed, covering deviations of the naturally invariant $^{84}\text{Sr}/^{86}\text{Sr}$ ratio (Waight et al., 2002), correction protocols for the mass bias and the influence of matrix effects on accuracy and precision (Bizzarro et al., 2003; Ingle et al., 2003), and how to handle potential interferences on the Sr signals in different matrix materials (Ramos et al., 2004). A general overview of method development and application is given by Vroon et al. (2008). All studies showed that the benefits of laser ablation, such as spatial control and sample throughput, overcome the disadvantages in comparison to TIMS analyses, i.e. dealing with interferences, and is therefore the method of choice for studies where highest precision is not entirely necessary.

Environmental applications using LA-MC-ICP-MS for Sr isotopes were broadly applied in fishery science and archaeology using otoliths. Since otoliths grow from a central core in concentric layers, it is possible to reconstruct migration patterns of the fish using variations in Sr isotopes. For example, the high spatial resolution of LA-MC-ICP-MS enabled Outridge et al. (2002) to display the migration pattern of char between Canadian rivers during ontogenesis. Further studies followed (Barnett-Johnson et al., 2005; Rachel et al., 2008; Wolff et al., 2012; Woodhead et al., 2005) and resulted in the development of an otolith reference material FEBS-1 (Yang et al., 2011).

The analysis of Sr isotopes by LA-MC-ICP-MS is widely applied in the field of tooth analysis, i.e. archaeology and paleontology. Tooth enamel consists of 96 wt% inorganic (hydroxyl-)apatite with a Ca content of 33.6 to 39.4 wt% (Williams and Elliott, 1979). Despite wide application, *in-situ* analysis of teeth and bones using laser ablation generally suffer from higher Rb and REE mass fractions than carbonates. In addition, the well-known interference of $^{40}\text{Ca}^{31}\text{P}^{16}\text{O}$ and $^{40}\text{Ar}^{31}\text{P}^{16}\text{O}$ on mass 87, i.e. biases the monitored ^{87}Sr (De Jong et al., 2007; Horstwood et al., 2008; Irrgeher et al., 2016; Lewis et al., 2014; Lugli et al., 2017b; Simonetti et al., 2008; Willmes et al., 2016). Two major methods are used to overcome this issue, one is to add N_2 to reduce oxide formation in the plasma (Willmes et al., 2016) and the other is to calibrate the daily formation of CaPO and ArPO through the analysis using matrix-matched reference materials (Horstwood et al., 2008; Lugli et al., 2017b). The later approach is applied in chapter 4 and Weber et al. (2018b). However, not all studies report issues with the isobaric interference on mass 87, so it remains a matter of debate (Copeland et al., 2008; Müller and Anczkiewicz, 2016). The main application of Sr isotopes in bioapatite materials is to trace migration patterns and landscape use. This is possible due to the direct relationship between $^{87}\text{Sr}/^{86}\text{Sr}$ in bones and Sr/teeth and the ingested plants and waters $^{87}\text{Sr}/^{86}\text{Sr}$ of the animal (Burton and Wright, 1995; Pate, 1994). Since enamel preserves the isotopic signature of during formation, it is possible to reconstruct the potential origin of a specimen and evaluate changes in landscape use. There are numerous studies applying this technique (Copeland et al., 2010; Copeland et al., 2011; Hoogewerff et al., 2001; Lugli et al., 2017a; Lugli et al., 2017b), since even small changes in locality can result in large changes in the

$^{87}\text{Sr}/^{86}\text{Sr}$ ratio of a landscape. Therefore, the fast and almost non-destructive nature of LA-MC-ICP-MS is highly suitable for analysing these kind of materials and even valuable archaeological artefacts.

Although the analysis of Sr isotopes by LA-MC-ICP-MS has now been applied to various kinds of samples over the past two decades, few studies have applied this technique to speleothems (Weber et al., 2017; Wortham et al., 2017). One major limitation is the low Sr mass fraction of most speleothem samples, especially if they consist of calcite. However, progress in mass spectrometry (Wieser and Schwieters, 2005), laser ablation techniques (Jochum et al., 2014; Kimura and Chang, 2012; Koch and Gunther, 2007; Yang et al., 2011) and the development of suitable reference materials (Garbe-Schönberg and Müller, 2014; Jochum et al., in revision; Ohno and Hirata, 2007; Weber et al., 2018b; Weber et al., submitted; Yang et al., 2011), the lower limit for the *in-situ* analysis of Sr isotopes can be pushed further down and enables users to apply this technique to a broader variety of samples.

Chapter 3: Manuscript I: Sr isotope analysis of speleothems by LA-MC-ICP-MS: high temporal resolution and fast data acquisition

Sr isotope analysis of speleothems by LA-MC-ICP-MS: high temporal resolution and fast data acquisition

Michael Weber^{1,2}, Jasper A. Wassenburg^{1,2}, Klaus Peter Jochum², Sebastian F.M. Breitenbach³, Jessica Oster⁴, Denis Scholz¹

¹Institute of Geosciences, Johannes Gutenberg-Universität Mainz, J.-J.-Becher-Weg 21, 55128 Mainz, Germany

²Climate Geochemistry Department, Max Planck Institute for Chemistry (Otto-Hahn-Institute), Postbox 3060, 55020 Mainz, Germany

³Sediement and Isotope Geology, Ruhr-University Bochum, Universitätsstrasse 150, 44801 Bochum, Germany

⁴Department of Earth and Environmental Science, Vanderbilt University, Nashville, TN, 37240, USA

This manuscript is published in a similar version in *Chemical Geology*, Vol. 468, 63 – 74 (2017).

3.1 Abstract

Speleothems are well established climate archives. A wide array of geochemical proxies, including stable isotopes and trace elements are present within speleothems to reconstruct past climate variability. However, each proxy is influenced by multiple factors, often hampering robust interpretation. Sr isotope ratios ($^{87}\text{Sr}/^{86}\text{Sr}$) can provide useful information about water residence time and water mixing in the host rock, as they are not fractionated during calcite precipitation. LA-MC-ICP-MS has rarely been used for determination of Sr isotope signatures in speleothems, as speleothems often do not possess appropriately high mass fractions of Sr to facilitate this analysis. Yet the advantages of this approach include rapid data acquisition, higher spatial resolution, larger sample throughput and the absence of chemical treatment prior to analysis. We present LA-MC-ICP-MS Sr isotope data from two speleothems from Morocco (Grotte de Piste) and India (Mawmluh Cave), and we compare line scan and spot analysis ablation techniques along speleothem growth axes. The analytical uncertainty of our LA-MC-ICP-MS Sr data is comparable to studies conducted on other carbonate materials. The results of both ablation techniques are reproducible within analytical uncertainty, implying that this technique yields robust results when applied to speleothems. In addition, several comparative measurements of different carbonate reference materials (i.e. MACS-3, JcT-1, JcP-1), including tests with standard bracketing and comparison of the $^{87}\text{Sr}/^{86}\text{Sr}$ ratios with a nanosecond laser ablation system and a state-of-the-art femtosecond laser ablation system, highlight the robustness of the method.

3.2 Introduction

Speleothems (cave CaCO_3 deposits) are well established climate archives and are found worldwide in karst environments (Asmerom et al., 2010; Cheng et al., 2016; Cruz et al., 2005; Genty et al., 2003; Hoffmann et al., 2016; Kennett et al., 2012; Luetscher et al., 2015; Wang et al., 2001; Wassenburg et al., 2016a). They can be dated with unprecedented precision using the $^{230}\text{Th}/\text{U}$ -dating method (Richards and Dorale, 2003; Scholz and Hoffmann, 2008), and provide a range of climate proxies that record a number of environmental processes and can be analysed at up to sub-annual resolution.

Oxygen isotopes in speleothems ($\delta^{18}\text{O}$ values) depend on paleo-temperature and rainfall properties, such as amount, seasonality and moisture sources (e.g. Fairchild et al., 2006; McDermott, 2004), whereas carbon isotopes can provide information on soil productivity, vegetation characteristics and effective rainfall (McDermott, 2004). In addition, trace elements (e.g. Sr, Mg, P, Ba) may be interpreted in terms of effective infiltration, prior calcite precipitation, water residence time, source and reservoir effects, weathering processes in the epikarst zone and soil composition (Ayalon et al., 1999; Fairchild et al., 2000; Fairchild and Treble, 2009; Verheyden et al., 2000; Wassenburg et al., 2016a; Wassenburg et al., 2016b). Within the epikarst and soil zone, different sources of trace elements (for example aeolian dust vs. host rock) may be present and display varying compositions. A change in the dripwater pathway or

in the relative contribution of different sources, may thus affect the dripwater trace element composition, which often renders their interpretation a challenging task (Banner et al., 1994).

Important information on the influence of different sources of trace elements in dripwaters may be provided by Sr isotopes, which have been shown to provide additional insights on precipitation and water residence time in the host rock (Banner et al., 1996; Oster et al., 2010). In CaCO_3 , the Sr^{2+} ion substitutes at the Ca^{2+} ion sites in the mineral lattices due to their similar properties and ionic radii (Banner, 2004). No isotopic fractionation of Sr isotopes is observed during precipitation of CaCO_3 and the incorporation of Sr into the crystal lattice. Thus, the $^{87}\text{Sr}/^{86}\text{Sr}$ ratio of carbonates is identical to that of the parent solution (Banner and Kaufman, 1994).

Although the first Sr isotope analyses on speleothems were conducted in 1990 (Avigour et al., 1990), relatively few studies have focused on this topic so far. The main source for Sr in speleothems is the host rock, but several factors have been proposed to affect Sr isotope ratios: varying water residence time in the epikarst (Banner et al., 1996; Oster et al., 2010; Oster et al., 2014; Verheyden et al., 2000), changes in aeolian input in response to sea-level changes or atmospheric circulation (Ayalon et al., 1999; Bar-Matthews et al., 1999; Goede et al., 1998; Li et al., 2005; Zhou et al., 2009), changes in weathering intensity of soil and host rock in response to rainfall (Avigour et al., 1990), changes in the distance to the shoreline and incorporation of sea-salt signals (Fisher et al., 2010), as well as mixing of the Sr signals of different rock types and soils (Frumkin and Stein, 2004; Hori et al., 2013). All these studies either used TIMS (Avigour et al., 1990; Frumkin and Stein, 2004; Goede et al., 1998; Hori et al., 2013; Li et al., 2005; Zhou et al., 2009), or solution MC-ICP-MS (Ayalon et al., 1999; Bar-Matthews et al., 1999; Fisher et al., 2010; Oster et al., 2010; Oster et al., 2014; Verheyden et al., 2000). For both techniques samples need to be drilled/milled, and require chemical separation prior to mass spectrometric analysis. This is time-consuming, and limits the achievable spatial resolution of $^{87}\text{Sr}/^{86}\text{Sr}$ records. Strontium isotope analysis by LA-MC-ICP-MS offers the opportunity to measure the $^{87}\text{Sr}/^{86}\text{Sr}$ ratio *in-situ* at high spatial resolution and without any prior chemical treatment. Although this technique has been widely applied to petrological samples (e.g. Bizzarro et al., 2003; Christensen et al., 1995; Davidson et al., 2001; Jackson and Hart, 2006; Ramos et al., 2004; Waight et al., 2002) and carbonate and phosphate materials, such as gastropods, otoliths, teeth, clam shells, fine- and coarse-grained carbonates and corals (Bizzarro et al., 2003; Christensen et al., 1995; Copeland et al., 2008; Ehrlich et al., 2001; Outridge et al., 2002; Ramos et al., 2004; Woodhead et al., 2005) it has only recently been used for measuring $^{87}\text{Sr}/^{86}\text{Sr}$ in speleothems (Wortham et al., 2017).

Here we present a LA-MC-ICP-MS method for measuring Sr isotopes on speleothems, based on previously mentioned studies on different sample materials. We show results from two speleothem samples and compare different sampling techniques. Both samples consist of aragonite and have a rather high Sr mass fraction $> 300 \mu\text{g/g}$, which makes them highly suitable to apply LA-MC-ICP-MS. We also

discuss the effects of different tuning parameters and compare results obtained by two different laser systems (a New Wave UP 213 nm laser and a NWR Femto200 laser ablation system).

3.3 Speleothem samples

The investigated speleothem samples stem from two different caves. Stalagmite GP5 was sampled at Grotte de Piste (Morocco), and stalagmite MAW-4 stems from Mawmluh Cave (Meghalaya, India). Stalagmite GP5 has a total length of 78 cm. A detailed description of the cave and the sample is given in Wassenburg et al. (2012) and Wassenburg et al. (2013). In this study, an approximately 15 cm long part of the sample (Fig. 3.1) was studied which corresponds to the time span from ca. 800 to 1760 AD. Previous data is published in Wassenburg et al. (2013) and only briefly summarised here. GP5 was precisely dated by the $^{230}\text{Th}/\text{U}$ -method. Furthermore, the mineralogy of the sample was investigated by XRD and showed that GP5 is mainly aragonitic, with minor calcitic parts (<2%). Strontium mass fractions range from 200 to 500 $\mu\text{g/g}$, with an average mass fraction of 426 (± 49) $\mu\text{g/g}$. In some parts, the sample is characterized by mm-scale layering of porous and less porous layers.

Stalagmite MAW-4 (Fig. 3.1) from Mawmluh cave is a small sample with a total length of 3 cm. The upper part of the sample (~ 15 mm), consists of aragonite, and covers the time span from 1950 to 2006 AD (Wassenburg et al., 2016b). It has an average growth rate of ~ 293 $\mu\text{m/a}$, and can thus provide very high resolution. The stalagmite was actively growing at the time of collection (March 2006). The lower part of the sample consists of calcite, the base is dated 395 ± 55 a BP. The calcite-to-aragonite transition is clearly visible by a change in colour from greyish (calcite) to white/beige (aragonite). In the upper aragonitic part, this stalagmite has a relatively high Sr mass fraction (1458 – 1729 $\mu\text{g/g}$, Wassenburg et al., 2016b), and is thus extremely suitable for Sr isotope measurements by LA-MC-ICP-MS. The calcite section has a Sr mass fraction of a few hundred $\mu\text{g/g}$, and was not investigated in this study. For more information about the cave setting and microclimatic conditions, see Breitenbach et al. (2010) and Breitenbach et al. (2015).

3.4 Materials and methods

The following chapter deals with the analytical setup, including two types of laser ablation systems, coupled to a MC-ICP-MS. Besides the presented speleothem samples, international RMs have been analysed to provide traceability of the method.

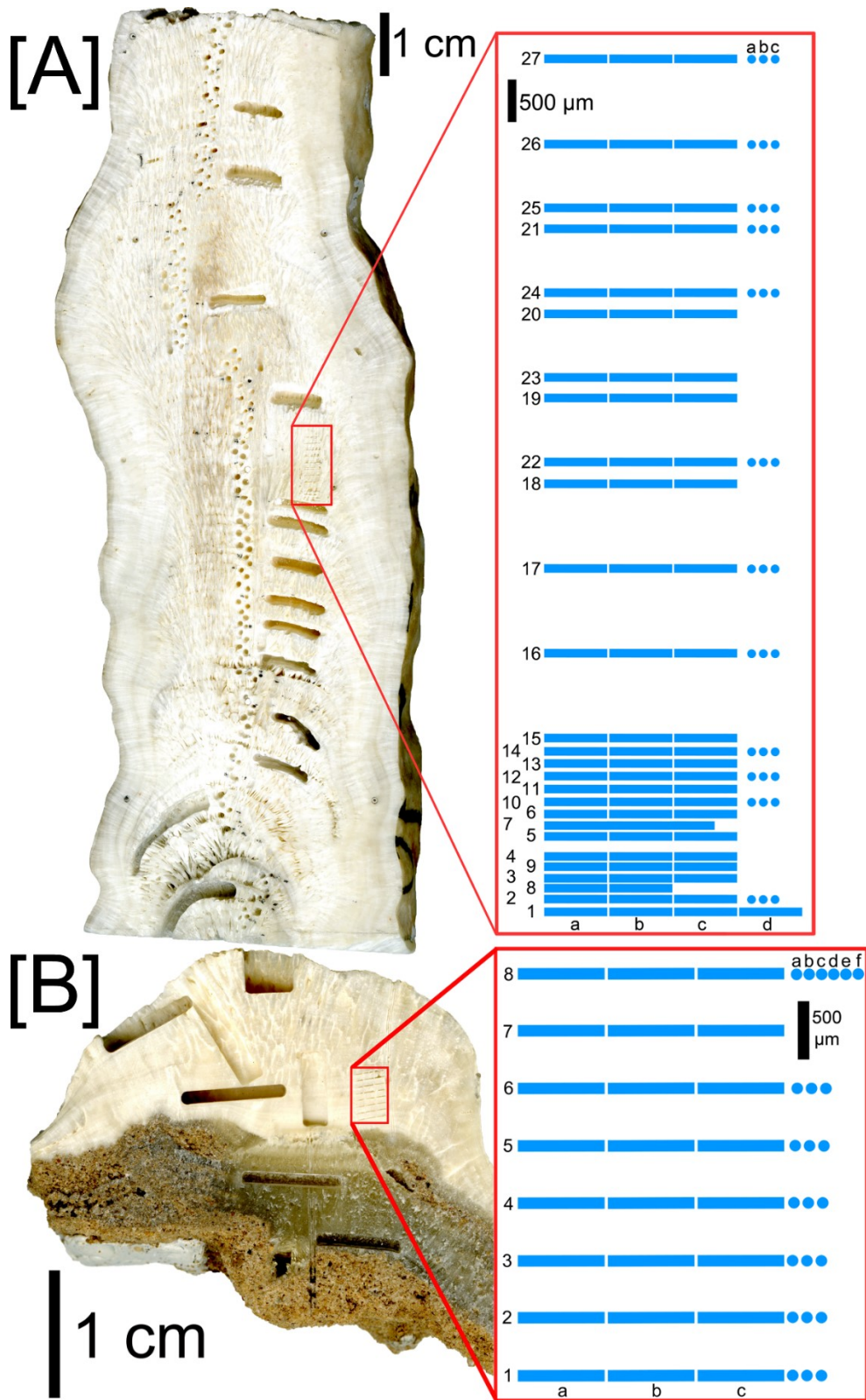


Fig.3.1: [A] Sampling approach for speleothem GP5. The red rectangle indicates the sampling section, blue lines show the LA-MC-ICP-MS line scan positions. The spot analyses were performed near the right end of the third line scan as indicated by the blue spots. [B] Sampling approach for speleothem MAW-4. The red rectangle indicates the sampling section. Line scan and spot analyses are similarly indicated as in [A]. All line lengths, widths and distances are on scale.

3.4.1 Analytical setup

The measurement routine was developed with a Nu Plasma MC-ICP-MS (see Table 3.1 for cup-configuration) coupled with a New Wave UP213 nm Nd:YAG laser ablation system at the Max Planck Institute for Chemistry, Mainz. Measurements were also performed with the MC-ICP-MS coupled to a NWR Femto200 laser ablation system to compare results obtained with two laser ablation systems. The femtosecond laser is less sensitive to matrix effects that may cause isotope fractionation (Poitrasson et al., 2003; Vanhaecke et al., 2010). Prior to laser ablation, the MC-ICP-MS was coupled to a CETAC Aridus II Desolvating Nebulizer system for tuning. The Sr reference solution NIST SRM 987 was used for optimizing the peak shape and coincidence of the individual Sr isotopes (^{88}Sr , ^{87}Sr , ^{86}Sr , ^{84}Sr) and to test the influence of different tuning parameters on ion beam intensity and the $^{87}\text{Sr}/^{86}\text{Sr}$ ratio. Several tuning parameters were changed systematically. Tests showed that the gas flows of the Aridus introduction system have a significant effect on the Sr isotope ratios. Furthermore, the torch position and the tuning of the high voltage lenses are important, since they affect the sample introduction into the system and the ion beam inside the mass spectrometer. Finally, the source lenses have been shown to have a significant effect on the $^{87}\text{Sr}/^{86}\text{Sr}$ ratio. In order to test the effects of changes in the lens settings, we started with seven measurements of NIST SRM 987 to test stability of the $^{87}\text{Sr}/^{86}\text{Sr}$ ratio over time. In a first step, the lens settings were tuned for maximum ^{88}Sr intensity. Subsequently, the different source and transfer lens settings were changed systematically. For each lens, three measurements were performed: First, the voltage of the lens was decreased by 10 V, then increased by 20 V, and finally decreased by 10 V to return to the original value. This procedure was performed for all seven source and transfer lenses. Results are presented in Fig. 3.2 and Table A3.1.

Settings were then further optimised with the Nu MC-ICP-MS coupled to the LA system. Since the UP213 nm laser ablation system offers higher fluence values (20 – 30 J/cm²) and count rates than the femtosecond laser (0.7 – 0.8 J/cm²), this system allows measurement of samples with comparably low Sr mass fractions (>200 µg/g). Potential matrix effects are assessed by comparison with the femtosecond laser. All samples and reference materials have a low Rb content (Table 3.2). The operating parameters for the MC-ICP-MS and the laser ablation systems are given in Table 3.3.

Table 3.1: Nu Plasma collector block assignments used for *in-situ* LA-MC-ICP-MS Sr isotope analysis of speleothems. Collectors H1, H2, H4, Ax and L1 – L5 are Faraday cups, IC-1 is an ion counter.

Collector	H4	H2	H1	Ax	L1	L2	L3	IC-1	L4	L5
Single Mass	88	87	86.5	86	85.5	85	<u>84</u>	83.5	83	82
Double Mass	176	174	173	172	171	170	168	167	166	164
Isotope of interest	$^{88}\text{Sr}_{82.58\%}$	$^{87}\text{Sr}_{7.00\%}$	-	$^{86}\text{Sr}_{9.86\%}$	-	-	$^{84}\text{Sr}_{0.56\%}$	-	-	-
Singly-charged interferences	-	$^{87}\text{Rb}_{27.83\%}$	-	$^{86}\text{Kr}_{17.28\%}$	-	$^{85}\text{Rb}_{72.17\%}$	$^{84}\text{Kr}_{56.99\%}$	-	$^{83}\text{Kr}_{11.50\%}$	$^{82}\text{Kr}_{11.59\%}$
Doubly-charged interferences	$^{176}\text{Yb}_{12.99\%}$	$^{174}\text{Yb}_{32.03\%}$	$^{173}\text{Yb}_{16.10\%}$	$^{172}\text{Yb}_{21.68\%}$	$^{171}\text{Yb}_{14.09\%}$	$^{170}\text{Yb}_{2.98\%}$	$^{168}\text{Yb}_{0.12\%}$	-	-	-
Molecular interferences	-	-	-	-	-	$^{170}\text{Er}_{14.91\%}$	$^{168}\text{Er}_{26.98\%}$	$^{167}\text{Er}_{22.87\%}$	$^{166}\text{Er}_{33.50\%}$	$^{164}\text{Er}_{1.60\%}$
Molecular interferences	$^{40}\text{Ca}^{48}\text{Ca}$	$^{44}\text{Ca}^{43}\text{Ca}$	-	$^{40}\text{Ca}^{46}\text{Ca}$	-	$^{42}\text{Ca}^{43}\text{Ca}$	$^{40}\text{Ca}^{44}\text{Ca}$	-	$^{40}\text{Ca}^{43}\text{Ca}$	$^{40}\text{Ca}^{42}\text{Ca}$
Molecular interferences	$^{40}\text{Ar}^{48}\text{Ca}$	-	-	$^{40}\text{Ar}^{46}\text{Ca}$	-	-	$^{40}\text{Ar}^{44}\text{Ca}$	-	$^{40}\text{Ar}^{43}\text{Ca}$	$^{40}\text{Ar}^{42}\text{Ca}$

Note that only collectors used during analysis are shown in this table. Potential interferences affecting the Sr masses are also illustrated along with natural abundances for Sr, Rb, Kr, Yb and Er (Berglund and Wieser (2011)). Abundances for molecular interferences of Ca dimers and argides are not shown for reasons of clarity. Some masses have a large number of potential interferences of Ca argides and dimers (e.g. mass 86 with $^{43}\text{Ca}^{43}\text{Ca}$, $^{40}\text{Ca}^{46}\text{Ca}$, $^{42}\text{Ca}^{44}\text{Ca}$, $^{48}\text{Ca}^{38}\text{Ar}$, $^{46}\text{Ca}^{40}\text{Ar}$). Here, only the two most common molecular interferences are shown. Prior to each analysis, the peak center was determined on mass 84 (L3) using the signal of ^{84}Kr in the gas flow of Ar. Therefore, mass 84 is underlined.

3.4.2 Reference materials

The reference material (RM) Jct-1 was measured to determine the accuracy and precision of the method. This modern marine carbonate sample originates from a recent giant clam and has a $^{87}\text{Sr}/^{86}\text{Sr}$ -ratio comparable to modern sea water ($^{87}\text{Sr}/^{86}\text{Sr}$ of 0.70918 ± 0.00001 , 2 SE, Faure and Mensing, 2005), as confirmed by solution MC-ICP-MS measurements ($^{87}\text{Sr}/^{86}\text{Sr} = 0.70915 \pm 0.00005$, Ohno and Hirata, 2007). Recently, a $^{87}\text{Sr}/^{86}\text{Sr}$ ratio of 0.70917 ± 0.00001 has been obtained for Jct-1 by MC-ICP-MS (Weber et al., 2018b). Due to its comparable Sr content of 1400 $\mu\text{g/g}$ (Aizawa, 2008), Jct-1 was chosen as RM for the measurements of samples GP5 and MAW-4. Furthermore, the RMs JcP-1, a modern coral with $^{87}\text{Sr}/^{86}\text{Sr} = 0.70916 \pm 0.00002$ (Ohno and Hirata, 2007) and MACS-3, a synthetic carbonate pellet ($^{87}\text{Sr}/^{86}\text{Sr} = 0.7075532 \pm 0.0000037$; Jochum et al., 2011a), were also tested. Both of these RM samples have a very high Sr mass fraction (7500 $\mu\text{g/g}$ for JcP-1, Aizawa, 2008, and 6760 $\mu\text{g/g}$ for MACS-3 Jochum et al., 2012) and are well suited for femtosecond laser analysis. For tuning and test measurements, we used a modern day bivalve shell of *Glycymeris* sp., which has two distinct areas of different Sr mass fractions of ca. 1000 and 5000 $\mu\text{g/g}$.

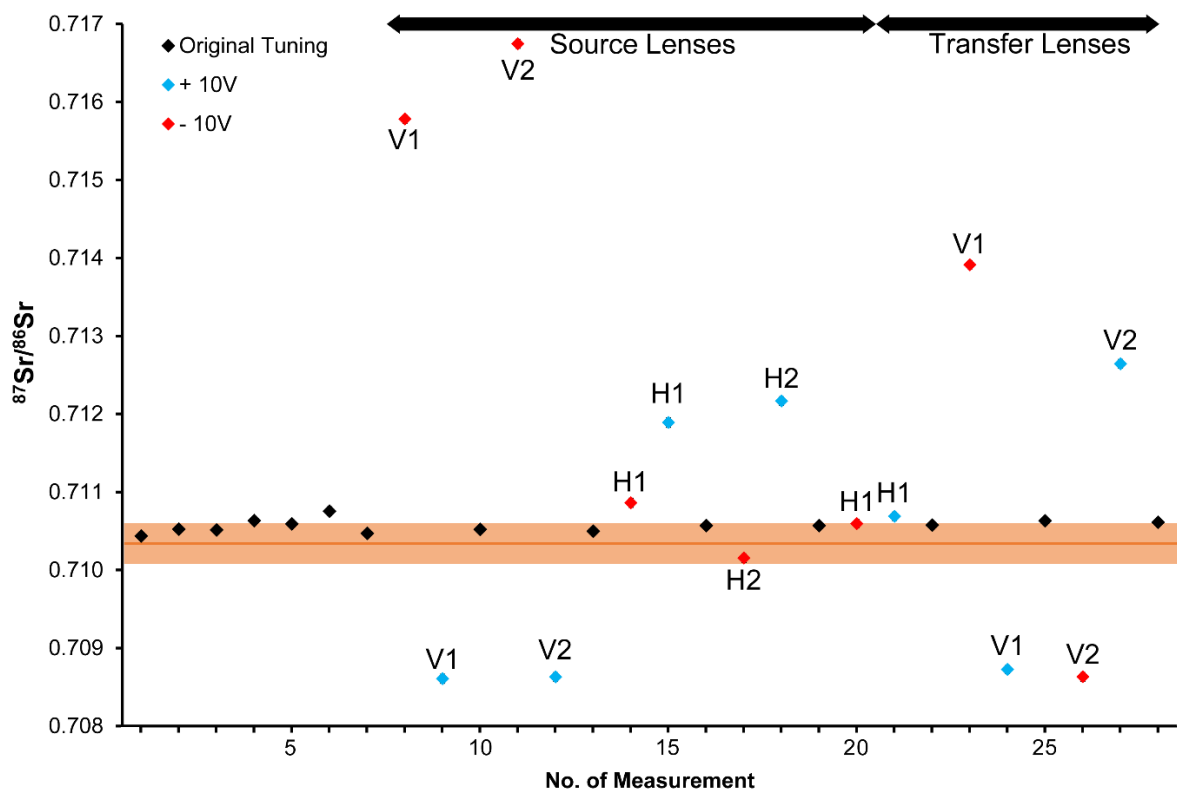


Fig. 3.2: $^{87}\text{Sr}/^{86}\text{Sr}$ ratios obtained on reference solution NIST SRM 987. The orange line represents the literature value of $^{87}\text{Sr}/^{86}\text{Sr} = 0.71034 \pm 0.00026$ (GeoReM, Jochum et al., 2005), the shading in bright orange shows the 2 SE. The large fluctuations in the Sr isotope ratio are caused by changes in the settings of the source and transfer lenses of the Nu Plasma MC-ICP-MS, marked by the black arrows. Black diamonds represent measurements with the original lens settings, while blue (red) diamonds represent measurements with a 10 V increase (decrease) in lens voltage in comparison to the original lens setting.

3.4.3 Laser ablation sampling method

Multiple LA-MC-ICP-MS measurements were performed perpendicular to the growth axis of the speleothem samples, parallel to and within the same distinct growth layers to check for reproducibility. In order to identify the best method for analysing Sr isotope ratios in speleothems by LA-MC-ICP-MS, we applied two different sampling methods. First, we used the line scan technique, which has the advantage that a high signal intensity can be maintained for a relatively long measurement interval, improving counting statistics. In contrast, for spot analyses, the signal intensity slowly decreases with ablation depth. However, for spot analyses, mixing of material from different growth layers is excluded. The line scans followed individual growth bands and each of usually three line scans per growth layer had a circular spot size of 80 – 100 μm and a length of 750 μm (except line scan GP5-7, which was 2000 μm). They were scanned with a scan speed of 5 $\mu\text{m}/\text{s}$, providing about 150 s per line scan measurement. This sampling approach enables us to identify potential changes in the $^{87}\text{Sr}/^{86}\text{Sr}$ ratio at a very high spatial resolution. Prior to each analysis, a pre-ablation was performed with a spot size of

110 μm and a scan speed of 80 $\mu\text{m/s}$ (Table 3.3). The first 5 s are discarded due to high intensities when the laser starts, which is typical for laser ablation analyses. Spots were analysed with a circular spot size of 100 μm and a dwell time of 120 s. To test the reproducibility of the method, three line scans were placed parallel to each other within the same growth band with less than 50 μm between the end and start of each line scan (Fig. 3.1). The distance between the measured layers varied between 150 μm and 850 μm for GP5 and 500 μm for MAW-4. The spot analyses of GP5 were performed for a few layers only. Each spot analysis is located near the end of the respective line scan. For correction purposes, RM JcT-1 was measured three times before and after each set of samples (usually six measurements in total).

To compare both laser ablation systems, we performed measurements with different RMs. Since the Sr mass fraction of JcP-1 is almost six times that of JcT-1, the laser settings for the UP213 laser ablation system were adjusted to prevent the ^{88}Sr intensity from reaching critical values (>10 V). We used a laser energy of 60 %, a repetition rate of 5 Hz and a spot size of 55 μm . All measurements were performed as spot analyses. To test the robustness of the results, we also applied our standard bracketing approach on JcP-1 by measuring samples of JcT-1 before and after JcP-1. The laser settings for JcT-1 were chosen as described in Table 3.3.

Our NWR Femto200 laser ablation system only allows spot sizes up to 65 μm , therefore we only measured RMs with high Sr mass fractions, such as JcP-1 and MACS-3. The laser parameters for these measurements are presented in Table 3.3. Spot measurements with the femtosecond laser ablation system suffer from a rapid decrease in signal intensity. Thus, all measurements were performed as line scans. We measured three samples of JcP-1, followed by six measurements of MACS-3 and again three samples of JcP-1.

3.5 Correction procedure for LA-MC-ICP-MS

Strontium isotopes were measured on cups H4 (^{88}Sr), H2 (^{87}Sr), Ax (^{86}Sr) and L3 (^{84}Sr) (Table 3.1). The major advantage of Sr isotope analysis with LA-MC-ICP-MS is that Sr isotopes are measured *in-situ*, without the need of chemical separation. This means, however, that the matrix contains several other isotopes that potentially affect the Sr isotope signal (i.e. ^{87}Rb , but also doubly charged ions, such as ^{176}Yb , ^{174}Yb , ^{172}Yb , ^{168}Yb , ^{168}Er , and molecular interferences, such as Ca-argides and/or -dimers, Table 3.1). In addition, the Ar gas may contain impurities of Kr, with interfering isotopes of ^{86}Kr and ^{84}Kr (Table 3.1). Some masses are affected by several interferences. For example, the ^{84}Sr signal on mass 84 may be affected by $^{84}\text{Kr}^+$, $^{168}\text{Er}^{2+}$, $^{168}\text{Yb}^{2+}$ and Ca argides/dimers. Therefore, it is necessary to find another mass that is not affected by other interferences, which can be used to correct for other masses of the same ion using known isotopic abundances. For example, we used mass number 86.5 that is mostly unaffected by other signals to correct for the Yb-interference by monitoring $^{173}\text{Yb}^{2+}$. Thus, the order of the corrections is important. The correction procedure is outlined in detail below. Fig. 3.3 shows

the magnitude of the individual correction steps on the $^{87}\text{Sr}/^{86}\text{Sr}$ ratio for measurements on Jct-1, GP5 and MAW-4.

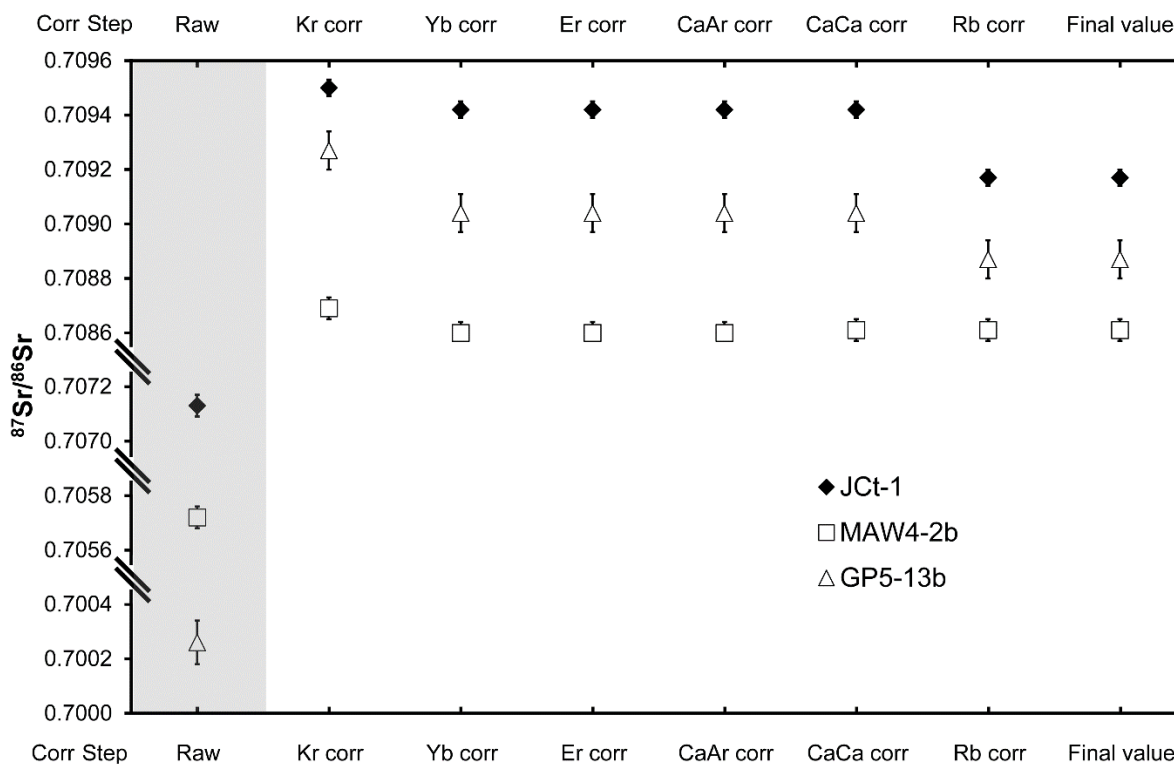


Fig. 3.3: Influence of the different correction steps on the $^{87}\text{Sr}/^{86}\text{Sr}$ ratio of Jct-1 (black diamonds), MAW-4 (squares) and GP5 (triangles). Note that all results are mass bias corrected.

3.5.1 Background correction

Potential interferences of ^{86}Kr , ^{84}Kr , ^{83}Kr and ^{82}Kr from minor contaminations in the Ar gas supply are corrected by a blank measurement. For this reason, prior to each analysis an on-peak background correction is performed for 45 s during the laser warm-up time. Then, the median for each signal intensity is subtracted from the measured signal. This removes all Kr interferences as well as potential remains of Sr from previous measurements.

3.5.2 Rare-earth elements (REE)

After background correction, different interferences must be eliminated. Doubly-charged isotopes of Er and Yb can be detected on half masses (Table 3.1). $^{173}\text{Ytterbium}$ is the only isotope measured on cup H1 on half-mass 87.5, and ^{171}Yb is the only one measured on cup L1 on half mass 85.5. Thus, ^{173}Yb and ^{171}Yb can be measured without any interferences. By assuming constant isotope ratios for Yb (Berglund

and Wieser (2011), the signal for all Yb isotopes can be calculated. Although Yb is quite rare in speleothem samples (Table 3.2), this correction may have a minor influence on the $^{87}\text{Sr}/^{86}\text{Sr}$ ratios.

The second step is to correct for Er. ^{167}Er Erbium is the only isotope measured on ion counter IC-1 on half mass 83.5, and other Er isotopes can be calculated assuming constant isotope ratios in the same way as Yb (Berglund and Wieser, 2011). Erbium is uncommon in speleothem samples (Table 3.2) and this correction is only of minor importance. Several laser ablation studies on other sample materials did not even correct for rare earth elements (REE) during Sr isotope analysis (e.g. Christensen et al., 1995; Barnett-Johnson et al., 2005; Jochum et al., 2009; Copeland et al., 2010).

3.5.3 Molecular interferences

The next step is to correct for molecular interferences of Ca dimers and argides. Since it is impossible to differentiate between the signals resulting from argides and dimers, the relative amounts of each signal are taken into account to correct for those interferences in relation to the signal on mass 82. This mass is used as a reference since it has insignificant interferences and a potentially higher signal of argides and dimers than mass 83, which is also free of significant interferences (Table 3.1). As an example, we briefly describe the correction of mass 84 for Ca argides and dimers.

After correcting for background and REEs, the correction for Ca argides is performed by the following relationship:

$$84_{ArCorr} = 84_{uncorr} - 82_{uncorr} * \left(\frac{\sum \text{CaAr}_{84}}{\sum \text{CaAr}_{82}} \right) \quad (\text{Eq. 3.I})$$

where 84_{ArCorr} is the corrected signal on mass 84, 84_{uncorr} is the uncorrected signal (besides background and REE correction) on mass 84 and 82_{uncorr} is the signal on mass 82. $\sum \text{CaAr}_{84}$ is the sum of the relative portion of Ca argides on mass 84, and $\sum \text{CaAr}_{82}$ is the sum of the relative portion of Ca argides on mass 82, based on their natural occurrence (Berglund and Wieser, 2011). This correction is performed for masses 88, 86, 84 and 83. For the interferences from Ca dimers, the correction is done in a similar way, again using the signal on mass 82 as a reference:

$$84_{Corr} = 84_{ArCorr} - 82_{uncorr} * \left(\frac{\sum \text{CaCa}_{84}}{\sum \text{CaCa}_{82}} \right) \quad (\text{Eq. 3.II})$$

where 84_{Corr} is the corrected signal on mass 84, 84_{ArCorr} is the background corrected intensity on mass 84, REEs and Ca argides, and 82_{uncorr} is the uncorrected signal (besides background and REE correction) on mass 82. $\sum \text{CaCa}_{84}$ is the sum of the relative portion of Ca dimers on mass 84 and $\sum \text{CaCa}_{82}$ is the sum of the relative portion of Ca dimers on mass 82. This correction is performed for masses 88, 87, 86, 85, 84 and 83 and only applied for signals >0 V. All other signals remain uncorrected because the intensity of Ca argides and dimers is too small to detect and does not affect the results.

3.5.4 Mass bias

After correcting the raw signals for interferences, the mass bias needs to be corrected. This correction is performed prior to the correction for the interference of Rb, because the mass bias obtained from the $^{86}\text{Sr}/^{88}\text{Sr}$ ratio is subsequently used to obtain the mass bias corrected $^{85}\text{Rb}/^{87}\text{Rb}$ ratio (section 3.5.5). Based on the signals corrected for background, REEs, Ca argides and dimers, raw values for the ratios of $^{86}\text{Sr}/^{88}\text{Sr}$, $^{84}\text{Sr}/^{86}\text{Sr}$ and $^{87}\text{Sr}/^{86}\text{Sr}$ are calculated. Then, a mass fractionation factor α is calculated to correct for the instrumental mass fractionation based on the $^{86}\text{Sr}/^{88}\text{Sr}$ ratio and the exponential law described in Ingle et al. (2003):

$$R_{corr} = R_{meas} * \left(m_{87\text{Sr}}/m_{86\text{Sr}} \right)^\alpha \quad (\text{Eq. 3.III})$$

where m_{87} and m_{86} are the masses of ^{87}Sr and ^{86}Sr . The mass fractionation factor α is calculated as described in Ehrlich et al. (2001):

$$\alpha = \left(\frac{\ln\left(\frac{\left(\frac{^{86}\text{Sr}}{^{88}\text{Sr}}\right)_{true}}{\left(\frac{^{86}\text{Sr}}{^{88}\text{Sr}}\right)_{meas}}\right)}{\ln(m_{86}/m_{88})} \right) \quad (\text{Eq. 3.IV})$$

where $(^{86}\text{Sr}/^{88}\text{Sr})_{true}$ is the accepted value of 0.1194 (Steiger and Jäger, 1977) and m_{88} and m_{86} are the masses of ^{88}Sr and ^{86}Sr .

3.5.5 Interference of Rb

The final step in the correction procedure is to correct the $^{87}\text{Sr}/^{86}\text{Sr}$ ratio for the interference of ^{87}Rb . Due to the previous corrections, mass 85 only consists of ^{85}Rb (Table 3.1), which can be used to calculate the fraction of ^{87}Rb by using the constant ratio of $^{87}\text{Rb}/^{85}\text{Rb} = 0.3857$ (Berglund and Wieser, 2011). This was done following equation 3.V:

$$^{87}\text{Rb} = \left(\frac{^{87}\text{Rb}}{^{85}\text{Rb}_{Lit}} * ^{85}\text{Rb}_{meas} \right) * \left(m_{87}/m_{85} \right)^\alpha \quad (\text{Eq. 3.V})$$

where $^{87}\text{Rb}/^{85}\text{Rb}_{Lit}$ is the literature value (Berglund and Wieser, 2011), $^{85}\text{Rb}_{meas}$ is the Rb signal on mass 85 corrected for background, REEs and Ca argides/dimers, m_{87} is the mass of ^{87}Rb , m_{85} is the mass of ^{85}Rb , and α is the mass fractionation factor. The correction on $^{87}\text{Sr}/^{86}\text{Sr}$ is then performed using the following equation:

$$\frac{^{87}\text{Sr}}{^{86}\text{Sr}_{\text{RbCorr}}} = \left[\frac{(^{87}\text{Sr}_{uncorr} - ^{87}\text{Rb})}{^{86}\text{Sr}} \right] * \left(m_{87}/m_{86} \right)^\alpha \quad (\text{Eq. 3.VI})$$

where $^{87}\text{Sr}_{uncorr}$ is the Sr signal on mass 87 corrected for background, REEs and argides/dimers (not for Rb), ^{87}Rb and ^{86}Sr are the corrected signals for Rb on mass 87 and Sr on mass 86, respectively, m_{87} and m_{86} are the masses for Sr and α is the mass fractionation factor. This Rb correction is only considered

robust for samples with a Rb/Sr ratio <0.02 (Irrgeher et al., 2016). For samples with higher Rb content, an alternative Rb-correction is necessary (Müller and Anczkiewicz, 2016). All speleothem samples and RMs analysed in this study are below this threshold (Table 3.2).

3.5.6 Data processing

After calculating the interference-free $^{87}\text{Sr}/^{86}\text{Sr}$ ratio, the results are calibrated by standard bracketing using RMs with well-known $^{87}\text{Sr}/^{86}\text{Sr}$ ratios, as has been recommended as calibration strategy for Sr isotope analysis (Irrgeher et al., 2016). Furthermore, to avoid effects of individual large peak values, we performed a 2 SD outlier test for the median of all $^{87}\text{Sr}/^{86}\text{Sr}$ values, removing all values deviating >2 SD from the median.

Usually, the final $^{87}\text{Sr}/^{86}\text{Sr}$ ratios obtained for the RMs deviate slightly from the reference values, necessitating an additional correction step. Each sample is therefore bracketed by a set of three individual measurements of a suitable RM. The mean value of the three RMs is calculated, and a correction factor for the sample is calculated according to the following equation:

$$Sr_{Corr} = \frac{{}^{87}\text{Sr}/{}^{86}\text{Sr}_{true}}{{}^{87}\text{Sr}/{}^{86}\text{Sr}_{meas}} \quad (\text{Eq. 3.VII})$$

where $^{87}\text{Sr}/^{86}\text{Sr}_{true}$ is the literature value of the RM and $^{87}\text{Sr}/^{86}\text{Sr}_{meas}$ is the measured ratio of the RM. We then use the mean value of the two correction factors from the two sets of RMs (measured prior and subsequent to the sample) and apply it to the measured sample $^{87}\text{Sr}/^{86}\text{Sr}$ ratio. Since the measurements of the RMs are associated with an uncertainty, error propagation is performed by adding the relative 2 SE for the measurement of the RM (2 Std Err_{Ref}) to the relative 2 SE of the measured sample (2 Std Err_{Spl}):

$$2 \text{ Std Err}_{SampleCorr} [\%] = \sqrt{(2 \text{ Std Err}_{Ref} [\%])^2 + (2 \text{ Std Err}_{Spl} [\%])^2} \quad (\text{Eq. 3.VIII})$$

The 2 Std Err_{Ref} value is calculated from the mean of the relative 2 SE of all RMs, while the 2 Std Err_{Spl} is calculated from the mean of the line scans or spot measurements for each sample layer. By applying the error propagation, the 2 SE of each sample usually increases by $\pm 0.00001 - 0.00002$ (0.01 – 0.03 ‰).

3.6 Results

The results from the speleothem samples obtained with the two sampling methods (line scans and spot analyses, respectively) are presented in Table 3.2. Due to the extensive correction procedure, we show the effect of each correction step on the $^{87}\text{Sr}/^{86}\text{Sr}$ value for one LA-MC-ICP-MS measurement of JcT-1, MAW-4 and GP5, respectively. The results are presented in Fig. 3.3. The correction step associated with

the largest effect is the background correction and, depending on the sample, the corrections for interferences of Yb and Rb. Corrections for Ca argides and dimers are insignificant for our results.

3.6.1 Influence of tuning parameters on the $^{87}\text{Sr}/^{86}\text{Sr}$ ratio

Our solution MC-ICP-MS measurements show that tuning for maximum Sr intensity does not necessarily lead to a “true” $^{87}\text{Sr}/^{86}\text{Sr}$ ratio, but may deviate from the accepted value of the reference solution NIST SRM 987 ($^{87}\text{Sr}/^{86}\text{Sr} = 0.71034 \pm 0.00026$, GeoReM, Jochum et al. (2005) on the third or fourth decimal. This can be avoided by tuning the mass spectrometer to obtain the Sr isotope ratio known from the literature (at the expense of signal intensity). The procedure is described in chapter 3.1. While some changes have a large influence on the isotope ratio (e.g. the decrease by 10 V for source lenses V1 and V2), others only have a minor influence, such as the changes at transfer lens H1 (Fig. 3.2). We note that this might be a specific pattern for our mass spectrometer and may differ in other laboratories. After restoring to the original setting, the $^{87}\text{Sr}/^{86}\text{Sr}$ ratio was comparable to the starting value (Fig. 3.2).

Fig. 3.4 (data in Table A3.1) shows the evolution of the $^{87}\text{Sr}/^{86}\text{Sr}$ ratio during consecutive days of LA-MC-ICP-MS measurements of RM Jct-1. While the Sr isotope ratio increased during the first measurements, source lens adjustments brought the $^{87}\text{Sr}/^{86}\text{Sr}$ ratio back towards the reference value.

These results highlight the necessity of the standard bracketing approach, which corrects the described effects. Nevertheless, we minimised the influence of these effects by tuning the $^{87}\text{Sr}/^{86}\text{Sr}$ ratio towards the reference value prior to the measurement, or, if necessary, again afterwards.

3.6.2 Tests with reference materials

Reference materials are a basic requirement for reliable measurements, since they allow traceability of the obtained dataset. Therefore, the methodology was tested with three internationally available RMs.

3.6.2.1 Nanosecond LA-MC-ICP-MS

For the nanosecond laser ablation system, we chose the carbonate RMs Jct-1, Jcp-1 and MACS-3 and applied the method described above (section 3.4.3). These RMs have a large range of Sr mass fractions, and we are aware that changes of the laser parameters between different samples can affect the measurements. Nevertheless, all measurements showed sufficient fluence ($\sim 10 \text{ J/cm}^2$ for Jcp-1 and MACS-3 and $>22 \text{ J/cm}^2$ for Jct-1) and the obtained $^{87}\text{Sr}/^{86}\text{Sr}$ ratios showed the expected results within uncertainty. The mean value of the Jcp-1 measurements was $^{87}\text{Sr}/^{86}\text{Sr} = 0.70913 \pm 0.00008$ ($n = 3$) and agree with the literature value of 0.70916 ± 0.00002 (Ohno and Hirata, 2007). In addition, the uncorrected Jcp-1 $^{87}\text{Sr}/^{86}\text{Sr}$ ratio is 0.70914 ± 0.00007 ($n = 3$) and the uncorrected $^{87}\text{Sr}/^{86}\text{Sr}$ ratio of Jct-1 is 0.70917 ± 0.00005 ($n = 5$), thus both are indistinguishable from the literature values. The results for

MACS-3 provide an average $^{87}\text{Sr}/^{86}\text{Sr}$ value of 0.70753 ± 0.00005 ($n = 16$), which is in agreement with the literature value of 0.7075532 ± 0.0000037 (Jochum et al., 2011a).

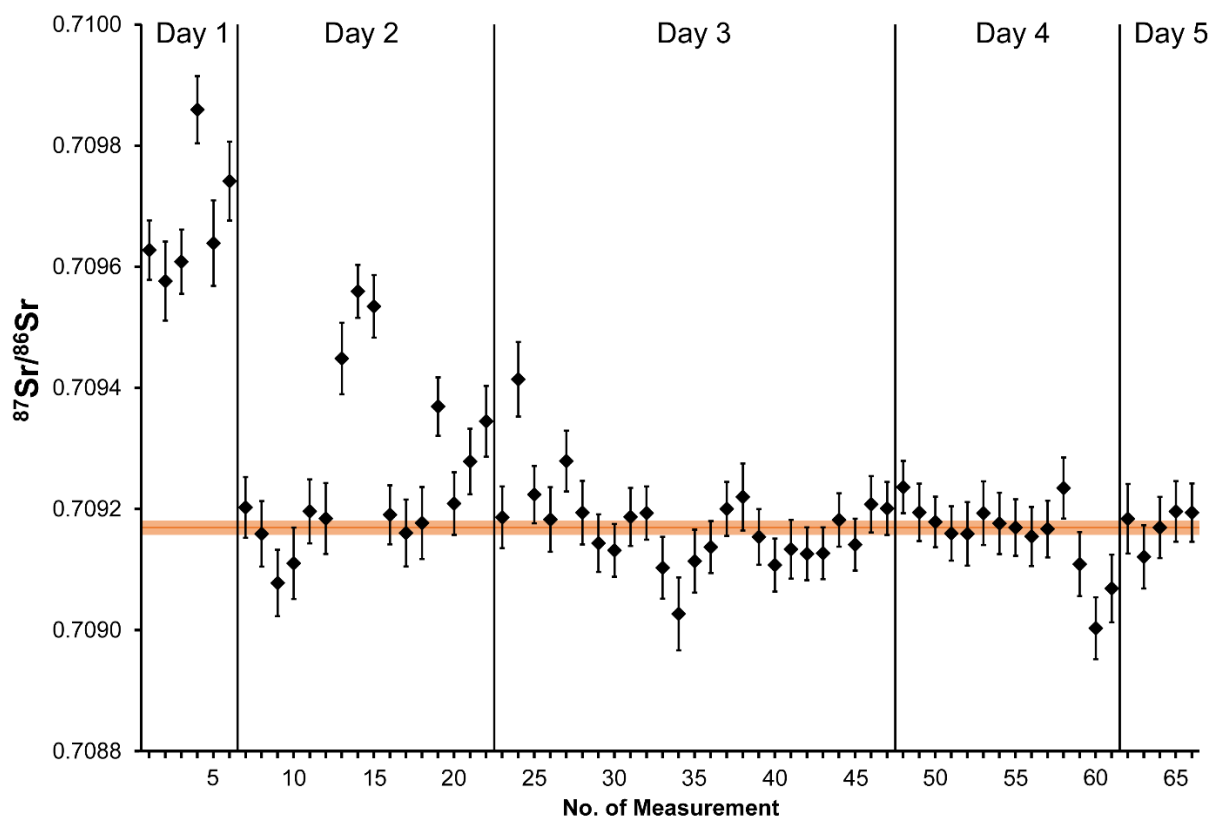


Fig. 3.4: $^{87}\text{Sr}/^{86}\text{Sr}$ ratios of reference material Jct-1 obtained during different days, showing the tuning influence during the first measurements. The orange line represents the reference value of Jct-1 of $^{87}\text{Sr}/^{86}\text{Sr} = 0.70917 \pm 0.00001$ (Weber et al., 2018b), the shading in bright orange corresponds to its 2 SE. Dashed vertical lines separate different days of measurements.

3.6.2.2 Femtosecond LA-MC-ICP-MS

In order to further test our methodology, we used a femtosecond laser ablation system on carbonate RMs with high Sr mass fractions (JcP-1 and MACS3) following the method as described in chapter 3.4.3. All measurements were corrected by the standard bracketing approach yielding $^{87}\text{Sr}/^{86}\text{Sr}$ ratios in agreement with the reference values (Fig. 3.5). An exception is measurement MACS-3-8, which shows a strongly elevated $^{87}\text{Sr}/^{86}\text{Sr}$ ratio. This sample may have been affected by changes in the Kr signal intensity because unusual peak intensities in ^{84}Kr were observed during the blank measurement. It is thus likely that similar fluctuations occurred during the measurement which affected the $^{87}\text{Sr}/^{86}\text{Sr}$ ratio. The measured raw $^{87}\text{Sr}/^{86}\text{Sr}$ ratios before the standard bracketing correction for JcP-1 are 0.70920 ± 0.00004 ($n = 6$) and 0.70757 ± 0.00005 for MACS-3 (without MACS3-8, $n = 5$), in agreement with the

literature values. After performing the standard bracketing approach, the average $^{87}\text{Sr}/^{86}\text{Sr}$ ratio is 0.70917 ± 0.00006 for JCp-1 ($n = 6$) and 0.70752 ± 0.00006 for MACS-3 (without MACS3-8, $n = 5$).

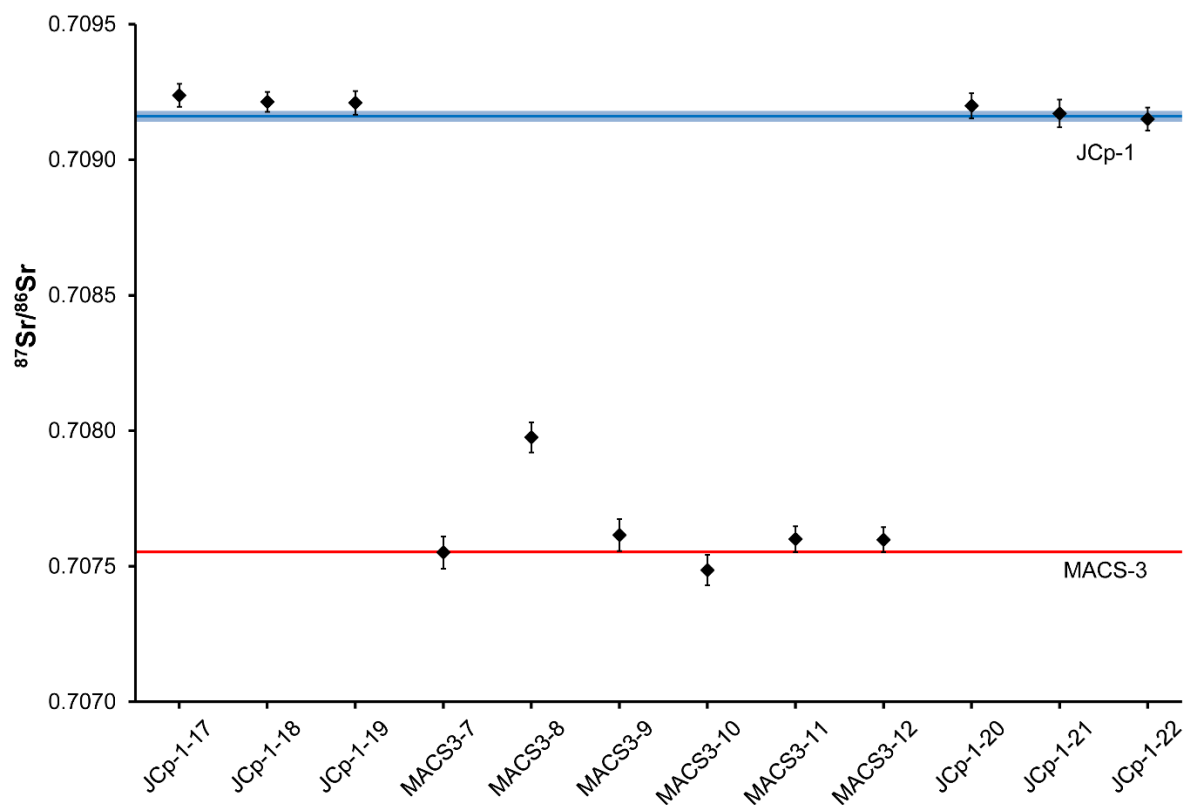


Fig. 3.5: $^{87}\text{Sr}/^{86}\text{Sr}$ ratios of reference materials JCp-1 and MACS-3 obtained by fs-LA-MC-ICP-MS. The red line represents the literature value of MACS-3 of $^{87}\text{Sr}/^{86}\text{Sr} = 0.7075532 \pm 0.0000037$ (Jochum et al., 2011a), the blue line shows the literature value of JCp-1 of $^{87}\text{Sr}/^{86}\text{Sr} = 0.70916 \pm 0.00002$ (Ohno and Hirata, 2007), with its 2 SE shown as bright blue shading. The uncertainty range for the reference value of MACS-3 is too small to be visible in the figure. Note that sample MACS-3-8 was strongly affected by very variable ^{84}Kr intensities during the blank measurement and probably during the sample measurement as well.

3.6.3 Speleothem GP5

On sample GP5, a total number of 27 different layers were measured (Fig. 3.6 [A]). In the area between ~ 116 to 118.5 mm distance from top (DFT) the resolution is high (i.e. less than $100 \mu\text{m}$ between line scans). Further measurements were performed with a distance of $\sim 1000 \mu\text{m}$ between each other. Some measurements suffer from changing mass bias and low intensities ($^{88}\text{Sr} < 1$ V), resulting in decreasing values of $^{87}\text{Sr}/^{86}\text{Sr}$ (in particular line scans GP5-17-21, Table 3.2). The $^{87}\text{Sr}/^{86}\text{Sr}$ ratios generally show only minor variations, ranging from 0.70856 ± 0.00017 to 0.70920 ± 0.00007 . The low-resolution measurements from 108.3 to 115.3 mm DFT show a relatively stable Sr isotope composition with

$^{87}\text{Sr}/^{86}\text{Sr}$ ratios between 0.70890 ± 0.00011 and 0.70913 ± 0.00008 . The average $^{87}\text{Sr}/^{86}\text{Sr}$ ratio of all line scans is 0.70892 ± 0.00006 ($n = 79$).

36 spot analyses were performed on stalagmite GP5. These were placed near the right end of the third line scan within the same growth layer (Fig. 3.1). At signal intensities lower than ca. 0.6 V on ^{88}Sr , we found a significant decrease of the $^{87}\text{Sr}/^{86}\text{Sr}$ ratio. Corresponding measurements are marked with double diamonds \blacklozenge in Table 3.2. The $^{87}\text{Sr}/^{86}\text{Sr}$ ratios of the spot measurements from GP5 are presented as circles in Fig. 3.6 [A]. The results show a similar pattern as the line scans, even though the 2 SE are slightly larger. The $^{87}\text{Sr}/^{86}\text{Sr}$ ratio varies between 0.70872 ± 0.00024 and 0.70907 ± 0.00011 . The mean of all spot measurements is $^{87}\text{Sr}/^{86}\text{Sr} = 0.70897 \pm 0.00005$ ($n = 32$) and in good agreement with the line scan data.

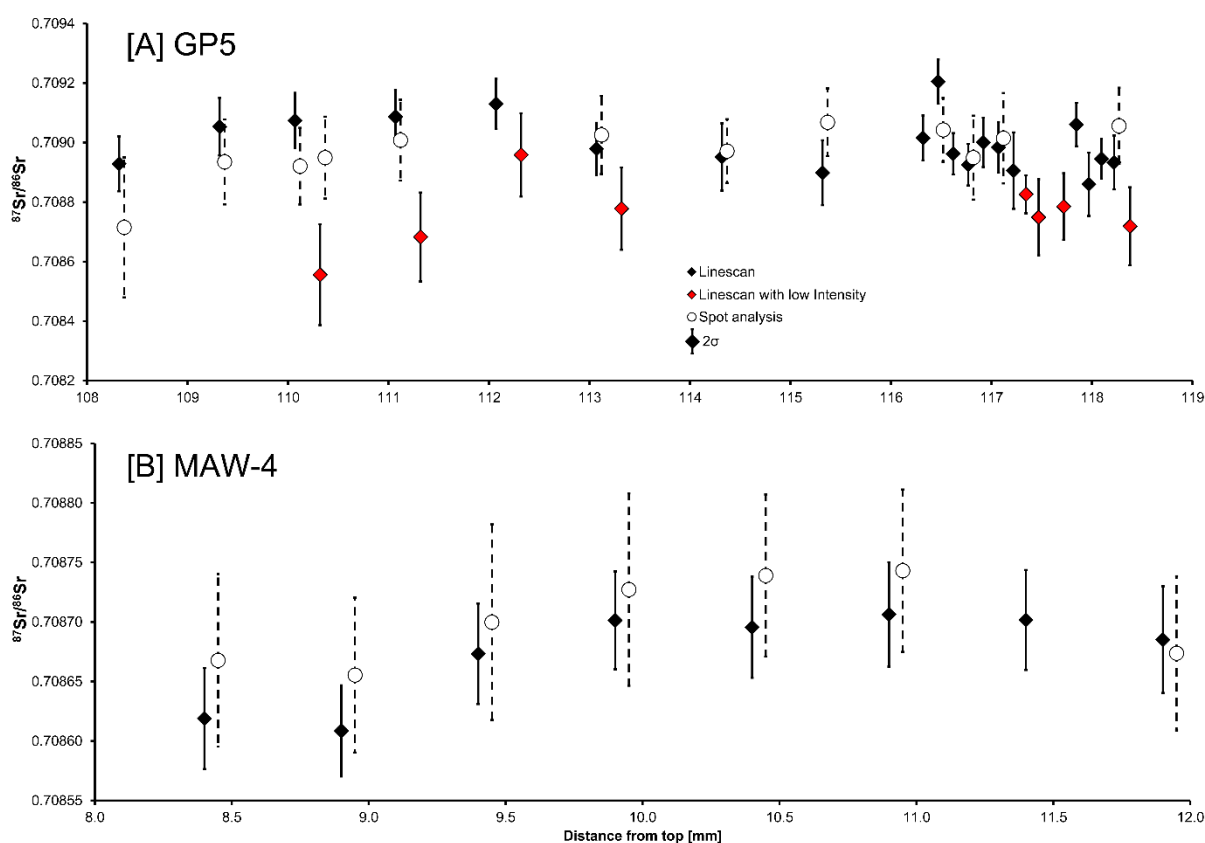


Fig. 3.6: [A] $^{87}\text{Sr}/^{86}\text{Sr}$ ratios are plotted against the distance from top of speleothem GP5. Line scan measurements affected by low signal intensities are marked red. [B] $^{87}\text{Sr}/^{86}\text{Sr}$ ratios of speleothem MAW-4 against distance from top [mm] for the line scan as well as the spot analyses. For better visualization of the error bars, spot analyses data were shifted to the right by 0.05 mm.

Table 3.2: Results of the line scan and spot analysis from speleothem samples GP5 and MAW-4. The alignment of the different cups is presented with the corresponding signal intensities. For most sample layers, three runs were performed. For these samples, the mean of all runs is shown.

Sample	Distance from top [mm]	\bar{x} \blacklozenge Sr conc [$\mu\text{g/g}$]	\bar{x} Total Sr [V]	\bar{x} Total Rb [mV]	\bar{x} Rb/Sr $\cdot 10^{-3}$	\bar{x} Er/Sr $\cdot 10^{-6}$	\bar{x} Yb/Sr $\cdot 10^{-6}$	\bar{x} $^{87}\text{Sr}/^{86}\text{Sr}$	\bar{x} 2 SE	\bar{x} Mass Bias $^{87}\text{Sr}/^{86}\text{Sr}$
<i>Linescans</i>										
<i>GP5</i>										
GP5-1	118.4	344	0.9	0.08	0.09	1.3	703	0.70872	0.00013	1.23%
GP5-2	118.2	349	1.4	0.08	0.06	1.3	257	0.70893	0.00009	1.22%
GP5-3	118.0	354	1.2	0.12	0.10	1.0	419	0.70886	0.00011	1.22%
GP5-4	117.7	310	1.1	0.08	0.07	1.0	~ 0	0.70879	0.00011	1.21%
GP5-5	117.5	292	1.2	0.10	0.09	1.0	1136	0.70875	0.00013	1.20%
GP5-6	117.2	354	1.1	0.10	0.09	1.1	664	0.70891	0.00013	1.20%
GP5-7	117.3	328	1.3	0.06	0.04	1.3	~ 0	0.70883	0.00006	1.18%
GP5-8	118.1	357	2.1	0.12	0.05	1.2	363	0.70895	0.00007	1.02%
GP5-9	117.8	335	2.0	0.13	0.06	1.2	497	0.70906	0.00007	1.05%
GP5-10	117.1	343	1.5	0.19	0.13	1.0	121	0.70898	0.00009	1.14%
GP5-11	116.9	321	1.6	0.12	0.07	0.9	424	0.70900	0.00008	1.31%
GP5-12	116.8	348	1.9	0.16	0.08	1.0	349	0.70893	0.00007	1.05%
GP5-13	116.6	338	1.9	0.15	0.08	1.1	289	0.70896	0.00007	1.07%
GP5-14	116.5	340	1.8	0.11	0.06	1.0	268	0.70920	0.00007	1.38%
GP5-15	116.3	336	1.8	0.13	0.07	1.0	803	0.70902	0.00008	1.61%
GP5-16	115.3	385	1.2	0.20	0.17	1.0	405	0.70890	0.00011	1.75%
GP5-17	114.3	416	1.1	0.10	0.10	1.0	501	0.70895	0.00011	2.03%
GP5-18	113.3	353	0.9	0.14	0.16	1.1	441	0.70878	0.00014	2.09%
GP5-19	112.3	363	0.8	0.17	0.22	1.1	179	0.70896	0.00014	1.82%
GP5-20	111.3	381	0.7	0.16	0.22	0.9	136	0.70868	0.00015	1.87%
GP5-21	110.3	427	0.7	0.13	0.19	1.1	285	0.70856	0.00017	2.23%
GP5-22	113.1	351	1.4	0.26	0.18	1.4	435	0.70898	0.00009	1.19%
GP5-23	112.1	425	1.5	0.19	0.13	1.6	~ 0	0.70913	0.00008	1.18%
GP5-24	111.1	384	1.4	0.16	0.12	1.6	91	0.70909	0.00009	1.16%
GP5-25	110.1	497	1.3	0.16	0.12	1.5	~ 0	0.70907	0.00009	1.16%
GP5-26	109.3	412	1.3	0.20	0.16	1.7	~ 0	0.70905	0.00010	1.16%
GP5-27	108.3	373	1.4	0.23	0.17	1.6	233	0.70893	0.00009	1.16%
<i>Linescans</i>										
<i>MAW4</i>										
MAW4-1	8.4	1729	4.8	0.06	0.01	0.4	1181	0.70862	0.00004	1.24%
MAW4-2	8.9	1629	5.7	0.03	0.01	0.4	2295	0.70861	0.00004	1.25%
MAW4-3	9.4	1526	4.8	0.04	0.01	0.5	623	0.70867	0.00004	1.25%
MAW4-4	9.9	1585	5.0	0.04	0.01	0.4	925	0.70870	0.00004	1.25%
MAW4-5	10.4	1600	4.9	0.06	0.01	0.4	1421	0.70870	0.00004	1.26%
MAW4-6	10.9	1560	4.5	0.06	0.01	0.4	149	0.70871	0.00004	1.26%

Table A3.2 (continued):

Sample	Distance from top [mm]	\bar{x} \blacklozenge Sr conc [$\mu\text{g/g}$]	\bar{x} Total Sr [V]	\bar{x} Total Rb [mV]	\bar{x} Rb/Sr $\cdot 10^{-3}$	\bar{x} Er/Sr $\cdot 10^{-6}$	\bar{x} Yb/Sr $\cdot 10^{-6}$	\bar{x} $^{87}\text{Sr}/^{86}\text{Sr}$	\bar{x} 2 SE	\bar{x} Mass Bias $^{87}\text{Sr}/^{86}\text{Sr}$
MAW4-7	11.4	1595	4.7	0.12	0.02	0.4	552	0.70870	0.00004	1.27%
MAW4-8	11.9	1458	4.2	0.07	0.02	0.5	624	0.70869	0.00004	1.27%
<i>Spotskans</i>										
<i>GP5</i>										
GP5-Spot-2	118.2	349	1.4	0.12	0.08	3.4	529	0.70906	0.00013	1.18%
GP5-Spot-10	117.1	343	1.0	0.10	0.09	3.5	865	0.70901	0.00015	1.12%
GP5-Spot-12	116.8	348	1.4	0.11	0.08	2.7	919	0.70895	0.00014	1.95%
GP5-Spot-14	116.5	340	1.7	0.13	0.08	2.7	327	0.70904	0.00011	1.92%
GP5-Spot-16	115.3	385	1.6	0.08	0.05	2.7	487	0.70907	0.00011	1.93%
GP5-Spot-17 $\blacklozenge\blacklozenge$	114.3	416	1.1	0.08	0.08	2.6	1116	0.70897	0.00011	1.87%
GP5-Spot-21	110.3	427	1.1	0.08	0.07	3.5	867	0.70895	0.00014	1.94%
GP5-Spot-22	113.1	351	1.2	0.07	0.06	2.9	757	0.70903	0.00013	1.91%
GP5-Spot-24 $\blacklozenge\blacklozenge$	111.1	384	0.9	0.11	0.12	3.0	763	0.70901	0.00014	1.93%
GP5-Spot-25	110.1	497	1.3	0.08	0.06	2.9	244	0.70892	0.00013	1.96%
GP5-Spot-26 $\blacklozenge\blacklozenge$	109.3	412	1.1	0.12	0.12	3.3	564	0.70894	0.00014	1.98%
GP5-Spot-27 $\blacklozenge\blacklozenge$	108.3	373	0.5	0.06	0.12	2.8	708	0.70872	0.00024	2.00%
<i>Spotskans</i>										
<i>MAW-4</i>										
MAW4-Spot-1	8.4	1729	4.1	0.15	0.04	1.3	432	0.70867	0.00007	0.92%
MAW4-Spot-2	8.9	1629	3.6	0.08	0.02	1.2	694	0.70866	0.00007	0.97%
MAW4-Spot-3	9.4	1526	4.2	0.09	0.02	1.3	1155	0.70870	0.00008	0.95%
MAW4-Spot-4	9.9	1585	3.9	0.07	0.02	1.4	1011	0.70873	0.00008	0.88%
MAW4-Spot-5	10.4	1600	4.3	0.08	0.02	1.3	654	0.70874	0.00007	0.45%
MAW4-Spot-6	10.9	1560	4.2	0.05	0.01	1.3	1116	0.70874	0.00007	0.49%
MAW4-Spot-8	11.9	1458	5.6	0.10	0.02	0.8	609	0.70867	0.00006	1.99%

\blacklozenge Sr mass fractions for sample GP5 were taken from Wassenburg et al. (2013) and Sr mass fractions for sample MAW-4 were taken from Wassenburg et al. (2016b).

$\blacklozenge\blacklozenge$ Not all of the three measurements from each spot were taken into account due to shifts in the $^{87}\text{Sr}/^{86}\text{Sr}$ ratio of measurements with low Sr-intensities (approximately below 0.7 V for ^{88}Sr).

3.6.4 Speleothem MAW-4

On MAW-4, 24 line scans were performed at a sampling resolution of 500 μm (Fig. 3.1). The $^{87}\text{Sr}/^{86}\text{Sr}$ ratios are presented in Fig. 3.6 [B]. While the first two measurements at 8.4 and 8.9 mm DFT are similar,

the following measurements show a slightly increasing trend towards higher values, reaching a maximum of 0.70871 ± 0.00004 . The 2 SE of all measurements is ± 0.00004 with an average $^{87}\text{Sr}/^{86}\text{Sr}$ ratio over all line scans of 0.70867 ± 0.00003 ($n = 24$).

24 spot analyses were performed on stalagmite MAW-4, placed near the right end of the third line scan within the same growth layer (Fig. 3.1). Note that layer MAW-4-7 was not measured. For layer MAW-4-8, a total number of six spot measurements were performed to test the reproducibility. The mean of MAW-4-Spot-8a-c is within uncertainty of the mean of MAW-4-Spot-8d-f. Since MAW-4-Spot-8a-f are in perfect agreement, they were combined as a single measurement (MAW-4-Spot-8). The $^{87}\text{Sr}/^{86}\text{Sr}$ ratios of the spot measurements of MAW-4 are presented as circles in Fig. 3.6 [B]. A pattern, similar to the line scans can be observed with two measurements at 8.4 and 8.9 mm DFT showing lower $^{87}\text{Sr}/^{86}\text{Sr}$ ratios compared to the other values. In contrast to the line scan measurements, this increase is not significant due to larger uncertainties. Nevertheless, an increase and a plateau at the same distance from top is visible for the spot analyses. The 2 SE of all measurements is in the range of ± 0.00006 to ± 0.00008 and therefore higher than for the line scans. The average $^{87}\text{Sr}/^{86}\text{Sr}$ ratio over all spot measurements is 0.70870 ± 0.00002 ($n = 24$), in agreement with the $^{87}\text{Sr}/^{86}\text{Sr}$ ratio derived from the line scans.

3.7 Discussion

The following chapters discuss the data obtained by LA-MC-ICP-MS and will results in the most appropriate sampling technique for the Sr isotope analysis of speleothem.

3.7.1 Line scan versus spot analysis

We used two different laser ablation methods for this study, i.e. line scans along growth bands and spots, to test which is the best approach. In general, the line scan method provides much smaller 2 SE than the spot analysis. For RM Jct-1, the final $^{87}\text{Sr}/^{86}\text{Sr}$ ratio usually has a 2 SE in the range of $\pm 0.00002 - 0.00005$ for line scan measurements, representing a total uncertainty in the range of 0.003 – 0.01 %. For spot analyses, the 2 SE was in the range of $\pm 0.00005 - 0.00007$. The 2 SE is highly dependent on the Sr mass fraction of the sample (Fig. 3.7). The different precision in spot and line scan analyses is caused by: 1) the longer integration time for the line scan approach, and 2) decreasing signal intensity during spot analysis caused by deepening of the laser crater. Therefore, the spot analysis approach might be insufficiently precise to resolve small scale changes in the $^{87}\text{Sr}/^{86}\text{Sr}$ ratio. This is exemplified in MAW-4, where an increase in the $^{87}\text{Sr}/^{86}\text{Sr}$ ratio was significant for the line scan approach, but not for the spot analyses due to larger uncertainties. A disadvantage of the line scan approach, however, is that unwanted sampling of material from different growth layers (with a different $^{87}\text{Sr}/^{86}\text{Sr}$ ratio) may occur. Furthermore, line scans require a larger sample surface compared to spot analysis. We recommend using

the line scan approach only for speleothems with a regular (parallel) layering that provides a relatively large sample surface (ca. 3 mm width and length). For speleothems with irregular layering, spot analysis may be the preferable choice. Tests with spot analyses showed that higher repetition rates (>10 Hz) result in a higher signal intensity and precision, which is desirable for samples with relatively low Sr mass fraction (200 – 500 $\mu\text{g/g}$), such as GP5. However, the sample material should be dense and stable enough to resist such a high ablation efficiency. Higher repetition rates also result in deeper laser craters and thus potentially in ablating into different layers. However, for repetition rates in the range of 5 – 10 Hz the depth of the crater should be in the range ≤ 12 and even less for line scan measurements (≤ 2 μm). Thus, this effect should be only important for very slowly or irregularly growing speleothems.

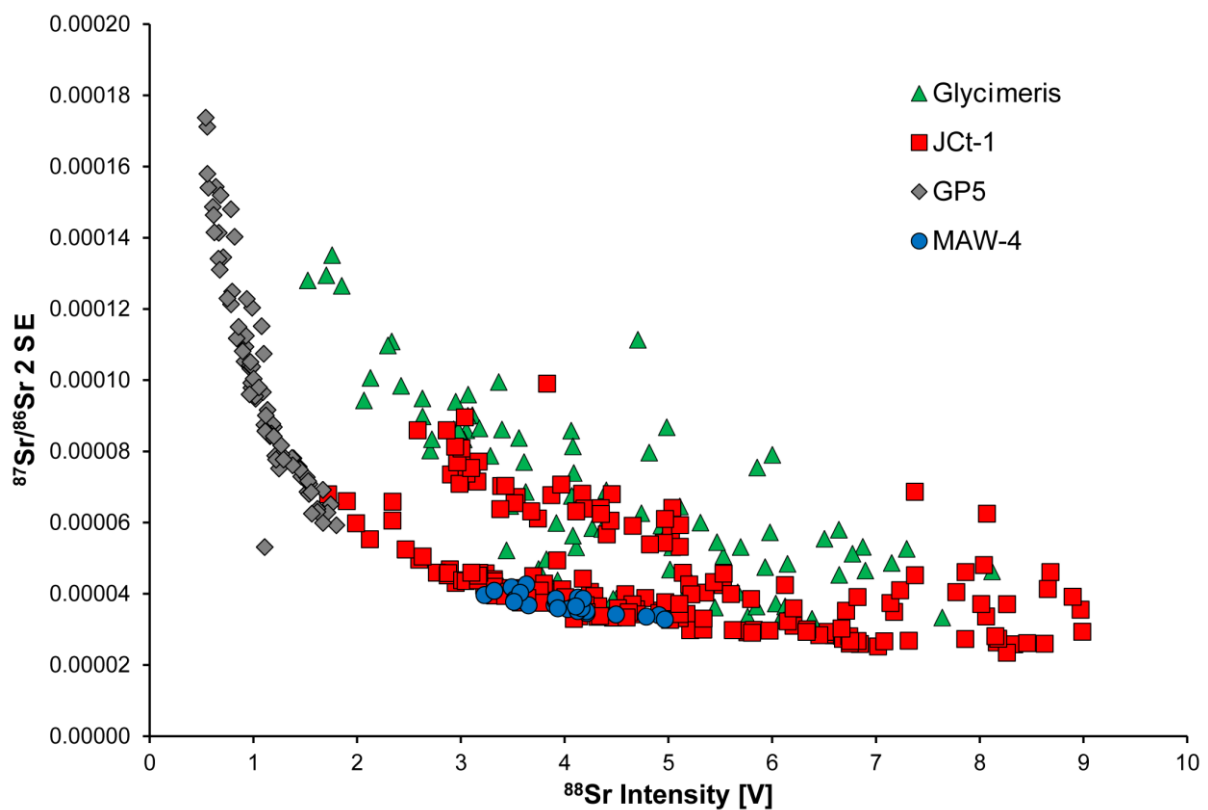


Fig. 3.7: Scatter plot of ^{88}Sr intensity vs. $^{87}\text{Sr}/^{86}\text{Sr}$ 2 SE. The dependency of the $^{87}\text{Sr}/^{86}\text{Sr}$ 2 SE on the ^{88}Sr intensity is shown for the line scan measurements of JcT-1, *Glycimeris* sp., GP5 and MAW-4.

3.7.2 Nanosecond versus femtosecond laser systems

Ablating RMs JcP-1 and MACS-3 with either a nanosecond or femtosecond laser gives similar results. While the nanosecond laser provides the advantage of measuring lower mass fraction samples with higher precision, the femtosecond laser is less vulnerable to fractionation effects and offers better control on the ablation process (Glaus et al., 2010; Koch and Gunther, 2007). In addition, the refractory Sr is generally less affected by matrix, elemental and isotopic fractionation effects in comparison to the

volatile Rb (Horn and von Blanckenburg, 2007). However, with our setup, the femtosecond laser approach requires much higher Sr mass fractions ($>1400 \mu\text{g/g}$) to achieve sufficient precision. For instance, we were not able to accurately measure JCT-1 and our speleothem samples with the femtosecond laser due to insufficient Sr mass fraction. In contrast, the standard bracketing approach with JCT-1 and JCp-1 with the nanosecond laser was successful and the data from MACS-3 were similar to literature values. The results from the femtosecond LA-MC-ICP-MS measurements show that our approach can be transferred to other laser ablation systems. The raw measurements of JCp-1 and MACS-3 are in good agreement with literature values and the performance of our standard bracketing approach does not affect the resulting $^{87}\text{Sr}/^{86}\text{Sr}$ significantly. Overall, the $^{87}\text{Sr}/^{86}\text{Sr}$ RM data obtained with both laser ablation systems agree within uncertainty and are therefore probably not affected by differences in matrix effects between the different setups.

3.7.3 Tuning parameters and suitable reference materials

An aspect of major importance identified during the development of the LA-MC-ICP-MS technique is to adjust the tuning after changing the cones to obtain correct $^{87}\text{Sr}/^{86}\text{Sr}$ ratios of a reference solution. Tuning for maximum signal intensity does not always result in the $^{87}\text{Sr}/^{86}\text{Sr}$ ratio of the RM (Fig. 3.2). To achieve the correct $^{87}\text{Sr}/^{86}\text{Sr}$ ratio we adjusted the lens settings. In comparison to the tuning of the high voltage lenses, the source and transfer lenses had a larger effect on stability and reliability of the $^{87}\text{Sr}/^{86}\text{Sr}$ ratios with our Nu Plasma MC-ICP-MS (Fig. 3.2). In addition, the laser ablation system itself alters the $^{87}\text{Sr}/^{86}\text{Sr}$ ratios of the measurements. Since different RMs and samples have variable Sr contents, the laser energy and spot size may have to be adjusted to prevent signal intensities larger than $\sim 10 \text{ V}$ on cup H4 (^{88}Sr signal). It is important to use similar measurement parameters for RMs and speleothem samples when the standard bracketing technique is applied. Therefore, it is essential to use a RM with similar Sr mass fraction and a similar matrix as the speleothem sample. By not using matrix-matched samples and RMs, potential differences in interferences may alter the correction (Irrgeher et al., 2016). In case of different matrices and/or large differences in Sr mass fraction, the resulting $^{87}\text{Sr}/^{86}\text{Sr}$ ratio of the unknown sample needs to be handled with care and might be less precise. For instance, the use of RM JCT-1 for correcting GP5 measurements was critical, due to low intensities on the sample ($1 - 2 \text{ V}$, ^{88}Sr) and high intensities on the RM (up to $8 - 9 \text{ V}$, ^{88}Sr) when using the same laser parameters. Fluence decreases with laser energy and it is not guaranteed that the same measurement parameters are available for all samples and RMs. For speleothem samples with much higher Sr mass fraction than in this study, JCp-1 and MACS-3 are suitable RMs.

Table 3.3: Operating parameters of the Nu Plasma MC-ICP-MS and the two laser ablation systems.

Nu Plasma MC-ICP-MS			
RF Power	1300 W		
Argon cooling gas flow rate	13 L/min		
Auxiliary gas flow rate	0.93 L/min		
Interface cones	Ni		
Lens settings	Optimized for maximum signal intensity and $^{87}\text{Sr}/^{86}\text{Sr}$ ratio		
Mass resolution	Low		
Mass analyser pressure	$3\text{-}5 \times 10^{-9}$ mbar		
Detection system	Nine Faraday collectors and one Ion Counter		
Sampling mode	Time Resolved Analysis		
	New Wave UP213 nm Laser ablation system		NWR Femto 200 Laser ablation system
Type of analysis	Line analysis	Spot analysis	Line analysis
Wavelength	213 nm	213 nm	200 nm
Line length	750 μm		750 μm
Ar flow rate	0.65-0.79 L/min	0.68-0.78 L/min	0.77 L/min
He flow rate	0.65-0.81 L/min	0.68-0.78 L/min	0.77 L/min
<i>Pre-Ablation</i>			
Frequency	10 Hz	10 Hz	5 Hz
Translation rate	80 $\mu\text{m}/\text{s}$		60 $\mu\text{m}/\text{s}$
Beam width	100-110 μm	110 μm	65 μm
<i>Ablation</i>			
Frequency	10 Hz	5-10 Hz	25 Hz
Translation rate	5 $\mu\text{m}/\text{s}$		5 $\mu\text{m}/\text{s}$
Beam width	80-100 μm	100 μm	55 μm
Dwelling time		120 s	
Fluence	20-30 J/cm^2	20-30 J/cm^2	0.7-0.8 J/cm^2
<i>Data Collection</i>			
Gas background	45 s	45 s	45 s
Sample	145 s	115 s	145 s
Integration	0.2 s	0.2 s	0.2 s

Furthermore, the signal intensity of the Sr isotope measurements is important. Measurements suffering from very low intensities on ^{88}Sr ($\sim <1$ V) show large uncertainties. A scatter plot of the intensity of the ^{88}Sr -signal against the 2 SE for the line scan measurements of JCT-1, the bivalve shell of *Glycimeris* sp., GP5 and MAW-4 (Fig. 3.7) reveals in particular for GP5 a high dependency on a sufficiently high Sr signal for precise measurements. Intensities of ^{88}Sr below ~ 1.5 V cause a dramatic shift towards large uncertainties. Similar patterns are visible for JCT-1 and the *Glycimeris* sp. shell. The Sr intensity

difference found in MAW-4 is too small to show the effect of signal intensity on the uncertainty. All measurements with low Sr intensities suffer from low counting statistics and the background correction of Kr might be insufficient.

Another effect that can have major detrimental influence on the analysis is progressive clogging of the cones. When a decrease in Sr intensity is observed, it is important to evaluate if this change results from a change of the Sr content in the sample or from clogging of the cones by deposition of Ca. Additional information on the performance of the mass spectrometer is provided by monitoring the mass bias. In our study, the mass bias for the $^{87}\text{Sr}/^{86}\text{Sr}$ -ratio was usually between 0.45 – 2.09 % ($R_{\text{corr}}/R_{\text{meas}} = 0.9791 - 0.9955$, Eq. 3.III). Especially for the line scans of sample MAW-4, the mass bias remained very stable (1.24 – 1.27 %; $R_{\text{corr}}/R_{\text{meas}} = 0.9873 - 0.9877$, Eq. 3.III). When the mass bias shows increased variability over the day, careful evaluation of the results is necessary. We observed that a decrease in the $^{87}\text{Sr}/^{86}\text{Sr}$ ratio and an increase in the 2 SE is often related to a high mass bias (e.g. for samples GP5-17-21, Table 3.2).

3.7.4 Standard Bracketing

Our results highlight the importance of the standard bracketing correction scheme for LA-MC-ICP-MS Sr isotope analysis. Prior to the first sample measurements, a test of the standard bracketing method was performed using Jct-1. For this purpose, Jct-1 was used as a RM and also treated as a sample. The raw and corrected results are shown in Fig. 3.8. The standard bracketing method seems to be generally applicable for $^{87}\text{Sr}/^{86}\text{Sr}$ ratio correction, since the corrected Sr isotope ratios of Jct-1 agree within uncertainties. A similar test performed on the RMs JcP-1 and MACS-3 with the femtosecond LA-MC-ICP-MS setup also showed reliable results (Fig. 3.5).

3.7.5 LA-MC-ICP-MS of Sr isotopes on speleothem samples

Traditional Sr isotopes analysis by solution MC-ICP-MS or TIMS requires careful chemical treatment. A recent study by Wortham et al. (2017) presented a speleothem Sr isotope record obtained by LA-MC-ICP-MS. These authors performed line scan measurements parallel to the growth axis of a speleothem from Brazil and traced an increasing $^{87}\text{Sr}/^{86}\text{Sr}$ ratio over the last two millennia. Their approach is slightly different to ours. While their line scan is performed parallel to the growth axis, we measure three line scans for each growth layer perpendicular to the growth axis, which enables us to test whether results from individual growth layers are reproducible (similar to the Hendy test for stable carbon and oxygen isotopes, Hendy (1971)). In addition, the change of the $^{87}\text{Sr}/^{86}\text{Sr}$ ratio in the Brazilian speleothem was on the third decimal, which is relatively large.

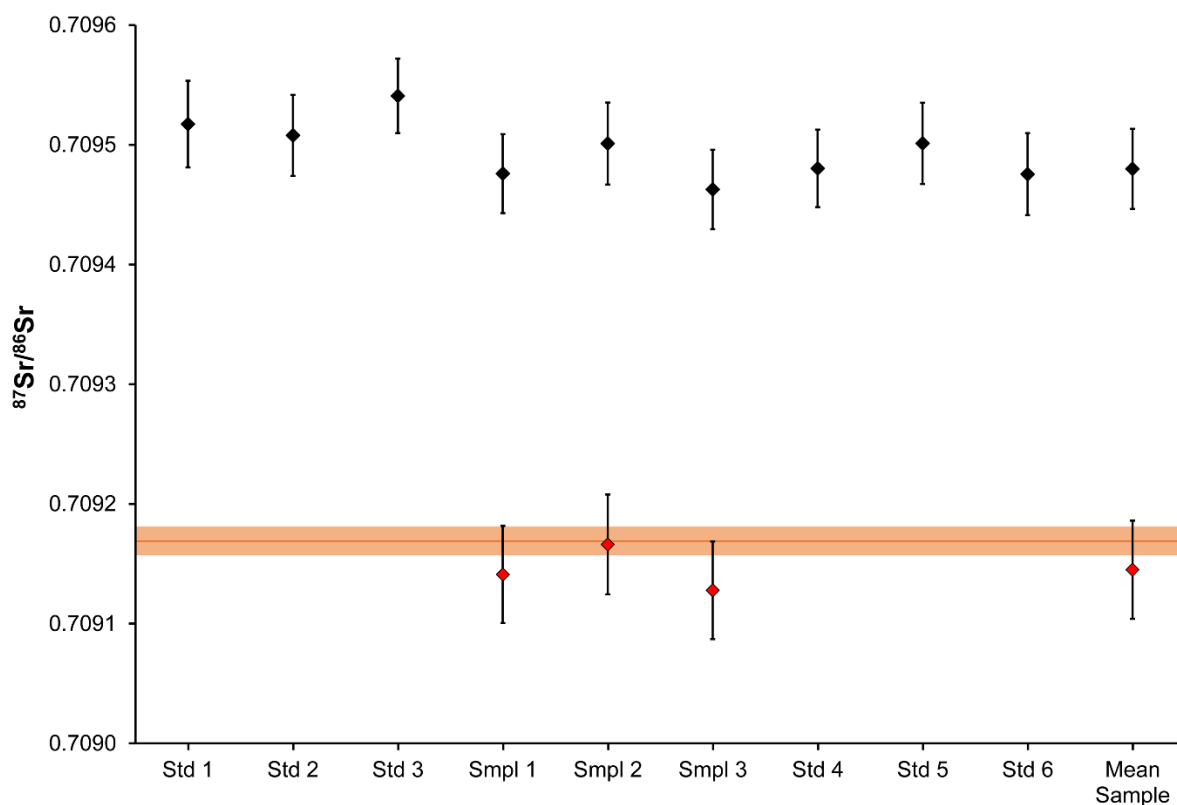


Fig. 3.8: Black diamonds show the raw results of the $^{87}\text{Sr}/^{86}\text{Sr}$ LA-MC-ICP-MS line scan measurements performed using Jct-1 as a reference material and a sample. Corrected $^{87}\text{Sr}/^{86}\text{Sr}$ ratios of Jct-1 are shown as red diamonds. Note that the uncertainties increased in comparison to the raw data due to correction via the reference material. The orange line represents the reference value of Jct-1 of 0.70917 ± 0.00001 (Weber et al., 2018b).

Detecting smaller changes (i.e. on the fourth to fifth decimal), is only possible by conducting a set of measurements perpendicular to the growth axis. Otherwise the obtained $^{87}\text{Sr}/^{86}\text{Sr}$ ratio is largely influenced by a time-averaging effect. Wortham et al. (2017) used a different sampling approach and do not provide the Sr mass fraction of their speleothem and the used RM which complicates the comparison of both studies. Nevertheless, they showed that it is possible to track large changes in speleothem Sr isotope ratios using line scans parallel to the growth axis. Our results show that it is also possible to obtain higher precision Sr isotope data by LA-MC-ICP-MS using a set of line scans, as well as spot analyses orientated perpendicular to the growth axis. With the state-of-the-art MC-ICP-MS systems it is unlikely that small scale changes in Sr isotope composition can be detected by performing a line scan parallel to the growth axis. This is further complicated by the typically low Sr mass fraction of speleothems (few hundred $\mu\text{g/g}$ or even less). However, aragonitic speleothems can have much higher

Sr mass fractions of several thousand $\mu\text{g/g}$. Thus, in some aragonitic, a line scan parallel to the growth axis may reveal small scale changes in Sr isotope composition.

3.8 Conclusions

We show that LA-MC-ICP-MS is a powerful tool for the analysis of Sr isotopes in speleothems. Best results are obtained from samples with Sr mass fractions of $>1000 \mu\text{g/g}$. For our setup, the minimum ^{88}Sr mass fraction required to obtain reliable $^{87}\text{Sr}/^{86}\text{Sr}$ ratios was ca. $300 \mu\text{g/g}$. In order to retrieve reliable results, appropriate tuning of both the mass spectrometer and the laser ablation system is of great importance. Tuning for maximum intensity does not always result in correct $^{87}\text{Sr}/^{86}\text{Sr}$ ratios. We highly recommend to tune for the correct Sr isotope ratio of a reference material prior to an analytical session. The Sr mass fraction of the RM should be in the same range as that in the samples. In order to account for potential drifts in the mass spectrometer during an analytical session, we recommend to apply standard bracketing using appropriate RMs.

Line scans provide higher precision than spot analyses. The latter might be advantageous however if only a limited surface is available for sampling, for instance in case of an irregular layering. While speleothem samples tested here contain only low amounts of REEs and Rb, appropriate correction procedures are required to minimise the influence of interferences from these elements. In addition, potential interferences resulting from Ca argides and dimers should be accounted for.

The use of a femtosecond laser ablation system provides a more stable signal intensity and therefore more precise measurements, but its application on samples with low Sr mass fractions (ca. $>1400 \mu\text{g/g}$, since measurements with Jct-1 were not precise enough) is not recommended due to lower signal intensities compared to the nanosecond laser leading to less precise results.

3.9 Acknowledgements

M. Weber, J.A. Wassenburg, K.P. Jochum and D. Scholz are thankful to the Max Planck Graduate Center and the German Research Foundation (DFG WA3532-1/1 and DFG SCHO 1274/9-1) for funding. S. Breitenbach and D. Scholz acknowledge financial support from the European Union's Horizon 2020 Research and Innovation program under the Marie Skłodowska-Curie grant agreement No 691037 (QUEST). We also thank B. Schwager, B. Stoll, U. Weis, C. Obert, A. Budsky and F. Lugli for assistance in the laboratory. The authors thank the editor Klaus Mezger, Alison Koleszar and one anonymous referee for their thorough reviews and constructive comments which helped to improve the manuscript.

3.10 Supplement

Table A3.1: Results of the solution measurements of reference solution NIST SRM 987 for solution MC-ICP-MS and reference material Jct-1 for LA-MC-ICP-MS.

Sample	Total Sr [V]	Total Rb [mV]	Rb/Sr	Er/Sr *10 ⁻⁶	Yb/Sr *10 ⁻⁶	⁸⁷ Sr/ ⁸⁶ Sr	2 SE	Mass Bias ⁸⁷ Sr/ ⁸⁶ Sr
<i>NIST SRM 987</i>								
987-1	4.9	0.64	0.00013	0.2	0	0.71044	0.00004	0.36%
987-2	5.0	0.66	0.00013	0.2	10	0.71052	0.00005	0.34%
987-3	5.0	0.75	0.00015	0.3	11	0.71051	0.00004	0.33%
987-4	4.4	0.69	0.00016	0.2	0	0.71063	0.00005	0.34%
987-5	4.8	0.65	0.00014	0.2	0	0.71059	0.00005	0.38%
987-6	4.4	0.63	0.00015	0.2	10	0.71075	0.00005	0.16%
987-7	4.9	0.72	0.00015	0.3	19	0.71047	0.00004	0.54%
987-8	3.7	0.55	0.00015	0.4	0	0.71578	0.00005	-0.60%
987-9	3.5	0.51	0.00014	0.2	22	0.70861	0.00005	2.11%
987-10	4.8	0.69	0.00014	0.3	23	0.71052	0.00004	0.63%
987-11	3.3	0.51	0.00016	0.3	28	0.71675	0.00005	-0.35%
987-12	3.6	0.52	0.00015	0.0	0	0.70863	0.00005	2.15%
987-13	4.9	0.71	0.00015	0.2	23	0.71050	0.00005	0.69%
987-14	3.8	0.62	0.00016	0.1	24	0.71086	0.00005	1.11%
987-15	3.5	0.48	0.00014	0.2	33	0.71189	0.00006	1.14%
987-16	4.8	0.68	0.00014	0.2	0	0.71057	0.00004	0.62%
987-17	3.7	0.53	0.00015	0.2	4	0.71015	0.00005	1.43%
987-18	4.0	0.58	0.00015	0.1	1	0.71217	0.00005	0.67%
987-19	4.8	0.71	0.00015	0.2	6	0.71057	0.00005	0.64%
987-20	3.8	0.53	0.00014	0.1	0	0.71060	0.00005	1.24%
987-21	4.1	0.56	0.00014	0.3	0	0.71069	0.00005	0.82%
987-22	4.7	0.67	0.00014	0.2	0	0.71058	0.00004	0.64%
987-23	4.2	0.65	0.00015	0.5	38	0.71391	0.00005	0.00%
987-24	4.0	0.63	0.00016	0.1	0	0.70873	0.00005	1.98%
987-25	4.6	0.62	0.00014	0.2	12	0.71063	0.00004	0.63%
987-26	3.3	0.45	0.00014	0.1	30	0.70863	0.00005	2.09%
987-27	3.8	0.64	0.00017	0.4	21	0.71264	0.00005	0.85%
987-28	4.6	0.62	0.00014	0.2	9	0.71061	0.00005	0.62%
<i>Line scans</i>								
<i>Jct-1</i>								
Jct-1-1	6.9	0.58	0.00008	1.1	10	0.70963	0.00005	1.17%
Jct-1-2	5.5	0.51	0.00009	1.1	21	0.70958	0.00007	1.14%
Jct-1-3	5.4	0.51	0.00009	1.0	12	0.70961	0.00005	1.12%
Jct-1-4	5.1	0.41	0.00008	1.1	17	0.70986	0.00006	0.92%
Jct-1-5	5.0	0.41	0.00008	1.0	21	0.70964	0.00007	0.99%
Jct-1-6	4.4	0.38	0.00009	1.1	0	0.70974	0.00007	1.02%
Jct-1-7	4.4	0.46	0.00010	1.6	6	0.70920	0.00005	0.98%

Table A3.1 (continued):

Sample	Total Sr [V]	Total Rb [mV]	Rb/Sr	Er/Sr *10 ⁻⁶	Yb/Sr *10 ⁻⁶	⁸⁷ Sr/ ⁸⁶ Sr	2 SE	Mass Bias ⁸⁷ Sr/ ⁸⁶ Sr
<i>Line scans</i>								
<i>JCt-1</i>								
JCt-1-8	3.9	0.39	0.00010	1.4	35	0.70916	0.00005	0.97%
JCt-1-9	3.8	0.45	0.00012	1.4	0	0.70908	0.00005	0.98%
JCt-1-10	3.5	0.37	0.00011	1.5	6	0.70911	0.00006	0.99%
JCt-1-11	3.7	0.35	0.00010	1.5	0	0.70920	0.00005	1.01%
JCt-1-12	3.9	0.42	0.00011	1.5	23	0.70918	0.00006	1.01%
JCt-1-13	3.8	0.32	0.00008	1.5	0	0.70945	0.00006	0.88%
JCt-1-14	5.3	0.71	0.00013	1.5	29	0.70956	0.00004	0.93%
JCt-1-15	4.2	0.43	0.00010	1.5	16	0.70953	0.00005	0.92%
JCt-1-16	4.6	0.54	0.00012	1.3	29	0.70919	0.00005	0.47%
JCt-1-17	4.3	0.40	0.00009	1.4	23	0.70916	0.00006	0.46%
JCt-1-18	3.2	0.38	0.00012	1.4	63	0.70918	0.00006	0.45%
JCt-1-19	4.9	0.55	0.00011	1.3	0	0.70937	0.00005	0.50%
JCt-1-20	4.0	0.39	0.00010	1.3	34	0.70921	0.00005	0.49%
JCt-1-21	4.0	0.43	0.00011	1.2	8	0.70928	0.00005	0.50%
JCt-1-22	3.7	0.44	0.00012	1.3	13	0.70934	0.00006	0.50%
JCt-1-23	5.4	0.94	0.00018	0.8	3	0.70919	0.00005	2.29%
JCt-1-24	5.3	1.53	0.00029	0.8	21	0.70941	0.00006	2.22%
JCt-1-25	6.4	0.86	0.00013	0.9	0	0.70922	0.00005	1.98%
JCt-1-26	5.3	0.61	0.00011	0.8	23	0.70918	0.00005	1.97%
JCt-1-27	4.7	0.61	0.00013	1.0	-1	0.70928	0.00005	1.96%
JCt-1-28	6.7	0.65	0.00010	0.8	1	0.70919	0.00005	1.92%
JCt-1-29	5.0	0.50	0.00010	1.0	0	0.70914	0.00005	1.92%
JCt-1-30	6.0	0.89	0.00015	0.9	14	0.70913	0.00004	1.94%
JCt-1-31	6.6	0.78	0.00012	0.9	8	0.70919	0.00005	1.91%
JCt-1-32	6.9	0.91	0.00013	0.9	18	0.70919	0.00004	1.90%
JCt-1-33	6.3	0.90	0.00014	0.9	33	0.70910	0.00005	1.81%
JCt-1-34	5.7	0.61	0.00011	1.0	17	0.70903	0.00006	1.82%
JCt-1-35	6.4	0.65	0.00010	1.0	0	0.70911	0.00005	1.81%
JCt-1-36	7.4	0.67	0.00009	0.8	11	0.70914	0.00004	1.91%
JCt-1-37	8.0	0.88	0.00011	0.8	16	0.70920	0.00004	1.89%
JCt-1-38	4.2	0.72	0.00017	0.9	1	0.70922	0.00006	1.90%
JCt-1-39	7.4	0.60	0.00008	0.8	0	0.70915	0.00005	1.94%
JCt-1-40	6.4	0.71	0.00011	0.8	3	0.70911	0.00004	1.92%
JCt-1-41	6.3	0.72	0.00012	0.9	18	0.70913	0.00005	1.92%
JCt-1-42	7.6	0.71	0.00009	0.8	0	0.70913	0.00004	1.96%
JCt-1-43	7.0	0.65	0.00009	0.9	0	0.70913	0.00004	1.94%
JCt-1-44	7.1	0.68	0.00010	0.7	0	0.70918	0.00004	1.95%
JCt-1-45	6.2	0.61	0.00010	0.8	20	0.70914	0.00004	1.99%
JCt-1-46	7.0	0.97	0.00014	0.8	4	0.70921	0.00005	1.98%
JCt-1-47	7.5	0.87	0.00012	0.7	0	0.70920	0.00004	1.98%

Table A3.1 (continued):

Sample	Total Sr [V]	Total Rb [mV]	Rb/Sr	Er/Sr *10 ⁻⁶	Yb/Sr *10 ⁻⁶	⁸⁷ Sr/ ⁸⁶ Sr	2 SE	Mass Bias ⁸⁷ Sr/ ⁸⁶ Sr
<i>Line scans</i>								
<i>JCt-1</i>								
JCt-1-48	7.6	0.90	0.00012	0.7	0	0.70924	0.00004	2.03%
JCt-1-49	5.6	0.61	0.00011	0.9	27	0.70919	0.00005	1.98%
JCt-1-50	7.8	0.80	0.00010	0.9	1	0.70918	0.00004	1.97%
JCt-1-51	5.6	1.09	0.00020	0.9	17	0.70916	0.00004	1.98%
JCt-1-52	5.7	0.70	0.00012	0.7	18	0.70916	0.00005	2.04%
JCt-1-53	4.4	0.52	0.00012	0.9	12	0.70919	0.00005	2.01%
JCt-1-54	4.8	0.54	0.00011	0.8	22	0.70918	0.00005	1.99%
JCt-1-55	6.2	0.69	0.00011	0.8	6	0.70917	0.00005	2.01%
JCt-1-56	6.1	0.65	0.00011	0.7	14	0.70915	0.00005	2.00%
JCt-1-57	6.1	0.67	0.00011	0.8	13	0.70917	0.00005	1.99%
JCt-1-58	6.4	0.92	0.00014	0.7	13	0.70923	0.00005	1.99%
JCt-1-59	5.2	0.70	0.00013	0.8	6	0.70911	0.00005	1.99%
JCt-1-60	3.9	0.46	0.00012	0.9	29	0.70900	0.00005	2.01%
JCt-1-61	4.6	0.54	0.00012	0.8	18	0.70907	0.00006	2.02%
JCt-1-62	4.1	0.57	0.00014	0.9	18	0.70918	0.00006	1.95%
JCt-1-63	4.4	0.90	0.00020	0.7	35	0.70912	0.00005	1.95%
JCt-1-64	5.6	0.61	0.00011	0.8	10	0.70917	0.00005	1.97%
JCt-1-65	5.7	0.65	0.00011	0.8	1	0.70920	0.00005	1.97%
JCt-1-66	6.2	0.71	0.00012	0.8	20	0.70919	0.00005	1.98%

Table A3.2: Raw ⁸⁷Sr/⁸⁶Sr measurements for each line scan and spot measurement of GP5.

Sample	⁸⁷ Sr/ ⁸⁶ Sr	2 SE	Sampling Technique
GP5-1a	0.70918	0.00010	Line scan
GP5-1b	0.70879	0.00012	Line scan
GP5-1c	0.70841	0.00014	Line scan
GP5-1d	0.70849	0.00016	Line scan
GP5-2a	0.70900	0.00008	Line scan
GP5-2b	0.70887	0.00009	Line scan
GP5-2c	0.70893	0.00010	Line scan
GP5-3a	0.70892	0.00011	Line scan
GP5-3b	0.70873	0.00010	Line scan
GP5-3c	0.70893	0.00011	Line scan
GP5-4a	0.70863	0.00013	Line scan
GP5-4b	0.70876	0.00011	Line scan
GP5-4c	0.70896	0.00010	Line scan
GP5-5a	0.70846	0.00015	Line scan
GP5-5b	0.70884	0.00012	Line scan
GP5-5c	0.70894	0.00011	Line scan

Table A3.2 (continued):

Sample	$^{87}\text{Sr}/^{86}\text{Sr}$	2 SE	Sampling Technique
GP5-6a	0.70884	0.00014	Line scan
GP5-6b	0.70897	0.00013	Line scan
GP5-6c	0.70891	0.00012	Line scan
GP5-7	0.70885	0.00006	Line scan
GP5-8a	0.70884	0.00007	Line scan
GP5-8b	0.70905	0.00006	Line scan
GP5-9a	0.70892	0.00007	Line scan
GP5-9b	0.70904	0.00007	Line scan
GP5-9c	0.70921	0.00008	Line scan
GP5-10a	0.70898	0.00008	Line scan
GP5-10b	0.70893	0.00008	Line scan
GP5-10c	0.70904	0.00009	Line scan
GP5-11a	0.70888	0.00008	Line scan
GP5-11b	0.70899	0.00008	Line scan
GP5-11c	0.70914	0.00008	Line scan
GP5-12a	0.70897	0.00007	Line scan
GP5-12b	0.70891	0.00006	Line scan
GP5-12c	0.70889	0.00008	Line scan
GP5-13a	0.70895	0.00007	Line scan
GP5-13b	0.70900	0.00007	Line scan
GP5-13c	0.70895	0.00007	Line scan
GP5-14a	0.70908	0.00007	Line scan
GP5-14b	0.70927	0.00007	Line scan
GP5-14c	0.70926	0.00008	Line scan
GP5-15a	0.70915	0.00007	Line scan
GP5-15b	0.70899	0.00007	Line scan
GP5-15c	0.70890	0.00008	Line scan
GP5-16a	0.70888	0.00011	Line scan
GP5-16b	0.70897	0.00011	Line scan
GP5-16c	0.70885	0.00011	Line scan
GP5-17a	0.70896	0.00011	Line scan
GP5-17b	0.70883	0.00012	Line scan
GP5-17c	0.70907	0.00011	Line scan
GP5-18a	0.70850	0.00015	Line scan
GP5-18b	0.70883	0.00013	Line scan
GP5-18c	0.70901	0.00014	Line scan
GP5-19a	0.70899	0.00015	Line scan
GP5-19b	0.70886	0.00014	Line scan
GP5-19c	0.70903	0.00013	Line scan
GP5-20a	0.70845	0.00014	Line scan
GP5-20b	0.70883	0.00016	Line scan
GP5-20c	0.70877	0.00015	Line scan
GP5-21a	0.70838	0.00017	Line scan
GP5-21b	0.70858	0.00016	Line scan

Table A3.2 (continued):

Sample	$^{87}\text{Sr}/^{86}\text{Sr}$	2 SE	Sampling Technique
GP5-21c	0.70870	0.00018	Line scan
GP5-22a	0.70890	0.00009	Line scan
GP5-22b	0.70914	0.00009	Line scan
GP5-22c	0.70890	0.00009	Line scan
GP5-23a	0.70913	0.00009	Line scan
GP5-23b	0.70914	0.00008	Line scan
GP5-23c	0.70912	0.00008	Line scan
GP5-24a	0.70907	0.00009	Line scan
GP5-24b	0.70905	0.00010	Line scan
GP5-24c	0.70913	0.00009	Line scan
GP5-25a	0.70910	0.00009	Line scan
GP5-25b	0.70902	0.00009	Line scan
GP5-25c	0.70909	0.00010	Line scan
GP5-26a	0.70904	0.00009	Line scan
GP5-26b	0.70921	0.00010	Line scan
GP5-26c	0.70890	0.00010	Line scan
GP5-27a	0.70879	0.00011	Line scan
GP5-27b	0.70916	0.00008	Line scan
GP5-27c	0.70884	0.00009	Line scan
GP5-Spot-2a	0.70900	0.00014	Spot analysis
GP5-Spot-2b	0.70912	0.00014	Spot analysis
GP5-Spot-2c	0.70905	0.00011	Spot analysis
GP5-Spot-10a	0.70914	0.00013	Spot analysis
GP5-Spot-10b	0.70889	0.00017	Spot analysis
GP5-Spot-10c	0.70875	0.00060	Spot analysis
GP5-Spot-12a	0.70916	0.00011	Spot analysis
GP5-Spot-12b	0.70891	0.00011	Spot analysis
GP5-Spot-12c	0.70878	0.00021	Spot analysis
GP5-Spot-14a	0.70906	0.00010	Spot analysis
GP5-Spot-14b	0.70898	0.00011	Spot analysis
GP5-Spot-14c	0.70908	0.00011	Spot analysis
GP5-Spot-16a	0.70916	0.00010	Spot analysis
GP5-Spot-16b	0.70906	0.00011	Spot analysis
GP5-Spot-16c	0.70899	0.00013	Spot analysis
GP5-Spot-17a	0.70868	0.00018	Spot analysis
GP5-Spot-17b	0.70861	0.00019	Spot analysis
GP5-Spot-17c	0.70897	0.00011	Spot analysis
GP5-Spot-22a	0.70905	0.00013	Spot analysis
GP5-Spot-22b	0.70901	0.00013	Spot analysis
GP5-Spot-22c	0.70901	0.00013	Spot analysis
GP5-Spot-24a	0.70697	0.00045	Spot analysis
GP5-Spot-24b	0.70893	0.00015	Spot analysis
GP5-Spot-24c	0.70909	0.00013	Spot analysis
GP5-Spot-21a	0.70902	0.00014	Spot analysis

Table A3.2 (continued):

Sample	$^{87}\text{Sr}/^{86}\text{Sr}$	2 SE	Sampling Technique
GP5-Spot-21b	0.70905	0.00014	Spot analysis
GP5-Spot-21c	0.70878	0.00014	Spot analysis
GP5-Spot-25a	0.70879	0.00013	Spot analysis
GP5-Spot-25b	0.70897	0.00012	Spot analysis
GP5-Spot-25c	0.70901	0.00014	Spot analysis
GP5-Spot-26a	0.70891	0.00012	Spot analysis
GP5-Spot-26b	0.70896	0.00016	Spot analysis
GP5-Spot-26c	0.70863	0.00020	Spot analysis
GP5-Spot-27a	0.70746	0.00037	Spot analysis
GP5-Spot-27b	0.70892	0.00022	Spot analysis
GP5-Spot-27c	0.70851	0.00025	Spot analysis

Table A3.3: Raw $^{87}\text{Sr}/^{86}\text{Sr}$ measurements for each line scan and spot measurement of MAW-4.

Sample	$^{87}\text{Sr}/^{86}\text{Sr}$	2 SE	Sampling Technique
MAW4-1a	0.70866	0.00005	Line scan
MAW4-1b	0.70854	0.00004	Line scan
MAW4-1c	0.70866	0.00004	Line scan
MAW4-2a	0.70860	0.00004	Line scan
MAW4-2b	0.70861	0.00004	Line scan
MAW4-2c	0.70861	0.00004	Line scan
MAW4-3a	0.70863	0.00005	Line scan
MAW4-3b	0.70873	0.00004	Line scan
MAW4-3c	0.70866	0.00004	Line scan
MAW4-4a	0.70866	0.00004	Line scan
MAW4-4b	0.70875	0.00004	Line scan
MAW4-4c	0.70870	0.00004	Line scan
MAW4-5a	0.70867	0.00004	Line scan
MAW4-5b	0.70874	0.00004	Line scan
MAW4-5c	0.70867	0.00004	Line scan
MAW4-6a	0.70869	0.00004	Line scan
MAW4-6b	0.70869	0.00004	Line scan
MAW4-6c	0.70873	0.00004	Line scan
MAW4-7a	0.70872	0.00004	Line scan
MAW4-7b	0.70870	0.00004	Line scan
MAW4-7c	0.70869	0.00004	Line scan
MAW4-8a	0.70867	0.00005	Line scan
MAW4-8b	0.70869	0.00005	Line scan
MAW4-8c	0.70869	0.00004	Line scan
MAW4-Spot-1a	0.70876	0.00007	Spot analysis
MAW4-Spot-1b	0.70860	0.00007	Spot analysis
MAW4-Spot-1c	0.70865	0.00007	Spot analysis
MAW4-Spot-2a	0.70862	0.00006	Spot analysis

Table A3.3 (continued):

Sample	$^{87}\text{Sr}/^{86}\text{Sr}$	2 SE	Sampling Technique
MAW4-Spot-2b	0.70869	0.00007	Spot analysis
MAW4-Spot-2c	0.70866	0.00007	Spot analysis
MAW4-Spot-3a	0.70870	0.00008	Spot analysis
MAW4-Spot-3b	0.70869	0.00008	Spot analysis
MAW4-Spot-3c	0.70871	0.00008	Spot analysis
MAW4-Spot-4a	0.70877	0.00008	Spot analysis
MAW4-Spot-4b	0.70877	0.00008	Spot analysis
MAW4-Spot-4c	0.70864	0.00008	Spot analysis
MAW4-Spot-5a	0.70875	0.00007	Spot analysis
MAW4-Spot-5b	0.70875	0.00007	Spot analysis
MAW4-Spot-5c	0.70872	0.00007	Spot analysis
MAW4-Spot-6a	0.70874	0.00007	Spot analysis
MAW4-Spot-6b	0.70874	0.00007	Spot analysis
MAW4-Spot-6c	0.70875	0.00007	Spot analysis
MAW4-Spot-8a	0.70867	0.00006	Spot analysis
MAW4-Spot-8b	0.70866	0.00007	Spot analysis
MAW4-Spot-8c	0.70871	0.00007	Spot analysis
MAW4-Spot-8d	0.70870	0.00006	Spot analysis
MAW4-Spot-8e	0.70869	0.00006	Spot analysis
MAW4-Spot-8f	0.70861	0.00006	Spot analysis

Chapter 4: Manuscript II: Calcium Carbonate and Phosphate Reference Materials for Monitoring Bulk and Microanalytical Determination of Sr Isotopes

Calcium Carbonate and Phosphate Reference Materials for Monitoring Bulk and
Microanalytical Determination of Sr Isotopes

Michael Weber^{1,2}, Federico Lugli³, Klaus Peter Jochum², Anna Cipriani^{3,4}, Denis Scholz¹

¹Institute of Geosciences, Johannes Gutenberg-University Mainz, J.-J.-Becher-Weg 21, 55128 Mainz, Germany

²Climate Geochemistry Department, Max-Planck-Institute for Chemistry (Otto-Hahn-Institute), P.O. Box 3060, 55020 Mainz, Germany

³Department of Chemical and Geological Sciences, University of Modena and Reggio Emilia, Via Campi 103, 41125 Modena, Italy

⁴Lamont-Doherty Earth Observatory, Columbia University, Palisades, New York 10964, USA.

This manuscript is published in a similar version in *Geostandards and Geoanalytical Research*, Vol. 42, 77 – 89 (2018).

4.1 Abstract

In-situ laser ablation analyses rely on the microanalytical homogeneity of reference materials (RMs) and a similar matrix and mass fraction between unknown samples and RMs to obtain reliable results. Suitable carbonate and phosphate RMs for determination of Sr isotope ratios in such materials are limited. Thus, we determined $^{87}\text{Sr}/^{86}\text{Sr}$ ratios of several carbonate (JCt-1, JCp-1, MACS-1, MACS-3) and phosphate (MAPS-4, MAPS-5, NIST SRM 1400, NIST SRM 1486) international RMs using dissolved samples and two different MC-ICP-MS systems. Our Sr isotope data are in agreement with published data and have an improved analytical precision for some RMs. For MACS-1, we present the first $^{87}\text{Sr}/^{86}\text{Sr}$ value. We tested the suitability of these materials for microanalytical analyses by LA-MC-ICP-MS, with two different laser ablation systems: a conventional nanosecond laser and a state-of-the-art femtosecond laser. We investigated the RMs micro-homogeneity and compared the data with our solution data. Both laser ablation systems yielded identical $^{87}\text{Sr}/^{86}\text{Sr}$ ratios within uncertainty to the solution data for RMs with low interferences of REEs. Therefore, these carbonate and phosphate RMs can be used to achieve accurate and precise results for *in-situ* Sr isotope investigations by LA-MC-ICP-MS of similar materials.

4.2 Introduction

Reference materials (RMs) are essential for calibration, method validation, quality control and assurance as well as to establish metrological traceability (Jochum and Enzweiler, 2014). In addition, they allow testing for long-term reproducibility. This is especially important for microanalytical techniques, such as LA-MC-ICP-MS or SIMS, where homogeneity should be in the range of test portion masses in the μg -range. Traceability of results can only be achieved if users calibrate, normalise and publish their data using published, preferably certified reference values. The accuracy and precision of results from unknown samples is highly dependent on the quality and characterisation of RMs (Jochum and Nohl, 2008). When applied to laser ablation studies, not only the quality of the analytical data is important, but also a similar mass fraction and, depending on the application, a matching matrix of the RMs and the unknown sample is preferable (Jochum and Enzweiler, 2014). Here we present new high-precision MC-ICP-MS radiogenic Sr isotope data for carbonate and phosphate RMs and compare the results with data from a LA-MC-ICP-MS approach.

Strontium naturally occurs in the form of four isotopes, three of them are stable (^{84}Sr , ^{86}Sr and ^{88}Sr), while ^{87}Sr is the radiogenic daughter isotope of ^{87}Rb via β -decay. This Rb-Sr decay scheme is widely applied for geological purposes, such as geochronology and as a geological tracer (Banner, 2004). Furthermore, Sr isotopes are applied in different scientific fields, such as isotope geochemistry (in particular archaeology, palaeontology and forensics) or for stratigraphic purposes in carbonate samples (McArthur et al., 2012).

Strontium isotope data (in particular the $^{87}\text{Sr}/^{86}\text{Sr}$ ratio) for carbonate RMs are not widely available in the geoanalytical literature. While for solution Sr isotope measurements, the NIST SRM 987 solution is widely accepted as a reference solution, the availability of suitable RM for laser ablation studies is limited (e.g. JcT-1, JcP-1, FEBS-1; Ohno and Hirata, 2007; Yang et al., 2011). Further carbonate RMs for *in-situ* laser analyses would allow to avoid extensive additional laboratory work, such as solution MC-ICP-MS or TIMS analyses of the same samples, or relying on modern-day marine carbonates, which are believed to show the same $^{87}\text{Sr}/^{86}\text{Sr}$ ratio as modern-day seawater (Barnett-Johnson et al., 2005; Outridge et al., 2002; Woodhead et al., 2005). Although LA-MC-ICP-MS analysis of Sr isotopes of phosphate materials is much more common (in particular teeth; Copeland et al., 2008; Copeland et al., 2010; Le Roux et al., 2014; Lugli et al., 2017b; Willmes et al., 2016) only a few RMs for phosphate matrices are available (Yang et al., 2014). The same is true for carbonate materials. This lack of RMs often requires calibration with in-house reference materials that themselves are calibrated against a certified RM via solution work.

Here we present new high-precision MC-ICP-MS radiogenic Sr isotope data for carbonate and phosphate RMs and a comparison with LA-MC-ICP-MS data. To improve the data availability for carbonate and phosphate RMs suitable for laser ablation Sr isotope studies, we present high-precision solution data of different RMs that are also available as pellets for laser ablation purposes. These solution data are compared with LA-MC-ICP-MS data of selected RMs obtained by nanosecond and femtosecond laser ablation systems.

4.3 Reference materials

For this study, we investigated eight different RMs, as listed here below. Four of them have a carbonate matrix, the other four have a phosphate matrix. Not all of the RMs could be analysed by laser. In fact, the Sr mass fraction of MACS-1 and MAPS-5 were too low for Sr isotope analysis with our femtosecond laser ablation setup with the Nu MC-ICP-MS (^{88}Sr intensities <1.5 V, similar threshold as reported by Müller and Anczkiewicz (2016) and, as a consequence, the interferences of REEs were too large for both our LA-MC-ICP-MS approaches ($\text{REE}/\text{Sr} \sim 0.04 - 0.07$ for MAPS-5 and ~ 0.60 for MACS-1, according to the GeoReM database, Jochum et al., 2005). The REE interferences of MAPS-4 were also too large for reliable measurements with both our laser ablation systems, whereas some of the femtosecond laser ablation measurements also suffered from low ^{88}Sr intensities <1.5 V. Therefore, for these RMs, the MC-ICP-MS measurements provide the most reliable $^{87}\text{Sr}/^{86}\text{Sr}$ ratios. We note, however, that MACS-1, MAPS-4 and MAPS-5 can be analysed with LA-ICP-MS/MS-techniques using reaction cells (e.g. Bolea-Fernandez et al., 2016; Zack and Hogmalm, 2016). In this sense, the solution measurements here presented can be helpful as reference values.

JCp-1: This material is supplied by the GSJ and of biological origin. It is a recent *Porites* sp. coral, sampled on Ishigaki Island in Japan and consists of aragonite (Okai et al., 2002). According to the GeoReM database (Jochum et al., 2005), its Sr mass fraction is in the range of 7260 – 7500 µg/g. Previously published data for $^{87}\text{Sr}/^{86}\text{Sr}$ show a ratio of approximately 0.70916 (see Table 4.3 for references).

JCt-1: JCt-1 is also supplied by the GSJ and originates from Kume Island in Japan. This RM is a fossil (mid Holocene) giant clam (*Tridachna gigas*) and consists of aragonite (Inoue et al., 2004). Its Sr mass fraction was determined to be 1400 µg/g (GeoReM). So far, only one measurement of the $^{87}\text{Sr}/^{86}\text{Sr}$ ratio of 0.70915 ± 0.00005 (SD) is available (Ohno and Hirata, 2007).

MACS-1: This RM is a synthetic carbonate pellet, provided by the USGS for microanalytical purposes. It was first investigated by Munksgaard et al. (2004) and published Sr mass fractions are in the range of 196-249 µg/g. There is no previously published $^{87}\text{Sr}/^{86}\text{Sr}$ value available for this material.

MACS-3: This is a synthetic carbonate pellet similar to MACS-1, also supplied by the USGS. The first Sr isotope study with this microanalytical reference material MRM was published by Jochum et al. (2011a), providing a $^{87}\text{Sr}/^{86}\text{Sr}$ ratio of 0.7075532 ± 0.0000037 (2 SD). The Sr mass fraction of this MRM is in the range of 6260-8012 µg/g (GeoReM), much higher than for MACS-1.

MAPS-4: This synthetic phosphate MRM is available as a pellet and is supplied by the USGS. Neymark et al. (2014) determined a $^{87}\text{Sr}/^{86}\text{Sr}$ ratio for this sample of 0.707800 ± 0.000006 (2 SE). The Sr mass fraction is in the range of 3110-3300 µg/g (GeoReM).

MAPS-5: This MRM is available from the USGS and is a synthetic phosphate pellet. In contrast to MAPS-4, it has a much lower Sr mass fraction of 214-230 µg/g (GeoReM) and a higher $^{87}\text{Sr}/^{86}\text{Sr}$ ratio of 0.707910 ± 0.000005 (2 SE, Neymark et al., 2014).

NIST SRM 1400: This RM is available from NIST as a bone ash powder since 1992. The Sr mass fraction is in the range of 246-255 µg/g (GeoReM), and the previously measured $^{87}\text{Sr}/^{86}\text{Sr}$ ratio is in the range of 0.71312 – 0.71314 (see Table 4.3 for references).

NIST SRM 1486: This RM from NIST is a bone meal powder and available since 1992. The Sr mass fraction is similar to NIST SRM 1400 and in the range of 255-310 µg/g (GeoReM), while the $^{87}\text{Sr}/^{86}\text{Sr}$ ratio is much lower and in the range of approximately 0.7093 (see Table 4.3 for references).

4.4 Analytical techniques

Different mass spectrometers and laser ablation systems housed at different institutions were used during the course of this investigation. The LA-MC-ICP-MS work was performed at the Max Planck Institute for Chemistry (MPIC), Mainz, with a Nu Plasma MC-ICP-MS (Nu Instruments™) coupled to a 213 nm

Nd:YAG laser ablation system (New Wave Research™ UP-213) and a 200 nm femtosecond laser ablation system (New Wave Research™ Femto200), respectively. The solution MC-ICP-MS work was performed with a Neptune MC-ICP-MS (Thermo Fisher Scientific, Neptune™) at the Centro Interdipartimentale Grandi Strumenti (CIGS) of the University of Modena and Reggio Emilia (Modena, Italy). In addition, laser ablation measurements of the Jct-1, NIST SRM 1400 and NIST SRM1486 RMs were collected with the Neptune coupled to a 213 nm Nd:YAG laser ablation system (New Wave Research™ UP-213). Typical operating conditions for both mass spectrometers and laser ablation systems are shown in Table 4.1. The reference materials used in this study were cross-checked against each other by measuring the different RMs directly after each other on the respective days of analysis.

Table 4.1: Operating parameters of the Neptune and Nu-Plasma MC-ICP-MS systems and the NWR UP-213 and NWR Femto200 laser ablation systems. Note that the NWR UP-213 operating parameters here are those used for the coupling to the Nu-MC-ICP-MS. A short summary of operating parameters for the coupling to the Neptune is described in the analytical section 4.4.3.

Parameters	Values	Parameters	Values	Parameters	Values
<i>MC-ICP-MS Neptune</i>		<i>New Wave UP 213</i>		<i>NWR Femto 200</i>	
Cool gas flow rate	15 L/min	He flow rate	~0.75 L/min	He flow rate	~0.75 L/min
Auxiliary gas flow	0.8 L/min				
Sample gas flow	0.9-1 L/min	<i>Ablation</i>		<i>Ablation</i>	
Plasma power	1200 W	Spot size	100 μm	Spot size	55-65 μm
Resolution	Low	Frequency	10 Hz	Frequency	50-250 Hz
		Fluence	20-30 J/cm ²	Fluence	0.1 - 1 J/cm ²
<i>MC-ICP-MS Nu</i>		Sampling scheme	Line	Sampling scheme	Line
Cool gas flow rate	13 L/min	Translation rate	5 μm/s	Translation rate	5 μm/s
Auxiliary gas flow	0.93 L/min				
Sample gas flow	0.75 L/min	<i>Pre-Ablation</i>		<i>Pre-Ablation</i>	
Plasma power	1300 W	Spot size	110 μm	Spot size	65 μm
Resolution	Low	Frequency	10 Hz	Frequency	5 Hz
		Translation rate	80 μm/s	Translation rate	60 μm/s

4.4.1 Column chemistry

Ion-exchange chromatography has been performed on carbonate and phosphate samples after chemical digestion, following the protocol presented in Lugli et al. (2017b). About 5–10 mg of sample were digested in 1 ml of 14 mol/L HNO₃ and, after evaporation at 100°C, re-dissolved in 3 mL of 3 mol/L HNO₃. In addition, an oxidation step with suprapure H₂O₂ (30%) was performed prior to the 3 mol/L HNO₃ digestion to remove organic matter residuals. The Sr separation uses columns with a 300 μl volume filled with Eichrom Sr spec-resin (100-150 μm bead size). The resin was first cleaned with MilliQ® water and fines were pipetted out after settling. After resin filling, the columns were preflushed with 1 ml of 3 mol/L HNO₃ and washed three times with MilliQ® water (1 mL each). Then the resin was conditioned with 1 ml of 3 mol/L HNO₃. Samples (3 mL) were then loaded into columns. Matrix ions

were removed by stepwise addition of 3 mol/L HNO₃ (3 mL overall). Strontium was then eluted with MilliQ® water (5 steps, 0.5 mL per step) and collected in clean Teflon beakers. Each solution was then adjusted to 0.8 mol/L HNO₃ for the subsequent MC-ICP-MS analysis. The whole procedure was conducted in a clean lab at the MPIC, with a Sr blank typically lower than 100 pg.

4.4.2 Solution MC-ICP-MS

Seven Faraday detectors were used to collect signals of the following masses: ⁸²Kr, ⁸³Kr, ⁸⁴Sr, ⁸⁵Rb, ⁸⁶Sr, ⁸⁷Sr, ⁸⁸Sr. 10¹² Ω resistors were employed for ⁸²Kr, ⁸³Kr, ⁸⁴Sr; while 10¹¹ Ω resistors were used for the remaining masses. Strontium solutions were diluted to 250 ng/ml and introduced into the Neptune via a quartz spray chamber and a 100 μL/min nebulizer.

Samples, RMs and blanks were analysed in a static multi-collection mode in a single block of 100 cycles, with an integration time of 8.4 s per cycle. To monitor and correct possible drifts of the instrument we employed a bracketing sequence.

Masses 82 and 83 were collected to monitor the presence of Kr in the Ar. Data were corrected using a ⁸⁶Kr/⁸³Kr ratio of 1.505657. Mass 85 was used to correct the signal on mass 87 for the presence of isobaric Rb, using a ⁸⁷Rb/⁸⁵Rb ratio of 0.3856656. Mass bias normalization was performed through the exponential law, using a ⁸⁸Sr/⁸⁶Sr ratio of 8.375209. We are aware of the temperature dependent stable isotope fractionation in carbonates which affects the ⁸⁸Sr/⁸⁶Sr ratio (Fietzke and Eisenhauer, 2006). Nevertheless, we believe that such effect (0.0054 ± 0.0005 ‰/°C, Fietzke and Eisenhauer, 2006) did not significantly influence our ⁸⁷Sr/⁸⁶Sr measurements and should be corrected via bracketing. Mass fractionation for both Kr and Rb has been assumed to be equal to that of Sr. The ⁸⁷Sr/⁸⁶Sr ratios were corrected for instrumental bias to an NIST SRM 987 value of 0.710248 (McArthur et al., 2001), averaging the results of the RM measured before and after each sample. Repeated analyses of NIST SRM 987 yielded a ⁸⁷Sr/⁸⁶Sr ratio of 0.710267 ± 0.000016 (2 SE; n = 14). The long-term reproducibility (c.a. three years of analyses; n >2000) of the MC-ICP-MS gave a ⁸⁷Sr/⁸⁶Sr ratio of 0.71027 ± 0.00002 (2 SE; Durante et al., 2015).

4.4.3 Laser ablation systems

During this study, we used two different laser ablation systems at MPIC. While the nanosecond laser ablation system was chosen for samples with lower Sr mass fraction (250 - 1400 μg/g), the femtosecond laser ablation system was used for samples with higher mass fractions (approximately >3000 μg/g). For low Sr mass fraction samples, the 213 nm laser ablation system is more suitable, due to the higher ablation caused by the higher fluence (20-30 J/cm² vs. 0.1-1 J/cm²). This enables us to measure even low mass fraction samples with sufficient precision. For the femtosecond laser ablation system, sample heating is reduced allowing a better and more controlled ablation (Glaus et al., 2010; Koch and Gunther,

2007). Furthermore, matrix-matching is not important with this kind of laser system, and elemental and isotopic fractionation effects are minimized (Poitrasson et al., 2003; Vanhaecke et al., 2010). However, the refractory Sr is less influenced by these factors than for example the volatile Rb. A detailed comparison of the 213 nm laser ablation system and the femtosecond laser ablation system is given by Jochum et al. (2014).

4.4.4 LA-MC-ICP-MS analysis

Laser ablation measurements were performed with both multi-collector ICP mass spectrometers, the Neptune and the Nu MC-ICP-MS. An overview of the cup configuration of both mass spectrometers and the possible interfering signals is given in Table 4.2. For the Neptune, the international RM Jct-1 as well as NIST SRM 1400 and NIST SRM 1486 have been analyzed as circular manual-pressed pellets (diameter ~2 cm, thickness ~0.5 cm).

Table 4.2: Cup configuration for Nu Plasma and Neptune MC-ICP-MS and possible interferences during analysis.

Mass	88	87	86.5	86	85.5	85	84	83.5	83	82
Isotope of interest	⁸⁸ Sr	⁸⁷ Sr		⁸⁶ Sr			⁸⁴ Sr			
				⁸⁶ Kr			⁸⁴ Kr		⁸³ Kr	⁸² Kr
		⁸⁷ Rb				⁸⁵ Rb				
	¹⁷⁶ Yb	¹⁷⁴ Yb	¹⁷³ Yb	¹⁷² Yb	¹⁷¹ Yb	¹⁷⁰ Yb	¹⁶⁸ Yb			
Possible interferences						¹⁷⁰ Er	¹⁶⁸ Er	¹⁶⁷ Er	¹⁶⁶ Er	¹⁶⁴ Er
										¹⁶⁴ Dy
	<i>Ca dimers</i>	<i>Ca dimers</i>		<i>Ca dimers</i>		<i>Ca dimers</i>	<i>Ca dimers</i>		<i>Ca dimers</i>	<i>Ca dimers</i>
	<i>Ca argides</i>	⁴⁰ Ca ³¹ P ¹⁶ O		<i>Ca argides</i>			<i>Ca argides</i>		<i>Ca argides</i>	<i>Ca argides</i>
		⁴⁰ Ar ³¹ P ¹⁶ O								
Collector Nu	H4	H2	H1	Ax	L1	L2	L3	IC-1	L4	L5
Collector Neptune	H4	H3	H2	H1	C	L1	L2		L3	L4

⁴⁰Ca³¹P¹⁶O and ⁴⁰Ar³¹P¹⁶O interferences can arise during the analysis of apatite samples.

Prior to LA analysis, the instrument was tuned using the NIST SRM987 reference solution, monitoring both the signals and the isotopic ratios of interest. Strontium data from the Nu were obtained by either a coupling to a 213 nm Nd:YAG laser ablation system and a 200 nm femtosecond laser ablation system. The mass spectrometer was tuned similarly as the Neptune.

For both instruments, peaks of the following masses were acquired during the analysis: ⁸²Kr, ⁸³Kr, ⁸⁴Sr, ⁸⁵Rb, ⁸⁶Sr, ⁸⁷Sr, ⁸⁸Sr and half masses 85.5 and 86.5. The half masses were monitored to check for the

contributions of doubly charged rare earth elements ($^{171}\text{Yb}^{2+}$ and $^{173}\text{Yb}^{2+}$) and to eventually correct their interference.

The “on peak zero” method was employed to correct for the presence of Kr in the plasma by measuring a 60 s gas background for the Neptune and a 45 s gas background for the Nu prior to each analysis (laser off) and subtracting these signals from the corresponding peak. After background subtraction, the remaining signal of mass 82 was used to check the formation of Ca dimers and argides, which are isobars to masses ^{84}Sr , ^{86}Sr , ^{87}Sr and ^{88}Sr . Ca dimer and argide signals on mass 82 were generally around 0.1 mV or less. Similarly, the remaining signal of mass 83 was used to check for the presence of $^{166}\text{Er}^{2+}$ (Copeland et al., 2008). Rb interferences were corrected using the same procedure as explained for the solution method. For phosphate samples (NIST SRM 1400 and NIST SRM 1486), we employed a further mathematical model to correct for the presence of $^{40}\text{Ca}^{31}\text{P}^{16}\text{O}$ and $^{40}\text{Ar}^{31}\text{P}^{16}\text{O}$ on mass 87. While some analysts have never experienced them (Copeland et al., 2008; Müller and Anczkiewicz, 2016), these polyatomic interferences have been reported by several authors (e.g. De Jong et al., 2007; Horstwood et al., 2008; Irrgeher et al., 2016; Lewis et al., 2014; Lugli et al., 2017b; Nowell and Horstwood, 2009; Reitmaier et al., 2017; Scharlotta and Weber, 2014; Simonetti et al., 2008; Vroon et al., 2008; Willmes et al., 2016) and can strongly bias the final $^{87}\text{Sr}/^{86}\text{Sr}$ ratio of low-Sr mass fraction samples. Two general approaches are employed to overcome this issue: (1) reduction of the oxide levels through a customized plasma interface (Lewis et al., 2014) or by adding nitrogen to the plasma (Willmes et al., 2016); (2) a data calibration with a daily regression line based on known apatite RMs (Horstwood et al., 2008; Lugli et al., 2017b). For the LA analysis of NIST SRM 1400 and NIST SRM 1486, we built a daily calibration line ($^{87}\text{Sr}/^{86}\text{Sr}$ accuracy vs. $1/^{88}\text{Sr}$ signal) using three in-house bioapatite RMs with different Sr mass fraction (from ca. 1000 to 200 $\mu\text{g}/\text{g}$), as presented in Lugli et al. (2017b). The $^{87}\text{Sr}/^{86}\text{Sr}$ ratio of each bioapatite has been determined at least five times to build the calibration line. The resulting slope of the calibration line was 0.001717, while the intercept was 1.000063, with an r^2 of 0.93.

During Neptune analyses, RM pellets have been sampled using linear scans (500 μm length), with a spot size of 100 μm . We employed a scan speed of 5 $\mu\text{m}/\text{s}$, a frequency of 10 Hz and a He flux of 0.6 L/min. The resulting fluence with a 100% energy output was $\sim 20 \text{ J}/\text{cm}^2$.

The Nu analyses were performed as a linear scan (750 μm length) with a scan speed of 5 $\mu\text{m}/\text{s}$, a spot size between 55 and 100 μm and frequencies between 10 and 250 Hz, depending on the laser ablation system. The resulting fluence varied between 0.1 – 1 J/cm^2 (Femtosecond laser) and 20 – 30 J/cm^2 (Nanosecond laser, see Table 4.1).

4.5 Results

The results of all techniques used for the analysis of the $^{87}\text{Sr}/^{86}\text{Sr}$ ratios on the different RMs are compiled in Table 4.3. In the following paragraphs, the results of each RM are presented in more detail. All uncertainties are given as 2 SE.

JCp-1: The coral RM JCp-1 has a high Sr mass fraction of about 7260 – 7500 $\mu\text{g/g}$. This enabled us to measure this material with three different approaches (i.e. solution MC-ICP-MS and LA-MC-ICP-MS with nanosecond and femtosecond laser ablation, respectively). The high-precision $^{87}\text{Sr}/^{86}\text{Sr}$ results from the solution MC-ICP-MS measurements of 0.709170 ± 0.000006 ($^{84}\text{Sr}/^{86}\text{Sr} = 0.056486 \pm 0.000002$, $n = 3$) are in agreement with the highest-precision literature value of 0.709164 ± 0.000005 (Krabbenhöft et al., 2009). The results from nanosecond ($^{87}\text{Sr}/^{86}\text{Sr} = 0.709182 \pm 0.000064$, $^{84}\text{Sr}/^{86}\text{Sr} = 0.05634 \pm 0.00003$, $n = 20$) and femtosecond ($^{87}\text{Sr}/^{86}\text{Sr} = 0.709171 \pm 0.000054$, $^{84}\text{Sr}/^{86}\text{Sr} = 0.5615 \pm 0.00005$, $n = 19$) laser ablation have a larger uncertainty, but are both in agreement within uncertainty with the solution and the literature data.

JCt-1: This RM was measured with two different nanosecond LA-MC-ICP-MS setups and solution MC-ICP-MS. So far, there is only one literature value of $^{87}\text{Sr}/^{86}\text{Sr} = 0.70915 \pm 0.00005$ (SD, MC-ICP-MS) available (Ohno and Hirata (2007)). Our solution value of 0.709169 ± 0.000009 ($^{84}\text{Sr}/^{86}\text{Sr} = 0.056484 \pm 0.000002$, $n = 3$) is in perfect agreement with this value. The Neptune LA-MC-ICP-MS setup yielded an average $^{87}\text{Sr}/^{86}\text{Sr}$ ratio of 0.70915 ± 0.00004 ($^{84}\text{Sr}/^{86}\text{Sr} = 0.0565 \pm 0.0002$, $n = 5$), and the Nu setup an average $^{87}\text{Sr}/^{86}\text{Sr}$ ratio of 0.70917 ± 0.00005 ($^{84}\text{Sr}/^{86}\text{Sr} = 0.05639 \pm 0.00005$, $n = 92$), which both agree within uncertainty with the solution data.

MACS-1: The synthetic carbonate MRM MACS-1 has the lowest Sr mass fraction of all RMs investigated in this study. Thus, we were not able to provide reliable $^{87}\text{Sr}/^{86}\text{Sr}$ data by laser ablation analysis due to the large influence of REEs and Rb (mass fraction of 128 $\mu\text{g/g}$ for Er, 133 $\mu\text{g/g}$ for Yb and 131 $\mu\text{g/g}$ for Dy; $\text{Er}/\text{Sr} \cdot 10^{-6} \sim 1000\text{-}2200$; $\text{Yb}/\text{Sr} \cdot 10^{-6} \sim 2600\text{-}4500$, $\text{Rb}/\text{Sr} \cdot 10^{-3} \sim 0.7\text{-}1.5$, $^{87}\text{Sr}/^{86}\text{Sr} = 0.706409 \pm 0.000130$, $n = 8$, see supplemental Table A4.5 and Fig. A4.3). Solution work resulted in a $^{87}\text{Sr}/^{86}\text{Sr}$ ratio of 0.707948 ± 0.000007 ($^{84}\text{Sr}/^{86}\text{Sr} = 0.056510 \pm 0.000002$, $n = 3$). Although MACS-1 was first used more than a decade ago by Munksgaard et al. (2004), this is, to our knowledge, the first Sr isotope data for MACS-1.

MACS-3: This synthetic carbonate MRM is widely used for geochemical analyses. The high Sr mass fraction makes this RM especially useful for laser ablation analysis. However, so far only a single $^{87}\text{Sr}/^{86}\text{Sr}$ ratio of 0.7075532 ± 0.0000037 (Jochum et al., 2011a) has been published, which was determined by TIMS. We used three different setups to obtain Sr isotope ratios (solution MC-ICP-MS and both nanosecond and femtosecond LA-MC-ICP-MS). Our high-precision MC-ICP-MS data show a $^{87}\text{Sr}/^{86}\text{Sr}$ ratio of 0.707541 ± 0.000007 ($^{84}\text{Sr}/^{86}\text{Sr} = 0.056496 \pm 0.000002$, $n = 3$), which is in good agreement with the literature value. Our nanosecond laser ablation setups provided an average $^{87}\text{Sr}/^{86}\text{Sr}$

ratio of 0.707535 ± 0.000049 ($^{84}\text{Sr}/^{86}\text{Sr} = 0.05600 \pm 0.00004$, $n = 16$), and our femtosecond approach an average ratio of 0.707560 ± 0.000047 ($^{84}\text{Sr}/^{86}\text{Sr} = 0.05580 \pm 0.00005$, $n = 58$), which are both in agreement within uncertainty with each other as well with the solution MC-ICP-MS and TIMS data.

MAPS-4: For this USGS phosphate RM, currently only one $^{87}\text{Sr}/^{86}\text{Sr}$ reference value is available in the literature (0.707800 ± 0.000006 , 2 SE, ID-TIMS, provided by Neymark et al., 2014). We determined Sr isotope data for this material by solution MC-ICP-MS and both femtosecond and nanosecond LA-MC-ICP-MS. The solution work yielded a $^{87}\text{Sr}/^{86}\text{Sr}$ ratio of 0.707813 ± 0.000011 ($^{84}\text{Sr}/^{86}\text{Sr} = 0.056487 \pm 0.000002$, $n = 3$), which is in agreement within uncertainty with the published value. The femtosecond LA-MC-ICP-MS data ($^{87}\text{Sr}/^{86}\text{Sr}$ ratio of 0.707697 ± 0.000165 ; $^{84}\text{Sr}/^{86}\text{Sr} = 0.0440 \pm 0.0002$, $n = 14$) shows deviating $^{87}\text{Sr}/^{86}\text{Sr}$ ratios from the solution data. For the nanosecond LA-MC-ICP-MS measurements, the $^{87}\text{Sr}/^{86}\text{Sr}$ ratio of 0.707834 ± 0.000068 ($n = 15$) is in agreement with the solution data. Both the $^{84}\text{Sr}/^{86}\text{Sr}$ datasets (0.0440 ± 0.0002 and 0.0387 ± 0.0006 respectively) show deviating values from the invariant literature ratio and both LA-MC-ICP-MS approaches resulted in elevated REE/Sr ratios of $\text{Er}/\text{Sr} \cdot 10^{-6}$ (~60-140) and $\text{Yb}/\text{Sr} \cdot 10^{-6}$ (~100-250).

MAPS-5: The MAPS-5 phosphate RM has a much lower Sr mass fraction than MAPS-4 and similar REE and Rb interferences ($\text{Er}/\text{Sr} \cdot 10^{-6} \sim 150\text{-}350$, $\text{Yb}/\text{Sr} \cdot 10^{-6} \sim 350\text{-}450$, $\text{Rb}/\text{Sr} \cdot 10^{-3} \sim 0.2\text{-}0.4$, see supplemental Tables A4.8-A4.10 and Fig. A4.4 and A4.5). Thus, it was not possible to obtain reliable LA-MC-ICP-MS data with our setups ($^{87}\text{Sr}/^{86}\text{Sr} = 0.710914 \pm 0.000830$, $n = 9$). Solution MC-ICP-MS analysis resulted in a $^{87}\text{Sr}/^{86}\text{Sr}$ ratio of 0.707924 ± 0.000009 ($^{84}\text{Sr}/^{86}\text{Sr} = 0.056462 \pm 0.000002$, $n = 3$), which is in agreement with the previously published value of 0.707910 ± 0.000005 (2SE, ID-TIMS, Neymark et al., 2014).

NIST SRM 1400: The bone RM NIST SRM 1400 was used to validate our solution measurements. Our solution $^{87}\text{Sr}/^{86}\text{Sr}$ results of 0.713125 ± 0.000005 ($^{84}\text{Sr}/^{86}\text{Sr} = 0.056481 \pm 0.000002$, $n = 3$) are in perfect agreement with the highest precision literature value of 0.71312 ± 0.00004 (2 SE, MC-ICP-MS, De Muynck and Vanhaecke (2009). Additional measurements by LA-MC-ICP-MS with the Neptune resulted in a $^{87}\text{Sr}/^{86}\text{Sr}$ ratio of 0.713222 ± 0.000106 ($^{84}\text{Sr}/^{86}\text{Sr} = 0.0563 \pm 0.0002$, $n = 11$), which is in agreement with both the literature and solution data.

NIST SRM 1486: Similarly to NIST SRM 1400, this RM was used to validate our solution data. The obtained $^{87}\text{Sr}/^{86}\text{Sr}$ ratio of 0.709285 ± 0.000006 ($^{84}\text{Sr}/^{86}\text{Sr} = 0.056488 \pm 0.000002$, $n = 3$) is in perfect agreement with the highest precision literature value of 0.709274 ± 0.000008 (2 SE, TIMS, Galiová et al., 2013). LA-MC-ICP-MS measurements with the Neptune yielded an average $^{87}\text{Sr}/^{86}\text{Sr}$ ratio of 0.709269 ± 0.000086 ($^{84}\text{Sr}/^{86}\text{Sr} = 0.0558 \pm 0.0005$, $n = 13$) in agreement with the literature and solution data.

Table 4.3: $^{87}\text{Sr}/^{86}\text{Sr}$ results of carbonate and phosphate RMs in the literature and this study in comparison. Compiled $^{87}\text{Sr}/^{86}\text{Sr}$ ratios are divided into reference (Ref) and information (Inf) values.

Reference material	JCP-1	JCI-1	MACS-1	MACS-3	MAPS-4	MAPS-5	NIST SRM 1400	NIST SRM 1486
Producer	Geological Survey of Japan	Geological Survey of Japan	United States Geological Survey	United States Geological Survey	United States Geological Survey	United States Geological Survey	National Institute of Standards and Technology	National Institute of Standards and Technology
Origin	Ishigaki Island (Japan)	Kume Island (Japan)	sythetic	sythetic	sythetic	sythetic		
Sample type	Coral (<i>Porites</i> sp.)	Giant clam (<i>Tidachna gigas</i>)	Carbonate pellet	Carbonate pellet	Phosphate pellet	Phosphate pellet	Bone ash powder	Bone meal powder
First published	Okai et al. 2002	Inoue et al. 2004	Munksgaard et al. 2004	Jochum et al. 2011	Neymark et al. 2014	Neymark et al. 2014	1992	1992
Sr [$\mu\text{g/g}$] ^a	7260-7500	1400	196-249	6260-8012	3110-3300	214-230	246-255	255-310
$^{87}\text{Sr}/^{86}\text{Sr}$ Literature	0.709160 ± 0.000020^b (SD)							
	0.709150 ± 0.000210^c (2 σ)							
	0.709164 ± 0.000005^d (2 SE)	0.709150 ± 0.000050^b (SD)	NA	0.707553 ± 0.000004^f (2 SD)	0.707800 ± 0.000006^g (2 SE)	0.707910 ± 0.000005^h (2 SE)	0.713140 ± 0.039000^h (2 RSD %)	0.709310 ± 0.017000^h (2 RSD %)
	0.709164 ± 0.000008^e (2 SD)						0.713400 ± 0.000500^i (2 σ)	0.709300 ± 0.000030^j (2 σ)
$^{87}\text{Sr}/^{86}\text{Sr}$ MC-ICP-MS this study*	0.709170 ± 0.000006 n = 3, 2 SE	0.709169 ± 0.000009 n = 3, 2 SE	0.707948 ± 0.000007 n = 3, 2 SE	0.707541 ± 0.000007 n = 3, 2 SE	0.707813 ± 0.000011 n = 3, 2 SE	0.707924 ± 0.000009 n = 3, 2 SE	0.713125 ± 0.000006 n = 3, 2 SE	0.709285 ± 0.000006 n = 3, 2 SE
$^{87}\text{Sr}/^{86}\text{Sr}$ ns-LA-MC-ICP-MS this study*	0.709182 ± 0.000064 n = 20, 2 SE	0.709170 ± 0.000050 n = 92, 2 SE 0.709155 ± 0.000040 n = 5**, 2 SE	***	0.707535 ± 0.000049 n = 16, 2 SE	***	***	0.713222 ± 0.000106 n = 11**, 2 SE	0.709269 ± 0.000086 n = 13**, 2 SE
$^{87}\text{Sr}/^{86}\text{Sr}$ fs-LA-MC-ICP-MS this study*	0.709171 ± 0.000064 n = 19, 2 SE	0.709179 ± 0.000085 n = 14, 2 SE	***	0.707560 ± 0.000047 n = 58, 2 SE	***	***		
Compiled $^{87}\text{Sr}/^{86}\text{Sr}$ 95% CL	0.709164 ± 0.000045 (Ref)	0.709160 ± 0.000054 (Inf)	0.707948 ± 0.000009 (Inf)	0.707547 ± 0.000090 (Inf)	0.707807 ± 0.000127 (Inf)	0.707917 ± 0.000112 (Inf)	0.713139 ± 0.000087 (Ref)	0.709297 ± 0.000099 (Ref)

a: GeoReM database (Jochum et al., 2005); b: Ohno and Hirata (2007); c: Sano et al. (2008); d: Krabbenhöft et al. (2009); e: Hori et al. (2013); f: Jochum et al. (2011a); g: Neymark et al. (2014); h: Galler et al. (2007); i: Balter et al. (2008); j: De Muynck and Vanhaecke (2009); k: Galiová et al. (2013); NA: not available; * all uncertainties are 2 SE; ** Measurement with Neptune LA-MC-ICP-MS; *** Interferences too large for laser ablation measurements.

4.6 Discussion

Our data of eight different RMs are in good agreement with the published values (Table 4.3). These measurements also yield new insights in the differences between different analytical techniques and their results. While for some RMs (e.g. JCp-1 and MACS-3), high precision $^{87}\text{Sr}/^{86}\text{Sr}$ ratios from TIMS and solution MC-ICP-MS are already available, for other RMs no high precision (e.g. JcT-1) or not any published values at all (MACS-1) are available.

The most important result of this study is the good agreement of the literature, solution and laser ablation data for the investigated RMs. A comparison of the results of different analytical techniques and the literature data is shown in supplemental Fig. A4.1 for JCp-1, JcT-1, MACS-3 and MAPS-4. In addition, both laser ablation systems show the same results within uncertainties for all studied RMs, except for those with large REEs interferences (MACS-1, MAPS-4 and MAPS-5). This shows that the 213 nm Nd:YAG laser ablation system is suitable for reliable laser ablation isotope data. In principle, the femtosecond laser ablation techniques should be preferred for samples and RMs with high Sr mass fractions due to less isotopic and elemental fractionation (Poitrasson et al., 2003; Vanhaecke et al., 2010), even if these effects were not visible in our study.

By comparing the data obtained from different multi-collector systems, we do not see any significant discrepancies. All solution ratios were measured with a Neptune MC-ICP-MS system at the Department of Chemical and Geological Sciences (University of Modena and Reggio Emilia) and are in agreement with the literature data and with the Nu LA-MC-ICP-MS of the MPIC, in absence of large REE and/or Rb interferences. Furthermore, a direct comparison of the same RM (JcT-1) with the same type of laser ablation system (NWR UP-213) provided similar results with the two mass spectrometers. The average ratio for the Nu setup was 0.709170 ± 0.000050 ($n = 92$), which is in perfect agreement with the solution data and the average Neptune laser ablation ratio of 0.709155 ± 0.000040 ($n = 5$). This documents the applicability of our Sr isotope values for future laser ablation and solution work (Weber et al., 2017). Furthermore, since some of the RMs are not widely available due to export restrictions or because they are too expensive for a daily use, a careful calibration against in-house reference materials is possible.

Our $^{84}\text{Sr}/^{86}\text{Sr}$ ratio laser ablation measurements of MACS-1, MAPS-4 and MAPS-5 RMs show a strongly deviation from the invariant literature value of 0.0565, which is commonly considered a good indicator of a successful interference correction of the $^{87}\text{Sr}/^{86}\text{Sr}$ isotope LA-MC-ICP-MS measurements (Müller and Anczkiewicz, 2016). Thus, even if the $^{87}\text{Sr}/^{86}\text{Sr}$ ratio is in agreement with the solution data for the nanosecond LA-MC-ICP-MS measurements of MAPS-4, we assume that the correction of REEs was not completely successful. With our cup configuration, we are only able to detect REE interferences of Er and Yb. However, measurements of MACS-1, MAPS-4 and MAPS-5 can also be affected by the interference of Dy, which was detected by additional measurements of MACS-1, where masses 81, 81.5 and 82 were monitored for the occurrence of doubly-charged $^{164}\text{Dy}^{2+}$ (see supplemental Fig. A4.3-A4.5 and Table A4.13). In principle, these datasets of $^{87}\text{Sr}/^{86}\text{Sr}$ ratios should be discarded and only the solution

data provide reliable results. However, as suggested by some authors (e.g. Copeland et al., 2010; Horstwood et al., 2008; Willmes et al., 2016), in some cases the $^{84}\text{Sr}/^{86}\text{Sr}$ ratio may not be diagnostic of high-quality $^{87}\text{Sr}/^{86}\text{Sr}$ ratios, mainly because both the 84 and 86 masses can be quite low in term of intensities (Willmes et al., 2016), yielding not so accurate/precise results. Moreover, some REE interferences may afflict the $^{84}\text{Sr}/^{86}\text{Sr}$, but not the $^{87}\text{Sr}/^{86}\text{Sr}$ ratio (e.g. this study). In addition, the over/under-correction of Ca dimers and argides can bias the final $^{84}\text{Sr}/^{86}\text{Sr}$ result (Horstwood et al., 2008), being these two masses highly affected by Ca and Ar interferences.

In general, solution data, as expected, have a much higher precision than LA data. Therefore, the first should be preferred when used as the true reference value for long-term reproducibility and correction/calibration purposes. However, the laser ablation approach has the advantage of a much faster data acquisition and a higher spatial resolution. In addition, in contrast to the solution work, no chemical separation has to be performed beforehand, which substantially reduces the total time of analysis as well as possible errors during sample preparation. However, the laser ablation work is limited in precision, and data evaluation is more complex due to potential interferences and additional error sources, such as laser setup and insufficient matching of elemental mass fraction between samples and RMs.

While for carbonates any issue regarding the RM-sample matrix-matching seems to be negligible, we suggest the use of proper matrix-matched RMs for the analysis of (bio)-apatites, due to more possible polyatomic interferences (e.g. CaPO – ArPO and often generally higher Rb and REE mass fractions). As reported in the analytical technique section, the two apatite RMs (NIST SRM 1400 and NIST SRM 1486) needed a daily calibration to overcome the CaPO – ArPO presence within the plasma. This issue is very well-known within the laser ablation community (De Jong et al., 2007; Horstwood et al., 2008; Irrgeher et al., 2016; Lewis et al., 2014; Lugli et al., 2017a; Lugli et al., 2017b; Nowell and Horstwood, 2009; Reitmaier et al., 2017; Scharlotta and Weber, 2014; Simonetti et al., 2008; Vroon et al., 2008; Willmes et al., 2016), although still a matter of debate (Müller and Anczkiewicz, 2016). The size-effect of these molecules on the accuracy of the final $^{87}\text{Sr}/^{86}\text{Sr}$ ratio highly depends on the Sr mass fraction of the sample itself. Thus, we feel that the use of multiple matrix-matched RMs with known and different Sr content may help the users to calibrate the sample $^{87}\text{Sr}/^{86}\text{Sr}$ ratio if needed or at least to check the accuracy of the analysis on the matched RMs. Otherwise, using for example carbonate RMs for the analysis of apatite samples, could yield high-quality results for the carbonate and poor-unknown quality results for the apatite samples because of the rise of 87-isobar polyatomic species. Even if the user method does not require the calibration using RMs calibration curve (e.g. Lewis et al., 2014; Willmes et al., 2016), the use of matrix-matched apatite RMs with known Sr content can be crucial to ensure the precision and the accuracy of the analysis over time.

Although the test portion mass varies in a wide range for the different samples and measurement techniques (Table 4.4), the resulting $^{87}\text{Sr}/^{86}\text{Sr}$ ratios are in agreement. While even RMs with low mass fractions of Sr, such as MACS-1 and MAPS-5, have a test mass portion of ~10 mg for the solution

measurements, the test mass portion for laser ablation measurements is much lower (1.25 – 2.5 μg for ns- and 0.5 – 0.7 μg for fs-LA-MC-ICP-MS). The comparison of the test portion masses for JcT-1 shows that even the small test portion mass of 1.25 – 2.5 μg during ns-LA-MC-ICP-MS is enough to obtain a result within uncertainties close to the solution measurement with test portion masses in the range of 5 - 10 mg. This shows that the samples are homogeneous on less than a μg -scale and highly suitable for microanalytical measurements of Sr isotope ratios.

Table 4.4: Test portion masses and Sr content of carbonate and phosphate RMs for different measurement techniques.

Type of Analysis	Test Portion Mass	Sr content [μg]
MC-ICP-MS	5 - 10 mg	2 - 45
ns-LA-MC-ICP-MS	1.25 - 2.5 μg	0.2 - $18 \cdot 10^{-3}$
fs-LA-MC-ICP-MS	0.5 - 0.7 μg	0.1 - $5 \cdot 10^{-3}$

4.7 Conclusions

We present new Sr isotope data for carbonate and phosphate RMs with different mass fractions from different distributors. We provide high-precision solution $^{87}\text{Sr}/^{86}\text{Sr}$ values for all RMs and present the first published $^{87}\text{Sr}/^{86}\text{Sr}$ ratios for the synthetic carbonate RM MACS-1. All solution measurements of carbonate and phosphate RMs are in good agreement with the literature values. The $^{87}\text{Sr}/^{86}\text{Sr}$ ratios determined by LA-MC-ICP-MS are reliable for all RMs with low interferences of REEs. This shows the reliability of our results and highlights the applicability of these RMs for validation and monitoring purposes for laser ablation work on carbonate and phosphate samples. The homogeneity on a μg -scale makes them suitable for the use as microanalytical RMs. All our analyses performed by solution work yielded identical results within uncertainties with literature values, whereas the laser ablation measurements showed deviations for RMs with a significant mass fraction of REEs (MACS-1, MAPS-4 and MAPS-5). Those RMs with no or low influences of REEs (JcT-1, JcP-1 and MACS-3) showed reliable laser ablation data within uncertainty of the solution work and are highly suitable for the use during LA analysis. However, for calibration and validation during laser ablation work, we recommend ultimately the use of high-precision TIMS or solution MC-ICP-MS $^{87}\text{Sr}/^{86}\text{Sr}$ reference values. These can either be used directly as RM or to calibrate in-house reference materials, which can then be used during further analysis. Finally, we recommend the use of matrix-matched RMs at least during laser ablation analysis of apatite samples because of the possible presence of polyatomic interferences on mass 87.

4.8 Acknowledgements

This study was funded by the Max Planck Graduate Center (to Michael Weber) and by the ‘Programma Giovani Ricercatori Rita Levi Montalcini’ to Anna Cipriani. Denis Scholz thanks the German Research Foundation for funding (DFG SCHO 1274/9-1). We also want to thank Beate Schwager, Brigitte Stoll and Ulrike Weis for assistance in the laboratory and T. Hirata and S. Wilson for providing RMs. The authors thank the editor Paul Sylvester and two anonymous referees for their review and constructive comments which helped to improve the manuscript.

4.9 Supplement

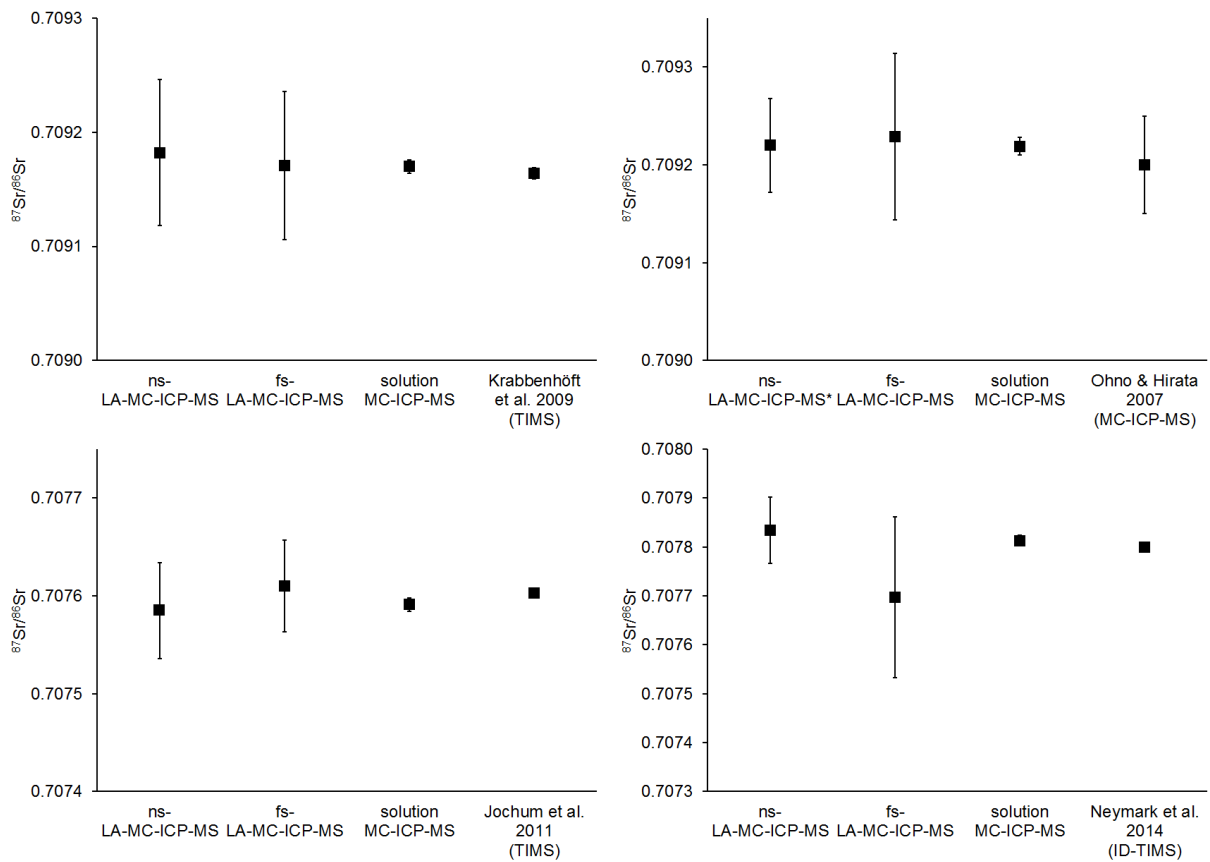


Fig. A4.1: Comparison of $^{87}\text{Sr}/^{86}\text{Sr}$ ratios of different measurement techniques and literature values for four selected RMs. Top left: JcP-1; Top right: JcT-1; Bottom left: MACS-3; Bottom right: MAPS-4. ns = nanosecond, referring to NWR UP-213; fs = femtosecond, referring to NWR Femto200. * Note that for clarity, only the ns-LA-MC-ICP-MS of the Nu setups for JcT-1 are shown. For a comparison of the $^{87}\text{Sr}/^{86}\text{Sr}$ ratios of ns-LA-MC-ICP-MS of JcT-1 between Nu and Neptune, see Table 4.3.

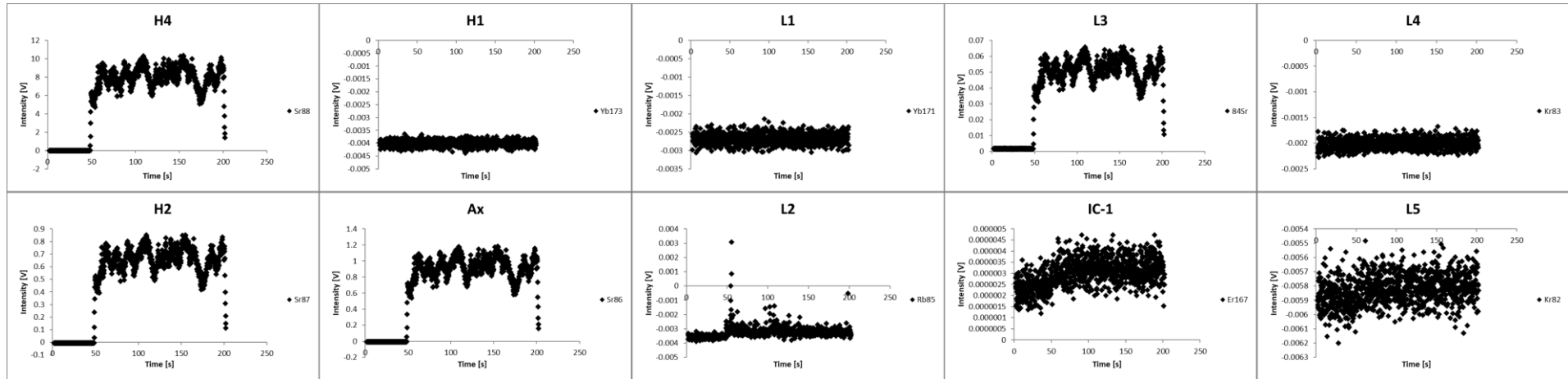


Fig. A4.2: Raw data for one measurement of JCp-1 (JCp-1-45) to demonstrate the measurement configuration used in this study. For details in cup configuration, see Table 4.2.

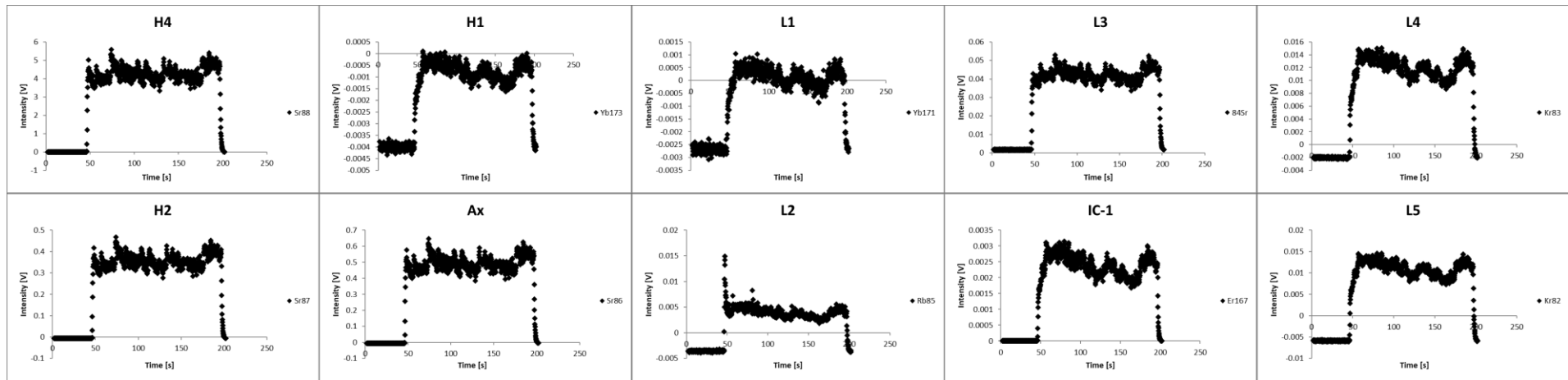


Fig. A4.3: Raw data for one measurement of MACS-1 (MACS-1-5) to demonstrate the measurement configuration used in this study. For details in cup configuration, see Table 4.2.

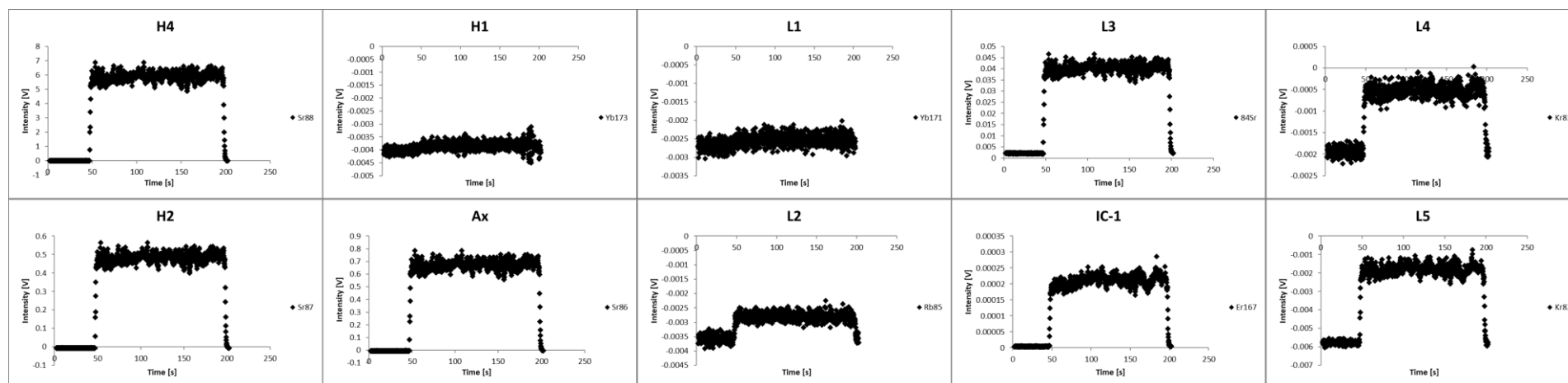


Fig. A4.4: Raw data for one measurement of MAPS-4 (MAPS-4-21) to demonstrate the measurement configuration used in this study. For details in cup configuration, see Table 4.2.

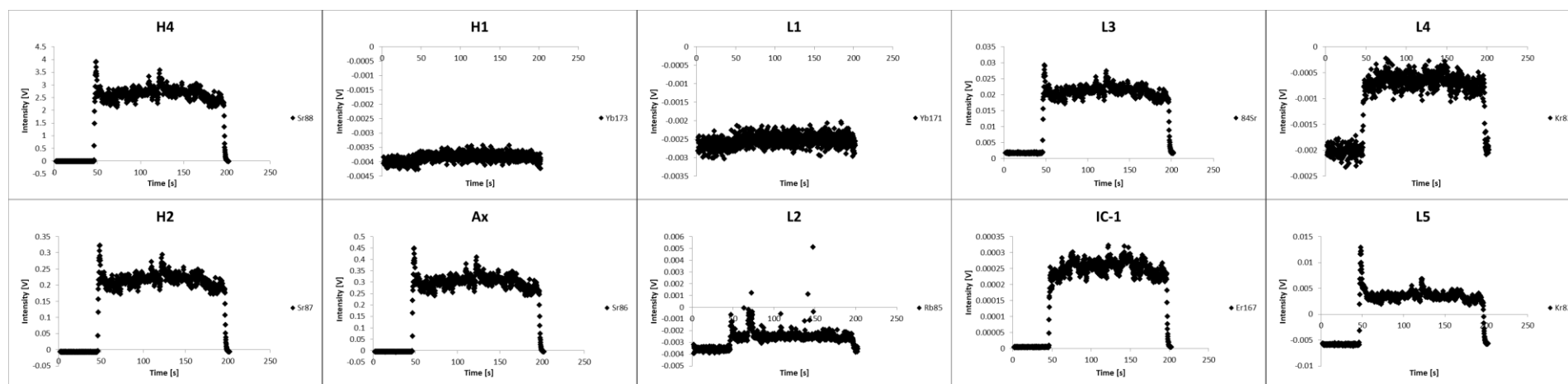


Fig. A4.5: Raw data for one measurement of MAPS-5 (MAPS-5-6) to demonstrate the measurement configuration used in this study. For details in cup configuration, see Table 4.2.

Table A4.1: Results for ns-LA-MC-ICP-MS measurements of RM Jct-1.

Sample	^{88}Sr [V]	$^{87}\text{Sr}/^{86}\text{Sr}$	2 SE	$^{84}\text{Sr}/^{86}\text{Sr}$	2 SE	Rb/Sr $\times 10^{-3}$	Er/Sr $\times 10^{-6}$	Yb/Sr $\times 10^{-6}$
JCt-1-1	4.7	0.70942	0.00004	0.05594	0.00004	0.1	1	9
JCt-1-2	3.7	0.70920	0.00005	0.05596	0.00006	0.1	2	6
JCt-1-3	3.3	0.70916	0.00005	0.05616	0.00006	0.1	1	35
JCt-1-4	3.2	0.70908	0.00005	0.05613	0.00006	0.1	1	0
JCt-1-5	2.9	0.70911	0.00006	0.05610	0.00007	0.1	1	6
JCt-1-6	3.0	0.70920	0.00005	0.05617	0.00006	0.1	1	0
JCt-1-7	3.2	0.70918	0.00006	0.05605	0.00007	0.1	1	23
JCt-1-8	3.8	0.70919	0.00005	0.05598	0.00005	0.1	1	29
JCt-1-9	3.6	0.70916	0.00006	0.05607	0.00006	0.1	1	23
JCt-1-10	2.6	0.70918	0.00006	0.05608	0.00007	0.1	1	63
JCt-1-11	4.1	0.70937	0.00005	0.05601	0.00006	0.1	1	0
JCt-1-12	3.3	0.70921	0.00005	0.05610	0.00006	0.1	1	34
JCt-1-13	3.3	0.70928	0.00005	0.05608	0.00006	0.1	1	8
JCt-1-14	3.1	0.70934	0.00006	0.05609	0.00006	0.1	1	13
JCt-1-15	3.4	0.70923	0.00005	0.05595	0.00006	0.1	1	44
JCt-1-16	2.9	0.70919	0.00006	0.05599	0.00006	0.1	1	21
JCt-1-17	3.9	0.70927	0.00005	0.05633	0.00006	0.1	1	30
JCt-1-18	7.1	0.70929	0.00004	0.05629	0.00004	0.2	1	5
JCt-1-19	4.2	0.70920	0.00005	0.05636	0.00005	0.2	1	4
JCt-1-20	4.5	0.70919	0.00005	0.05642	0.00005	0.2	1	3
JCt-1-21	4.4	0.70941	0.00006	0.05633	0.00006	0.3	1	21
JCt-1-22	5.3	0.70922	0.00005	0.05639	0.00004	0.1	1	0
JCt-1-23	4.4	0.70918	0.00005	0.05637	0.00005	0.1	1	23
JCt-1-24	3.9	0.70928	0.00005	0.05639	0.00005	0.1	1	0
JCt-1-25	5.6	0.70919	0.00005	0.05633	0.00005	0.1	1	1
JCt-1-26	4.1	0.70914	0.00005	0.05640	0.00005	0.1	1	0
JCt-1-27	5.0	0.70913	0.00004	0.05634	0.00005	0.1	1	14
JCt-1-28	5.4	0.70919	0.00005	0.05638	0.00005	0.1	1	7
JCt-1-29	5.7	0.70919	0.00004	0.05637	0.00004	0.1	1	18
JCt-1-30	5.2	0.70910	0.00005	0.05645	0.00004	0.1	1	32
JCt-1-31	4.7	0.70903	0.00006	0.05636	0.00005	0.1	1	17
JCt-1-32	5.3	0.70911	0.00005	0.05632	0.00005	0.1	1	0
JCt-1-33	6.2	0.70914	0.00004	0.05636	0.00004	0.1	1	11
JCt-1-34	6.7	0.70920	0.00004	0.05626	0.00004	0.1	1	16
JCt-1-35	3.5	0.70922	0.00006	0.05631	0.00007	0.2	1	1
JCt-1-36	6.1	0.70915	0.00005	0.05638	0.00005	0.1	1	0
JCt-1-37	5.3	0.70911	0.00004	0.05631	0.00005	0.1	1	3
JCt-1-38	5.2	0.70913	0.00005	0.05648	0.00004	0.1	1	17
JCt-1-39	6.3	0.70913	0.00004	0.05639	0.00004	0.1	1	0
JCt-1-40	5.8	0.70913	0.00004	0.05635	0.00004	0.1	1	0
JCt-1-41	5.9	0.70918	0.00004	0.05630	0.00004	0.1	1	0
JCt-1-42	5.1	0.70914	0.00004	0.05631	0.00005	0.1	1	20
JCt-1-43	5.8	0.70921	0.00005	0.05642	0.00004	0.1	1	4

Table A4.1 (continued):

Sample	^{88}Sr [V]	$^{87}\text{Sr}/^{86}\text{Sr}$	2 SE	$^{84}\text{Sr}/^{86}\text{Sr}$	2 SE	Rb/Sr $\times 10^{-3}$	Er/Sr $\times 10^{-6}$	Yb/Sr $\times 10^{-6}$
JCt-1-44	6.2	0.70920	0.00004	0.05630	0.00004	0.1	1	0
JCt-1-45	6.3	0.70924	0.00004	0.05634	0.00004	0.1	1	0
JCt-1-46	4.6	0.70919	0.00005	0.05640	0.00005	0.1	1	27
JCt-1-47	6.5	0.70918	0.00004	0.05638	0.00004	0.1	1	1
JCt-1-48	4.7	0.70916	0.00005	0.05640	0.00005	0.1	1	18
JCt-1-49	3.6	0.70919	0.00005	0.05641	0.00007	0.1	1	12
JCt-1-50	4.0	0.70918	0.00005	0.05645	0.00006	0.1	1	22
JCt-1-51	5.1	0.70917	0.00005	0.05632	0.00005	0.1	1	6
JCt-1-52	5.1	0.70915	0.00005	0.05646	0.00005	0.1	1	14
JCt-1-53	5.1	0.70917	0.00005	0.05641	0.00004	0.1	1	13
JCt-1-54	5.3	0.70923	0.00005	0.05647	0.00004	0.1	1	13
JCt-1-55	4.3	0.70911	0.00005	0.05640	0.00005	0.1	1	6
JCt-1-56	3.2	0.70900	0.00005	0.05654	0.00006	0.1	1	28
JCt-1-57	3.8	0.70907	0.00006	0.05631	0.00006	0.1	1	18
JCt-1-58	3.4	0.70918	0.00006	0.05639	0.00007	0.1	1	18
JCt-1-59	3.7	0.70912	0.00005	0.05632	0.00006	0.2	1	35
JCt-1-60	4.6	0.70917	0.00005	0.05632	0.00005	0.1	1	10
JCt-1-61	4.7	0.70920	0.00005	0.05621	0.00005	0.1	1	1
JCt-1-62	5.1	0.70919	0.00005	0.05633	0.00005	0.1	1	20
JCt-1-63	8.4	0.70929	0.00003	0.05637	0.00003	0.1	1	13
JCt-1-64	8.2	0.70925	0.00004	0.05640	0.00003	0.1	1	42
JCt-1-65	9.1	0.70924	0.00005	0.05639	0.00004	0.1	1	19
JCt-1-66	8.0	0.70918	0.00004	0.05642	0.00003	0.1	1	12
JCt-1-67	7.6	0.70921	0.00005	0.05647	0.00004	0.1	1	20
JCt-1-68	8.2	0.70916	0.00005	0.05641	0.00004	0.1	1	9
JCt-1-69	7.7	0.70913	0.00003	0.05641	0.00003	0.1	1	1
JCt-1-70	8.2	0.70917	0.00003	0.05645	0.00003	0.1	1	10
JCt-1-71	8.5	0.70917	0.00003	0.05648	0.00003	0.1	1	14
JCt-1-72	7.5	0.70910	0.00003	0.05646	0.00003	0.1	1	15
JCt-1-73	7.4	0.70915	0.00003	0.05641	0.00004	0.1	1	0
JCt-1-74	7.5	0.70919	0.00003	0.05639	0.00003	0.1	1	27
JCt-1-75	7.5	0.70916	0.00003	0.05638	0.00003	0.1	1	16
JCt-1-76	6.8	0.70917	0.00003	0.05646	0.00004	0.1	1	20
JCt-1-77	7.5	0.70914	0.00003	0.05640	0.00003	0.1	1	13
JCt-1-78	7.3	0.70920	0.00004	0.05648	0.00003	0.1	1	12
JCt-1-79	8.1	0.70920	0.00006	0.05652	0.00005	0.1	1	19
JCt-1-80	6.2	0.70915	0.00004	0.05647	0.00004	0.1	1	10
JCt-1-81	5.3	0.70915	0.00004	0.05650	0.00004	0.1	1	25
JCt-1-82	7.3	0.70921	0.00004	0.05645	0.00003	0.1	1	22
JCt-1-83	6.4	0.70917	0.00004	0.05648	0.00003	0.1	1	15
JCt-1-84	5.3	0.70910	0.00005	0.05636	0.00005	0.1	1	10
JCt-1-85	6.3	0.70915	0.00004	0.05642	0.00004	0.1	1	2
JCt-1-86	6.0	0.70917	0.00004	0.05650	0.00004	0.1	1	16

Table A4.1 (continued):

Sample	^{88}Sr [V]	$^{87}\text{Sr}/^{86}\text{Sr}$	2 SE	$^{84}\text{Sr}/^{86}\text{Sr}$	2 SE	Rb/Sr $\times 10^{-3}$	Er/Sr $\times 10^{-6}$	Yb/Sr $\times 10^{-6}$
JCt-1-87	5.0	0.70919	0.00004	0.05650	0.00005	0.1	1	9
JCt-1-88	5.0	0.70916	0.00004	0.05650	0.00004	0.1	1	0
JCt-1-89	5.8	0.70917	0.00004	0.05645	0.00004	0.1	1	4
JCt-1-90	4.9	0.70912	0.00004	0.05647	0.00005	0.1	1	17
JCt-1-91	5.9	0.70910	0.00004	0.05646	0.00004	0.1	1	6
JCt-1-92	4.9	0.70910	0.00004	0.05639	0.00004	0.1	1	15
JCt-1*	17.4	0.70916	0.00004	0.05623	0.00068	0.6	2	0
JCt-1*	22.4	0.70915	0.00004	0.05587	0.00077	0.1	2	1
JCt-1*	22.9	0.70915	0.00004	0.05606	0.00069	0.1	1	0
JCt-1*	22.0	0.70915	0.00004	0.05665	0.00050	0.1	1	0
JCt-1*	17.5	0.70916	0.00004	0.05668	0.00046	0.0	0	1

*Measurements performed with Neptune LA-MC-ICP-MS

Table A4.2: Results for fs-LA-MC-ICP-MS measurements of RM JCt-1.

Sample	^{88}Sr [V]	$^{87}\text{Sr}/^{86}\text{Sr}$	2 SE	$^{84}\text{Sr}/^{86}\text{Sr}$	2 SE	Rb/Sr $\times 10^{-3}$	Er/Sr $\times 10^{-6}$	Yb/Sr $\times 10^{-6}$
JCt-1-93	1.6	0.70908	0.00007	0.05595	0.00009	0.1	1	49
JCt-1-94	1.6	0.70922	0.00006	0.05599	0.00010	0.0	1	1
JCt-1-95	1.6	0.70922	0.00007	0.05604	0.00011	0.1	1	0
JCt-1-96	1.6	0.70929	0.00007	0.05587	0.00011	0.1	1	32
JCt-1-97	1.5	0.70901	0.00007	0.05591	0.00012	0.1	1	53
JCt-1-98	1.5	0.70897	0.00007	0.05619	0.00009	0.0	1	2
JCt-1-99	1.6	0.70904	0.00007	0.05603	0.00011	0.1	1	1
JCt-1-100	1.5	0.70920	0.00007	0.05592	0.00012	0.1	1	52
JCt-1-101	1.6	0.70921	0.00007	0.05602	0.00011	0.1	1	0
JCt-1-102	1.5	0.70921	0.00007	0.05592	0.00012	0.1	1	0
JCt-1-103	1.6	0.70903	0.00007	0.05605	0.00011	0.1	1	25
JCt-1-104	1.6	0.70909	0.00006	0.05600	0.00011	0.1	1	17
JCt-1-105	1.6	0.70916	0.00007	0.05599	0.00011	0.0	1	0
JCt-1-106	1.6	0.70921	0.00006	0.05623	0.00010	0.1	1	0

Table A4.3: Results for ns-LA-MC-ICP-MS measurements of RM JCp-1.

Sample	^{88}Sr [V]	$^{87}\text{Sr}/^{86}\text{Sr}$	2 SE	$^{84}\text{Sr}/^{86}\text{Sr}$	2 SE	Rb/Sr $\times 10^{-3}$	Er/Sr $\times 10^{-6}$	Yb/Sr $\times 10^{-6}$
JCp-1-1	5.1	0.70910	0.00006	0.05628	0.00004	0.0	0	8
JCp-1-2	5.2	0.70912	0.00006	0.05632	0.00004	0.0	0	20
JCp-1-3	5.1	0.70919	0.00006	0.05631	0.00004	0.0	0	0
JCp-1-4	4.1	0.70913	0.00005	0.05613	0.00004	0.0	0	10

Table A4.3 (continued):

Sample	^{88}Sr [V]	$^{87}\text{Sr}/^{86}\text{Sr}$	2 SE	$^{84}\text{Sr}/^{86}\text{Sr}$	2 SE	Rb/Sr $\times 10^{-3}$	Er/Sr $\times 10^{-6}$	Yb/Sr $\times 10^{-6}$
JCp-1-5	6.5	0.70912	0.00003	0.05635	0.00003	0.0	0	8
JCp-1-6	6.1	0.70913	0.00003	0.05635	0.00003	0.0	0	15
JCp-1-7	6.4	0.70912	0.00004	0.05640	0.00002	0.0	0	17
JCp-1-8	6.9	0.70914	0.00003	0.05641	0.00002	0.0	0	16
JCp-1-9	6.1	0.70913	0.00003	0.05633	0.00003	0.0	0	24
JCp-1-10	6.0	0.70927	0.00003	0.05636	0.00003	0.0	0	7
JCp-1-11	5.9	0.70928	0.00004	0.05633	0.00003	0.0	0	0
JCp-1-12	6.4	0.70932	0.00004	0.05632	0.00004	0.0	0	19
JCp-1-13	6.5	0.70919	0.00007	0.05648	0.00008	0.0	0	8
JCp-1-14	6.8	0.70920	0.00006	0.05634	0.00003	0.0	0	3
JCp-1-15	7.1	0.70919	0.00006	0.05632	0.00003	0.0	0	4
JCp-1-16	6.2	0.70917	0.00006	0.05644	0.00003	0.0	0	9
JCp-1-17	7.1	0.70925	0.00007	0.05632	0.00004	0.0	0	8
JCp-1-18	6.3	0.70925	0.00006	0.05597	0.00003	0.0	0	18
JCp-1-19	8.2	0.70920	0.00006	0.05639	0.00003	0.0	0	12
JCp-1-20	7.1	0.70918	0.00007	0.05649	0.00004	0.0	0	15

Table A4.4: Results for fs-LA-MC-ICP-MS measurements of RM JCp-1.

Sample	^{88}Sr [V]	$^{87}\text{Sr}/^{86}\text{Sr}$	2 SE	$^{84}\text{Sr}/^{86}\text{Sr}$	2 SE	Rb/Sr $\times 10^{-3}$	Er/Sr $\times 10^{-6}$	Yb/Sr $\times 10^{-6}$
JCp-1-21	5.4	0.70924	0.00004	0.05598	0.00003	0.0	0	3
JCp-1-22	6.0	0.70921	0.00004	0.05603	0.00002	0.0	0	24
JCp-1-23	5.4	0.70921	0.00004	0.05589	0.00003	0.0	0	13
JCp-1-24	4.3	0.70920	0.00005	0.05605	0.00004	0.0	0	0
JCp-1-25	3.8	0.70917	0.00005	0.05588	0.00004	0.0	0	4
JCp-1-26	4.0	0.70915	0.00004	0.05592	0.00004	0.0	0	0
JCp-1-27	3.7	0.70904	0.00005	0.05614	0.00005	0.0	0	2
JCp-1-28	3.8	0.70909	0.00006	0.05620	0.00004	0.0	0	0
JCp-1-29	3.9	0.70906	0.00006	0.05629	0.00004	0.0	0	20
JCp-1-30	3.7	0.70909	0.00006	0.05625	0.00005	0.0	0	24
JCp-1-31	3.6	0.70917	0.00006	0.05619	0.00005	0.0	0	16
JCp-1-32	3.6	0.70919	0.00006	0.05618	0.00005	0.0	0	18
JCp-1-33	3.6	0.70925	0.00006	0.05617	0.00005	0.0	0	17
JCp-1-34	3.6	0.70932	0.00006	0.05611	0.00005	0.0	0	17
JCp-1-35	3.5	0.70919	0.00006	0.05621	0.00005	0.0	0	0
JCp-1-36	3.4	0.70916	0.00006	0.05622	0.00005	0.0	1	39
JCp-1-37	3.5	0.70911	0.00006	0.05615	0.00005	0.0	0	32
JCp-1-38	3.5	0.70915	0.00006	0.05616	0.00005	0.0	1	9
JCp-1-39	3.3	0.70925	0.00006	0.05606	0.00005	0.0	1	10

Table A4.5: Results for ns-LA-MC-ICP-MS measurements of RM MACS-1.

Sample	^{88}Sr [V]	$^{87}\text{Sr}/^{86}\text{Sr}$	2 SE	$^{84}\text{Sr}/^{86}\text{Sr}$	2 SE	Rb/Sr $\times 10^{-3}$	Er/Sr $\times 10^{-6}$	Yb/Sr $\times 10^{-6}$
MACS-1-1	3.2	0.70639	0.00007	0.01749	0.00046	0.8	1048	2820
MACS-1-2	2.9	0.70663	0.00005	0.02154	0.00026	0.7	885	2666
MACS-1-3	2.9	0.70643	0.00005	0.01402	0.00043	0.8	1059	3182
MACS-1-4	4.2	0.70653	0.00005	-0.03323	0.00066	1.4	2079	4038
MACS-1-5	4.3	0.70622	0.00005	-0.03952	0.00055	1.5	2101	4238
MACS-1-6	4.6	0.70633	0.00005	-0.03846	0.00046	1.4	2058	4219
MACS-1-7	4.6	0.70654	0.00005	-0.04021	0.00077	1.5	2281	4455
MACS-1-8	4.7	0.70608	0.00005	-0.03959	0.00038	1.5	2007	4325

Table A4.6: Results for ns-LA-MC-ICP-MS measurements of RM MACS-3.

Sample	^{88}Sr [V]	$^{87}\text{Sr}/^{86}\text{Sr}$	2 SE	$^{84}\text{Sr}/^{86}\text{Sr}$	2 SE	Rb/Sr $\times 10^{-3}$	Er/Sr $\times 10^{-6}$	Yb/Sr $\times 10^{-6}$
MACS3-1	5.8	0.70750	0.00006	0.05595	0.00005	0.0	3	14
MACS3-2	5.4	0.70754	0.00004	0.05606	0.00004	0.0	3	16
MACS3-3	6.4	0.70753	0.00005	0.05606	0.00004	0.0	3	26
MACS3-4	5.5	0.70753	0.00004	0.05598	0.00004	0.0	3	24
MACS3-5	5.4	0.70754	0.00005	0.05605	0.00004	0.0	3	34
MACS3-6	5.9	0.70748	0.00005	0.05597	0.00004	0.0	3	22
MACS3-7	5.9	0.70754	0.00005	0.05600	0.00004	0.0	3	16
MACS3-8	5.9	0.70751	0.00004	0.05602	0.00004	0.1	3	1
MACS3-9	6.3	0.70758	0.00004	0.05600	0.00003	0.0	3	15
MACS3-10	6.3	0.70747	0.00004	0.05599	0.00003	0.0	3	20
MACS3-11	5.2	0.70757	0.00005	0.05599	0.00004	0.0	3	13
MACS3-12	6.5	0.70752	0.00005	0.05604	0.00003	0.0	3	14
MACS3-13	7.5	0.70755	0.00005	0.05591	0.00003	0.0	3	17
MACS3-14	7.2	0.70756	0.00005	0.05601	0.00003	0.0	3	18
MACS3-15	6.8	0.70758	0.00005	0.05597	0.00003	0.0	3	24
MACS3-16	5.3	0.70752	0.00005	0.05602	0.00004	0.0	3	29

Table A4.7: Results for fs-LA-MC-ICP-MS measurements of RM MACS-3.

Sample	^{88}Sr [V]	$^{87}\text{Sr}/^{86}\text{Sr}$	2 Std Err	$^{84}\text{Sr}/^{86}\text{Sr}$	2 Std Err	Rb/Sr $\times 10^{-3}$	Er/Sr $\times 10^{-6}$	Yb/Sr $\times 10^{-6}$
MACS3-17	2.6	0.70755	0.00006	0.05485	0.00006	0.0	3	35
MACS3-18	2.5	0.70762	0.00006	0.05494	0.00006	0.0	3	25
MACS3-19	2.6	0.70749	0.00006	0.05551	0.00007	0.0	3	21
MACS3-20	3.7	0.70760	0.00005	0.05551	0.00005	0.0	3	35
MACS3-21	3.7	0.70760	0.00005	0.05562	0.00005	0.0	4	19
MACS3-22	4.6	0.70744	0.00005	0.05540	0.00010	0.0	4	27
MACS3-23	4.4	0.70745	0.00004	0.05590	0.00004	0.0	4	32

Table A4.7 (continued):

Sample	^{88}Sr [V]	$^{87}\text{Sr}/^{86}\text{Sr}$	2 SE	$^{84}\text{Sr}/^{86}\text{Sr}$	2 SE	Rb/Sr * 10^{-3}	Er/Sr * 10^{-6}	Yb/Sr * 10^{-6}
MACS3-24	4.3	0.70751	0.00004	0.05580	0.00004	0.0	4	32
MACS3-25	4.2	0.70752	0.00004	0.05580	0.00005	0.0	4	12
MACS3-26	4.4	0.70755	0.00004	0.05570	0.00004	0.0	4	26
MACS3-27	4.4	0.70755	0.00004	0.05570	0.00004	0.0	4	14
MACS3-28	4.4	0.70757	0.00004	0.05580	0.00004	0.0	4	30
MACS3-29	4.3	0.70756	0.00004	0.05590	0.00005	0.0	4	24
MACS3-30	4.9	0.70758	0.00004	0.05590	0.00004	0.0	4	26
MACS3-31	4.6	0.70753	0.00004	0.05580	0.00004	0.0	4	27
MACS3-32	4.2	0.70754	0.00004	0.05580	0.00004	0.0	4	21
MACS3-33	4.3	0.70756	0.00004	0.05590	0.00004	0.0	4	20
MACS3-34	4.1	0.70756	0.00006	0.05581	0.00007	0.0	6	10
MACS3-35	3.8	0.70761	0.00005	0.05561	0.00005	0.0	5	27
MACS3-36	3.7	0.70761	0.00005	0.05580	0.00005	0.0	5	14
MACS3-37	3.6	0.70761	0.00005	0.05578	0.00005	0.0	5	29
MACS3-38	3.4	0.70765	0.00005	0.05587	0.00006	0.0	5	24
MACS3-39	3.4	0.70765	0.00005	0.05568	0.00005	0.0	5	16
MACS3-40	3.9	0.70757	0.00005	0.05581	0.00005	0.0	5	30
MACS3-41	3.9	0.70760	0.00004	0.05588	0.00005	0.0	5	13
MACS3-42	4.0	0.70759	0.00004	0.05585	0.00005	0.0	5	5
MACS3-43	3.9	0.70757	0.00004	0.05568	0.00005	0.0	5	16
MACS3-44	4.0	0.70765	0.00004	0.05570	0.00005	0.0	5	25
MACS3-45	3.9	0.70769	0.00004	0.05581	0.00005	0.0	5	13
MACS3-46	3.8	0.70751	0.00004	0.05574	0.00005	0.0	5	31
MACS3-47	3.9	0.70754	0.00004	0.05592	0.00005	0.0	5	43
MACS3-48	3.2	0.70753	0.00005	0.05579	0.00006	0.0	5	25
MACS3-49	3.1	0.70743	0.00005	0.05585	0.00006	0.0	5	42
MACS3-50	3.1	0.70746	0.00005	0.05588	0.00006	0.0	5	54
MACS3-51	3.4	0.70748	0.00005	0.05577	0.00005	0.0	5	21
MACS3-52	3.1	0.70746	0.00005	0.05575	0.00006	0.0	5	57
MACS3-53	3.2	0.70757	0.00006	0.05582	0.00006	0.0	5	0
MACS3-54	3.2	0.70758	0.00005	0.05577	0.00006	0.0	5	6
MACS3-55	5.3	0.70749	0.00006	0.05593	0.00006	0.0	6	33
MACS3-56	3.9	0.70744	0.00005	0.05584	0.00005	0.0	6	28
MACS3-57	4.8	0.70749	0.00003	0.05588	0.00004	0.0	6	46
MACS3-58	4.9	0.70756	0.00003	0.05589	0.00004	0.0	5	26
MACS3-59	4.4	0.70754	0.00004	0.05595	0.00005	0.0	5	35
MACS3-60	4.5	0.70755	0.00004	0.05591	0.00004	0.0	5	14
MACS3-61	4.5	0.70748	0.00004	0.05586	0.00005	0.0	5	29
MACS3-62	4.4	0.70750	0.00004	0.05590	0.00004	0.0	5	47
MACS3-63	4.4	0.70756	0.00004	0.05585	0.00004	0.0	5	22
MACS3-64	4.3	0.70753	0.00004	0.05590	0.00004	0.0	5	27
MACS3-65	4.1	0.70756	0.00004	0.05598	0.00005	0.0	5	39
MACS3-66	4.5	0.70754	0.00004	0.05596	0.00004	0.0	5	28

Table A4.7 (continued):

Sample	^{88}Sr [V]	$^{87}\text{Sr}/^{86}\text{Sr}$	2 SE	$^{84}\text{Sr}/^{86}\text{Sr}$	2 SE	Rb/Sr $\times 10^{-3}$	Er/Sr $\times 10^{-6}$	Yb/Sr $\times 10^{-6}$
MACS3-67	4.4	0.70759	0.00004	0.05590	0.00005	0.0	5	24
MACS3-68	4.6	0.70758	0.00004	0.05598	0.00004	0.0	5	19
MACS3-69	4.2	0.70758	0.00004	0.05584	0.00005	0.0	5	34
MACS3-70	4.1	0.70763	0.00004	0.05590	0.00005	0.0	5	35
MACS3-71	4.0	0.70759	0.00004	0.05595	0.00005	0.0	5	33
MACS3-72	4.3	0.70757	0.00003	0.05589	0.00005	0.0	5	2
MACS3-73	4.1	0.70758	0.00004	0.05598	0.00005	0.0	4	23
MACS3-74	4.1	0.70764	0.00004	0.05585	0.00005	0.0	5	12

Table A4.8: Results for ns-LA-MC-ICP-MS measurements of RM MAPS-4.

Sample	^{88}Sr [V]	$^{87}\text{Sr}/^{86}\text{Sr}$	2 SE	$^{84}\text{Sr}/^{86}\text{Sr}$	2 SE	Rb/Sr $\times 10^{-3}$	Er/Sr $\times 10^{-6}$	Yb/Sr $\times 10^{-6}$
MAPS-4-1	4.0	0.70787	0.00004	0.04824	0.00006	0.1	61	111
MAPS-4-2	4.1	0.70791	0.00005	0.04808	0.00006	0.1	61	128
MAPS-4-3	4.0	0.70799	0.00006	0.04814	0.00009	0.1	63	135
MAPS-4-4	4.0	0.70798	0.00006	0.04811	0.00006	0.1	62	131
MAPS-4-5	3.9	0.70812	0.00006	0.04795	0.00006	0.1	65	121
MAPS-4-6	6.5	0.70776	0.00005	0.03865	0.00007	0.1	109	166
MAPS-4-7	6.6	0.70779	0.00004	0.03854	0.00007	0.1	107	161
MAPS-4-8	6.8	0.70778	0.00004	0.03842	0.00007	0.1	114	174
MAPS-4-9	6.6	0.70779	0.00005	0.03851	0.00006	0.1	115	179
MAPS-4-10	5.8	0.70783	0.00004	0.03894	0.00006	0.1	125	157
MAPS-4-11	5.4	0.70792	0.00004	0.03907	0.00007	0.1	127	146
MAPS-4-12	6.6	0.70785	0.00004	0.03832	0.00008	0.1	134	185
MAPS-4-13	5.9	0.70782	0.00004	0.03845	0.00006	0.1	126	166
MAPS-4-14	6.7	0.70782	0.00004	0.03819	0.00006	0.1	131	165
MAPS-4-15	5.8	0.70791	0.00004	0.03869	0.00007	0.1	126	163

Table A4.9: Results for fs-LA-MC-ICP-MS measurements of RM MAPS-4.

Sample	^{88}Sr [V]	$^{87}\text{Sr}/^{86}\text{Sr}$	2 SE	$^{84}\text{Sr}/^{86}\text{Sr}$	2 SE	Rb/Sr $\times 10^{-3}$	Er/Sr $\times 10^{-6}$	Yb/Sr $\times 10^{-6}$
MAPS-4-16	0.7	0.70777	0.00015	0.04225	0.00035	0.1	NA	51
MAPS-4-17	1.1	0.70767	0.00010	0.04311	0.00021	0.1	NA	212
MAPS-4-18	1.4	0.70783	0.00008	0.04307	0.00017	0.1	NA	109
MAPS-4-19	1.5	0.70789	0.00007	0.04307	0.00017	0.1	NA	178
MAPS-4-20	1.5	0.70785	0.00008	0.04346	0.00017	0.1	NA	175
MAPS-4-21	1.5	0.70784	0.00008	0.04336	0.00016	0.1	NA	215
MAPS-4-22	1.5	0.70782	0.00008	0.04276	0.00018	0.1	NA	169
MAPS-4-23	0.6	0.70711	0.00018	0.04471	0.00043	0.1	137	224
MAPS-4-24	1.3	0.70752	0.00012	0.04491	0.00019	0.1	135	143

Table A4.9 (continued):

Sample	^{88}Sr [V]	$^{87}\text{Sr}/^{86}\text{Sr}$	2 SE	$^{84}\text{Sr}/^{86}\text{Sr}$	2 SE	Rb/Sr $\times 10^{-3}$	Er/Sr $\times 10^{-6}$	Yb/Sr $\times 10^{-6}$
MAPS-4-25	1.3	0.70745	0.00011	0.04491	0.00020	0.1	134	187
MAPS-4-26	1.2	0.70750	0.00012	0.04458	0.00019	0.1	135	232
MAPS-4-27	1.2	0.70772	0.00012	0.04497	0.00022	0.1	135	133
MAPS-4-28	1.0	0.70742	0.00014	0.04563	0.00024	0.1	129	152
MAPS-4-29	1.1	0.70746	0.00015	0.04587	0.00024	0.1	125	260

Table A4.10: Results for ns-LA-MC-ICP-MS measurements of RM MAPS-5.

Sample	^{88}Sr [V]	$^{87}\text{Sr}/^{86}\text{Sr}$	2 SE	$^{84}\text{Sr}/^{86}\text{Sr}$	2 SE	Rb/Sr $\times 10^{-3}$	Er/Sr $\times 10^{-6}$	Yb/Sr $\times 10^{-6}$
MAPS-5-1	1.2	0.71086	0.00013	0.00368	0.00030	0.3	214	392
MAPS-5-2	1.4	0.70837	0.00012	0.00438	0.00028	0.3	152	361
MAPS-5-3	1.5	0.70837	0.00009	0.00624	0.00020	0.2	162	375
MAPS-5-4	1.6	0.70859	0.00008	0.00739	0.00021	0.2	168	349
MAPS-5-5	2.3	0.71096	0.00008	-0.05247	0.00065	0.4	308	392
MAPS-5-6	2.7	0.71112	0.00006	-0.03703	0.00037	0.4	339	401
MAPS-5-7	2.6	0.71117	0.00007	-0.03930	0.00040	0.4	333	409
MAPS-5-8	2.6	0.71119	0.00006	-0.04095	0.00048	0.4	344	430
MAPS-5-9	2.7	0.71131	0.00007	-0.03852	0.00064	0.4	351	411

Table A4.11: Results for ns-LA-MC-ICP-MS measurements of RM NIST SRM 1400.

Sample	^{88}Sr [V]	$^{87}\text{Sr}/^{86}\text{Sr}$	2 SE	$^{84}\text{Sr}/^{86}\text{Sr}$	2 SE	Rb/Sr $\times 10^{-3}$	Er/Sr $\times 10^{-6}$	Yb/Sr $\times 10^{-6}$
NIST 1400-1	1.2	0.71330	0.00008	0.05596	0.00037	1.5	1	10
NIST 1400-2	1.2	0.71326	0.00009	0.05604	0.00085	2.2	10	1
NIST 1400-3	1.3	0.71318	0.00009	0.05580	0.00040	1.7	10	0
NIST 1400-4	1.2	0.71315	0.00009	0.05613	0.00044	1.6	-6	9
NIST 1400-5	1.2	0.71334	0.00009	0.05613	0.00043	3.7	11	0
NIST 1400-6	1.2	0.71322	0.00008	0.05628	0.00045	1.5	8	26
NIST 1400-7	1.2	0.71315	0.00009	0.05627	0.00040	1.5	6	0
NIST 1400-8	1.2	0.71339	0.00009	0.05639	0.00046	1.7	15	3
NIST 1400-9	1.2	0.71324	0.00008	0.05671	0.00048	1.6	-8	27
NIST 1400-10	1.1	0.71302	0.00009	0.05683	0.00045	1.6	4	16
NIST 1400-11	1.2	0.71308	0.00008	0.05657	0.00039	1.6	1	11

Table A4.12: Results for ns-LA-MC-ICP-MS measurements of RM NIST SRM 1486.

Sample	^{88}Sr [V]	$^{87}\text{Sr}/^{86}\text{Sr}$	2 SE	$^{84}\text{Sr}/^{86}\text{Sr}$	2 SE	Rb/Sr $\times 10^{-3}$	Er/Sr $\times 10^{-6}$	Yb/Sr $\times 10^{-6}$
NIST 1486-1	2.5	0.70915	0.00009	0.05542	0.00032	1.6	11	19
NIST 1486-2	3.1	0.70933	0.00007	0.05621	0.00057	1.3	0	0
NIST 1486-3	3.3	0.70921	0.00008	0.05579	0.00039	1.4	1	7
NIST 1486-4	3.0	0.70934	0.00009	0.05592	0.00050	1.5	0	1
NIST 1486-5	2.9	0.70931	0.00008	0.05584	0.00048	1.4	0	11
NIST 1486-6	3.2	0.70927	0.00007	0.05558	0.00048	1.4	1	19
NIST 1486-7	3.1	0.70920	0.00006	0.05593	0.00047	1.2	0	3
NIST 1486-8	3.2	0.70921	0.00009	0.05578	0.00047	1.3	0	21
NIST 1486-9	3.4	0.70918	0.00006	0.05568	0.00048	1.3	0	0
NIST 1486-10	3.4	0.70934	0.00008	0.05546	0.00053	1.1	5	16
NIST 1486-11	3.1	0.70930	0.00007	0.05584	0.00044	1.3	0	18
NIST 1486-12	3.8	0.70939	0.00006	0.05503	0.00060	1.1	5	9
NIST 1486-13	2.1	0.70926	0.00010	0.05445	0.00034	1.6	0	24

Table A4.13: Monitoring of Dy as potential interference on mass 82 during LA-MC-ICP-MS.

Cup	H6	H4	H3	H2	Ax	L1	L2
Isotope of interest	^{86}Sr	^{84}Sr	^{167}Er	^{83}Kr & ^{166}Er	^{82}Kr & ^{164}Dy	^{163}Dy	^{162}Dy
Signal intensity [mV]	30.1	28.0	4.2	12.3	17.9	14.3	12.3

Table A4.14: Results for solution MC-ICP-MS measurements of RMs analysed in this study.

Sample	$^{87}\text{Sr}/^{86}\text{Sr}$	2 SE	$^{84}\text{Sr}/^{86}\text{Sr}$	2 SE	Rb/Sr $\times 10^{-3}$	Er/Sr $\times 10^{-6}$
JCp-1-1	0.709162	0.000005	0.056482	0.000002	0.0	0
JCp-1-2	0.709175	0.000005	0.056487	0.000002	0.0	0
JCp-1-3	0.709174	0.000007	0.056489	0.000002	0.0	0
JCt-1-1	0.709173	0.000006	0.056492	0.000002	0.0	0
JCt-1-2	0.709177	0.000007	0.056459	0.000002	0.0	1
JCt-1-3	0.709156	0.000007	0.056510	0.000002	0.0	0
MACS-1-1	0.707954	0.000008	0.056519	0.000002	0.0	0
MACS-1-2	0.707943	0.000008	0.056497	0.000002	0.0	0
MACS-1-3	0.707945	0.000006	0.056513	0.000002	0.0	0
MACS-3-1	0.707546	0.000006	0.056490	0.000002	0.0	0
MACS-3-2	0.707532	0.000007	0.056500	0.000002	0.0	0
MACS-3-3	0.707544	0.000006	0.056500	0.000002	0.0	0
MAPS-4-1	0.707796	0.000007	0.056516	0.000002	0.0	0
MAPS-4-2	0.707823	0.000007	0.056476	0.000002	0.0	0
MAPS-4-3	0.707820	0.000007	0.056467	0.000002	0.0	1
MAPS-5-1	0.707935	0.000008	0.056444	0.000002	0.0	1

Table A4.14 (continued):

Sample	$^{87}\text{Sr}/^{86}\text{Sr}$	2 SE	$^{84}\text{Sr}/^{86}\text{Sr}$	2 SE	Rb/Sr *10^{-3}	Er/Sr *10^{-6}
MAPS-5-2	0.707914	0.000009	0.056488	0.000002	0.0	0
MAPS-5-3	0.707924	0.000008	0.056455	0.000002	0.0	1
NIST 1400-1	0.713127	0.000007	0.056476	0.000002	0.0	0
NIST 1400-2	0.713124	0.000007	0.056484	0.000002	0.0	0
NIST 1400-3	0.713123	0.000007	0.056482	0.000002	0.0	0
NIST 1486-1	0.709283	0.000005	0.056482	0.000002	0.0	0
NIST 1486-2	0.709273	0.000006	0.056484	0.000002	0.0	0
NIST 1486-3	0.709298	0.000006	0.056498	0.000002	0.0	0

Chapter 5: Manuscript III: NanoSr – A new carbonate microanalytical reference material for *in-situ* Sr isotope analysis

NanoSr - A new carbonate microanalytical reference material for *in-situ* Sr
isotope analysis

Michael Weber^{1,2}, Federico Lugli^{3,4}, Bodo Hattendorf⁵, Denis Scholz¹, Regina Mertz-Kraus¹, Damien Guinoiseau², Klaus Peter Jochum²

¹Institute of Geosciences, Johannes Gutenberg University Mainz, J.-J.-Becher-Weg 21, 55128 Mainz, Germany

²Climate Geochemistry Department, Max Planck Institute for Chemistry, Hahn-Meitner-Weg 1, 55128 Mainz, Germany

³Department of Chemical and Geological Sciences, University of Modena and Reggio Emilia, Via Campi 103, 41125 Modena, Italy

⁴Departement of Cultural Heritage, University of Bologna, 48121 Ravenna, Italy

⁵Laboratory of Inorganic Chemistry, ETH Zurich, Vladimir Prelog Weg 1, 8093 Zurich, Switzerland

This manuscript has been submitted in a similar version to *Geostandards and Geoanalytical Research*.

5.1 Abstract

The *in-situ* analysis of Sr isotopes in carbonates by MC-ICP-MS is limited by the availability of suitable microanalytical reference materials, which match the samples of interest in matrix composition. Whereas several well-characterised carbonate reference materials for Sr mass fractions >1000 µg/g, such as JCT-1, JCp-1, FEBS-1 and MACS-3, are available, there is a lack of well characterised carbonate microanalytical reference materials with lower Sr mass fractions.

Here we present a new, custom-made and homogeneous synthetic carbonate nanopowder reference material with a Sr mass fraction of ca. 500 µg/g suitable for microanalytical Sr isotope analysis (“NanoSr”). We analysed the new microanalytical reference material both as a powder by solution-based techniques and as a pressed nanopowder pellet by *in-situ* techniques. To determine element mass fractions of Sr and potential interfering elements, such as Rb and REEs, we used laser ablation and solution ICP-MS in different laboratories. The Ca mass fraction was determined by EPMA and then used as internal reference element for LA-ICP-MS analyses. The $^{87}\text{Sr}/^{86}\text{Sr}$ was determined by well-established methods for Sr isotope measurements (TIMS and MC-ICP-MS) and revealed a $^{87}\text{Sr}/^{86}\text{Sr}$ ratio of 0.70756 ± 0.00003 (2 SD). The Sr isotope microhomogeneity of the pressed nanopowder pellet was determined by LA-MC-ICP-MS, which resulted in a $^{87}\text{Sr}/^{86}\text{Sr}$ ratio in agreement with the solution data considering uncertainties. Thus, this new microanalytical reference material is well suited to monitor and correct microanalytical Sr isotope analysis of low-Sr, low-REE carbonate samples.

5.2 Introduction

The analysis of geological samples with state-of-the-art analytical techniques relies on the quality and availability of well-characterised reference materials (RMs). These RMs are a prerequisite for calibration, method validation, quality control and the establishment of metrological traceability (Jochum and Enzweiler, 2014). In comparison to solution-based analytical techniques, *in-situ* analyses, such as LA-(MC-)ICP-MS or SIMS, of unknown samples is limited by the availability of suitable RMs with microhomogeneity in the range of the respective test portion masses (µg – ng range). Furthermore, for laser ablation analysis, a similar matrix composition and mass fraction of the element of interest of the RM and the unknown sample is preferable (Jochum and Enzweiler, 2014), in particular when not using femtosecond laser ablation (Poitrasson et al., 2003; Vanhaecke et al., 2010).

Strontium isotopes are widely used by the geochemical community and applied in several different research fields, such as petrology, archaeology, palaeontology, palaeoclimatology, stratigraphy as well as forensics and food-traceability (Bolea-Fernandez et al., 2016; Durante et al., 2015; Kelly et al., 2005; Kimura et al., 2013; Lin et al., 2015; Lugli et al., 2017b; Lugli et al., 2018; McArthur et al., 2012; Weber et al., 2018a; Willmes et al., 2016; Zhou et al., 2009). However, for the application of radiogenic Sr isotopes to carbonate samples, the availability of suitable microanalytical reference materials (MRMs)

for *in-situ* analyses is limited. Typical carbonate RMs with well specified $^{87}\text{Sr}/^{86}\text{Sr}$ ratios, such as JCT-1, JCp-1 (both Geological Survey of Japan), FEBS-1 (National Research Council of Canada, NRCC) and MACS-3 (U.S. Geological Survey, USGS), have a high Sr mass fraction $>1000 \mu\text{g/g}$ (Jochum et al., 2011a; Ohno and Hirata, 2007; Weber et al., 2018b; Yang et al., 2011) and are therefore mainly suited for *in-situ* analyses of carbonate samples with similar mass fractions (e.g. corals, molluscs and otoliths). USGS MACS-1 is a low-Sr carbonate RM with known Sr isotope signature, but the high mass fraction of REEs (especially Dy, Er and Yb) limits its use as an *in-situ* RM due to isobaric interferences of the doubly-charged REEs (Weber et al., 2018b). Furthermore, not all available RMs show microanalytical homogeneity and potentially need further processing, i.e. by milling protocols (Garbe-Schönberg and Müller, 2014). In contrast to glass RMs with a broad availability and a large range of different compositions (Evans and Müller, 2018; Jochum et al., 2011a; Jochum et al., 2011b), the number of available carbonate RMs below $1000 \mu\text{g/g}$ suitable for microanalytical Sr isotope analysis is limited. Especially for MC-ICP-MS systems with a narrow limitation of potential intensities on Faraday cups, RMs with similar mass fractions are necessary to use the same laser parameters for samples and RMs. This shows the need of carbonate microanalytical RMs with a relatively low Sr mass fraction for *in-situ* Sr isotope analysis of low Sr, low REE carbonates, such as speleothems. For this type of carbonates, the application of LA-MC-ICP-MS is currently either restricted to high-Sr samples (Weber et al., 2017; Wortham et al., 2017) or to solution based analysis, which requires chemical separation prior to analysis (Banner et al., 1996; Goede et al., 1998; Hori et al., 2013; Oster et al., 2014; Weber et al., 2018a; Zhou et al., 2009).

Recent progress in the synthetic production of custom-made materials and further processing of established RMs, enables the geochemical community to design very specific materials of different compositions and by different techniques (Bao et al., 2017; Garbe-Schönberg and Müller, 2014; Tabersky et al., 2014; Wu et al., 2018). One possibility is the flame spray technique, which allows production of materials with a nano-scale grain size and a customised composition and matrix for different applications. As has been shown for glass matrices (Tabersky et al., 2014), Avantama® (Switzerland) is capable of producing a synthetic material with a carbonate matrix and a specified mass fraction of the elements of interest. The aim of this study is to produce and characterise a material with a calcium carbonate matrix and a homogeneous mass fraction of Sr in the range of $500 \mu\text{g/g}$ (“NanoSr”), which can be used as matrix-matched reference material for LA-MC-ICP-MS studies of a variety of carbonate samples.

5.3 Material

Production of the carbonate nanopowder (“NanoSr”) was performed in a similar way as described by Tabersky et al. (2014). Details of the production are intellectual property of Avantama® (Switzerland) and can therefore not be provided. The synthesis of the nanoparticles was performed by the flame spray

technique using an organic precursor with the elements of interest incorporated (Athanassiou et al., 2010), resulting in a total amount of 15 g synthetic carbonate material with a specific mass fraction of Sr. Prior to all *in-situ* measurements of the carbonate nanopowder, a hydraulic press (Perkin Elmer™) was used to obtain a carbonate nanopowder pellet (~100 mg per pellet) with a diameter of 13 mm and a thickness of approximately 2 mm (Fig. 5.1 [A]) without using any additional binding material. The nanopowder was pressed for 15 minutes with a load of 5000 kg. The final nanopowder pellets were mechanically stable and glued to microscope slides for the *in-situ* analyses. In total, nine different nanopowder pellets were produced and analysed.

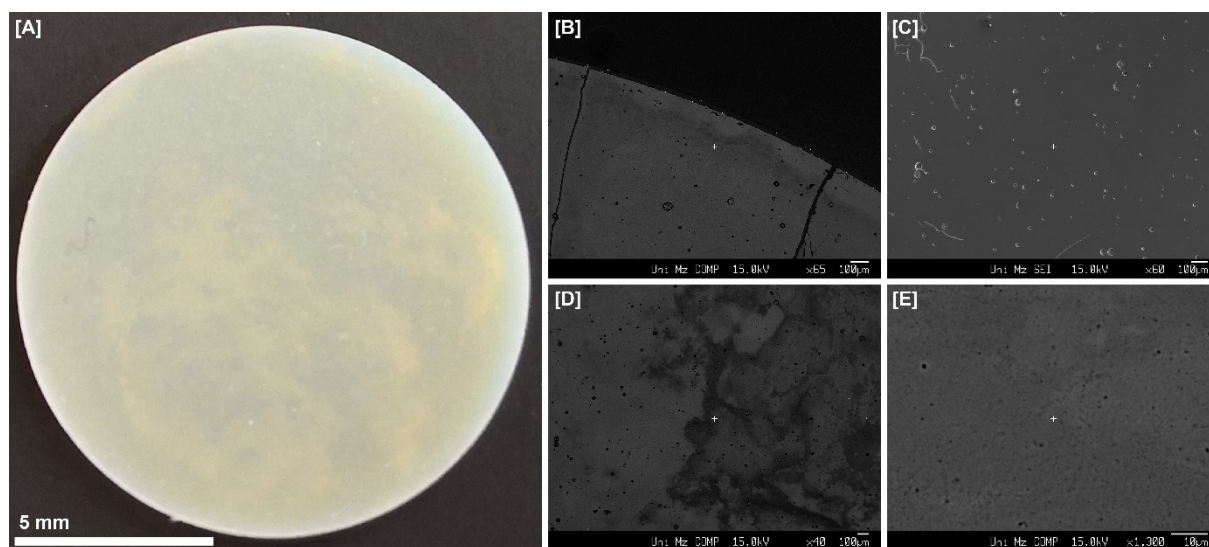


Fig. 5.1: [A] Top view of a pressed nanopowder pellet with a diameter of 13 mm and a thickness of ca. 2 mm. [B] Backscattered electron (BSE) image of the edge of the compacted nanopowder pellet. [C] Top view of the compacted nanopowder pellet as secondary electron image (SEI). [D] Top view of the compacted nanopowder pellet showing darker and brighter areas in the BSE-image. [E] BSE image of the compacted nanopowder pellet with a magnification of 1300, showing the compaction of the nanopowder and the small pore spaces below the μm -range.

5.4 Analytical techniques

To characterize the carbonate nanopowder, several analytical techniques were used. Electron microprobe analysis (EPMA) was used to determine the mass fraction of Ca. Trace element mass fractions were determined by ICP-MS and LA-ICP-MS in four different laboratories. To control the micro-homogeneity of the carbonate nanopowder, we applied LA-ICP-MS at several positions on the pressed nanopowder pellets. Since the nanopowder was specifically designed for Sr isotope analyses, we determined the $^{87}\text{Sr}/^{86}\text{Sr}$ ratio by different techniques (TIMS and (LA-)MC-ICP-MS) in three different laboratories.

5.4.1 Element mass fractions

Elemental mass fractions have been determined with three different types of instruments, both by solution based (ICP-MS) and *in-situ* techniques (EPMA and LA-ICP-MS) in five different laboratories.

5.4.1.1 Electron Microprobe

For EPMA, a sample of the pressed nanopowder pellet was embedded in epoxy resin, polished, cleaned and covered with a ~20 nm layer of carbon by sputtering. Analysis was carried out at the Institute of Geosciences, Mainz, using a Jeol JXA 8200 microprobe in wavelength-dispersive spectrometry (WDS) mode. A beam current of 12 nA and an acceleration potential of 15 kV were used, with the electron beam defocused to 20 μm . Peak counting time was 20 s for Ca in double-channel mode. Raw data were corrected using the routine of Armstrong (1995) and a well-characterised carbonate reference material was used for calibration. In total, 24 measurements at different positions of the pressed nanopowder pellet were performed.

5.4.1.2 Solution ICP-MS

Six aliquots of 5-10 mg of the carbonate nanopowder were dissolved in 3 mol/L HNO_3 . Prior to the ICP-MS measurement, final acid mass fraction was adjusted to 0.8 mol/L. Elemental analyses of the digested nanopowder were performed using a quadrupole ICP-MS (Thermo Scientific X-Series^{II}) housed at the Centro Interdipartimentale Grandi Strumenti (CIGS) of the University of Modena and Reggio Emilia. The samples were introduced into the mass spectrometer using a CETAC ASX 520 autosampler. The following mass-to-charge ratios (m/z) were measured during the session: 24, 85, 88, 138, 163, 166 and 172, representing ^{24}Mg , ^{85}Rb , ^{88}Sr , ^{138}Ba , ^{163}Dy , ^{166}Er and ^{172}Yb . A ^{115}In solution was aspirated and used as internal reference. A calibration was performed in the range 1 – 1000 ng/g using the IV-ICPMS-71A multi-element standard solution (Inorganic Ventures), whereas the less abundant elements (e.g. Eb, Dy, Er, Yb) were calibrated up to 200 ng/g.

5.4.1.3 LA-ICP-MS

Measurements by LA-ICP-MS were performed in three different laboratories. For all measurements, we employed ^{43}Ca as internal reference, and used ^{85}Rb and ^{88}Sr for the calculation of trace element mass fractions. Initial data acquisition (approximately 3 s) of each measurement was discarded to prevent surface contamination potentially influencing our results.

Measurements at the Max Planck Institute for Chemistry (MPIC), Mainz, were performed using a New Wave UP213 Nd:YAG laser ablation system, coupled to a Thermo Finnigan Element 2 SF-ICP-MS. Spot analyses were performed at a repetition rate of 10 Hz, using a spot size of 80 μm with an energy

output of 60 %, resulting in a fluence of $\sim 7.5 \text{ J/cm}^2$. Ablation time was set to 70 s. Line scan analyses were performed using a line length of 300 μm , a circular spot size of 55 μm , a repetition rate of 10 Hz, a transition speed of 5 $\mu\text{m/s}$ and an energy output of 60 %, resulting in a fluence of $\sim 5 \text{ J/cm}^2$. Background signals for spot and line scan analyses were measured for 14 s, followed by the ablation and a washout time of 20 s. The following m/z ratios were monitored during the sessions: 25, 43, 85, 88, 137, 163, 167 and 173, representing ^{25}Mg , ^{43}Ca , ^{85}Rb , ^{88}Sr , ^{137}Ba , ^{163}Dy , ^{167}Er and ^{173}Yb . For calibration purposes, NIST SRM 612 was analysed at the beginning, between each set of samples ($n = 36$) and at the end of the routine ($n = 18$). We used NIST SRM 610, USGS GSD-1G, GSE-1G and MACS-3 (each $n = 9$) as quality control materials (QCM) to monitor accuracy and reproducibility (Supplementary Table A5.1).

The trace element distribution within the nanopowder pellet was mapped by LA-ICP-MS at MPIC using MapIT! (Sforna and Lugli, 2017). The LA-ICP-MS setup was identical as described above, using NIST SRM 612 for calibration purposes and applying a total number of 66 line scans with a length of 13000 μm each, covering one half of the pressed nanopowder pellet (pellet 9). The spot size was set to 100 μm using a transition rate of 30 $\mu\text{m/s}$ and a repetition rate of 10 Hz with an energy output of 70 %, resulting in a fluence of 12.5 J/cm^2 . The following m/z ratios were monitored during the sessions: 25, 43, 85, 88 and 137. For the imaging via MapIT!, no pre-ablation was performed.

Measurements by LA-ICP-MS at the Institute of Geosciences, Mainz, were performed using an ArF Excimer 193 nm laser system (ESI NWR193) equipped with a TwoVol² ablation cell, coupled to an Agilent 7500ce ICP-MS. A spot size of 80 μm , a repetition rate of 10 Hz and a fluence of 3.5 J/cm^2 were used. 15 s laser warm-up time were followed by 60 s dwell time and 20 s washout time. NIST SRM 612 was used for calibration purposes and measured at the beginning, between the set of samples ($n = 36$) and at the end of the routine ($n = 9$). For quality control, we used NIST SRM 610, USGS GSD-1G, GSE-1G, MACS-3 and BCR-2G (supplementary Table A5.2). The following m/z ratios were monitored during the sessions: 25, 43, 85, 88, 137, 163, 167 and 173. For all laser ablation measurements performed at MPIC and at the Institute of Geosciences, mass fractions for the RMs were obtained from GeoReM (Jochum et al., 2005), and data reduction was performed off-line, following the calculations given in Mischel et al. (2017a).

LA-ICP-MS analyses at the CIGS were performed using a 213nm laser ablation system (New Wave UP) and a quadrupole ICP-MS (Thermo Scientific X-Series^{II}). The pressed nanopowder pellet (pellet 7) was analysed employing a spot size of 80 μm , a pulse repetition rate of 10 Hz and a fluence of $\sim 5 \text{ J/cm}^2$. The surface of the nanopowder pellet was pre-ablated before each spot analysis. The following m/z ratios were acquired during the session: 43, 85, 88, 163 and 172. NIST SRM 612 and GSJ Jct-1 were used as calibration materials and data reduction was performed off-line.

Operating parameters for all LA-ICP-MS measurements are presented in Table 5.1.

5.4.2 Strontium isotopes

Radiogenic Sr isotope ratios have been determined in five different laboratories, using solution based (TIMS and MC-ICP-MS) and *in-situ* techniques (LA-MC-ICP-MS).

5.4.2.1 TIMS

Strontium separation was performed using Eichrom Sr specTM ion exchange resin columns at CIGS as described for MC-ICP-MS in the next section 5.4.2.2. The Sr isotope composition of the carbonate nanopowder was determined by TIMS at the MPIC, Mainz, using a Thermo Scientific Triton. For that purpose, about 100 ng Sr was transferred onto a W filament, surrounded by a TaF activator. Measurements were performed in static multi-collection mode, simultaneously collecting m/z ratios representing ⁸⁴Sr, ⁸⁵Rb, ⁸⁶Sr, ⁸⁷Sr and ⁸⁸Sr for 10 blocks of 20 cycles each (integration time of 16.8 s per cycle). All isotope ratios were corrected for internal mass fractionation using the stable ⁸⁸Sr/⁸⁶Sr ratio of 8.375209 (Berglund and Wieser, 2011). The isobaric interference of ⁸⁷Rb on ⁸⁷Sr is corrected recording the ⁸⁵Rb peak and by using a ⁸⁷Rb/⁸⁵Rb of 0.386010. The long-term reproducibility of the international NIST SRM 987 gives a ⁸⁷Sr/⁸⁶Sr value of 0.710256 ± 0.000012 (2 SD, n = 25), in agreement with reported values in literature.

5.4.2.2 MC-ICP-MS

MC-ICP-MS measurements were performed at the CIGS and the MPIC. All samples were processed at the Laboratory of Isotope Geochemistry of the Department of Chemical and Geological Sciences (University of Modena and Reggio Emilia, Italy), following the protocol of Lugli et al. (2017b) and Weber et al. (2018b). Around 5 – 10 mg of nanopowder were digested with 3 ml of 3 mol/L HNO₃ (suprapur) and loaded into 300 µl columns filled with Eichrom Sr-specTM resin (100-150 µm bead size). Matrix ions were removed by stepwise addition of 3 mol/L HNO₃. Strontium was then eluted with MilliQ® water and collected in clean beakers. The final solutions were adjusted to 0.8 mol/L HNO₃. The entire procedure was conducted in a clean room equipped with a class 10 laminar flow hood.

To determine the ⁸⁷Sr/⁸⁶Sr ratio, a Neptune MC-ICP-MS was used at CIGS following Lugli et al. (2017b). The following m/z ratios were collected simultaneously using seven Faraday cups equipped with 10¹¹ Ω and 10¹² Ω resistors: 82, 83, 84, 85, 86, 87 and 88, representing ⁸²Kr, ⁸³Kr, ⁸⁴Sr, ⁸⁵Rb, ⁸⁶Sr, ⁸⁷Sr, ⁸⁸Sr. Strontium solutions were diluted to ~250 ng/ml and introduced into the mass spectrometer system through a quartz spray chamber using a 100 µl/min nebulizer. A static multi-collection mode with a single block of 100 cycles (integration time 8.4 s per cycle) was used to analyse the samples, as well as NIST SRM 987 and blanks. A bracketing sequence was employed to correct for instrumental drifts. Krypton as a potential contamination in the Ar gas was monitored and corrected using a ⁸⁶Kr/⁸³Kr ratio of 1.505657 (Berglund and Wieser, 2011). To correct for the presence of isobaric Rb on m/z 87, a

$^{87}\text{Rb}/^{85}\text{Rb}$ ratio of 0.3856656 (Berglund and Wieser, 2011) was used. Mass bias normalization was performed applying the exponential law, using the accepted $^{88}\text{Sr}/^{86}\text{Sr}$ ratio of 8.375209 (Steiger and Jäger, 1977). We are aware of the of the observed natural variations in $\delta^{88}\text{Sr}$ (Fietzke and Eisenhauer, 2006; Krabbenhöft et al., 2009), however, by convention, radiogenic Sr isotope measurements are usually corrected assuming the stable $^{88}\text{Sr}/^{86}\text{Sr}$ ratio (Fietzke et al., 2008), which we follow within this study. In addition, variability in $^{87}\text{Sr}/^{86}\text{Sr}$ is far bigger than the whole range reported for stable Sr isotopes ratios in literature. Rubidium mass bias was assumed to be the same as for Sr. Daily repeated measurements of NIST SRM 987 yielded a mean $^{87}\text{Sr}/^{86}\text{Sr}$ ratio of 0.71024 ± 0.00001 (2 SD; $n = 20$). Strontium isotope ratios of the samples were corrected to the NIST SRM 987 $^{87}\text{Sr}/^{86}\text{Sr}$ ratio of 0.710248 (McArthur et al., 2001).

Sr isotope ratios at the MPIC were determined using a Nu Plasma MC-ICP-MS coupled to a CETAC Aridus II desolvating nebulizer system, following the methods described by Lugli et al. (2017b). Samples were diluted to ~ 100 ng/ml, and signals of the following m/z ratios were monitored using Faraday cups equipped with 10^{11} Ω resistors during analysis: 82, 83, 84, 85, 86, 87 and 88. Analysis was performed in a standard bracketing sequence, using a static multi-collection mode with 100 cycles and an integration time of 5 s. Krypton and Rb correction was performed as described for the measurements at CIGS. Repeated measurements of NIST SRM 987 yielded a mean $^{87}\text{Sr}/^{86}\text{Sr}$ ratio of 0.71030 ± 0.00003 (2 SD; $n = 10$). Resulting $^{87}\text{Sr}/^{86}\text{Sr}$ ratios were corrected to the NIST SRM 987 $^{87}\text{Sr}/^{86}\text{Sr}$ ratio of 0.710248 (McArthur et al., 2001).

5.4.2.3 LA-MC-ICP-MS

Microanalytical homogeneity for Sr isotopes was investigated using LA-MC-ICP-MS at the MPIC and the CIGS. Operational parameter for both (LA-)MC-ICP-MS system are provided in Table 5.1. Analyses at the MPIC were performed following the protocol of Weber et al. (2017) using a Nu Plasma MC-ICP-MS coupled to a New Wave UP213 Nd:YAG laser ablation system. Peak shape and coincidence of the Sr isotopes of interest (^{84}Sr , ^{86}Sr , ^{87}Sr , ^{88}Sr) were tuned using the Sr reference solution NIST SRM 987, while the mass spectrometer was coupled to a CETAC Aridus II desolvating nebulizer system, prior to connecting the laser ablation system. For the laser ablation measurements, line scans of 750 μm length with a spot size of 100 μm , a translation speed of 5 $\mu\text{m}/\text{s}$ and an energy output of 80 % were applied, resulting in a fluence of 20 – 25 J/cm^2 . Pre-ablation was performed prior to each analysis. Krypton was corrected by subtracting the on-peak baseline during the laser warm-up time (45 s). Interferences of REEs were corrected by monitoring ^{171}Yb and ^{167}Er . Molecular interferences were found to be negligible by monitoring m/z 82 and 83 (signals usually below 0.2 mV). Mass bias correction was performed using the exponential law (Ingle et al., 2003) and an $^{88}\text{Sr}/^{86}\text{Sr}$ ratio of 8.375209 (Steiger and Jäger, 1977). Mass/charge 85 was used to monitor the occurrence of ^{85}Rb and to correct m/z 87 by

calculating the fraction of ^{87}Rb using the constant $^{87}\text{Rb}/^{85}\text{Rb}$ ratio of 0.3857 (Berglund and Wieser, 2011).

Analyses at the CIGS were performed using a Neptune MC-ICP-MS coupled to a New Wave UP213 Nd:YAG laser ablation system, following the method described by Lugli et al. (2017b). Nine Faraday detectors equipped with $10^{11}\Omega$ and $10^{12}\Omega$ resistors were employed to acquire peaks of the m/z ratios 82, 83, 84, 85, 86, 87 and 88, as well as the doubly-charged $^{171}\text{Yb}^{2+}$ on m/z 85.5 and $^{173}\text{Yb}^{2+}$ on m/z 86.5. For the LA measurements, we employed a linear raster of $100 \times 500 \mu\text{m}$, a fluence of $\sim 6 \text{ J/cm}^2$, a repetition rate of 10 Hz and a scan speed of $5 \mu\text{m/s}$. Prior to each analysis, the sample was pre-ablated to avoid surface contaminations. A He flow of ca. 0.6 L/min was used to carry the ablated material into the mass spectrometer. Krypton was corrected by subtracting the on-peak baseline during the laser warm-up ($\sim 60 \text{ s}$). REEs and Ca dimers/argides were monitored, but not corrected because their interference with the analyses is negligible. Mass bias and Rb were corrected as previously reported for the measurements performed at the MPIC. During the analytical session, we also measured a modern marine bivalve shell as an in-house reference material, which yielded an $^{87}\text{Sr}/^{86}\text{Sr}$ ratio of 0.70916 ± 0.00002 (2SE, $n = 1$), in agreement with the modern seawater value (McArthur et al., 2012).

5.5 Results

The analytical results obtained for NanoSr are presented in the following for the Ca and the trace element mass fraction, as well as for the Sr isotope composition.

5.5.1 Calcium mass fractions

EPMA analysis yielded a CaO %m/m of 52.6 ± 1.5 ($n = 24$, 2 SD, pellet 8), equivalent to a Ca mass fraction of $376000 \pm 11000 \mu\text{g/g}$ ($n = 24$, 2 SD, pellet 8). These analyses were performed at different positions of the pressed nanopowder pellet, both in the brighter and darker areas (Fig. 5.1 [D]) and did not yield significantly different results. The overall uncertainty of the Ca mass fraction obtained by EPMA is about 3 % and therefore in a similar range as expected for the (LA-)ICP-MS analyses. Therefore, we used the resulting Ca mass fraction of $376000 \pm 11000 \mu\text{g/g}$ ($n = 24$, 2 SD) for the internal reference for the calibration of the trace element analyses.

Table 5.1: Operational parameters for the different (LA-MC-)ICP-MS systems used during this study.

	ICP parameters	Values	Laser parameters*	Values	ICP parameters	Values	Laser parameters*	Values				
Sr isotopes	MC-ICP-MS Neptune		New Wave UP 213		MC-ICP-MS NU Plasma		New Wave UP 213					
		Cool gas flow rate	15 L/min	<i>Ablation</i> Spot size	100 µm		Cool gas flow rate	13 L/min	<i>Ablation</i> Spot size	100 µm		
		Auxiliary gas flow	0.8 L/min		Repetition rate	10 Hz		Auxiliary gas flow	0.93 L/min		Repetition rate	10 Hz
		Sample gas flow	0.9 - 1 L/min		Fluence	6 J/cm ²		Sample gas flow	0.75 L/min		Fluence	20 - 25 J/cm ²
		Plasma power	1200 W		Sampling scheme	Line		Plasma power	1300 W		Sampling scheme	Line
		Resolution	Low		Translation rate	5 µm/s		Resolution	Low		Translation rate	5 µm/s
		He flow rate*	0.6 L/min					He flow rate*	0.75 L/min			
Trace elements	ICP-MS Element 2		New Wave UP 213		ICP-MS Agilent 7500ce		ESI NWR193					
		Cool gas flow rate	16 L/min	<i>Ablation</i> Spot size	55/80/100 µm		Cool gas flow rate	15 L/min	<i>Ablation</i> Spot size	80 µm		
		Auxiliary gas flow	1 L/min		Repetition rate	10 Hz		Auxiliary gas flow	0.9 L/min		Repetition rate	10 Hz
		Sample gas flow	0.6 L/min		Fluence	5 - 12.5 J/cm ²		Sample gas flow	0.8 L/min		Fluence	3.5 J/cm ²
		Plasma power	1150 W		Sampling scheme	Spot/Line		Plasma power	1200 W		Sampling scheme	Spot
		Resolution	Low		Dwell time	70 s		Resolution	0.65 - 0.75**		Dwell time	60 s
		He flow rate*	0.75 L/min		Translation speed	5/30 µm/s		He flow rate*	0.8 L/min			
		ICP-MS X-Series^{II}		New Wave UP 213								
		Cool gas flow rate	13 L/min	<i>Ablation</i> Spot size	100 µm							
		Auxiliary gas flow	1.08 L/min		Repetition rate	10 Hz						
		Sample gas flow	0.75 L/min		Fluence	5 J/cm ²						
		Plasma power	1400 W		Sampling scheme	Spot						
		Resolution	Low		Dwell time	60 s						
		He flow rate*	0.6 L/min									

*only for laser ablation measurements, ** (amu), peak width at 10 % of its height.

5.5.2 Mass fractions of Sr and potential interfering elements

Solution-based ICP-MS yielded an average Sr mass fraction of $495 \pm 51 \mu\text{g/g}$ ($n = 6$, 2 SD) for NanoSr. Analyses of potential interfering materials resulted in average mass fractions $<0.2 \mu\text{g/g}$ (Fig. 5.2). Rubidium, as a major potential isobaric interference for *in-situ* Sr isotope analyses yielded an average mass fraction of $0.075 \pm 0.036 \mu\text{g/g}$ ($n = 6$, 2 SD). This results in a maximum Rb/Sr ratio of 0.0002, much lower than the suggested Rb/Sr threshold of 0.02 for successful LA-(MC-)ICP-MS measurements of Sr isotopes (Irrgeher et al., 2016). Further potential interfering elements yielded very low mass fractions (Dy = $0.16 \pm 0.04 \mu\text{g/g}$; Er = $0.02 \pm 0.04 \mu\text{g/g}$; Yb = $0.05 \pm 0.04 \mu\text{g/g}$, all uncertainties (2 SD) are for $n = 6$) and are thus considered to be negligible for *in-situ* Sr isotope measurements, as has been shown for reference materials with a higher mass fraction of these elements (Weber et al., 2018b).

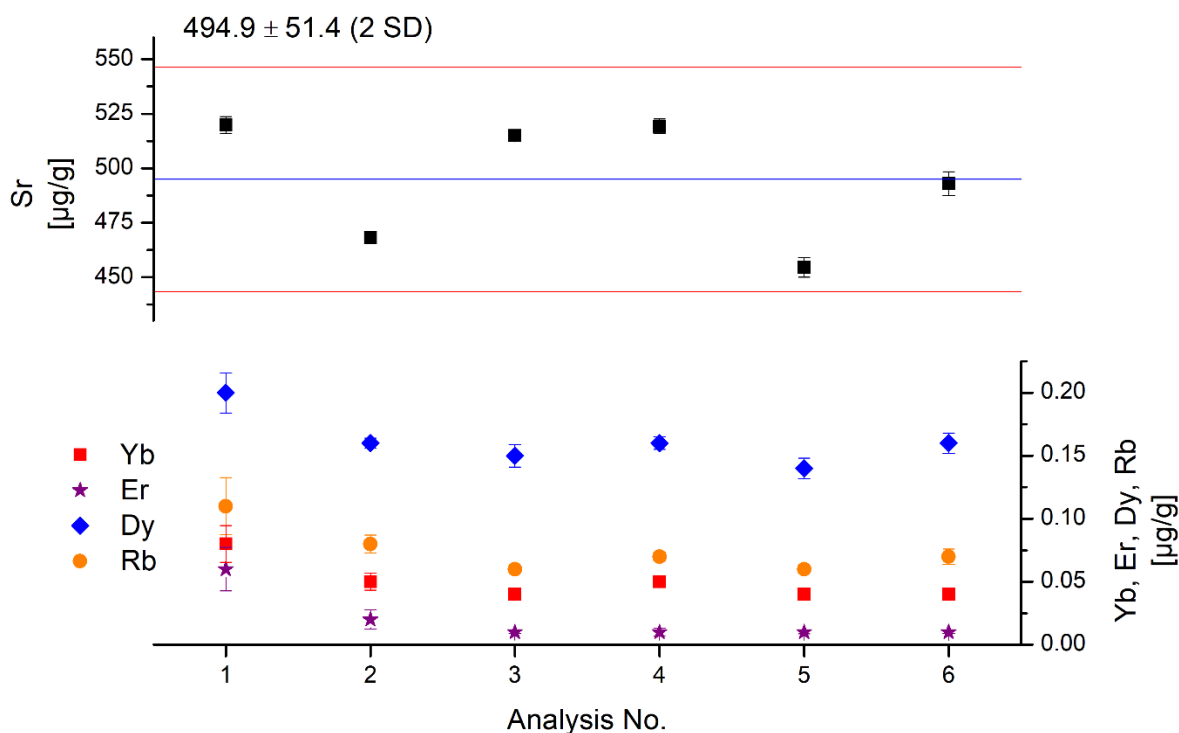


Fig. 5.2: Solution-based ICP-MS results for the mass fractions of Sr (black square, top graph) and Yb (red square), Er (purple star), Dy (blue diamond) and Rb (orange circle, bottom graph) for digestion of six samples. The blue line represents the average mass fraction of Sr ($495 \pm 51 \mu\text{g/g}$, $n = 6$) with the respective 2 SD uncertainties expressed as red lines. All uncertainties in the bottom panel are 2 SD.

Mass fractions of Sr and Rb were determined by LA-ICP-MS in three different laboratories as described above. The results are shown in Fig. 5.3. Analyses from the Institute of Geosciences, Mainz (Fig. 5.3 [A]), yielded an average mass fraction of $484 \pm 12 \mu\text{g/g}$ for Sr and of $0.05 \pm 0.02 \mu\text{g/g}$ for Rb ($n = 72$, 2 SD, pellets 1 – 6, for both Sr and Rb). Results from CIGS (Fig. 5.3 [B]), show average mass fractions

of $502 \pm 8 \mu\text{g/g}$ for Sr and $0.05 \pm 0.02 \mu\text{g/g}$ for Rb (both $n = 5$, 2 SD, pellet 7) and are in good agreement with the results from the Institute of Geosciences, Mainz. Analyses at MPIC, have been performed by spot (Fig. 5.3 [C]) and line scan analyses (Fig. 5.3 [D]). Spot analyses yielded an average mass fraction of $505 \pm 12 \mu\text{g/g}$ for Sr and $0.071 \pm 0.005 \mu\text{g/g}$ for Rb (both $n = 72$, 2 SD, pellets 1 – 6), while line scan analyses resulted in an average mass fraction of $479 \pm 26 \mu\text{g/g}$ for Sr and $0.06 \pm 0.01 \mu\text{g/g}$ for Rb (both $n = 18$, 2 SD). An overview of the mass fractions of the elements of interest determined by the different analytical techniques is provided in Table 5.2. Barium ($<0.20 \pm 0.03 \mu\text{g/g}$) mass fraction is provided to indicate the purity of the carbonate material. All laser ablation analyses performed in this study are in agreement with the results obtained by solution ICP-MS within uncertainty.

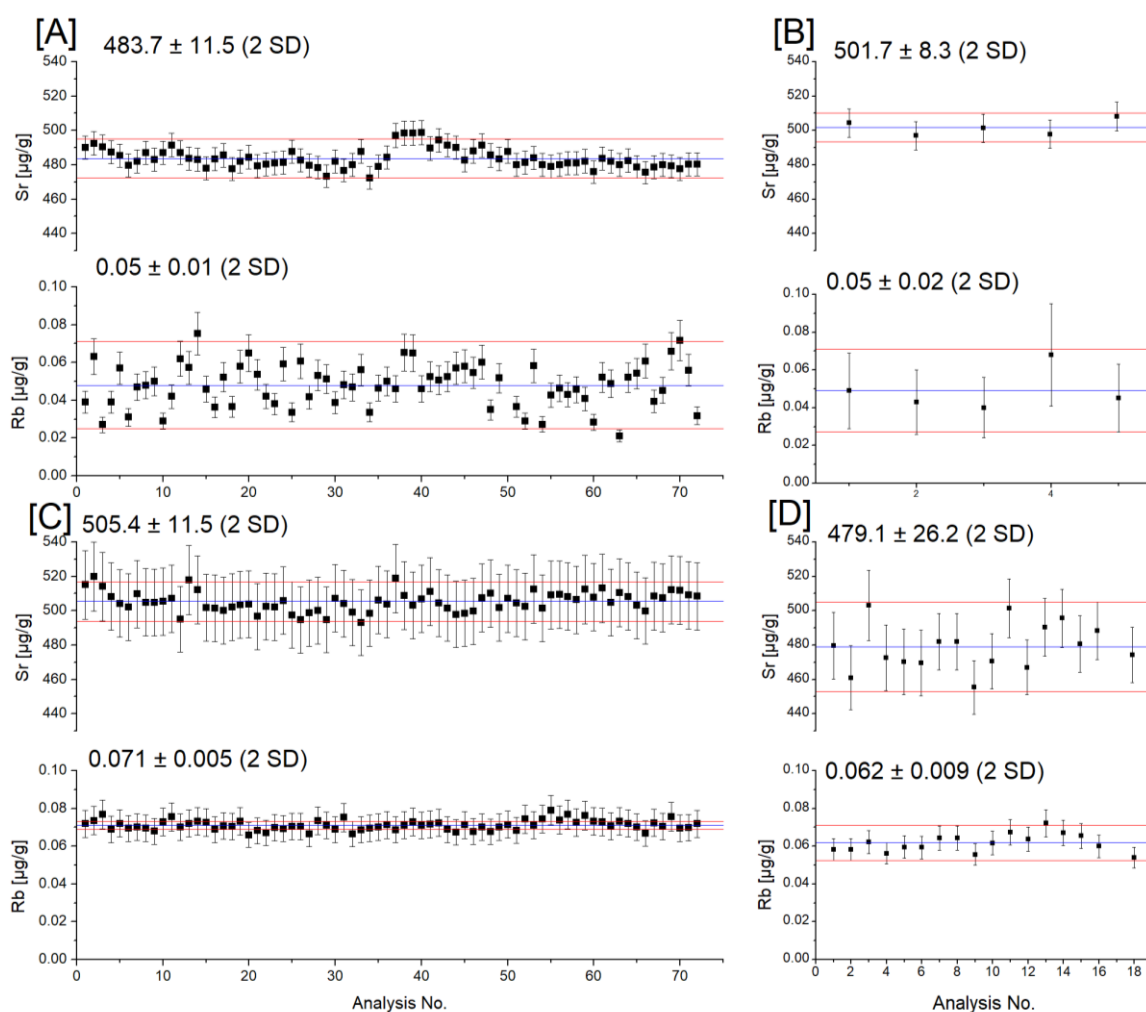


Fig. 5.3: LA-ICP-MS results obtained in different laboratories. In total, seven different nanopowder pellets were analysed. [A] Strontium and Rb mass fractions obtained at the Institute of Geosciences, Mainz ($n = 72$, pellet 1 – 6). [B] Strontium and Rb mass fractions obtained at the CIGS, Modena ($n = 5$, pellet 7). [C] Strontium and Rb mass fractions obtained at MPIC, Mainz by spot ($n = 72$, pellet 1 – 6) and [D] line scan analyses ($n = 18$, pellet 1). The blue line represents the average mass fractions for Sr

and Rb with the respective 2 SD uncertainties expressed as red lines. All uncertainties of single measurements are 1 SD.

Table 5.2: Mass fractions of Mg, Rb, Sr, Ba, Dy, Er and Yb, as well as respective test portion mass for the different analytical techniques. Typical RSF (relative sensitivity factor) values for carbonate reference materials used during data acquisition usually agree within 10 % uncertainty with the GeoReM values (Jochum et al., 2005) for all presented elements (supplementary Tables A5.1 and A5.2). 1 = Institute of Geosciences, Mainz; 2 = CIGS, Modena; 3 = MPIC, Mainz; NA = not available, b.d.l. = below detection limit.

	Mg [$\mu\text{g/g}$]	Rb [$\mu\text{g/g}$]	Sr [$\mu\text{g/g}$]	Ba [$\mu\text{g/g}$]	Dy [$\mu\text{g/g}$]	Er [$\mu\text{g/g}$]	Yb [$\mu\text{g/g}$]	Test portion mass [μg]
LA-ICP-MS ¹ Spot analysis	2.7 ± 0.4	0.05 ± 0.02	483.7 ± 11.5	b.d.l.	0.13 ± 0.03	b.d.l.	b.d.l.	0.8 - 1.0
LA-ICP-MS ² Spot analysis	NA	0.05 ± 0.02	501.7 ± 8.3	0.17 ± 0.06	0.20 ± 0.02	NA	0.05 ± 0.02	1.5 - 2.0
ICP-MS ² bulk	NA	0.08 ± 0.02	494.9 ± 51.4	0.21 ± 0.05	0.16 ± 0.02	0.02 ± 0.02	0.05 ± 0.02	5000 - 10000
LA-ICP-MS ³ Spot analysis	3.1 ± 0.2	0.07 ± 0.01	505.4 ± 11.5	0.18 ± 0.04	0.18 ± 0.01	0.004 ± 0.002	0.04 ± 0.01	1.5 - 2.0
LA-ICP-MS ³ Line scan	3.0 ± 0.5	0.06 ± 0.01	479.1 ± 26.2	0.17 ± 0.04	0.20 ± 0.03	0.004 ± 0.010	0.05 ± 0.02	0.4 - 0.5

5.5.3 Trace element imaging

The results from the imaging using MapIT! are presented in Fig. 5.4. The mass fraction of Sr is between 450 and 500 $\mu\text{g/g}$, does not show any significant variability and is thus homogeneously distributed across the pressed nanopowder pellet (pellet 9). Individual pixels however resulted in substantially higher values, which might be related to a heterogeneous distribution but is considered more likely to be caused by instrumental artefacts. Rubidium as a major potential interference for *in-situ* analyses of Sr isotopes only has a low mass fraction (<0.2 $\mu\text{g/g}$), although yielding higher values than obtained by the other methods (Table 5.2 and Fig. 5.3). However, the Rb mass fraction is still sufficiently low to not affect the Sr isotope measurements significantly (Irrgeher et al., 2016). Magnesium and Ba are usually minor components of carbonate materials and were therefore monitored for the NanoSr pellet. Barium does not show substantial variability and is generally below 0.2 $\mu\text{g/g}$. Magnesium, in contrast, exhibits areas of higher mass fraction, especially at the edge of the nanopowder pellet, which were caused by spikes in the data and are therefore considered as an artefact. No pre-ablation was performed prior to the mapping, so either Mg contained in the glue, molecular ions (e.g. C₂ with $m/z = 24$) from organic components in the glue, or Mg contamination during the production/post-production processes. In general, the Mg mass fraction is low (<5 $\mu\text{g/g}$) and is unlikely to affect Sr isotope analysis, even if Mg is not entirely homogeneous within the nanopowder pellet. All imaged element mass fractions are in

reasonable agreement with the conventional element mass fractions obtained by (LA-)ICP-MS, although showing some general noise in the element distribution, which is usually common for mapping techniques (Sforna and Lugli, 2017).

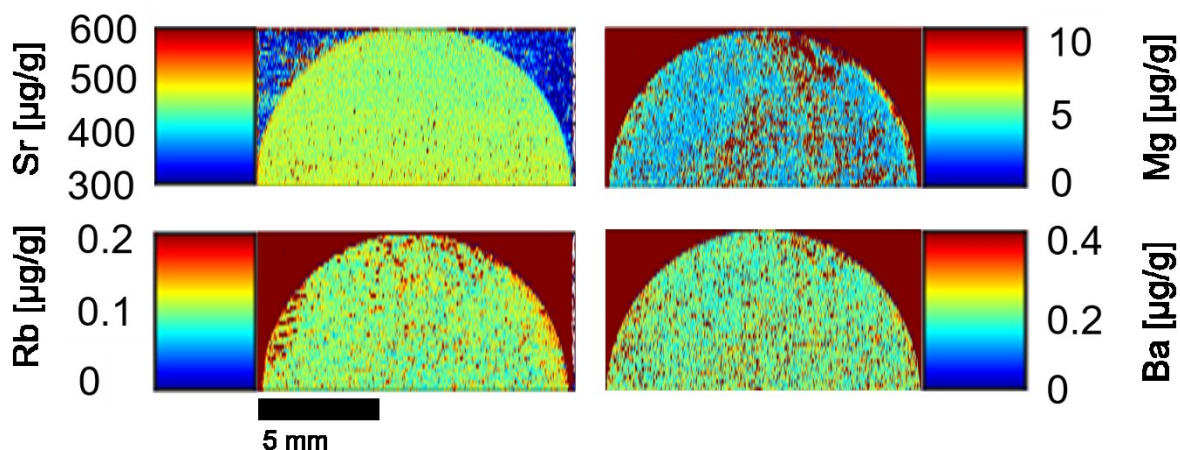


Fig. 5.4: Element distribution for Sr (top left), Rb (bottom left), Mg (top right) and Ba (bottom right) of the pressed nanopowder pellet (pellet 9) obtained with the MapIT! software (Sforna and Lugli, 2017). The upper half of the nanopowder pellet was analysed. The length of the x-axis is 13 mm (diameter of the pellet) and the y-distance 6.6 mm for each image obtained.

5.5.4 Solution Sr isotope analyses

The $^{87}\text{Sr}/^{86}\text{Sr}$ ratio determined by TIMS yielded in average 0.707563 ± 0.000009 (2 SD, $n = 6$), which is in agreement with both MC-ICP-MS analyses (Table 5.3). The $^{84}\text{Sr}/^{86}\text{Sr}$ ratio obtained by TIMS yielded an average ratio of 0.056493 ± 0.000003 (2 SD, $n = 6$). Strontium isotope analyses at CIGS yielded an average $^{87}\text{Sr}/^{86}\text{Sr}$ ratio of 0.70755 ± 0.00001 (2 SD, $n = 19$) and an average $^{84}\text{Sr}/^{86}\text{Sr}$ ratio of 0.05648 ± 0.00001 (2 SD, $n = 19$, Fig. 5.5A). A pressed nanopowder pellet was dissolved to monitor potential contamination during the nanopowder pellet production. The results for this nanopowder pellet agree with the other samples, both for $^{87}\text{Sr}/^{86}\text{Sr}$ (0.70755 ± 0.00001 , 2 SE) and for $^{84}\text{Sr}/^{86}\text{Sr}$ (0.056488 ± 0.000002 , 2 SE, Fig. 5.5A grey square). Sr isotope ratios determined at the MPIC agree within uncertainty with the data obtained at CIGS. The average $^{87}\text{Sr}/^{86}\text{Sr}$ ratio is 0.70756 ± 0.00004 (2 SD, $n = 21$), and the average $^{84}\text{Sr}/^{86}\text{Sr}$ ratio is 0.05648 ± 0.00010 (2 SD, $n = 21$, Fig. 5.5B). Again, the analysis of the previously pressed sample did not significantly deviate from the other measurements for $^{87}\text{Sr}/^{86}\text{Sr}$ (0.70758 ± 0.00002 , 2 SE) and $^{84}\text{Sr}/^{86}\text{Sr}$ (0.056535 ± 0.000010 , 2 SE, Fig. 5.5B grey square). Analyses performed with the Neptune MC-ICP-MS show a better reproducibility than those obtained with the Nu MC-ICP-MS at MPIC for both $^{87}\text{Sr}/^{86}\text{Sr}$ and $^{84}\text{Sr}/^{86}\text{Sr}$. This is most likely related to the higher sensitivity of the Neptune system and does not represent inhomogeneity of the NanoSr powder. In summary, all

solution-based techniques yielded the same results for the $^{87}\text{Sr}/^{86}\text{Sr}$ ratio of the NanoSr with an average ratio of 0.70756 ± 0.00003 (2 SD, $n = 46$).

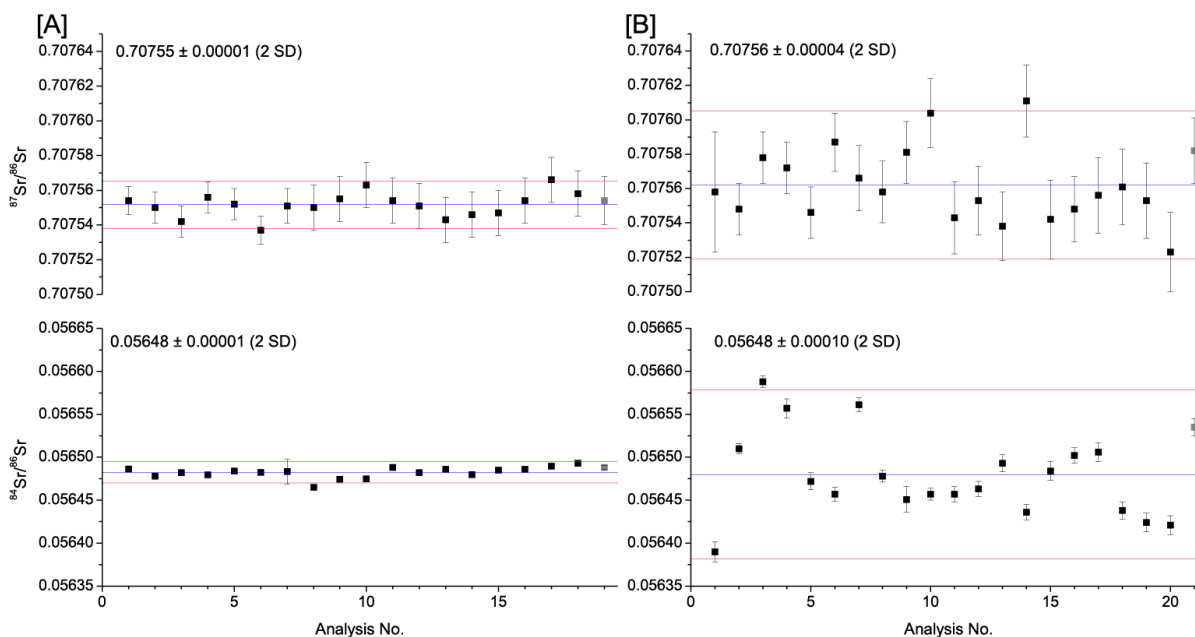


Fig. 5.5: [A] MC-ICP-MS Neptune data from CIGS ($n = 19$). [B] MC-ICP-MS Nu Plasma data from MPIC ($n = 21$). Black squares represent the $^{87}\text{Sr}/^{86}\text{Sr}$ and $^{84}\text{Sr}/^{86}\text{Sr}$ ratios, respectively, of the individual measurements. Blue lines show the average ratios with the corresponding 2 SD uncertainties as red lines. The grey square represents the results from the pressed nanopowder pellet, which was dissolved for solution analysis.

5.5.5 Laser ablation Sr isotope analyses

Laser ablation Sr isotope analyses were performed at two different laboratories to validate the microhomogeneity of the carbonate nanopowder in terms of Sr isotope signature. The $^{87}\text{Sr}/^{86}\text{Sr}$ ratios as well as the $^{84}\text{Sr}/^{86}\text{Sr}$ ratios showed a greater variability in comparison to the solution data. However, the $^{87}\text{Sr}/^{86}\text{Sr}$ ratio agree within uncertainty with the solution data with an average ratio of 0.70753 ± 0.00007 (2 SD, $n = 58$, Fig. 5.6A, pellets 1 – 6) for the analyses at the MPIC, and an average ratio 0.70757 ± 0.00006 (2 SD, $n = 10$, Fig. 5.6B, pellet 7) for the analyses at the CIGS. The average $^{84}\text{Sr}/^{86}\text{Sr}$ at MPIC was 0.05617 ± 0.00024 (2 SD, $n = 58$, Fig. 5.6A, pellets 1 – 6). The $^{84}\text{Sr}/^{86}\text{Sr}$ ratios obtained at CIGS were significantly higher and agree with the natural ratio with an average ratio of 0.05656 ± 0.00012 (2 SD, $n = 10$, Fig. 5.6B, pellet 7). Again, the analyses performed with the Neptune system show a better reproducibility than those performed with the Nu MC-ICP-MS system. To allow traceability of the obtained dataset, three international microanalytical carbonate RMs (JcT-1, JcP-1 and MACS-3) were analysed at MPIC using the same instrumentation and methodology. All $^{87}\text{Sr}/^{86}\text{Sr}$ ratios of the analysed RMs are within the expected literature values (see Weber et al. (2018b) and references therein), yielding

Sr isotope ratios of $^{87}\text{Sr}/^{86}\text{Sr} = 0.70918 \pm 0.00008$ and $^{84}\text{Sr}/^{86}\text{Sr} = 0.05635 \pm 0.00006$ for JcT-1 (2 SD, n = 10), $^{87}\text{Sr}/^{86}\text{Sr} = 0.70917 \pm 0.00007$ and $^{84}\text{Sr}/^{86}\text{Sr} = 0.05603 \pm 0.00006$ for JcP-1 (2 SD, n = 10) and $^{87}\text{Sr}/^{86}\text{Sr} = 0.70757 \pm 0.00004$ and $^{84}\text{Sr}/^{86}\text{Sr} = 0.05637 \pm 0.00007$ for MACS-3 (2 SD, n = 10).

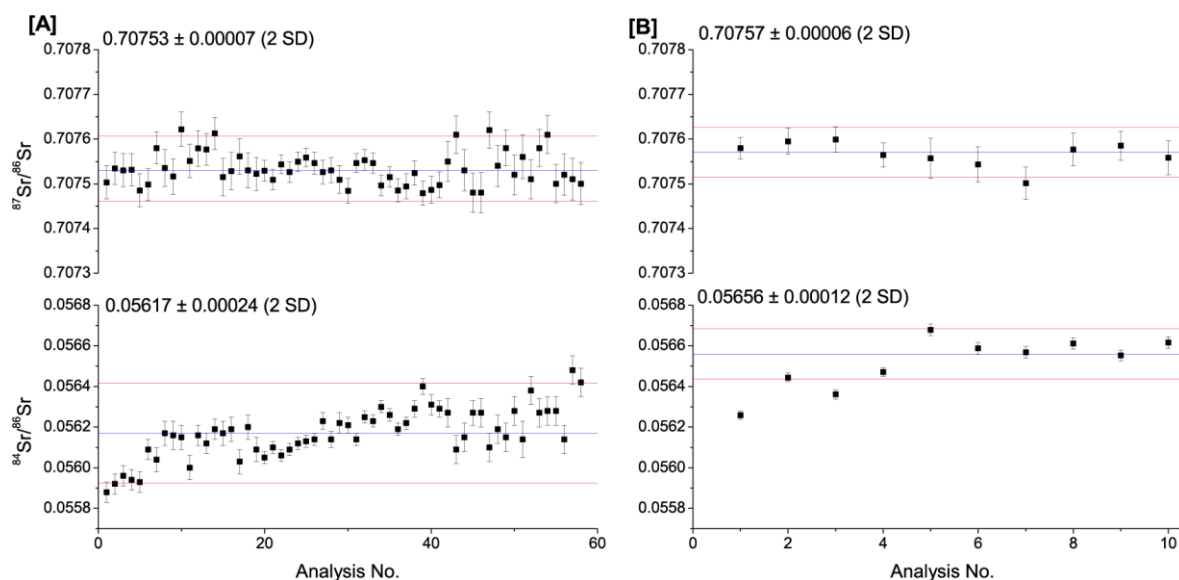


Fig. 5.6: Laser ablation MC-ICP-MS data obtained at the MPIC, Mainz [A] (pellets 1 – 6), and the CIGS [B] (pellet 7). The $^{87}\text{Sr}/^{86}\text{Sr}$ as well as the $^{84}\text{Sr}/^{86}\text{Sr}$ ratio of the individual measurements (black squares) are shown as well as the average ratio (blue line) and the respective 2 SD uncertainties (red lines).

5.6 Discussion

For any MRMs, the homogeneity is a fundamental requirement. This should be true for element and isotope composition in case the MRM is used for *in-situ* isotope studies, independent on the typical test portion mass used for analysis (Kane et al., 2003). We therefore used techniques with different test portion masses, i.e. solution based vs. laser ablation, to test homogeneity on the ng - μg range and check if potential inhomogeneity in this range can significantly influence the resulting $^{87}\text{Sr}/^{86}\text{Sr}$ ratios obtained by LA-MC-ICP-MS.

5.6.1 Element mass fraction

The Ca mass fraction was determined by EPMA in both the darker and brighter areas of the compacted nanopowder pellet (Fig. 5.1 [D]) and yielded an average value of $376000 \pm 11000 \mu\text{g/g}$ (n = 24, 2 SD, pellet 8) and did not show significant differences. As shown in Fig. 5.1 [E], the pore space of the pressed nanopowder pellet is less than $1 \mu\text{m}$, indicating a well-compacted material, which is a prerequisite for microhomogeneity.

Solution analysis of the synthetic carbonate nanopowder revealed an average Sr mass fraction of $495 \pm 51 \mu\text{g/g}$ (2 SD). *In-situ* analyses at different laboratories revealed Sr mass fraction of the nanopowder pellet ranging from $479 \pm 26 \mu\text{g/g}$ to $505 \pm 20 \mu\text{g/g}$. However, all laser ablation results lie within the uncertainty range of each other and the solution measurements. Furthermore, the variability during one day of measurement and within one laboratory did not exceed the 2 SD uncertainty of the bulk analysis. The imaging of the nanopowder pellet also showed minor Sr variability in the 2 SD range of the conventional LA-ICP-MS analysis, implying that the material is suitable for microanalysis. The small differences between the different laboratories could be caused by the different ablation conditions, calibration strategies and instruments used for this study, as has been recently shown for several common glass and carbonate RMs (Evans and Müller, 2018).

The average Sr mass fraction of the new synthetic carbonate reference material is $495 \pm 51 \mu\text{g/g}$, which was the overall aim prior to production. Since the material is mainly intended for *in-situ* Sr isotope studies, a variability of the element mass fraction in the range observed in this study is not expected to affect the intended use. Potential interfering elements, such as Rb and the REEs, were not found to be incorporated in the nanopowder at significant levels. The Rb mass fraction was found to be $<0.2 \mu\text{g/g}$ and the mathematical correction does thus not impose a substantial limitation for the application for *in-situ* Sr isotope studies. Imaging of the Rb distribution in the nanopowder pellet neither revealed areas of significantly higher mass fraction. REE mass fractions were determined by solution ICP-MS and are of minor concern. Therefore, doubly-charged REEs, which would potentially hamper the quality of the results, are not expected to affect Sr isotope ratio measurements. Neither during material production nor during the preparation of a nanopowder pellet, a significant contamination with any other relevant element occurred.

5.6.2 Strontium isotope composition

The primary aim for producing the new NanoSr as MRM was to create a material for matrix-matched calibration of *in-situ* Sr isotope analyses of carbonate samples with low Sr abundance. Therefore, it is highly important to precisely characterise the Sr isotope signature of this material. In this study, the material was analysed in five different laboratories using TIMS, two different MC-ICP-MS and two different LA-MC-ICP-MS systems. All Sr isotope measurements yield identical results within uncertainty. We further analysed a sample, which was previously pressed as a nanopowder pellet and then dissolved for the solution analysis to investigate the potential contamination during pellet production. The results of these measurements do agree with the overall average Sr isotope ratio. Therefore, we define a Sr isotope ratio of 0.70756 ± 0.00003 (2 SD, $n = 46$) for NanoSr (Table 5.3).

Table 5.3: $^{87}\text{Sr}/^{86}\text{Sr}$ and $^{84}\text{Sr}/^{86}\text{Sr}$ ratios for the different analytical techniques with the respective test portion masses of the measurements. The resulting $^{87}\text{Sr}/^{86}\text{Sr}$ ratio for NanoSr is the mean of all solution-based measurements. *The test portion mass for the solution based analyses take the total amount of samples material into account, which was dissolved and homogenised for each aliquot. The actual Sr amount used for the measurements are usually much smaller, i.e. 100 ng for TIMS and 50 – 500 ng for MC-ICP-MS, depending on the analysis time and used mass fraction for analysis. All uncertainties are given as 2 SD. In addition, we provide the mean $^{87}\text{Sr}/^{86}\text{Sr}$ ratio based on a 95 % confidence level (CL). 1 = MPIC, Mainz, 2 = CIGS, Modena; NA = not available.

	$^{87}\text{Sr}/^{86}\text{Sr}$	$^{84}\text{Sr}/^{86}\text{Sr}$	Test portion mass* [μg]
TIMS ¹ , n = 6	0.70756 ± 0.00001	0.056493 ± 0.000003	2500 - 5000
MC-ICP-MS ¹ , n = 21	0.70756 ± 0.00004	0.05648 ± 0.00010	2500 - 5000
MC-ICP-MS ² , n = 19	0.70755 ± 0.00001	0.05648 ± 0.00001	2500 - 5000
LA-MC-ICP-MS ¹ , n = 58	0.70753 ± 0.00007	0.05617 ± 0.00024	2 - 3
LA-MC-ICP-MS ² , n = 10	0.70757 ± 0.00006	0.05656 ± 0.00012	2 - 3
NanoSr, 2 SD, n = 46	0.70756 ± 0.00003		
NanoSr, 95% CL, n = 46	0.707558 ± 0.000009		

Although the solution analyses yielded, within uncertainty, the same average ratio as the LA-ICP-MS method, the large test portion masses of the solution-based analyses are not considering potential inhomogeneities in the μg -range, which is usually the test portion mass for *in-situ* analyses. Therefore, the analysis by LA-MC-ICP-MS is necessary to assess homogeneity at a scale of 10s of μm . Individual measurements from the LA-MC-ICP-MS measurements at MPIC yielded results for the $^{87}\text{Sr}/^{86}\text{Sr}$ isotope ratios with small deviations in comparison with the average solution ratio. Cross-checking with deviations in the $^{84}\text{Sr}/^{86}\text{Sr}$ ratio, as suggested by Müller and Anczkiewicz (2016), did not show an obvious correlation between a bias in $^{87}\text{Sr}/^{86}\text{Sr}$ and an elevated or reduced $^{84}\text{Sr}/^{86}\text{Sr}$ ratio, although the $^{84}\text{Sr}/^{86}\text{Sr}$ ratios of the LA-MC-ICP-MS analyses performed at MPIC are lower than expected from the naturally invariant ratio. The trend in $^{84}\text{Sr}/^{86}\text{Sr}$ during both LA-MC-ICP-MS measurements (Fig. 5.6) shows furthermore no relation to the formation of Ca argides/dimers, since monitoring of m/z 83 and 82 did not show a significant increase between the gas-blank period and during the ablation. In addition, the measurements were randomly distributed on different nanopowder pellets (pellets 1 – 6 for MPIC and pellet 7 for CIGS). Due to the solely use of $10^{11} \Omega$ resistors, a more precise monitoring of the small signals observed at m/z 83 and 82 was not possible to potentially detect small changes in Ca argide/dimer formation rate. Both LA-MC-ICP-MS setups, however, yielded individual and average $^{87}\text{Sr}/^{86}\text{Sr}$ ratios in agreement with the solution data ($^{87}\text{Sr}/^{86}\text{Sr} = 0.70756 \pm 0.00003$, 2 SD). In addition, the laser ablation trace element analyses were performed with even smaller test portion masses than the Sr isotope

measurements. No significant deviation within one pellet was observed with this technique, further indicating that the NanoSr can be considered homogeneous for microanalytical *in-situ* Sr isotope analyses on a scale of 10s of μm . This implies, that the flame spray technique is suitable to produce a custom-made microanalytical carbonate RM, which fulfils the requirements for microanalytical Sr isotope analysis.

5.6.3 Availability of NanoSr

In total, 15 g of the synthetic carbonate nanopowder NanoSr have been produced. A single pressed pellet equals about 100 mg of carbonate nanopowder. Due to the intended use as widely available low-Sr carbonate reference material for the *in-situ* analysis of Sr isotopes, aliquots of NanoSr are available on request from the corresponding author.

5.7 Conclusions

This study characterised a custom-made reference material with a specified mass fraction of Sr and a carbonate matrix. Due to the lack of a suitable low-Sr microanalytical carbonate reference material for *in-situ* LA-MC-ICP-MS analysis of Sr isotopes, a synthetic carbonate nanomaterial with a relatively low Sr mass fraction was produced using the flame spray method. The material can be easily pressed to stable nanopowder pellets and yielded clean ablation tracks. The trace element mass fraction was determined after digestion and using laser ablation ICP-MS and yielded a mass fraction of Sr of approximately 500 $\mu\text{g/g}$. Potentially interfering elements, such as Rb and REEs, were of minor concerns due to their low mass fraction. Determination of the Sr isotope ratios using LA-MC-ICP-MS in two laboratories agree with three different and independent solution-based techniques yielded an average $^{87}\text{Sr}/^{86}\text{Sr}$ ratio of 0.70756 ± 0.00003 (2 SD). This value is in agreement with LA-MC-ICP-MS analyses in two different laboratories. Therefore, the NanoSr can be used as a matrix-matched reference material for carbonate samples to monitor the accuracy and precision of microanalytical analyses of Sr isotopes. Furthermore, this proof-of-concept study confirms the possibility for researchers to produce their own microanalytical custom-made reference materials using the flame spray technique, not only for glass matrices but also for carbonates.

5.8 Acknowledgements

M. Weber, K.P. Jochum and D. Scholz are thankful to the Max Planck Graduate Center and the German Research Foundation (DFG SCHO 1274/9-1 and DFG SCHO 1274/11-1). We are indebted to Anna Cipriani for the use of geochemical facilities at University of Modena and Reggio Emilia, as well as Steve Galer for the access to the TIMS instrument at MPIC. We also thank B. Stoll, U. Weis and M. Großkopf for assistance in the laboratory and S. Buhre and N. Groschopf for providing the EPMA data.

5.9 Supplement

Table A5.1: Quality control materials from the LA-ICP-MS measurements at the Max Planck Institute for Chemistry, Mainz.

Element Monitored Isotope	Mg ²⁵ Mg	Rb ⁸⁵ Rb	Sr ⁸⁸ Sr	Ba ¹³⁷ Ba	Dy ¹⁶³ Dy	Er ¹⁶⁷ Er	Yb ¹⁷³ Yb
NIST SRM 612							
Mean [µg/g] (n = 9)	57.3	32.7	78.3	39.2	37.6	40.6	39.2
1SD [µg/g]	1.2	0.9	1.1	2.6	1.5	1.9	2.2
GeoReM [µg/g]	68.0	31.4	78.4	39.3	35.5	38.0	39.2
RSF	0.84	1.04	1.00	1.00	1.06	1.07	1.00
USGS MACS-3							
Mean [µg/g] (n = 9)	1455.9	0.01	6164.7	56.8	6.9	7.0	6.8
1SD [µg/g]	49.6	0.00	207.6	8.8	0.4	0.4	0.4
GeoReM [µg/g]	1756.0	0.02	6760.0	58.7	10.7	11.2	11.2
RSF	0.83	0.28	0.91	0.97	0.64	0.63	0.61
USGS GSD-1G							
Mean [µg/g] (n = 9)	19767.9	40.30	68.7	69.1	49.4	38.1	46.8
1SD [µg/g]	511.8	0.94	0.3	5.3	2.1	1.9	2.6
GeoReM [µg/g]	21712.0	37.30	69.1	67.0	51.2	40.1	50.9
RSF	0.91	1.08	0.99	1.03	0.96	0.95	0.92
USGS GSE-1G							
Mean [µg/g] (n = 9)	18687.2	386.81	455.3	423.7	476.2	480.2	463.7
1SD [µg/g]	381.2	8.19	5.7	36.7	25.2	18.9	20.7
GeoReM [µg/g]	21109.0	356.00	447.0	427.0	524.0	595.0	520.0
RSF	0.89	1.09	1.02	0.99	0.91	0.81	0.89

Table A5.2: Quality control materials from the LA-ICP-MS measurements at the Institute of Geosciences, Mainz.

Element Monitored Isotope	Mg ²⁵ Mg	Rb ⁸⁵ Rb	Sr ⁸⁸ Sr	Ba ¹³⁷ Ba	Dy ¹⁶³ Dy	Er ¹⁶⁷ Er	Yb ¹⁷³ Yb
NIST SRM 612							
Mean [$\mu\text{g/g}$] (n = 9)	54.8	32.3	79.8	41.0	37.8	40.6	40.4
1SD [$\mu\text{g/g}$]	1.2	0.6	0.9	0.6	0.8	0.9	1.0
GeoReM [$\mu\text{g/g}$]	68.0	31.4	78.4	39.3	35.5	38.0	39.2
RSF	0.81	1.03	1.02	1.04	1.07	1.07	1.03
USGS BCR-2G							
Mean [$\mu\text{g/g}$] (n = 9)	19513.6	49.0	342.5	706.1	6.2	3.6	3.2
1SD [$\mu\text{g/g}$]	117.8	0.5	2.0	8.8	0.2	0.1	0.1
GeoReM [$\mu\text{g/g}$]	21471.0	47.0	342.0	683.0	6.4	3.7	3.4
RSF	0.91	1.04	1.00	1.03	0.96	0.97	0.94
USGS MACS-3							
Mean [$\mu\text{g/g}$] (n = 9)	1613.6	0.03	6922.4	56.8	10.5	10.8	10.9
1SD [$\mu\text{g/g}$]	13.7	0.01	82.2	1.1	0.3	0.2	0.2
GeoReM [$\mu\text{g/g}$]	1756.0	0.02	6760.0	58.7	10.7	11.2	11.2
RSF	0.92	1.41	1.02	0.97	0.98	0.97	0.97
USGS GSD-1G							
Mean [$\mu\text{g/g}$] (n = 9)	20551.5	39.50	70.2	71.5	50.9	39.9	49.9
1SD [$\mu\text{g/g}$]	215.0	0.32	0.5	1.1	1.0	0.9	1.2
GeoReM [$\mu\text{g/g}$]	21712.0	37.30	69.1	67.0	51.2	40.1	50.9
RSF	0.95	1.06	1.01	1.07	0.99	0.99	0.98
USGS GSE-1G							
Mean [$\mu\text{g/g}$] (n = 9)	20851.3	394.93	461.4	448.8	520.0	569.1	510.1
1SD [$\mu\text{g/g}$]	198.7	3.53	2.5	4.6	3.5	5.8	5.2
GeoReM [$\mu\text{g/g}$]	21109.0	356.00	447.0	427.0	524.0	595.0	520.0
RSF	0.99	1.11	1.03	1.05	0.99	0.96	0.98
USGS BCR-2G							
Mean [$\mu\text{g/g}$] (n = 9)	19513.6	49.00	342.5	706.1	6.2	3.6	3.2
1SD [$\mu\text{g/g}$]	117.8	0.51	2.0	8.8	0.2	0.1	0.1
GeoReM [$\mu\text{g/g}$]	21471.0	47.00	342.0	683.0	6.4	3.7	3.4
RSF	0.91	1.04	1.00	1.03	0.96	0.97	0.94

Table A5.3: LA-ICP-MS spot analyses of NanoSr at the Institute of Geosciences, Mainz.

Sample ID	Mg [$\mu\text{g/g}$]	Rb [$\mu\text{g/g}$]	Sr [$\mu\text{g/g}$]	Dy [$\mu\text{g/g}$]
Nano-1-1	2.34	0.039	490.0	0.165
Nano-1-2	2.51	0.063	492.5	0.155
Nano-1-3	2.91	0.027	490.5	0.135
Nano-1-4	2.68	0.039	487.3	0.134
Nano-1-5	2.84	0.057	485.3	0.141
Nano-1-6	2.53	0.031	479.7	0.114
Nano-1-7	2.71	0.047	482.1	0.125
Nano-1-8	2.45	0.048	487.0	0.120
Nano-1-9	2.76	0.050	483.0	0.146
Nano-1-10	2.81	0.029	486.9	0.100
Nano-1-11	2.99	0.042	491.4	0.096
Nano-1-12	2.85	0.062	487.1	0.142
Nano-2-1	2.80	0.057	483.7	0.142
Nano-2-2	2.91	0.075	483.0	0.156
Nano-2-3	2.71	0.046	477.9	0.136
Nano-2-4	2.67	0.036	483.4	0.127
Nano-2-5	2.87	0.052	485.5	0.142
Nano-2-6	2.66	0.037	477.7	0.124
Nano-2-7	2.73	0.058	481.9	0.148
Nano-2-8	2.69	0.065	484.5	0.156
Nano-2-9	2.43	0.054	479.4	0.145
Nano-2-10	2.71	0.042	480.4	0.136
Nano-2-11	2.58	0.038	480.8	0.133
Nano-2-12	3.11	0.059	481.3	0.118
Nano-3-1	2.80	0.034	487.7	0.134
Nano-3-2	2.62	0.061	482.5	0.137
Nano-3-3	2.32	0.042	479.5	0.138
Nano-3-4	2.40	0.053	478.4	0.136
Nano-3-5	2.45	0.051	473.4	0.121
Nano-3-6	2.72	0.039	481.9	0.128
Nano-3-7	2.62	0.048	476.8	0.127
Nano-3-8	2.62	0.047	479.9	0.136
Nano-3-9	2.66	0.056	487.8	0.140
Nano-3-10	2.89	0.034	472.4	0.134
Nano-3-11	2.46	0.046	479.0	0.122
Nano-3-12	2.56	0.050	484.3	0.156
Nano-4-1	2.84	0.046	497.1	0.123
Nano-4-2	2.59	0.065	498.4	0.126
Nano-4-3	2.45	0.065	498.4	0.137
Nano-4-4	2.85	0.046	498.7	0.163
Nano-4-5	3.04	0.052	489.6	0.131
Nano-4-6	2.61	0.051	494.3	0.127
Nano-4-7	2.72	0.052	491.4	0.141
Nano-4-8	2.94	0.057	490.0	0.154
Nano-4-9	2.56	0.058	482.7	0.153

Table A5.3 (continued):

Sample ID	Mg [$\mu\text{g/g}$]	Rb [$\mu\text{g/g}$]	Sr [$\mu\text{g/g}$]	Dy [$\mu\text{g/g}$]
Nano-5-1	2.08	0.052	483.5	0.161
Nano-5-2	2.63	NA	487.8	0.127
Nano-5-3	2.63	0.037	480.0	0.136
Nano-5-4	2.49	0.029	481.4	0.098
Nano-5-5	2.72	0.058	484.0	0.107
Nano-5-6	2.44	0.027	479.9	0.101
Nano-5-7	2.66	0.043	478.9	0.140
Nano-5-8	2.28	0.046	479.9	0.103
Nano-5-9	2.59	0.043	481.1	0.143
Nano-5-10	2.83	0.046	481.1	0.112
Nano-5-11	2.98	0.041	482.1	0.123
Nano-5-12	2.75	0.028	475.8	0.128
Nano-6-1	2.69	0.052	483.7	0.154
Nano-6-2	2.90	0.049	481.8	0.141
Nano-6-3	2.50	0.021	480.0	0.141
Nano-6-4	2.67	0.052	482.5	0.134
Nano-6-5	2.56	0.054	478.8	0.146
Nano-6-6	2.84	0.061	475.5	0.128
Nano-6-7	2.48	0.039	478.7	0.159
Nano-6-8	2.72	0.045	480.0	0.142
Nano-6-9	2.63	0.066	479.2	0.148
Nano-6-10	2.73	0.072	477.5	0.153
Nano-6-11	2.81	0.056	480.2	0.145
Nano-6-12	2.38	0.032	480.3	0.118

Table A5.4: LA-ICP-MS spot analyses at the Max Planck Institute for Chemistry, Mainz.

Sample ID	Mg [$\mu\text{g/g}$]	Rb [$\mu\text{g/g}$]	Sr [$\mu\text{g/g}$]	Ba [$\mu\text{g/g}$]	Dy [$\mu\text{g/g}$]	Er [$\mu\text{g/g}$]	Yb [$\mu\text{g/g}$]
Nano-1-1	3.13	0.072	515.0	0.22	0.188	0.005	0.044
Nano-1-2	3.24	0.074	519.8	0.20	0.193	0.004	0.044
Nano-1-3	3.21	0.077	514.1	0.30	0.188	0.005	0.043
Nano-1-4	3.20	0.069	508.3	0.18	0.189	0.006	0.039
Nano-1-5	3.11	0.072	504.2	0.20	0.190	0.004	0.038
Nano-1-6	3.08	0.069	502.0	0.19	0.189	0.005	0.040
Nano-1-7	3.16	0.070	509.7	0.19	0.189	0.005	0.038
Nano-1-8	3.19	0.070	504.9	0.18	0.188	0.004	0.041
Nano-1-9	3.09	0.068	504.9	0.18	0.193	0.004	0.038
Nano-1-10	3.26	0.073	505.4	0.20	0.187	0.004	0.041
Nano-1-11	3.15	0.076	507.0	0.21	0.191	0.004	0.040
Nano-1-12	3.29	0.070	495.1	0.20	0.190	0.005	0.045
Nano-2-1	3.26	0.072	517.9	0.20	0.200	0.006	0.043
Nano-2-2	3.42	0.073	512.1	0.20	0.188	0.006	0.040
Nano-2-3	3.16	0.073	501.9	0.19	0.191	0.005	0.045

Table A5.4 (continued):

Sample ID	Mg [$\mu\text{g/g}$]	Rb [$\mu\text{g/g}$]	Sr [$\mu\text{g/g}$]	Ba [$\mu\text{g/g}$]	Dy [$\mu\text{g/g}$]	Er [$\mu\text{g/g}$]	Yb [$\mu\text{g/g}$]
Nano-2-4	3.16	0.069	501.3	0.20	0.183	0.005	0.043
Nano-2-5	3.10	0.071	500.0	0.19	0.183	0.005	0.040
Nano-2-6	3.18	0.070	502.1	0.18	0.177	0.005	0.041
Nano-2-7	3.40	0.073	503.4	0.20	0.185	0.005	0.040
Nano-2-8	3.28	0.066	503.9	0.19	0.179	0.004	0.044
Nano-2-9	3.23	0.068	496.7	0.18	0.179	0.005	0.042
Nano-2-10	3.10	0.067	502.4	0.18	0.187	0.004	0.043
Nano-2-11	3.14	0.070	502.0	0.17	0.191	0.004	0.040
Nano-2-12	3.15	0.069	505.9	0.18	0.185	0.005	0.039
Nano-3-1	3.14	0.070	497.5	0.19	0.186	0.003	0.042
Nano-3-2	3.16	0.071	494.6	0.18	0.183	0.005	0.042
Nano-3-3	3.12	0.066	498.7	0.18	0.179	0.003	0.042
Nano-3-4	3.19	0.074	500.1	0.19	0.181	0.005	0.039
Nano-3-5	3.10	0.071	494.7	0.17	0.178	0.004	0.039
Nano-3-6	3.13	0.069	507.2	0.16	0.184	0.004	0.037
Nano-3-7	3.22	0.075	504.1	0.19	0.182	0.004	0.038
Nano-3-8	3.15	0.066	498.9	0.18	0.181	0.005	0.033
Nano-3-9	3.14	0.069	492.9	0.18	0.179	0.004	0.041
Nano-3-10	3.14	0.070	498.5	0.19	0.183	0.004	0.040
Nano-3-11	3.10	0.070	506.3	0.19	0.187	0.006	0.043
Nano-3-12	3.12	0.071	503.7	0.18	0.183	0.004	0.036
Nano-4-1	3.23	0.069	518.7	0.17	0.203	0.006	0.048
Nano-4-2	3.15	0.071	508.8	0.18	0.196	0.006	0.042
Nano-4-3	3.12	0.073	503.0	0.18	0.192	0.005	0.042
Nano-4-4	3.18	0.071	506.9	0.18	0.187	0.005	0.040
Nano-4-5	3.05	0.072	511.0	0.16	0.186	0.004	0.041
Nano-4-6	3.12	0.072	504.5	0.18	0.184	0.004	0.040
Nano-4-7	3.13	0.069	501.6	0.17	0.180	0.004	0.038
Nano-4-8	3.11	0.067	497.9	0.18	0.183	0.004	0.042
Nano-4-9	3.25	0.071	498.5	0.17	0.191	0.005	0.044
Nano-4-10	3.12	0.068	499.6	0.17	0.182	0.005	0.040
Nano-4-11	3.03	0.070	507.5	0.19	0.177	0.005	0.039
Nano-4-12	3.09	0.068	510.0	0.17	0.184	0.004	0.038
Nano-5-1	3.15	0.070	501.7	0.17	0.179	0.004	0.042
Nano-5-2	3.09	0.071	507.0	0.18	0.183	0.004	0.040
Nano-5-3	3.07	0.068	504.4	0.17	0.180	0.004	0.040
Nano-5-4	3.03	0.074	502.4	0.17	0.170	0.004	0.041
Nano-5-5	3.08	0.071	512.7	0.19	0.177	0.003	0.037
Nano-5-6	3.01	0.074	501.5	0.17	0.177	0.003	0.036
Nano-5-7	3.09	0.079	509.1	0.19	0.177	0.005	0.041
Nano-5-8	3.02	0.074	509.3	0.16	0.184	0.005	0.038
Nano-5-9	3.12	0.077	508.2	0.17	0.179	0.005	0.042
Nano-5-10	3.16	0.073	506.4	0.18	0.181	0.006	0.040
Nano-5-11	3.08	0.076	512.4	0.18	0.183	0.004	0.039
Nano-5-12	3.10	0.073	507.9	0.17	0.183	0.004	0.041

Table A5.4 (continued):

Sample ID	Mg [$\mu\text{g/g}$]	Rb [$\mu\text{g/g}$]	Sr [$\mu\text{g/g}$]	Ba [$\mu\text{g/g}$]	Dy [$\mu\text{g/g}$]	Er [$\mu\text{g/g}$]	Yb [$\mu\text{g/g}$]
Nano-6-1	3.09	0.073	513.1	0.17	0.185	0.005	0.040
Nano-6-2	3.03	0.071	504.8	0.16	0.184	0.004	0.044
Nano-6-3	3.11	0.073	510.4	0.18	0.188	0.004	0.040
Nano-6-4	3.17	0.072	508.2	0.17	0.191	0.005	0.040
Nano-6-5	3.08	0.070	503.2	0.17	0.181	0.005	0.042
Nano-6-6	3.10	0.067	499.8	0.17	0.179	0.005	0.038
Nano-6-7	3.05	0.072	508.5	0.17	0.187	0.005	0.039
Nano-6-8	3.08	0.070	507.5	0.17	0.181	0.004	0.039
Nano-6-9	3.06	0.076	512.2	0.17	0.182	0.004	0.041
Nano-6-10	3.05	0.070	511.7	0.18	0.184	0.004	0.042
Nano-6-11	3.05	0.070	509.0	0.18	0.188	0.003	0.042
Nano-6-12	3.12	0.072	508.4	0.17	0.187	0.004	0.043

Table A5.5: LA-ICP-MS line scan analyses at Max Planck Institute for Chemistry, Mainz.

Sample ID	Mg [$\mu\text{g/g}$]	Rb [$\mu\text{g/g}$]	Sr [$\mu\text{g/g}$]	Ba [$\mu\text{g/g}$]	Dy [$\mu\text{g/g}$]	Yb [$\mu\text{g/g}$]
Nano-1-1	3.3	0.05815	479.72904	0.18	0.2	0.04
Nano-1-2	3.47	0.05823	460.97603	0.17	0.2	0.06
Nano-1-3	3.45	0.06222	503.00683	0.18	0.23	0.05
Nano-1-4	3.15	0.05613	472.61572	0.17	0.2	0.06
Nano-1-5	2.97	0.05951	470.36974	0.18	0.2	0.08
Nano-1-6	2.79	0.05944	469.59324	0.16	0.2	0.04
Nano-1-1	2.63	0.06443	482.07046	0.18	0.21	0.06
Nano-1-2	2.63	0.06443	482.07046	0.18	0.21	0.06
Nano-1-3	2.7	0.05562	455.34979	0.16	0.17	0.05
Nano-1-4	2.78	0.06171	470.52421	0.18	0.21	0.04
Nano-1-5	2.81	0.06732	501.35312	0.17	0.2	0.06
Nano-1-6	2.88	0.06368	467.0117	0.15	0.18	0.05
Nano-1-7	3.16	0.07216	490.32026	0.17	0.21	0.05
Nano-1-8	3.33	0.06716	495.61966	0.16	0.19	0.05
Nano-1-9	3.17	0.06553	480.62347	0.17	0.2	0.05
Nano-1-10	2.98	0.05994	488.33712	0.19	0.21	0.04
Nano-1-12	2.98	0.054	474.33767	0.15	0.19	0.06

Table A5.6: LA-ICP-MS spot analyses at Centro Interdipartimentale Grandi Strumenti, University of Modena and Reggio Emilia.

Sample ID	Rb [$\mu\text{g/g}$]	Sr [$\mu\text{g/g}$]	Ba [$\mu\text{g/g}$]	Dy [$\mu\text{g/g}$]	Yb [$\mu\text{g/g}$]
Nano-7-1	0.049	504.32	0.14	0.20	0.05
Nano-7-2	0.043	496.96	0.19	0.19	0.05
Nano-7-3	0.040	501.33	0.14	0.20	0.03
Nano-7-4	0.068	497.85	0.18	0.21	0.06
Nano-7-5	0.045	508.15	0.20	0.21	0.05

Table A5.7: ICP-MS analyses at Centro Interdipartimentale Grandi Strumenti, University of Modena and Reggio Emilia.

Sample ID	Rb [$\mu\text{g/g}$]	Sr [$\mu\text{g/g}$]	Ba [$\mu\text{g/g}$]	Dy [$\mu\text{g/g}$]	Er [$\mu\text{g/g}$]	Yb [$\mu\text{g/g}$]
Nano-1-1	0.11	519.9	0.21	0.20	0.06	0.08
Nano-1-2	0.08	468.1	0.17	0.16	0.02	0.05
Nano-1-3	0.06	515.0	0.31	0.15	0.01	0.04
Nano-1-4	0.07	519.2	0.24	0.16	0.01	0.05
Nano-1-5	0.06	454.5	0.18	0.14	0.01	0.04
Nano-1-6	0.07	492.9	0.17	0.16	0.01	0.04

Table A5.8: MC-ICP-MS analyses at Centro Interdipartimentale Grandi Strumenti, University of Modena and Reggio Emilia.

Sample ID	$^{87}\text{Sr}/^{86}\text{Sr}$	2 SE	$^{84}\text{Sr}/^{86}\text{Sr}$	2 SE
N1-1	0.707554	0.000008	0.056486	0.000002
N1-2	0.707550	0.000009	0.056478	0.000002
N1-3	0.707542	0.000009	0.056482	0.000002
N2-1	0.707556	0.000009	0.056479	0.000002
N2-2	0.707552	0.000009	0.056484	0.000002
N2-3	0.707537	0.000008	0.056482	0.000002
N3-1	0.707551	0.000010	0.056483	0.000014
N3-2	0.707550	0.000013	0.056465	0.000002
N3-3	0.707555	0.000013	0.056474	0.000002
N4-1	0.707563	0.000013	0.056475	0.000002
N4-2	0.707554	0.000013	0.056488	0.000002
N4-3	0.707551	0.000013	0.056482	0.000002
N5-1	0.707543	0.000013	0.056486	0.000002
N5-2	0.707546	0.000013	0.056480	0.000002
N5-3	0.707547	0.000013	0.056485	0.000002
N6-1	0.707554	0.000013	0.056486	0.000002
N6-2	0.707566	0.000013	0.056490	0.000002
N6-3	0.707558	0.000013	0.056493	0.000002

Table A5.8 (continued):

Sample ID	$^{87}\text{Sr}/^{86}\text{Sr}$	2 SE	$^{84}\text{Sr}/^{86}\text{Sr}$	2 SE
NP19	0.707554	0.000014	0.056488	0.000002

Table A5.9: MC-ICP-MS analyses at Max Planck Institute for Chemistry, Mainz.

Sample ID	$^{87}\text{Sr}/^{86}\text{Sr}$	2 SE	$^{84}\text{Sr}/^{86}\text{Sr}$	2 SE
N1-1	0.707558	0.000035	0.056390	0.000012
N1-1b	0.707548	0.000015	0.056510	0.000006
N1-1c	0.707578	0.000015	0.056588	0.000007
N1-2	0.707572	0.000015	0.056557	0.000011
N1-3	0.707546	0.000015	0.056472	0.000010
N2-1	0.707587	0.000017	0.056457	0.000008
N2-2	0.707582	0.000019	0.056535	0.000010
N2-3	0.707566	0.000019	0.056561	0.000008
N3-1	0.707558	0.000018	0.056478	0.000007
N3-2	0.707581	0.000018	0.056451	0.000015
N3-3	0.707604	0.000020	0.056457	0.000007
N4-1	0.707543	0.000021	0.056457	0.000009
N4-2	0.707553	0.000020	0.056463	0.000009
N4-3	0.707538	0.000020	0.056493	0.000010
N5-1	0.707611	0.000021	0.056436	0.000009
N5-2	0.707542	0.000023	0.056484	0.000011
N5-3	0.707548	0.000019	0.056502	0.000009
N6-1	0.707556	0.000022	0.056506	0.000011
N6-2	0.707561	0.000022	0.056438	0.000010
N6-3	0.707553	0.000022	0.056424	0.000011
NP19	0.707523	0.000023	0.056421	0.000011

Table A5.10: LA-MC-ICP-MS analyses at Centro Interdipartimentale Grandi Strumenti, University of Modena and Reggio Emilia.

Sample ID	$^{87}\text{Sr}/^{86}\text{Sr}$	2 SE	$^{84}\text{Sr}/^{86}\text{Sr}$	2 SE
Nano-7-1	0.70758	0.00002	0.05626	0.00002
Nano-7-2	0.70760	0.00003	0.05644	0.00002
Nano-7-3	0.70760	0.00003	0.05636	0.00002
Nano-7-4	0.70756	0.00003	0.05647	0.00002
Nano-7-5	0.70756	0.00005	0.05668	0.00003
Nano-7-6	0.70754	0.00004	0.05659	0.00003
Nano-7-7	0.70750	0.00004	0.05657	0.00003
Nano-7-8	0.70758	0.00004	0.05661	0.00003
Nano-7-9	0.70758	0.00003	0.05655	0.00003
Nano-7-10	0.70756	0.00004	0.05662	0.00003
seashell	0.70916	0.00002	0.05655	0.00001

Table A5.11: LA-MC-ICP-MS analyses at Max Planck Institute for Chemistry, Mainz.

Sample ID	$^{87}\text{Sr}/^{86}\text{Sr}$	2 SE	$^{84}\text{Sr}/^{86}\text{Sr}$	2 SE
Nano-1	0.70750	0.00004	0.05588	0.00005
Nano-2	0.70753	0.00004	0.05592	0.00005
Nano-3	0.70753	0.00004	0.05596	0.00005
Nano-4	0.70753	0.00004	0.05594	0.00005
Nano-5	0.70749	0.00004	0.05593	0.00005
Nano-6	0.70750	0.00004	0.05609	0.00005
Nano-7	0.70758	0.00004	0.05604	0.00006
Nano-8	0.70754	0.00004	0.05617	0.00006
Nano-9	0.70752	0.00004	0.05616	0.00007
Nano-10	0.70762	0.00004	0.05615	0.00006
Nano-11	0.70755	0.00004	0.05600	0.00006
Nano-12	0.70758	0.00004	0.05616	0.00005
Nano-13	0.70758	0.00004	0.05612	0.00005
Nano-14	0.70761	0.00004	0.05619	0.00005
Nano-15	0.70752	0.00004	0.05617	0.00006
Nano-16	0.70753	0.00004	0.05619	0.00006
Nano-17	0.70756	0.00004	0.05603	0.00006
Nano-18	0.70753	0.00004	0.05620	0.00006
Nano-19	0.70752	0.00004	0.05609	0.00006
Nano-20	0.70753	0.00002	0.05605	0.00003
Nano-21	0.70751	0.00002	0.05610	0.00003
Nano-22	0.70754	0.00002	0.05606	0.00003
Nano-23	0.70753	0.00002	0.05609	0.00003
Nano-24	0.70755	0.00002	0.05612	0.00003
Nano-25	0.70756	0.00002	0.05613	0.00003
Nano-26	0.70755	0.00003	0.05614	0.00003
Nano-27	0.70753	0.00003	0.05623	0.00004
Nano-28	0.70753	0.00003	0.05614	0.00004
Nano-29	0.70751	0.00003	0.05622	0.00005
Nano-30	0.70748	0.00003	0.05621	0.00004
Nano-31	0.70755	0.00002	0.05614	0.00003
Nano-32	0.70755	0.00002	0.05625	0.00003
Nano-33	0.70755	0.00002	0.05623	0.00003
Nano-34	0.70750	0.00002	0.05630	0.00003
Nano-35	0.70752	0.00002	0.05626	0.00003
Nano-36	0.70749	0.00003	0.05619	0.00003
Nano-37	0.70749	0.00003	0.05622	0.00003
Nano-38	0.70752	0.00003	0.05629	0.00004
Nano-39	0.70748	0.00003	0.05640	0.00004
Nano-40	0.70749	0.00003	0.05631	0.00005
Nano-41	0.70750	0.00003	0.05629	0.00004
Nano-42	0.70755	0.00005	0.05627	0.00007
Nano-43	0.70761	0.00004	0.05609	0.00007
Nano-44	0.70753	0.00005	0.05615	0.00007

Table A5.11 (continued):

Sample ID	$^{87}\text{Sr}/^{86}\text{Sr}$	2 SE	$^{84}\text{Sr}/^{86}\text{Sr}$	2 SE
Nano-45	0.70748	0.00004	0.05627	0.00006
Nano-46	0.70748	0.00005	0.05627	0.00007
Nano-47	0.70762	0.00004	0.05610	0.00007
Nano-48	0.70754	0.00005	0.05619	0.00007
Nano-49	0.70758	0.00004	0.05615	0.00007
Nano-50	0.70752	0.00005	0.05628	0.00007
Nano-51	0.70756	0.00005	0.05614	0.00009
Nano-52	0.70751	0.00004	0.05638	0.00007
Nano-53	0.70758	0.00004	0.05627	0.00007
Nano-54	0.70761	0.00004	0.05628	0.00007
Nano-55	0.70750	0.00004	0.05628	0.00007
Nano-56	0.70752	0.00005	0.05614	0.00007
Nano-57	0.70751	0.00005	0.05648	0.00007
Nano-58	0.70750	0.00005	0.05642	0.00007
JCt-1-1	0.70922	0.00004	0.05633	0.00004
JCt-1-2	0.70920	0.00003	0.05640	0.00002
JCt-1-3	0.70923	0.00003	0.05629	0.00003
JCt-1-4	0.70922	0.00003	0.05637	0.00003
JCt-1-5	0.70918	0.00003	0.05634	0.00003
JCt-1-6	0.70918	0.00003	0.05637	0.00003
JCt-1-7	0.70914	0.00003	0.05639	0.00003
JCt-1-8	0.70911	0.00003	0.05636	0.00003
JCt-1-9	0.70914	0.00004	0.05634	0.00003
JCt-1-10	0.70916	0.00003	0.05634	0.00003
MACS3-1	0.70758	0.00003	0.05607	0.00003
MACS3-2	0.70757	0.00003	0.05602	0.00003
MACS3-3	0.70758	0.00003	0.05606	0.00003
MACS3-4	0.70755	0.00004	0.05600	0.00003
MACS3-5	0.70757	0.00003	0.05599	0.00003
MACS3-6	0.70755	0.00003	0.05600	0.00003
MACS3-7	0.70760	0.00003	0.05606	0.00003
MACS3-8	0.70754	0.00004	0.05601	0.00003
MACS3-9	0.70755	0.00003	0.05605	0.00003
MACS3-10	0.70758	0.00003	0.05605	0.00003
JCp-1-1	0.70915	0.00005	0.05635	0.00003
JCp-1-2	0.70921	0.00004	0.05641	0.00003
JCp-1-3	0.70922	0.00004	0.05639	0.00003
JCp-1-4	0.70922	0.00004	0.05637	0.00003
JCp-1-5	0.70915	0.00004	0.05629	0.00003
JCp-1-6	0.70916	0.00004	0.05639	0.00003
JCp-1-7	0.70913	0.00004	0.05634	0.00003
JCp-1-8	0.70916	0.00004	0.05638	0.00003
JCp-1-90	0.70913	0.00004	0.05638	0.00002
JCp-1-10	0.70917	0.00004	0.05641	0.00002

Table A5.12: TIMS analyses at Max Planck Institute for Chemistry, Mainz.

Sample ID	$^{87}\text{Sr}/^{86}\text{Sr}$	2 SE
N1-1	0.707568	0.000007
N2-1	0.707560	0.000006
N3-1	0.707561	0.000007
N4-1	0.707564	0.000008
N5-1A	0.707556	0.000007
N5-1B	0.707569	0.000005

Table A5.13: EPMA analyses at Institute of Geosciences, Mainz.

Sample ID	Ca [$\mu\text{g/g}$]	2 SD
N1	370103	11103
N2	364729	10942
N3	367059	11012
N4	363421	10903
N5	380038	11401
N6	376936	11308
N7	377815	11334
N8	380674	11420
N9	376972	11309
N10	376579	11297
N11	373798	11214
N12	377415	11322
N13	381646	11449
N14	376600	11298
N15	378894	11367
N16	379230	11377
N17	379588	11388
N18	380352	11411
N19	379802	11394
N20	378423	11353
N21	381053	11432
N22	366294	10989
N23	380903	11427
N24	371676	11150

Chapter 6: Manuscript IV: Evidence of warm and humid interstadials in central Europe during early MIS 3 revealed by a multi-proxy speleothem record

Evidence of warm and humid interstadials in central Europe during early MIS 3
revealed by a multi-proxy speleothem record

Michael Weber^{1,2}, Denis Scholz¹, Andrea Schröder-Ritzrau³, Michael Deininger¹, Christoph Spötl⁴,
Federico Lugli^{5,6}, Regina Mertz-Kraus¹, Klaus Peter Jochum², Jens Fohlmeister^{7,8}, Cintia F. Stumpf⁹,
Dana F.C. Riechelmann¹

¹Institute of Geosciences, Johannes Gutenberg-University Mainz, Johann-Joachim-Becher-Weg 21,
55128 Mainz, Germany

²Climate Geochemistry Department, Max Planck Institute for Chemistry (Otto-Hahn-Institute), Postbox
3060, 55020 Mainz, Germany

³Institute for Environmental Physics, University Heidelberg, Im Neuenheimer Feld 229,
69120 Heidelberg, Germany

⁴Institute of Geology, University of Innsbruck, Innrain 52, 6020 Innsbruck, Austria

⁵Department of Chemical and Geological Sciences, University of Modena and Reggio Emilia, Via
Campi 103, 41125, Modena, Italy

⁶Department of Cultural Heritage, University of Bologna, 48121 Ravenna, Italy

⁷Institute for Earth and Environmental Sciences, University of Potsdam, Karl-Liebknecht-Str. 24-25,
14476 Potsdam-Golm, Germany

⁸GFZ German Research Centre for Geosciences, Section 5.2 Climate Dynamics and Landscape
Development, Telegrafenberg, 14473 Potsdam, Germany

⁹Universidade de Brasília, Instituto de Geociências, 70294-400 Brasília, Brazil

This manuscript is published in a similar version in *Quaternary Science Reviews* Vol. 200, 276 – 286
(2018).

6.1 Abstract

Marine Isotope Stage 3 (MIS 3, 57 – 27 ka) was characterised by numerous rapid climate oscillations (i.e. Dansgaard-Oeschger (D/O-) events), which are reflected in various climate archives. So far, MIS 3 speleothem records from Central Europe have mainly been restricted to caves located beneath temperate Alpine glaciers or close to the Atlantic Ocean. Thus, MIS 3 seemed to be too cold and dry to enable speleothem growth north of the Alps in Central Europe.

Here we present a new speleothem record from Bunker Cave, Germany, which shows two distinct growth phases from 52.0 (+0.8, -0.5) to 50.9 (+0.6, -1.3) ka and 47.3 (+1.0, -0.6) to 42.8 (\pm 0.9) ka, rejecting this hypothesis. These two growth phases potentially correspond to the two warmest and most humid phases in Central Europe during MIS 3, which is confirmed by pollen data from the nearby Eifel. The hiatus separating the two phases is associated with Heinrich stadial 5 (HS 5), although the growth stop precedes the onset of HS 5. The first growth phase is characterised by a fast growth rate, and Mg mass fractions and Sr isotope data suggest high infiltration and the presence of soil cover above the cave. The second growth phase was characterised by drier, but still favourable conditions for speleothem growth. During this phase, the $\delta^{13}\text{C}$ values show a significant decrease associated with D/O-event 12. The timing of this shift is in agreement with other MIS 3 speleothem data from Europe and Greenland ice core data.

6.2 Introduction

Marine Isotope Stage 3 (MIS 3, ca. 57-27 ka; Lisiecki and Raymo, 2005) was characterised by rapid climate oscillations (i.e. the Dansgaard-Oeschger (D/O) events). This high-frequency climate variability was first discovered in Greenland ice cores by Johnsen et al. (1992) and Dansgaard et al. (1993). Stable oxygen isotope ($\delta^{18}\text{O}$) records obtained from ice cores show the occurrence of high-magnitude climate cycles, where a rapid temperature increase (up to 10 to 16 °C on the summit of Greenland; (Huber et al., 2006; Kindler et al., 2014) occurred within decades and was followed by a gradual cooling. For MIS 3, eleven D/O-events have been described in Greenland ice cores (D/O 5 – 15), based on the GICC05 timescale (Rasmussen et al., 2014). Furthermore, MIS 3 was characterised by Heinrich events 3 to 5, triggered by freshwater input in the North Atlantic, slowing down North-Atlantic deep-water formation (Böhm et al., 2015) and identified by ice-rafted debris (IRD) layers (Heinrich, 1988). The corresponding Heinrich stadials were cold phases with a typical duration of few thousand years, identified both in Greenland ice cores and in North Atlantic and Mediterranean sediment cores (e.g. Bond et al., 1993; Cacho et al., 1999; Sánchez Goñi et al., 2002). These marine records, however, often lack independent and precise dating control, rendering the identification of leads and lags during D/O-events partly ambiguous.

Speleothems have been used as archives of past climate and environmental variability in Europe (e.g. Fankhauser et al., 2016; Fohlmeister et al., 2012; Genty et al., 2003; Luetscher et al., 2015). The U-

series disequilibrium method (Richards and Dorale, 2003; Scholz and Hoffmann, 2008) allows to obtain accurate and precise age-depth models. In addition, stable carbon and oxygen isotopes as well as trace elements can be measured at high temporal resolution in speleothems and have been widely used to investigate past climate change (Fairchild et al., 2006; Fairchild and Treble, 2009; Lachniet, 2009; McDermott, 2004). Furthermore, speleothem growth itself can be used as climate proxy, especially during glacial periods. Speleothem growth depends on several climatic and environmental factors, such as the availability of water (i.e. temperature >0 °C) and a high $p\text{CO}_2$ in the soil above the cave (Matthey et al., 2016). Consequently, speleothem growth is mainly restricted to relatively warm and humid climate periods that are characterised by the availability of water, sufficient soil development and vegetation cover above the cave, such as during the Holocene (Mangini et al., 2007; McDermott et al., 1999) and previous interglacials (Baker et al., 1993; Gordon et al., 1989; Hennig et al., 1983). This results in drip water supersaturated with respect to calcite entering the cave and, eventually, the precipitation of speleothem calcite.

European speleothem records from MIS 3 are limited. Besides some records from southern and south-eastern Europe with only single ages indicating growth during MIS 3 (Constantin et al., 2007; Hodge et al., 2008), the majority of MIS 3 speleothem records have so far been reported from the Alpine region (Holzkämper et al., 2005; Luetscher et al., 2015; Moseley et al., 2014; Spötl and Mangini, 2002; Spötl et al., 2006). These speleothems grew in caves underneath temperate glaciers, which provided enough meltwater to enable speleothem growth (Spötl and Mangini, 2002), despite of cold climate conditions at the surface. Therefore, their growth cannot be used as a direct climate indicator, in particular for Central Europe. Further speleothems from MIS 3 have been found in south-western (SW) and north-eastern (NE) France. In particular, MIS 3 stalagmites from Villars Cave (SW France) were subject of several studies and provided valuable information about climate variability during this period (Genty et al., 2003; Genty et al., 2005; Genty et al., 2010; Wainer et al., 2009). Another MIS 3 speleothem was found at Grotte des Puits de Pierra-la-Treiche (NE France, Pons-Branchu et al., 2010). The most north-western European MIS 3 speleothem record was published from Crag Cave (SW Ireland), where several broken stalagmites have been dated (Fankhauser et al., 2016). These authors showed that speleothem growth occurred episodically during MIS 3 interstadials, especially during mid to late MIS 3.

Here we present a new record of a stalagmite from Bunker Cave, central Germany, which grew during MIS 3. Currently, this is the northern-most MIS 3 speleothem record for Central Europe, where centennial-scale climate records of this time interval are rare (McDermott, 2004; Voelker, 2002). The record shows two warm and humid phases during early MIS 3 separated by a hiatus corresponding to the Heinrich 5 cold event (HS 5).

6.3 Site and sample description

The precise knowledge of the cave setting is essential for successful palaeoclimate reconstructions using speleothems, since the cave environment is highly influencing the resulting proxy data.

6.3.1 Bunker Cave

Bunker Cave has been described in detail by Riechelmann et al. (2011) and Fohlmeister et al. (2012) and is thus only briefly discussed here. The cave (51°22'03''N, 7°39'53''E) is located in western Germany (Sauerland, Fig. 6.1), the cave entrance at 184 m above sea level. The cave is developed in Middle to Upper Devonian low-Mg limestone, which contains dolomite veins, and the limestone overburden ranges from 15 to 30 m (Grebe, 1993). At present, the host rock is covered by up to 70 cm of brownish loamy soil, which developed from loess loam deposited during the last glacial (von Kamp and Ribbert, 2005). The thin soil horizon A (<10 cm) is humic, covering a brown/yellow soil horizon B. Soil horizon C is built up by this brown/yellow soil and the limestone host rock (Riechelmann et al., 2011). Today, the vegetation above the cave consists of C3-plants, mainly ash and beech trees as well as shrubs. The mean annual cave air and drip water temperature is 10.6°C (2006 – 2009). Mean annual precipitation in the area is 919 mm (1988 – 2007, weather station Hagen-Fley), equally distributed over the year. The $\delta^{18}\text{O}$ values of precipitation range from -5 ‰ in summer to -13 ‰ in winter (Riechelmann et al., 2017). The $\delta^{18}\text{O}$ values of cave drip water (mean $\delta^{18}\text{O} = -7.9 \pm 0.3$ ‰, 1 SD, n = 384, 2006 – 2013, Riechelmann et al., 2017) imply a well-mixed aquifer. Calcite precipitation in Bunker Cave was observed during the whole year by watch glass experiments at several drip sites (mean $\delta^{13}\text{C} = -8.6 \pm 0.6$ ‰, 1 SD, n = 16; mean $\delta^{18}\text{O} = -6.1 \pm 0.2$ ‰, 1 SD, n = 16, Riechelmann, 2010; Riechelmann et al., 2014). Therefore, Bunker Cave is highly suitable for reconstruction of long-term multi-annual climate trends in Central Europe (Fohlmeister et al., 2012; Riechelmann et al., 2011; Riechelmann et al., 2012a; Riechelmann et al., 2017).

6.3.2 Stalagmite Bu2

Bu2 (Fig. 6.2) is a 32 cm-long stalagmite, sampled under an active drip site, which was investigated in the framework of a long-term cave monitoring program (corresponding to drip site TS 7, Riechelmann et al., 2011). The upper 76 mm of Bu2 grew during the Holocene and were already studied by Fohlmeister et al. (2012). Bu2 consists of clear white to beige calcite with only few detrital layers (Fig. 6.2). A single brown layer at 76 mm distance from top (DFT), separating the Holocene growth phase from the older part of Bu2, is clearly visible. The base of the stalagmite (Fig. 6.2) consists of brownish calcite and was not analysed.

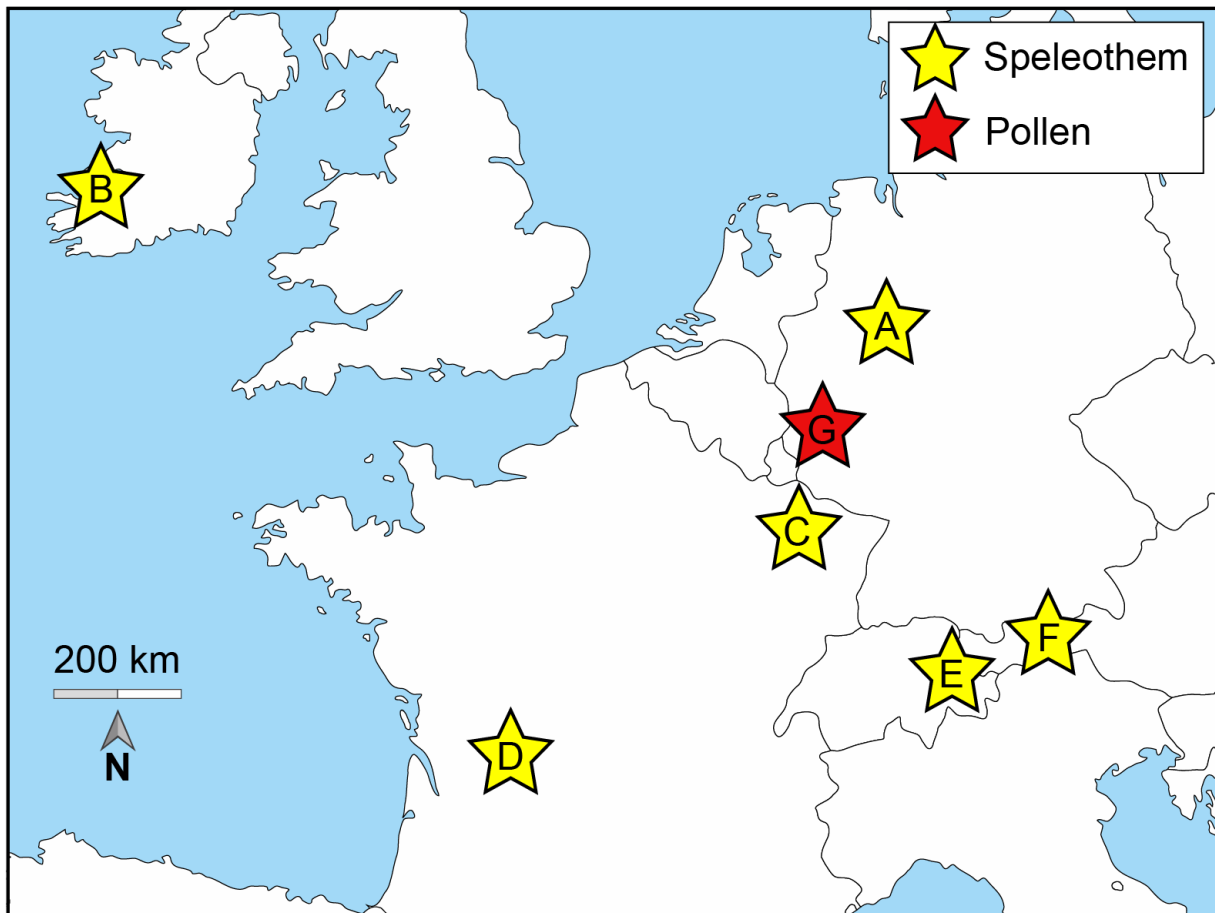


Fig. 6.1: Map showing north-western parts of Europe with the location of MIS 3 climate records from Bunker Cave [A, this study], Crag Cave [B, Fankhauser et al. (2016)], Grotte des Puits de Pierra-la-Treiche [C, Pons-Branchu et al. (2010)], Villars Cave [D, Genty et al. (2003)], Hölloch Cave [E, Moseley et al. (2014)], Klee gruben Cave [F, Spötl et al. (2006)] and the Eifel maar lakes [G, Sirocko et al. (2016)].

6.4 Methods

Several methods have been applied in the analysis of Bu2, including MC-ICP-MS, LA-ICP-MS and IRMS. Details of the different methods are provided in the following.

6.4.1 $^{230}\text{Th}/\text{U}$ -dating

In total, 25 samples were cut along the growth axis of Bu2 using a diamond wire saw. The samples were subsequently prepared for $^{230}\text{Th}/\text{U}$ -dating by MC-ICP-MS (23 samples) and TIMS (two samples). The TIMS analyses were performed at the Heidelberg Academy of Sciences, following the methods described by Scholz et al. (2004), using an updated spike re-calibration (Hoffmann et al., 2007). For the MC-ICP-MS analyses, sample amounts of approximately 0.3 g were used. After sawing, the samples were briefly leached in weak HNO_3 to remove potential surface contamination. The chemical separation

of U and Th was performed as described by Hoffmann (2008) with the respective adjustments described by Yang et al. (2015). Uranium and Th fractions were measured separately, using a Nu plasma MC-ICP-MS at the Max Planck Institute for Chemistry (MPIC) in Mainz. A standard bracketing approach was applied to correct for mass fractionation, ion counter gain and tailing. The mass spectrometric procedures were generally explained in Hoffmann et al. (2007) and in detail for the laboratory at the MPIC by Obert et al. (2016). The calibration of the U-Th-spike was described in detail by Gibert et al. (2016). Introduction of the sample solution was performed using a CETAC Aridus II desolvating nebulizer system, connected to the MC-ICP-MS. Daily tuning (including torch position, gas flows and ion lenses) was performed to obtain highest signal intensities at optimized peak shapes. Resulting ages were then used for the calculation of the age-depth relationship (Fig. 6.3), using the algorithm StalAge (Scholz and Hoffmann, 2011). Further details are summarised in supplementary Table A6.1.

6.4.2 Trace element analysis

Trace element mass fractions were determined by LA-ICP-MS. The upper 98 mm of the sample were analysed at the Goethe University Frankfurt, using a New Wave UP213 UV-laser system, connected to a Thermo-Finnigan Element II SF-ICP-MS (Gerdes and Zeh, 2006). For the measurements between 98 and 324 mm DFT, an ArF Excimer 193 nm laser system (ESI NWR193), coupled to an Agilent 7500ce ICP-MS at the Johannes Gutenberg University Mainz, was used (Jochum et al., 2012).

Prior to both LA-ICP-MS analyses, the signal was tuned for maximum intensities at low oxide formation rates measured as $^{238}\text{U}^{16}\text{O}/^{238}\text{U} < 0.2\%$ (Mainz) and $< 0.5\%$ (Frankfurt). Ion intensities for ^{25}Mg , ^{43}Ca , ^{88}Sr and ^{89}Y were continuously acquired parallel to the growth axis, located within 2 mm distance of the stable isotope track (Fig. 6.2). Prior to each analysis, a pre-ablation was performed. Background counts were measured for 15 s without the laser firing before each analysis and subtracted from the raw data. The transect was divided into consecutive lines of approximately 4 cm length, allowing to analyse NIST SRM 610 (Frankfurt) and NIST SRM 612 (Mainz) at the beginning, between each line and at the end of the routine for calibration purposes. To monitor accuracy and reproducibility, NIST SRM 610 ($n = 24$), USGS MACS-3 ($n = 24$) and USGS BCR-2G ($n = 24$) were monitored as unknowns during the analyses at the Johannes Gutenberg University Mainz (see supplementary Table A6.2). Data reduction was performed using an in-house Excel spreadsheet. Details of the calculations are given in Mischel et al. (2017a).

^{43}Ca was used as an internal reference, applying the corresponding Ca mass fraction from the GeoReM database (Jochum et al., 2005). For the stalagmite sample, a Ca-content of 39.4 wt% was assumed. Reference values for NIST SRM 610 and 612 were adapted from Jochum et al. (2011b). Further operational parameters are given in supplementary Table A6.3.

6.4.3 Stable isotope analysis

High-resolution stable carbon and oxygen isotopes values ($\delta^{13}\text{C}$ and $\delta^{18}\text{O}$) were obtained at the Institute of Geology, University of Innsbruck. In total, 1078 samples were drilled using a Merchantek video-controlled MicroMill device with a spatial resolution of 150 μm in the upper part of Bu2 (between 76 and 141.75 mm DFT) and 300 μm in the lower part of Bu2 (between 142 and 324 mm DFT, Fig. 6.2). The $\delta^{13}\text{C}$ and $\delta^{18}\text{O}$ analyses were performed using a Thermo Fisher Delta^{plus}XL isotope ratio mass spectrometer linked to a Gasbench II. Analytical precision for the $\delta^{13}\text{C}$ and $\delta^{18}\text{O}$ measurements is 0.07 ‰ for $\delta^{13}\text{C}$ and 0.09 ‰ for $\delta^{18}\text{O}$ (both at the 1σ level). All $\delta^{13}\text{C}$ and $\delta^{18}\text{O}$ values are reported relative to V-PDB.

To account for changes in seawater $\delta^{18}\text{O}$ values due to changing sea level and ice volume, we applied the correction factor of Duplessy et al. (2007) assuming a decrease of -0.008 ± 0.002 ‰ per meter of global sea-level rise and using the sea-level reconstruction of Bates et al. (2014a), which is based on the composite ODP record 162-980/981 (Bates et al., 2014b). The effect of the correction on the $\delta^{18}\text{O}_{\text{slc}}$ (slc = sea-level corrected) values of Bu2 is +0.56 ‰ between 76 and 139.3 mm DFT and +0.63 ‰ between 139.3 and 324 mm DFT. Thus, the difference between these two sections is only 0.07 ‰, which is comparable with the analytical uncertainty of the $\delta^{18}\text{O}$ measurements. The effect of the sea-level correction is shown in supplementary Fig A6.1.

6.4.4 Strontium isotope analysis

$^{87}\text{Sr}/^{86}\text{Sr}$ ratios were determined for Bu2 as well as for several other samples from the cave environment (i.e. soil and host rock). The samples of Bu2 (20 to 30 mg) were processed and analysed using a Neptune MC-ICP-MS at the Laboratory of Isotope Geochemistry of the Department of Chemical and Geological Sciences, University of Modena and Reggio Emilia, Italy, following the methods described by Lugli et al. (2017b) and Weber et al. (2018b) for dissolution analyses and separation of Sr from matrix elements.

Seven Faraday detectors were used to measure the ion beams of the following masses simultaneously: ^{82}Kr , ^{83}Kr , ^{84}Sr , ^{85}Rb , ^{86}Sr , ^{87}Sr , ^{88}Sr . Strontium solutions were diluted to ~ 0.25 mg/l and introduced into the mass spectrometer via a quartz spray chamber and a nebulizer with an uptake rate of 100 $\mu\text{l}/\text{min}$. Samples were analysed, together with RMs and blank solutions, in a static-multi-collection mode with single blocks of 100 cycles (integration time 8.4 s per cycle).

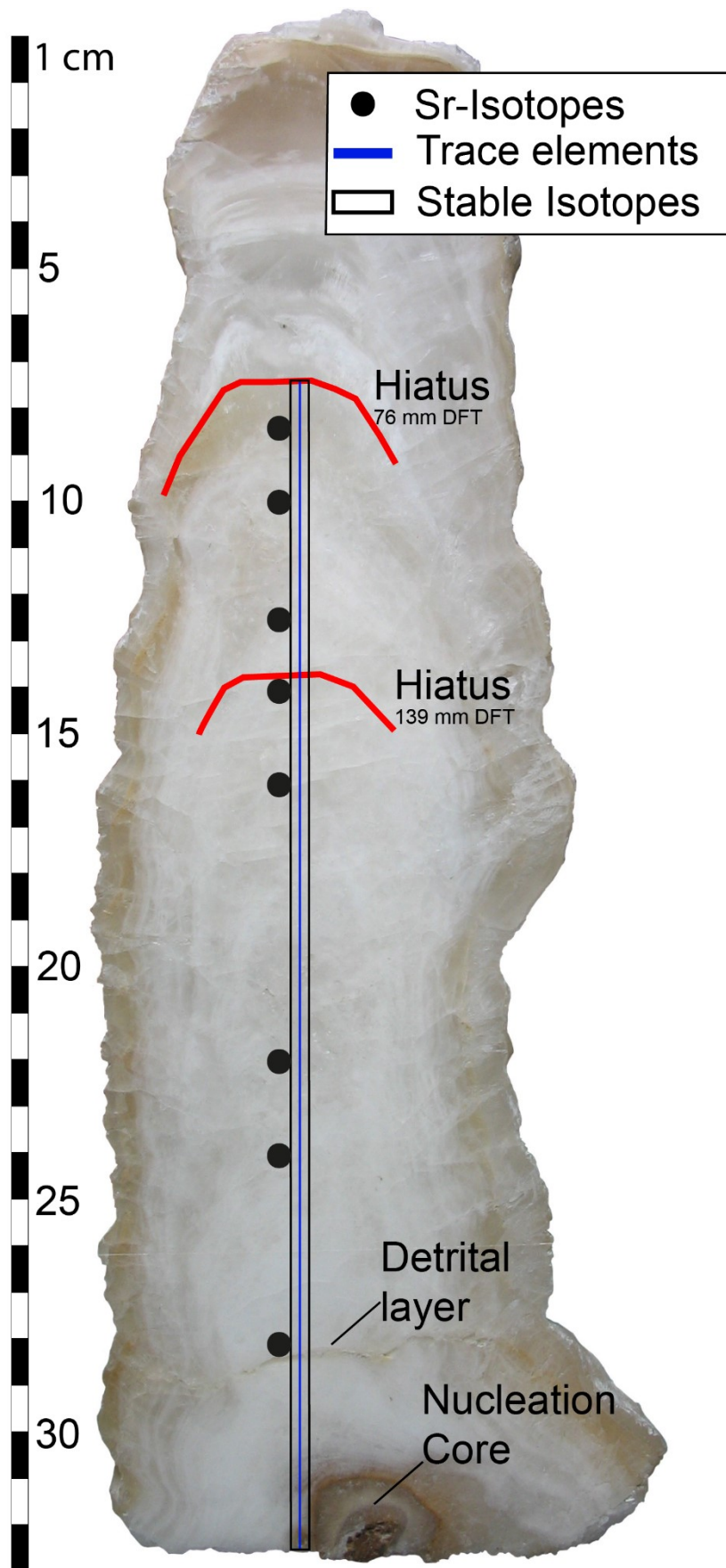


Fig. 6.2: Slab of speleothem Bu2 showing petrographic features and sampling details. Sample locations for $^{230}\text{Th}/\text{U}$ -dating are presented in supplementary Table A6.1.

A bracketing sequence was employed to correct for instrumental drifts. Krypton in the Ar gas was monitored and corrected using a $^{86}\text{Kr}/^{83}\text{Kr}$ ratio of 1.505657 and background subtraction. To correct for the presence of isobaric Rb on mass 87, a $^{87}\text{Rb}/^{85}\text{Rb}$ ratio of 0.3856656 was used. Mass bias correction was performed using an exponential law and a stable $^{88}\text{Sr}/^{86}\text{Sr}$ ratio of 8.375209. Strontium ratios were corrected using the NIST SRM 987 $^{87}\text{Sr}/^{86}\text{Sr}$ ratio of 0.710248 (McArthur et al., 2001). Daily repeated measurements of the NIST SRM 987 yielded a mean $^{87}\text{Sr}/^{86}\text{Sr}$ ratio of 0.710241 ± 0.000012 (2 SE; $n = 20$).

$^{87}\text{Sr}/^{86}\text{Sr}$ ratios of host rock and soil samples from Bunker Cave were measured by TIMS at the Institute of Environmental Physics, Heidelberg University. Strontium separation was performed using Sr specTM ion exchange resin columns. The sample size was chosen according to the Sr mass fraction providing approximately 100 ng of Sr on the filament and assuming 100% chemical yield. Soil samples were quantitatively extracted using HF. Column chemistry was performed two times using supra pure acids in order to receive sufficient chemical separation from CaCO_3 . The eluate was reduced to 2 μl and transferred onto a Re filament. Subsequent measurements (10 sequences \times 10 measurements) were performed using a Finnigan MAT 262 in multi-dynamic mode. All isotopes were measured on Faraday cups with minimum ^{86}Sr intensities of 0.5 V. Each measurement was checked for ^{85}Rb . Isotope ratios were corrected for internal mass fractionation assuming a stable $^{88}\text{Sr}/^{86}\text{Sr}$ ratio of 8.375209. Repeated measurements of NIST SRM 987 yielded $^{87}\text{Sr}/^{86}\text{Sr} = 0.710266 \pm 0.000010$ (2 SE; $n = 14$).

6.5 Results

Results from the different techniques are presented in the following with each method implemented in a separated chapter.

6.5.1 $^{230}\text{Th}/\text{U}$ -dating

Results of $^{230}\text{Th}/\text{U}$ -dating are presented in supplementary Table A6.1. In addition to the previously published Holocene part of Bu2 (Fohlmeister et al., 2012), dating revealed two distinct growth phases during early MIS 3. Based on the age model, the first growth phase (in the following referred to as MIS 3 phase 1) started at 52.0 (+0.8, -0.5) ka and ended at 50.9 (+0.6, -1.3) ka. The second growth phase (in the following referred to as MIS 3 phase 2) began at 47.3 (+1.0, -0.6) ka and ended at 42.8 (± 0.9) ka. The growth rates calculated based on the age-depth model are remarkably different between the two growth phases (supplementary Fig. A6.2). MIS 3 phase 1 is characterised by an exceptionally fast growth rate of 120 – 390 $\mu\text{m}/\text{a}$, which decreases to $\sim 40 - 60 \mu\text{m}/\text{a}$ at approximately 170 mm DFT. MIS 3 phase 2 starts with an average growth rate of $\sim 25 \mu\text{m}/\text{a}$, which further decreases to $\sim 8 \mu\text{m}/\text{a}$ at approximately 100 mm DFT.

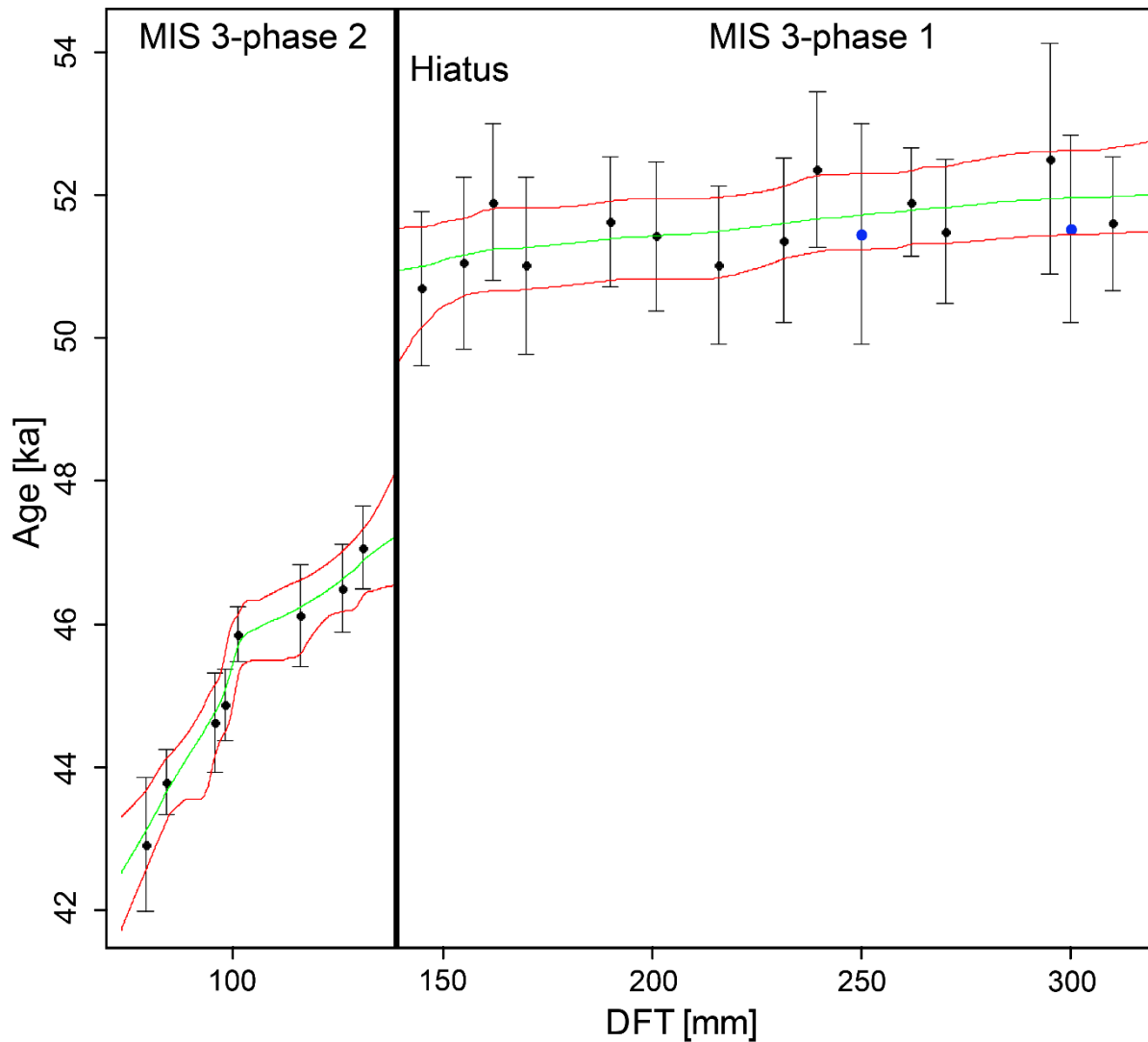


Fig. 6.3: Age-depth relationship for stalagmite Bu2. Black points show the MC-ICP-MS ^{230}Th -ages, blue points highlight the two ages measured by TIMS (supplementary Table A6.1). The green line represents the age model calculated by StalAge (Scholz and Hoffmann, 2011), while red lines show the corresponding age-uncertainties (95% confidence interval). The vertical black line marks the hiatus between the two growth phases and was guided by the abrupt change in Y mass fraction (see section 6.5.2).

In general, the ^{232}Th and ^{238}U mass fractions decrease with increasing age (supplementary Table A6.1). The $(^{230}\text{Th}/^{232}\text{Th})$ activity ratio, an indicator for the degree of detrital contamination, changes between the two growth phases. MIS 3 phase 1 shows generally higher $(^{230}\text{Th}/^{232}\text{Th})$ activity ratios between ~ 1000 and 5100 (mean = 2335 ± 1125 , 1 SD; besides sample Bu2-29), while MIS 3 phase 2 shows ratios between ~ 150 and 840 (mean = 371 ± 212 , 1 SD). Detrital correction does not have a significant influence on the ^{230}Th -ages (supplementary Table A6.1). An unsuccessful dating attempt at 291.5 mm DFT (Bu2-29), which included parts of the detrital layer, yielded an age of ~ 45 ka instead of an expected

age of ~51 ka, which indicates that this layer is possibly influenced by post-depositional U-addition (Bajo et al., 2016; Scholz et al., 2014).

We note that there is a step in the age model of Bu2 between 98 and 101 mm DFT (Fig. 6.3). To evaluate the possibility of a hiatus at this depth, thin sections (supplementary Fig. A6.4 and A6.5) and trace elements were analysed. As none of these analyses showed evidence of a growth interruption, the age model was constructed without including a hiatus resulting in a slow growth rate between these two data points of approximately 5 $\mu\text{m/a}$.

6.5.2 Trace elements and stable isotopes

The trace element records of Mg, Sr and Y as well as the stable isotope values are shown in Fig. 6.4. The trace element data were averaged by a 25 point-running mean. At 76.3 mm DFT, a rather high Mg mass fraction is visible. This corresponds to the growth stop between MIS 3 and the Holocene and is in agreement with the dating results showing the oldest Holocene age at 75 mm DFT and the youngest MIS 3 age at 79 mm DFT. Furthermore, the stalagmite shows a prominent brownish layer at this depth (Fig. 6.2). The boundary within the MIS 3 growth phase between approximately 47 and 51 ka (Fig. 6.3) can be also recognised in the trace element data. Based on the dating results, this hiatus is located between 145 and 131 mm DFT (Fig. 6.3). The mass fraction of the different trace elements changes between the two MIS 3 growth phases. Yttrium shows a significant peak of up to 7 $\mu\text{g/g}$ at 139.3 mm DFT, which is much higher than the usual background value of $\ll 1$ $\mu\text{g/g}$. At the same DFT, Mg shows a gradual increase from ~500 $\mu\text{g/g}$ up to ~800 $\mu\text{g/g}$ (Fig. 6.4). The Mg mass fraction ranges between 300 and 400 $\mu\text{g/g}$ for MIS 3 phase 1 and shows higher mass fractions during MIS 3 phase 2, ranging from 800 to 1000 $\mu\text{g/g}$. This is robust evidence for the location of the hiatus at ~139.3 mm DFT.

Magnesium and Y show a rapid increase at 280 – 282 mm DFT (Fig. 6.4), which corresponds to a layer of brownish calcite (Fig. 6.2). This increase is probably related to detrital material. Although we cannot exclude a short hiatus associated with this detrital layer, our age model cannot resolve it. Thus, we assume continuous growth during MIS 3 phase 1.

Strontium mass fractions vary between 40 and 90 $\mu\text{g/g}$. During MIS 3 phase 1, Sr shows a significant increase (20 up to 80 $\mu\text{g/g}$) at the beginning of the record followed by a general decrease towards the hiatus. During MIS 3 phase 2, Sr starts to increase again followed by a decreasing trend, which occurs around 100 mm DFT and is also observed in the Mg record.

The $\delta^{18}\text{O}_{\text{slc}}$ record can be divided into two parts: MIS 3 phase 1 shows, on average, less negative $\delta^{18}\text{O}_{\text{slc}}$ values (-4.8 ± 0.3 ‰, 1 SD) than phase 2 (-5.4 ± 0.3 ‰, 1 SD). In MIS 3 phase 2, the $\delta^{18}\text{O}_{\text{slc}}$ values show an increasing trend with decreasing DFT.

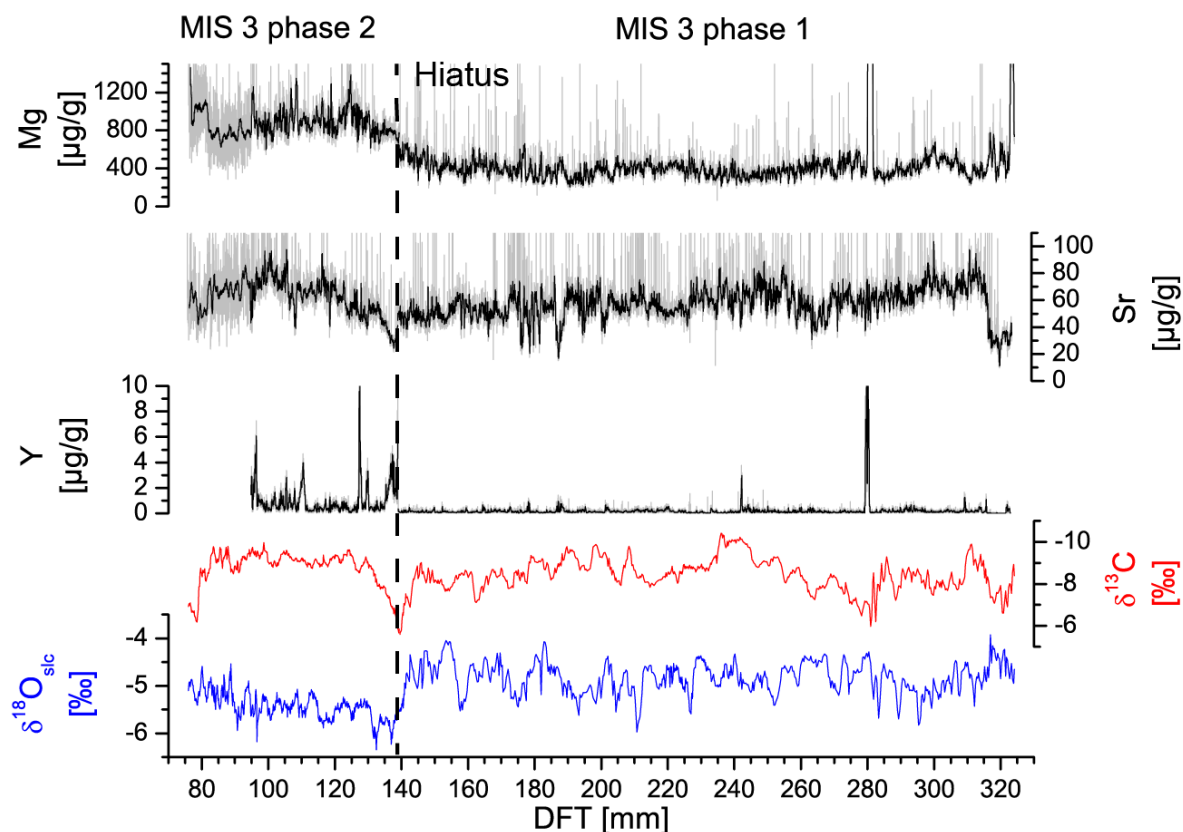


Fig. 6.4: Mass fractions of Mg, Sr and Y (high resolution data shown by grey lines) as well as $\delta^{18}\text{O}_{\text{slc}}$ (blue) and $\delta^{13}\text{C}$ (red) values of speleothem Bu2 shown versus distance from top (DFT). Note that the $\delta^{13}\text{C}$ axis is inverted. A hiatus was identified at 139.3 mm DFT. The spike in Mg and Y at 280 – 282 mm DFT is due to a detrital layer (see Fig. 6.2).

The $\delta^{13}\text{C}$ values of both growth phases vary between -5.6 ‰ and -10.4 ‰. MIS 3 phase 1 has a mean $\delta^{13}\text{C}$ value of -8.4 ‰ (± 0.8 ‰, 1 SD) and shows high-frequency variations. MIS 3 phase 2 is characterised by a mean value of -8.8 ‰ (± 0.9 ‰, 1 SD) and shows a rapid decrease from -5.6 ‰ up to approximately -9.0 ‰ between 139 and 130 mm DFT. The youngest section of MIS 3 phase 2 shows a rapid increase of the $\delta^{13}\text{C}$ values from -9.8 to -6.2 ‰.

6.5.3 Strontium isotopes

Bu2 Sr isotope data show significantly different values for the two growth phases (Fig 6.5). MIS 3 phase 1 shows $^{87}\text{Sr}/^{86}\text{Sr}$ ratios between 0.70923 ± 0.00001 and 0.70938 ± 0.00001 (mean value = 0.70931 ± 0.00005 , 1 SD), while ratios for phase 2 are lower (i.e. between 0.70907 ± 0.00001 and 0.70919 ± 0.00001 , mean value = 0.70915 ± 0.00005 , 1 SD). The Middle to Upper Devonian limestone at Bunker Cave has an average $^{87}\text{Sr}/^{86}\text{Sr}$ ratio of 0.70836 ± 0.00006 ($n = 4$, 1 SD, Fig. 6.5), which is in agreement

with the Sr isotope value expected from the seawater curve (McArthur et al., 2001). Soil horizon A at Bunker Cave has an average Sr isotope ratio of 0.7237 ± 0.0003 ($n = 2$, 1 SD, Fig. 6.5). The $^{87}\text{Sr}/^{86}\text{Sr}$ ratio of soil horizon C (0.71893 ± 0.00001 , $n = 1$) is lower than the $^{87}\text{Sr}/^{86}\text{Sr}$ ratio of soil horizon A, but still much more radiogenic than the limestone (Fig. 6.5).

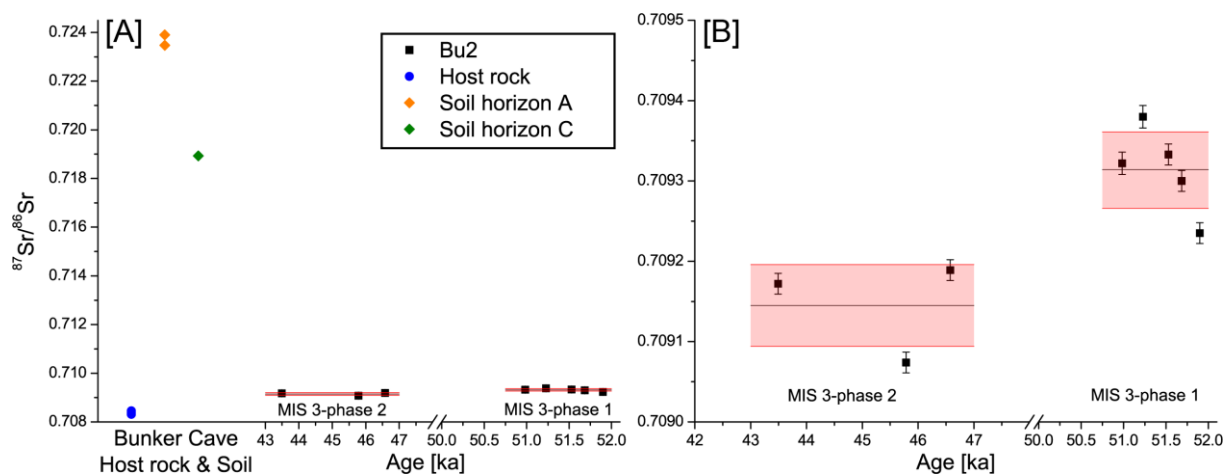


Fig. 6.5: [A] $^{87}\text{Sr}/^{86}\text{Sr}$ ratios of the host rock (blue circle), soil horizon A (orange diamond) and soil horizon C (green diamond) at Bunker Cave compared to stalagmite Bu2 values (black squares). [B] Close-up of Bu2 $^{87}\text{Sr}/^{86}\text{Sr}$ ratios during MIS 3 (black squares). The mean value is shown as a black line for each phase with the red box indicating the 1 SD. MIS 3 phase 1 shows generally higher $^{87}\text{Sr}/^{86}\text{Sr}$ ratios than MIS 3 phase 2. The soil samples show much more radiogenic $^{87}\text{Sr}/^{86}\text{Sr}$ ratios than the host rock and the speleothem. All measurement uncertainties are 2 SE.

6.6 Discussion

Implications of the obtained results for palaeoclimate in central Europe during the MIS 3 are discussed in the following chapters, starting with the timing of the Bu2 growth phases in relation to other MIS 3-palaeoclimate records.

6.6.1 Timing of growth phases

Based on the age-depth model, Bu2 started to grow at 52.0 (+0.8, -0.5) ka with high growth rates between 120 and 390 $\mu\text{m}/\text{a}$. In comparison, the growth rate of Bu2 during the Holocene was only 10 to 30 $\mu\text{m}/\text{a}$. Other Holocene speleothem samples from Bunker Cave also show low growth rates of <30 $\mu\text{m}/\text{a}$ (Bu6) and <70 $\mu\text{m}/\text{a}$ (Bu4), while a third sample (Bu1) shows growth rates around 100 $\mu\text{m}/\text{a}$ (Fohlmeister et al., 2012). In this context, the high growth rate of MIS 3 phase 1 is remarkable, especially for MIS 3 in Central Europe. Based on the $^{230}\text{Th}/\text{U}$ dating results, MIS 3 phase 1 corresponds to D/O-events 13 and 14 of the NGRIP record. Applying our age-depth model the age range for MIS 3

phase 1 is reduced to between 50.9 (+0.6, -1.3) ka and 52.0 (+0.8, -0.5) ka, rendering a correlation with D/O 14 unlikely. This is interesting given the fact that D/O 14 was the longest interstadial in MIS 3. However, at least the inception of growth of Bu2 may have been related to rather warm and humid conditions during D/O 14, despite the onset of growth was later than D/O 14.

The high growth rate of Bu2 is also exceptional in comparison with other speleothem records from Europe. For instance, the Villars Cave record (Vil-stm9, Genty et al., 2003) shows a growth rate of approximately 100 $\mu\text{m/a}$ during D/O 12 and 10 $\mu\text{m/a}$ during colder periods. Interestingly, Bu2 MIS 3 phase 1 coincides with a flooding event in Villars Cave (Genty et al., 2003; Genty et al., 2005; Genty et al., 2010), expressed by the lack of growth in Vil-stm27, suggesting wet climate conditions during this time interval. A speleothem record from Grotte des Puits de Pierra-la-Treiche (NE France) predates the onset of growth of Bu2 and shows a growth rate between 20 and 80 $\mu\text{m/a}$ for the time period from 55.4 ± 1.0 ka to 53.3 ± 0.7 ka (Pons-Branchu et al., 2010), which is also lower than most parts of MIS 3 phase 1. For Bu2 MIS 3 phase 2 the growth rate is much lower (40 – 50 $\mu\text{m/a}$ until ~46 ka, below 10 $\mu\text{m/a}$ between ~46 and ~42.8 ka), but still higher than in the Holocene. Between 47.3 (+1.0, -0.6) and 50.9 (+0.6, -1.3) ka, Bu2 stopped growing. Interestingly, stalagmite Vil-stm14 from Villars Cave showed a significantly diminished growth rate during this period. In contrast, stalagmite Vil-stm27 started to grow at this time around 48.5 ka and shows rapid growth between 47 and 44 ka (see supplementary Fig. A6.3). For this sample, growth inception was probably related to drier conditions subsequent to the flooding event in Villars Cave (Genty et al., 2010).

A similar pattern is visible in the speleothem record from Crag Cave (Fankhauser et al., 2016). One of their speleothem samples (CR032) revealed ^{230}Th -ages of 56.8 ± 0.3 ka and 47.9 ± 0.2 ka with a significant brownish layer in between, potentially related to a hiatus during HS 5. A further sample (CR008-B) yielded a ^{230}Th -age of 50.5 ± 0.4 ka, i.e. slightly predating the onset of HS 5 and coinciding within uncertainties with the growth stop of Bu2 at the end of MIS 3 phase 1. Combining these records results in a similar growth pattern as observed for Bu2, which shows a hiatus between 50.9 (+0.6, -1.3) ka and 47.3 (+1.0, -0.6) ka and is therefore in good agreement with Crag Cave (Fig. 6.6). The NALPS composite record (Moseley et al., 2014) shows a similar growth pattern with a slow growth rate between D/O-events 12 and 13 and a short break in speleothem deposition (Fig. 6.6).

The growth stop in Bu2 slightly predates the onset of HS 5 (~49.2 – 47.6 ka, Fig. 6.6), based on IRD and foraminifera data from the MD99-2331 drill core (Sánchez Goñi et al., 2013). This suggests that the climate at Bunker Cave was too cold and/or dry for speleothem growth even before the onset of HS 5 and that the short-termed D/O 13 was not sufficiently warm and humid to enable speleothem growth at Bunker Cave. This is coherent with the $\delta^{13}\text{C}$ data (see below). Based on the age uncertainty of MIS 3 phase 1, the offset between the hiatus and the start of HS 5 ranges from 400 to 2000 years.

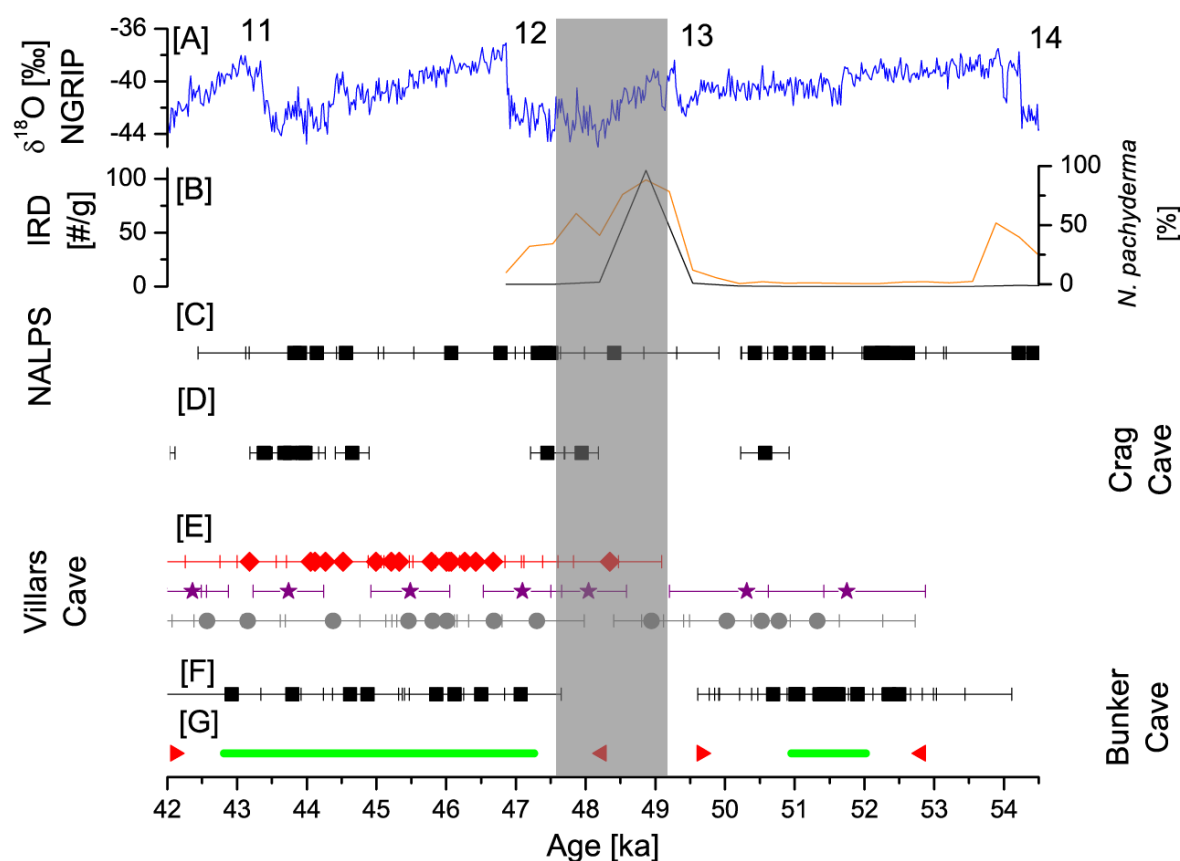


Fig. 6.6: Comparison of growth phases of different MIS 3 speleothems in Europe with the NGRIP $\delta^{18}\text{O}$ and the marine MD99-2331 records. [A] NGRIP $\delta^{18}\text{O}$ record (Svensson et al., 2008). [B] Abundance of the foraminifera *Neogloboquadrina pachyderma* (orange) and the number of IRD per gram of sediment (black) in marine core MD99-2331 (Sánchez Goñi et al., 2013). Heinrich event 5 is marked in the figure (grey box) based on these data. [C] $^{230}\text{Th}/\text{U}$ -ages of the NALPS record (Moseley et al., 2014). [D] $^{230}\text{Th}/\text{U}$ -ages from Crag Cave (Fankhauser et al., 2016). [E] $^{230}\text{Th}/\text{U}$ -ages of stalagmites Vil-stm27 (red diamond, Genty et al., 2010), Vil-stm9 (purple stars, Genty et al., 2010) and Vil-stm14 (grey circles, Wainer et al., 2009) from Villars Cave. [F] $^{230}\text{Th}/\text{U}$ -ages from Bunker Cave stalagmite Bu2 (this study) [G] Growth phases based on the age-depth model (green line) with the respective age uncertainties gives at 95 % confidence levels (red triangles) of Bu2 (this study).

6.6.2 Bu2 stable isotope data

There are several processes potentially affecting the $\delta^{13}\text{C}$ values of speleothems. An increase in speleothem $\delta^{13}\text{C}$ values may be caused by an increased drip interval and, as a consequence, enhanced disequilibrium fractionation on the stalagmite surface (Deininger et al., 2012; Mühlhous et al., 2009; Riechelmann et al., 2013; Scholz et al., 2009). Furthermore, an increase of the $\delta^{13}\text{C}$ values can be caused due to a larger contribution of host rock-derived carbon or a decrease in the soil CO_2 production rate by reduced root respiration and soil microbial activity (Cerling, 1984; Fohlmeister et al., 2011). Monitoring of Bunker Cave (Riechelmann et al., 2011) showed only small variations in the present-day annual $\delta^{13}\text{C}$

values of the dissolved inorganic carbon (DIC) of the drip water, collected at different drip sites of the cave. Modern calcite precipitation from a drip site close to the location where Bu2 was collected (watch glass VII, Riechelmann, 2010) revealed an average $\delta^{13}\text{C}$ -value of $-8.6 \pm 0.6 \text{ ‰}$, which is in the range of the more positive $\delta^{13}\text{C}$ values of the MIS 3 growth phase of Bu2 (Fig. 6.7). As described by Fohlmeister et al. (2012), vegetation density above Bunker Cave is assumed to be the major factor influencing the $\delta^{13}\text{C}$ values of speleothems. More positive $\delta^{13}\text{C}$ values of soil gas CO_2 will therefore also yield increased $\delta^{13}\text{C}$ values in the stalagmite, coherent with periods of lower drip rates. In contrast, more negative $\delta^{13}\text{C}$ values in the speleothem are associated with periods of denser vegetation as well as a thickening of the soil above the cave, increased biological soil activity and higher drip rates. The most negative $\delta^{13}\text{C}$ values during MIS 3 are in the range of the $\delta^{13}\text{C}$ values of the Holocene stalagmites and modern-day calcite samples (Fig. 6.7). This indicates, at least for some time intervals of MIS 3, an enhanced biological activity above the cave, almost as high as for present-day conditions.

Prior to the hiatus around 50.9 ka, the $\delta^{13}\text{C}$ values increase rapidly from around -9 ‰ to -5.5 ‰ (Fig. 6.8). This suggests a decrease in vegetation density and soil bioproductivity, resulting in more positive $\delta^{13}\text{C}$ values of soil gas CO_2 and ultimately in Bu2, similar to the $\delta^{13}\text{C}$ values of Villars Cave speleothem Vil-stm9 around the MIS 4 cold period (Genty et al., 2010). This climate deterioration recorded in Bu2 precedes the onset of HS 5 ($\sim 49.2 - 47.6 \text{ ka}$, Fig. 6.8) and implies that the climate at Bunker Cave was too cold and/or dry even before the onset of HS 5, potentially due to gradual cooling towards HS 5 and insufficient warming during D/O 13, related to its short duration.

Bu2 started to grow again at $\sim 47.3 \text{ ka}$ with similar $\delta^{13}\text{C}$ values as prior to the hiatus (-5.5 ‰ , Fig. 6.8). The following decrease in $\delta^{13}\text{C}$ values to $\sim -9 \text{ ‰}$ is associated with D/O 12 and occurred relatively slowly, in particular in comparison to other climate records, such as the $\delta^{18}\text{O}$ values of NGRIP and NALPS (Fig. 6.8). This may be related to biological and/or buffering processes in the soil, which are likely to occur on longer time scales than the processes controlling the $\delta^{18}\text{O}$ values of precipitation. Although in a different climate setting, a similar discrepancy between the evolution of $\delta^{13}\text{C}$ and $\delta^{18}\text{O}$ values in response to rapid climate change within a single stalagmite has been shown for Sofular Cave (Fleitmann et al., 2009). Another explanation for the discrepancy of the duration of the transition into D/O 12 are the dating uncertainties of the individual records, which is in the range of a few hundred years, in particular for the stalagmite records (Fig. 6.6). In general, the $\delta^{13}\text{C}$ values of Bu2 show a D/O-like pattern as the $\delta^{18}\text{O}$ values of the NGRIP (Svensson et al., 2008) and NALPS records (Moseley et al., 2014), making the correlation with D/O 12 plausible. The later part of MIS 3 phase 2 is characterised by rather stable $\delta^{13}\text{C}$ values around -9 to -10 ‰ until $\sim 44.5 \text{ ka}$ (Fig. 6.8). Subsequently, the $\delta^{13}\text{C}$ values increase until 44.1 ka , followed by a decrease by about 1 ‰ , which, however, is insignificant compared to the overall change in $\delta^{13}\text{C}$ during MIS 3 phase 2. Thus, although the timing of this decrease is synchronous within uncertainty with D/O 11 in the NALPS and NGRIP $\delta^{18}\text{O}$ records (Fig. 6.8), we cannot precisely identify D/O 11 in the Bu2 $\delta^{13}\text{C}$ record. This finding is coherent with the Villars Cave

record, where D/O 11 is also not obvious; probably due to its short duration (Genty et al., 2010). However, the significant increase in $\delta^{13}\text{C}$ values after ~ 43.3 ka indicates a climate deterioration, associated with the cooling phase after D/O 11. While the NAPLS record shows a growth stop during D/O 11, the Bu2 record shows a growth stop after D/O 11, about 1000 years later. In contrast to the NAPLS stalagmites, growth of the Bu2 stalagmite did not recommence until the onset of the Holocene, probably related to a further European cooling trend after ~ 45 ka, as described in the Villars Cave record (Genty et al., 2010).

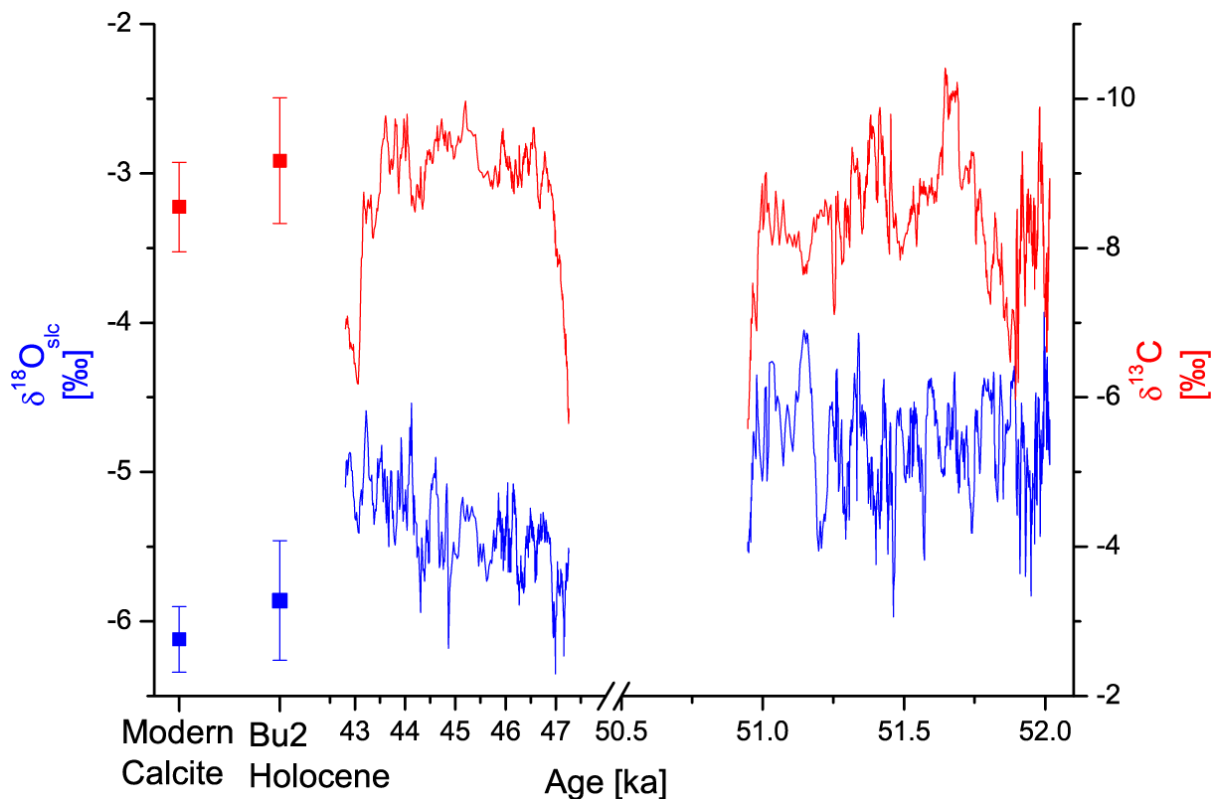


Fig. 6.7: Speleothem Bu2 $\delta^{13}\text{C}$ (red) and $\delta^{18}\text{O}_{\text{slc}}$ (blue) record plotted against age. Also shown are the $\delta^{13}\text{C}$ and $\delta^{18}\text{O}$ values from modern calcite precipitated on watch glasses (Riechermann, 2010) placed under a drip site (TS 7) close to the Bu2 drip site and the Holocene section of Bu2 (Fohlmeister et al., 2012). Note that the $\delta^{13}\text{C}$ axis is inverted.

The $\delta^{18}\text{O}_{\text{slc}}$ values of Bu2 do neither show a similar pattern as the $\delta^{13}\text{C}$ values (Fig. 6.7) nor strong variability during D/O-events, as would be expected from other records (NGRIP, NAPLS, Fig. 6.8). MIS 3 phase 1 shows higher $\delta^{18}\text{O}_{\text{slc}}$ values than phase 2. In addition, the second growth phase shows progressively increasing $\delta^{18}\text{O}_{\text{slc}}$ values. In general, the interpretation of the $\delta^{18}\text{O}$ values of Bu2 in terms of past climate variability is challenging, as has also been shown for other speleothems from Central

Europe (e.g. Mischel et al., 2017b; Scholz et al., 2012). Therefore, the discussion of the $\delta^{18}\text{O}$ values is only provided in the supplement (section 6.9.1).

6.6.3 Palaeoclimate implications

The Bunker Cave system has been intensively studied by both cave monitoring (Immenhauser et al., 2010; Riechelmann et al., 2011; Riechelmann et al., 2013; Riechelmann et al., 2012a; Riechelmann et al., 2014; Riechelmann et al., 2017) and speleothem-based palaeoclimate reconstructions (Fohlmeister et al., 2012; Riechelmann et al., 2012b). Based on the findings of von Kamp and Ribbert (2005), Fohlmeister et al. (2012) argued that loess with a higher Mg/Ca ratio than the Devonian limestone host rock was deposited above Bunker Cave during the last glacial maximum (LGM). They assumed that progressive leaching of this wind-blown dust resulted in elevated Mg/Ca ratios in the drip water and the speleothems at the beginning of the Holocene. MIS 3 phase 1 (52.0 – 50.9 ka) shows significantly lower Mg values compared to MIS 3 phase 2 (Fig. 6.4). Thus, the increase in the Mg/Ca ratio from MIS 3 phase 1 to phase 2 may be related to loess deposition during HS 5. This is consistent with the data of von Kamp and Ribbert (2005), who suggested loess deposition in the area around Bunker Cave during MIS 3. However, both speleothem growth phases show lower Mg/Ca ratios than during the Holocene. Since the Mg-content of loess can be highly variable (Gallet et al., 1998; Taylor et al., 1983), this may be related to different Mg/Ca ratios of the LGM and the MIS 3 loess. The Mg/Ca ratio of the loess above Bunker Cave has not been determined.

Another factor potentially affecting the Mg mass fraction of speleothems in Bunker Cave is prior calcite precipitation (PCP, Fairchild et al., 2000; Riechelmann et al., 2011), which accounts for calcite precipitation from the parent solution prior to dripping on top of the stalagmite. Reduced infiltration in the catchment above the cave will result in an increase of the residence time of the water in the host rock and in reduced drip rates. This results in increased PCP, which, in turn, results in increasing Mg/Ca ratios (Tooth and Fairchild, 2003). A third potential explanation affecting the Mg/Ca ratios of speleothems at Bunker Cave are the different dissolution characteristics of calcite and dolomite (Fairchild and Treble, 2009). With increasing residence times, the relative contribution from dissolution of dolomite will increase and therefore result in elevated Mg/Ca ratios of the drip water and the speleothem. In summary, those mechanisms suggest increasing Mg/Ca ratios during dry conditions. In general, the Mg mass fraction of Bunker Cave speleothems can, thus, be used as a proxy for precipitation amount (Fohlmeister et al., 2012; Wassenburg et al., 2016a). Thus, the lower Mg mass fraction of MIS 3 phase 1 indicates more humid conditions than during MIS 3 phase 2. This is also supported by the much higher growth rate during MIS 3 phase 1, which suggests higher rainfall amounts.

The Sr isotope ratio of all Bu2 samples is significantly higher than expected from the overlying hostrock, indicating an external radiogenic source. In most cases, this additional material is incorporated in the

soil above the cave area, e.g. by deposition of atmospheric dust (Banner et al., 1996; Frumkin and Stein, 2004; Zhou et al., 2009). We argue that the changes in the Sr isotope ratio of Bu2 are mainly attributed to changes in rainfall intensity and/or changes in soil $p\text{CO}_2$ resulting in varying Sr contribution from the soil and host rock. Smart and Friedrich (1987) developed a model where different amounts of rainfall caused changes in the routes of vadose ground-water flow. This model was adapted by Banner et al. (1996) and applied to the Sr isotope composition of the Barbados karst system. According to these studies, changes in the amount of rainfall above the cave affect the pathway of the water in the karst aquifer. During periods of diminished rainfall, the drip water preferentially percolates along seepage routes. During periods of elevated rainfall, the capacity of these seepage routes is exceeded, and the drip water is transported into the cave by conduit flow along paths with a higher permeability, resulting in an overflow (Riechelmann et al., 2011). This results in a decreased residence time and a reduced interaction of the percolating water with the host rock. Hence, we expect that the drip water composition and, ultimately, the Sr isotope signature of the speleothem sample, will evolve towards the soil signature ($^{87}\text{Sr}/^{86}\text{Sr} > 0.718$) during times of elevated rainfall. In contrast, periods with lower rainfall amounts should be characterised by a speleothem $^{87}\text{Sr}/^{86}\text{Sr}$ ratio shifted towards the host rock signature ($^{87}\text{Sr}/^{86}\text{Sr} = 0.70836 \pm 0.00006$). These patterns are clearly visible in the Bu2 $^{87}\text{Sr}/^{86}\text{Sr}$ record. MIS 3 phase 1, which exhibits a faster growth rate, shows an average $^{87}\text{Sr}/^{86}\text{Sr}$ ratio of 0.70931 ± 0.00005 (1 SD), significantly more radiogenic than MIS 3 phase 2. The latter, growing at a slower growth rate, shows an average $^{87}\text{Sr}/^{86}\text{Sr}$ ratio of 0.70915 ± 0.00005 (1 SD). Both the large growth rate and the Sr isotope signatures therefore indicate enhanced rainfall and infiltration during MIS 3 phase 1, consistent with the Mg record. A further explanation would be changes of drip water $^{87}\text{Sr}/^{86}\text{Sr}$ due to changes in the weathering of soil components as a result of differences in soil $p\text{CO}_2$ (Banner et al., 1996). Sr isotopes are widely used in the soil environment to trace weathering processes (Capo et al., 1998; Stewart et al., 1998). The most likely external soil component is loess, potentially deposited during MIS 4 and HS 5 in the Bunker Cave area (von Kamp and Ribbert, 2005). This loess usually has a high Si-content (Gallet et al., 1998) and a highly radiogenic $^{87}\text{Sr}/^{86}\text{Sr}$ ratio (Taylor et al., 1983). During warm periods with increased biological activity, as suggested for MIS 3 phase 1, weathering of silicate material is enhanced resulting in increased input of radiogenic Sr into the drip water and the speleothems. It is likely that the Sr isotope composition of the drip water was affected by both mechanisms

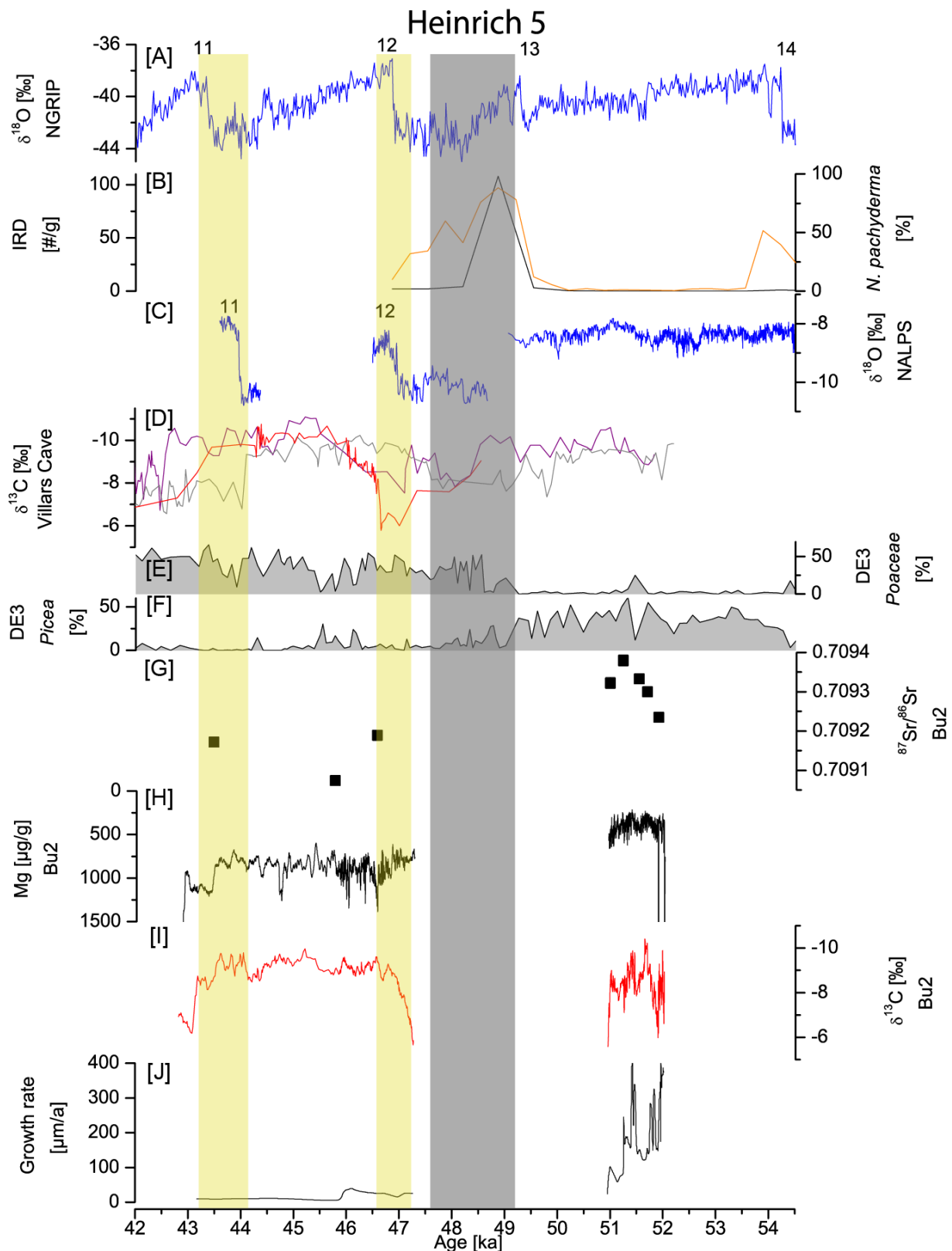


Fig. 6.8: Comparison of the Bu2 multi-proxy record with other MIS 3 climate records. Yellow boxes show the timing of D/O-events 12 and 11. [A] NGRIP $\delta^{18}\text{O}$ record (Svensson et al., 2008). [B] Abundance of the foraminifera *Neogloboquadrina pachyderma* (orange) and the number of IRD per gram of sediment (black) in marine core MD99-2331 (Sánchez Goñi et al., 2013). Heinrich 5 event is marked in the figure (grey box) based on these data. [C] NALPS oxygen isotope record from alpine

speleothem samples (Moseley et al., 2014). [D] Villars Cave stable carbon isotope records, Vil-stm9 (purple), Vil-stm14 (grey), Vil-stm27 (red, Genty et al., 2003; Genty et al., 2010; Wainer et al., 2009) [E] Percentage of *Poaceae*-pollen in drill core DE3 from the Eifel, Germany (Sirocko et al., 2016). [F] Percentage of *Picea*-pollen in drill core DE3 from the Eifel, Germany (Sirocko et al., 2016). [G] Sr isotope data of Bu2. [H] Mg mass fraction of Bu2. [I] $\delta^{13}\text{C}$ values of Bu2. Note inverted axis for Mg mass fractions and $\delta^{13}\text{C}$ values. [J] Growth rate of Bu2.

Although the minimum $\delta^{13}\text{C}$ values of the two MIS 3 growth phases of Bu2 are similar, the other proxy data (Sr isotopes, Mg mass fraction, growth rate, Fig. 6.8) suggest that MIS 3 phase 1 was characterised by a generally more humid climate compared to MIS 3 phase 2, in agreement with pollen records from the Eifel (Sirocko et al., 2016). The latter show more abundant *Picea* and *Carpinus* pollen during MIS 3 phase 1 (Fig. 6.8). Both plant species are indicators of rather humid and relatively warm conditions, indicating summer temperatures only slightly lower than modern-day temperatures, thus suggesting a mild climate during early MIS 3. High abundance of *Poaceae* pollen indicate dry conditions and open landscapes with less dense vegetation during MIS 3 phase 2, which was characterised by (at least seasonal) aridity indicated by the very low abundance of *Pinus* (Fig. 6.8). This implies a more open boreal forest with generally drier conditions. Interestingly, this change in vegetation is not reflected in the $\delta^{13}\text{C}$ record of our speleothem, potentially related to colder conditions in the Eifel than in nearby areas (Sirocko et al., 2016). Although precipitation decreased, it was obviously still sufficiently humid to enable vegetation and soil development above Bunker Cave, at least until the $\delta^{13}\text{C}$ values increased again around 43.5 ka. The high $\delta^{13}\text{C}$ values around 43 ka, shortly before the growth stop, coincide with Greenland Stadial 11 (Rasmussen et al., 2014). Consequently, a severe climate deterioration seems to be the most plausible cause for the increase of the $\delta^{13}\text{C}$ values and Mg mass fraction, as well as the following growth stop, possibly amplified by disequilibrium isotope fractionation on the stalagmite surface induced by a very slow drip rate (Deininger et al., 2012; Mühlinghaus et al., 2009). This is supported by the very low growth rate of $<10 \mu\text{m/a}$ towards the end of MIS 3 phase 2.

Overall, Bu2 recorded two generally humid and warm phases during early MIS 3. Based on the proxy data, the two growth phases were characterised by different climate conditions. While MIS 3 phase 1 was humid and warm, we observe a significant decrease in water availability subsequent to the hiatus associated with HS 5. However, climatic and environmental conditions were still favourable for speleothem growth at Bunker Cave. Thus, we assume that MIS 3 phase 2 was still a comparably humid and warm period, although it was probably drier and colder than during the first MIS 3 growth phase.

6.7 Conclusions

Speleothem Bu2 from Bunker Cave offers the possibility to investigate past climate variability during two early phases of MIS 3 north of the Alps in Central Europe. This MIS 3 speleothem record shows that the climatic conditions during this phase were, at least during some parts, favourable of speleothem growth. Therefore, speleothem Bu2 potentially recorded the two warmest and most humid phases of MIS 3 in Central Europe.

The timing of the hiatus between the two growth phases is coherent with HS 5 (Sánchez Goñi et al., 2013). The high growth rate, the elevated Sr isotopes and the low Mg content suggest increased water availability and enhanced precipitation during the initial MIS 3 growth phase of Bu2. This is further supported by the occurrence of thermophilous trees in a nearby Eifel pollen record (Sirocko et al., 2016). During the second MIS 3 growth phase, precipitation was substantially lower, as suggested by the slower growth rate, the lower Sr isotope ratios and the higher Mg content. This is consistent with the evidence of boreal forests in the Eifel (Sirocko et al., 2016). The $\delta^{13}\text{C}$ values clearly reflect D/O event 12, while the $\delta^{18}\text{O}$ record does not show a D/O-type pattern.

6.8 Acknowledgements

M. Weber, K.P. Jochum and D. Scholz are thankful to the Max Planck Graduate Center, the German Research Foundation (DFG SCHO 1274/9-1) and Palmod for funding. We are indebted to Anna Cipriani for the use of geochemical facilities at University of Modena and Reggio Emilia. We also thank B. Schwager, B. Stoll, U. Weis and M. Wimmer for assistance in the laboratory and F. Sirocko and F. Fuhrmann for the discussion of the pollen data. The authors thank the Editor, A. Moreno, as well as G. Zanchetta and two anonymous referees for their thorough reviews and constructive comments, which helped to improve the manuscript.

6.9 Supplement

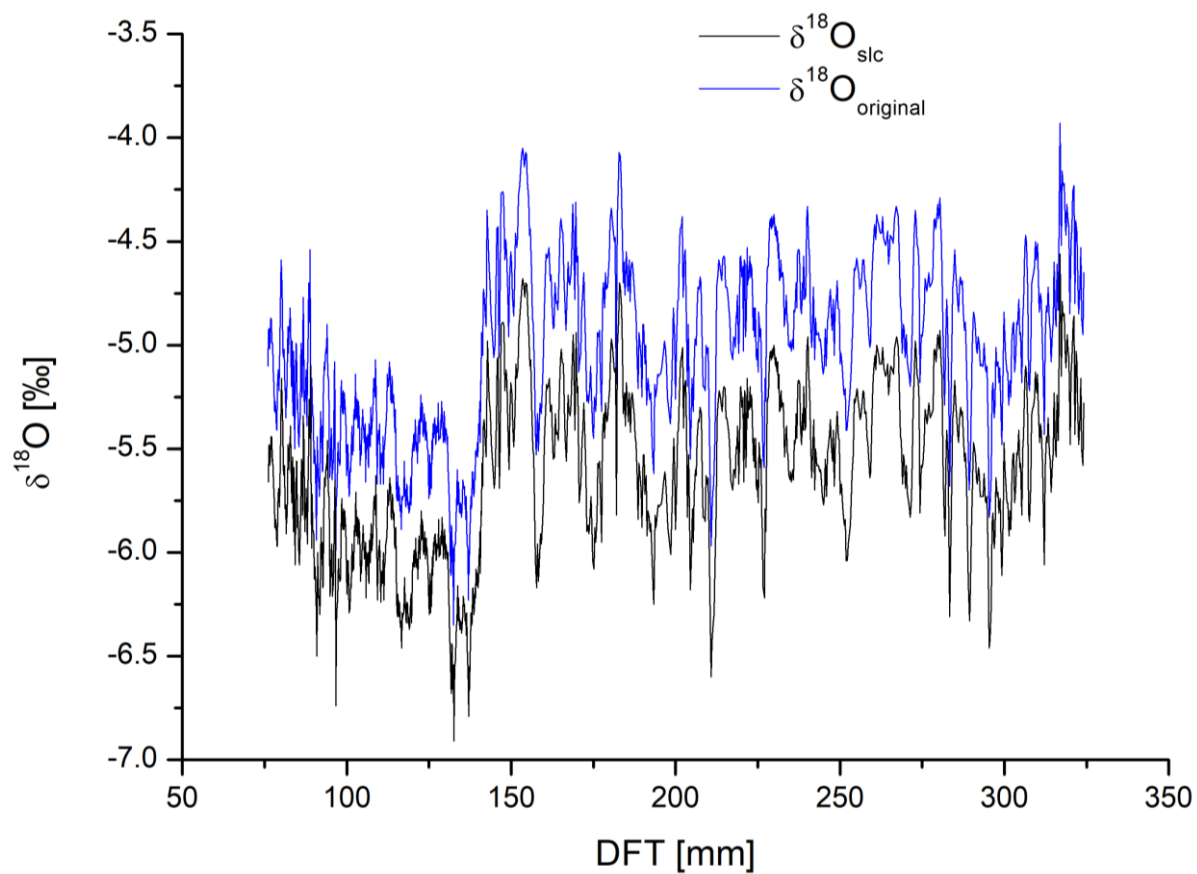


Fig. A6.1: Effect of the sea-level correction on the $\delta^{18}\text{O}$ values of Speleothem Bu2, based on the correction factor of Duplessy et al. (2007) and the sea-level reconstruction of Bates et al. (2014b) and Bates et al. (2014a).

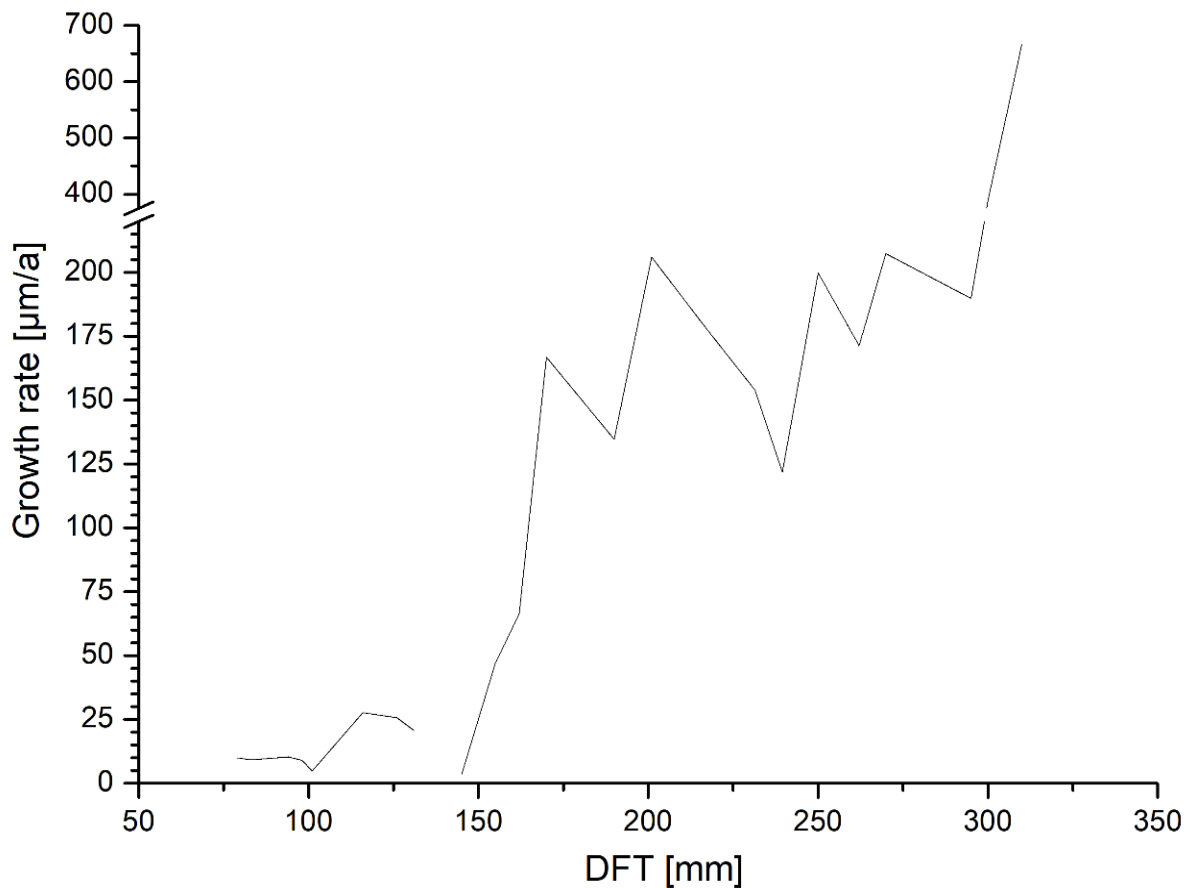


Fig. A6.2: Growth rate of Bu2 against DFT, based on the age-depth model constructed with StalAge (Scholz and Hoffmann, 2011).

A comparison of the age data of Bu2 with the Villars cave records from Genty et al. (2010) and Wainer et al. (2009) is shown in Fig. A6.3. Stalagmite Vil-stm14 starts to grow around 52 ka, which is in perfect agreement with MIS 3-phase 1 of our Bu2-record (Fig. 6.6). Stalagmite Vil-stm27 started to grow around 48 ka, simultaneously with the beginning of MIS 3-phase 2 of Bu2 (Fig. 6.6). Speleothem Vil-stm14 stopped growing at around 42 ka, in agreement with the end of MIS 3-phase 2 of Bu2. Growth of Vil-stm27 declined remarkably after 41 ka, when Bu2 and Vil-stm14 already had stopped growing. Compared to Bu2, both speleothems from Villars Cave show a generally faster growth rate of up to 280 $\mu\text{m/a}$ during the later growth phase.

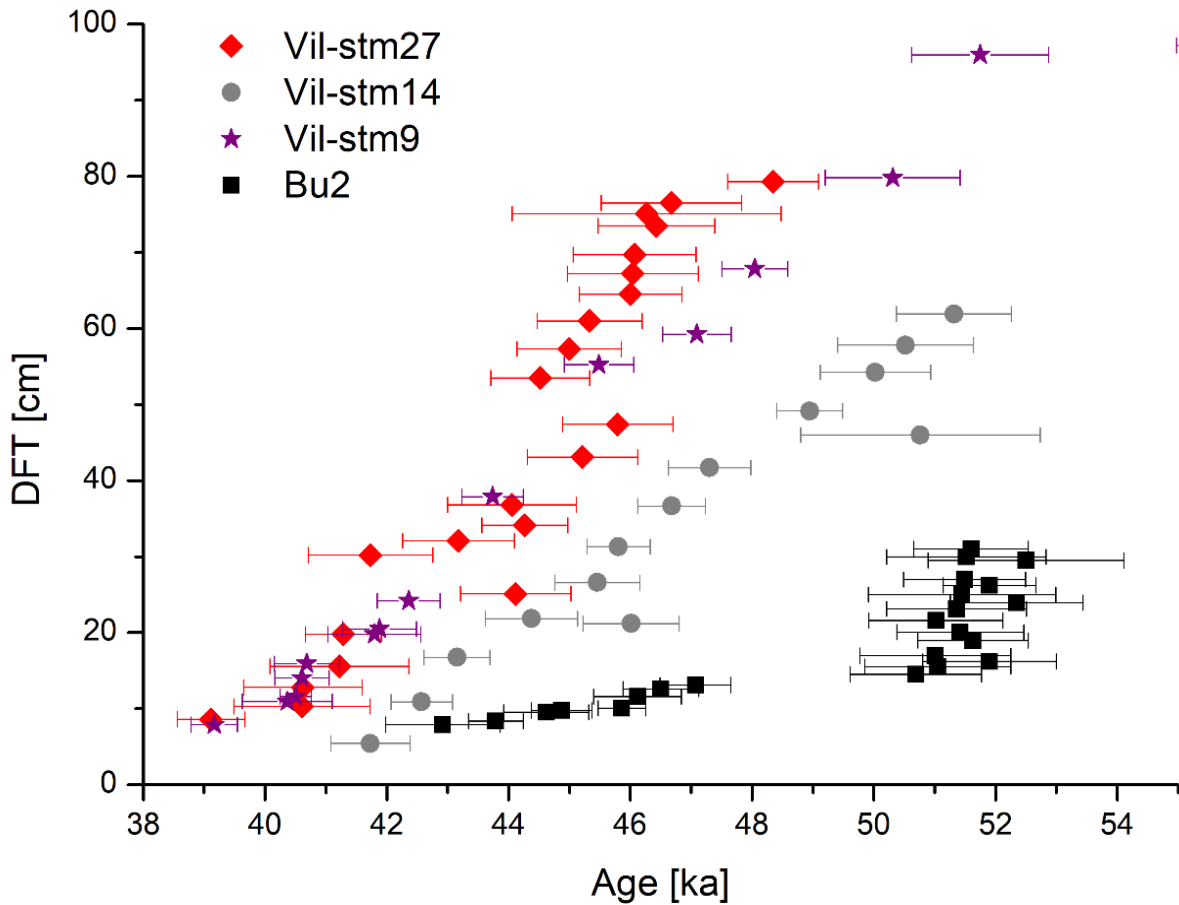


Fig. A6.3: Comparison of the age-depth relationships of four different European speleothems that cover MIS 3. Black closed squares are the ^{230}Th -ages from Bu2 (this study). ^{230}Th -ages from speleothems from Villars Cave are illustrated by red diamonds (Vil-stm27, Genty et al., 2010), grey circles (Vil-stm14, Wainer et al., 2009) and purple stars (Vil-stm-9, Genty et al., 2010). In general, there are only few data points between 48 and 50 ka, showing the inhibiting influence of the Heinrich 5 cold event on speleothem growth in Europe. Bu2 stopped growing completely, while the Vil-stm14 stalagmite showed a significantly diminished growth rate. Vil-stm27 started to grow at this time around 48.5 ka and shows rapid growth between 47 and 44 ka.

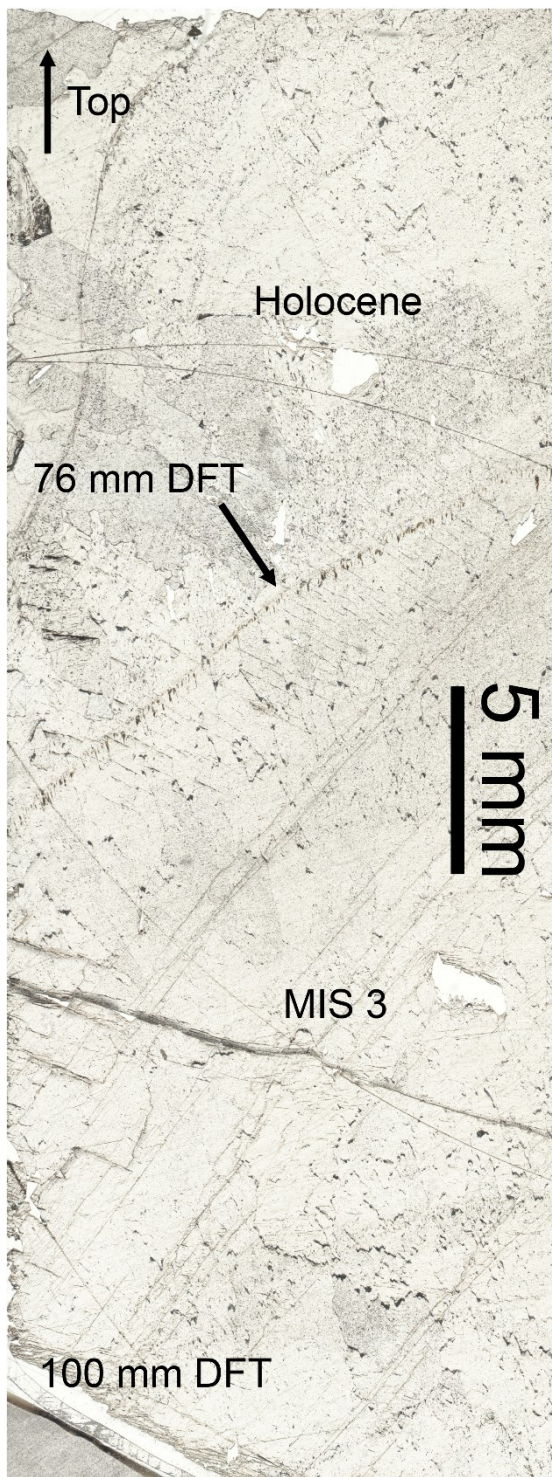


Fig. A6.4: Thin section of Bu2 between 63 and 101 mm DFT showing the hiatus between the Holocene and MIS 3 at 76 mm DFT. Around 100 mm DFT, no hiatus is visible.



Fig. A6.5: Thin section of Bu2 between 123 and 151mm DFT showing the hiatus between the two MIS 3 growth phases at 139 mm DFT.

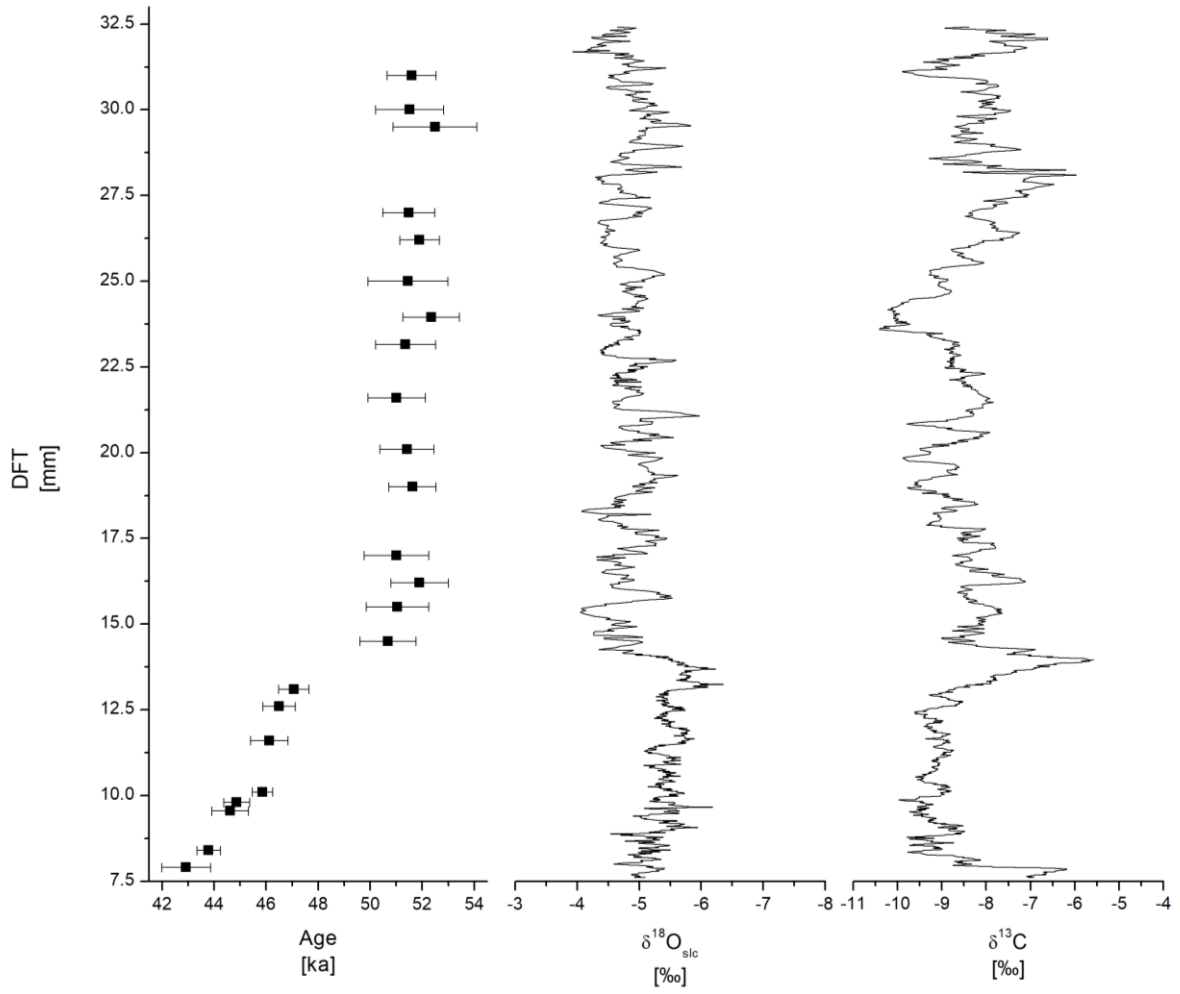


Fig. A6.6: $^{230}\text{Th}/\text{U}$ dating results and stable isotope data of Bu2 plotted against DFT.

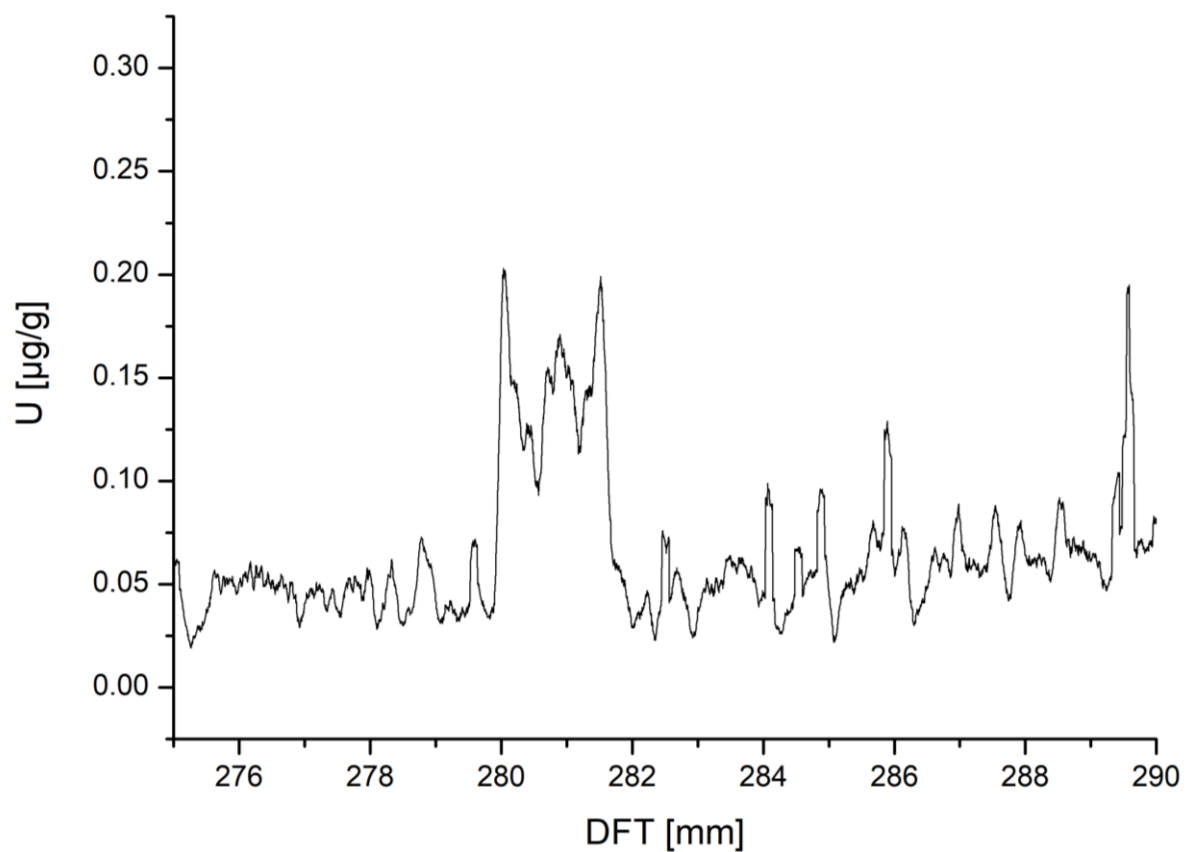


Fig. A6.7: Increase in U at the detrital layer (see Fig. 6.2) suggesting post-depositional mobilization of U probably resulting in an apparently too young age for sample Bu2-29 (see supplementary Table A6.1 and section 6.5.1 in the manuscript).

Table A6.1: Uranium and Th mass fractions, activity ratios and ^{230}Th -ages for stalagmite sample Bu2. All uncertainties are quoted as 2 SE. Samples marked with an asterisk were analysed by TIMS, all other samples by MC-ICP-MS. Ages are given in thousand years (ka) before 2017. All activity ratios and ages were corrected for detrital contamination, using a $^{232}\text{Th}/^{238}\text{U}$ mass ratio of 3.8, calculated from the average Th and U mass fractions of tonalities which are believed to be representative for the bulk continental crust (Wedepohl, 1995), assuming an uncertainty of 50 % and ^{230}Th , ^{234}U and ^{238}U in secular equilibrium for the detritus. Activity ratios were calculated using the half-lives from Cheng et al. (2000). Sample BU-2-29 was not used for the age model and is therefore presented in italic (see section 6.5.2).

Sample	DFT [mm]	Uncertainty	^{232}Th [ng/g]	Uncertainty	^{238}U [ng/g]	Uncertainty	$(^{234}\text{U}/^{238}\text{U})$	Uncertainty	$(^{230}\text{Th}/^{238}\text{U})$	Uncertainty	$(^{230}\text{Th}/^{232}\text{Th})$	Uncertainty	Uncorrected Age [ka]	Uncertainty	Corrected Age [ka]	Uncertainty [ka]
BU2-7.5	75	2.0	1.163	0.012	194.46	1.20	1.580	0.002	0.154	0.001	79.51	0.80	11.25	0.08	11.15	0.10
BU2-7.9	79	2.0	0.490	0.014	133.28	1.29	1.375	0.011	0.454	0.007	378.21	11.69	42.99	0.92	42.92	0.94
BU2-8.3	84	1.5	1.118	0.012	115.93	0.90	1.380	0.006	0.463	0.003	147.25	1.47	43.99	0.44	43.79	0.45
BU2-9.4	95.5	1.0	0.842	0.009	119.17	1.13	1.364	0.010	0.465	0.005	201.72	2.23	44.77	0.69	44.62	0.70
BU2-9.8	98	1.0	0.617	0.006	119.04	0.94	1.368	0.007	0.469	0.004	276.69	2.75	44.97	0.51	44.87	0.50
BU2-10	101	1.5	0.795	0.009	135.51	0.92	1.376	0.003	0.480	0.003	250.57	2.63	45.98	0.40	45.86	0.39
BU2-11.5	116	2.0	0.200	0.004	113.47	0.95	1.386	0.007	0.486	0.006	841.27	19.05	46.16	0.71	46.12	0.72
BU2-12.5	126	2.0	0.309	0.006	112.52	0.74	1.410	0.003	0.498	0.005	554.84	11.18	46.55	0.61	46.50	0.62
BU2-13.1	131	1.5	0.518	0.005	106.83	0.89	1.409	0.008	0.503	0.004	317.07	3.02	47.16	0.56	47.07	0.58
BU2-14.5	145	1.5	0.025	0.001	65.70	0.62	1.356	0.010	0.513	0.008	4119.23	122.50	50.69	1.09	50.69	1.08
BU2-15.5	155	1.5	0.021	0.001	68.07	0.69	1.357	0.011	0.516	0.009	5131.09	172.04	51.05	1.21	51.05	1.20
BU2-16	162	2.0	0.034	0.001	43.90	0.35	1.354	0.007	0.522	0.009	2040.88	58.16	51.91	1.11	51.90	1.10
BU2-17	170	1.5	0.032	0.001	56.59	0.55	1.345	0.011	0.511	0.009	2784.17	90.23	51.02	1.27	51.01	1.24
BU2-19	190	1.5	0.050	0.001	66.74	0.57	1.349	0.008	0.517	0.007	2125.74	55.10	51.64	0.92	51.63	0.91
BU2-20	201	1.5	0.043	0.001	69.30	0.47	1.355	0.003	0.518	0.008	2576.67	74.93	51.43	1.06	51.42	1.04
BU2-21.6	216	2.5	0.042	0.001	70.35	0.58	1.350	0.008	0.513	0.008	2625.68	68.01	51.03	1.12	51.02	1.10
BU2-23	231.5	1.5	0.090	0.002	56.93	0.40	1.350	0.004	0.516	0.009	1002.15	30.21	51.39	1.11	51.36	1.15
BU2-24	239.5	2.0	0.082	0.002	63.66	0.54	1.345	0.008	0.521	0.008	1232.36	34.92	52.37	1.08	52.35	1.09
BU2-25*	250	2.0	0.105	0.001	62.67	0.06	1.349	0.005	0.516	0.012	944.65	22.84	51.49	1.51	51.45	1.54
BU-2-26	262	2.0	0.042	0.001	50.32	0.37	1.356	0.004	0.522	0.006	1916.54	51.96	51.92	0.77	51.90	0.76
BU-2-27	270	2.5	0.039	0.001	48.07	0.33	1.351	0.005	0.517	0.008	1947.82	55.99	51.51	1.02	51.49	1.00
<i>BU-2-29</i>	<i>291.5</i>	<i>3.0</i>	<i>1.170</i>	<i>0.013</i>	<i>72.35</i>	<i>0.48</i>	<i>1.386</i>	<i>0.003</i>	<i>0.473</i>	<i>0.004</i>	<i>89.72</i>	<i>1.03</i>	<i>44.91</i>	<i>0.46</i>	<i>44.59</i>	<i>0.48</i>
BU2-29.5	295	1.0	0.073	0.003	63.27	0.65	1.343	0.012	0.522	0.012	1381.96	60.21	52.53	1.56	52.50	1.61
BU2-30*	300	2.5	~0	NA	64.68	0.13	1.350	0.010	0.517	0.010	NA	NA	51.52	1.33	51.52	1.31
BU-2-31	310	1.5	0.065	0.002	60.78	0.41	1.337	0.003	0.512	0.007	1473.25	43.30	51.62	0.95	51.60	0.94

Table A6.2: Quality control materials from the LA-ICP-MS measurements at the Institute of Geosciences, Johannes Gutenberg University Mainz.

Element	Mg	P	Sr	Y	Th	U
Measured Isotope	²⁵ Mg	³¹ P	⁸⁸ Sr	⁸⁹ Y	²³² Th	²³⁸ U
NIST SRM 610						
Mean [$\mu\text{g/g}$] (n = 24)	523	426	497	464	433	421
1SD [$\mu\text{g/g}$]	11	29	14	29	47	22
GeoReM [$\mu\text{g/g}$]	432	413	516	462	457	462
RSF	1.21	1.03	0.96	1.01	0.95	0.91
USGS BCR-2G						
Mean [$\mu\text{g/g}$] (n = 24)	22101	1488	329	35.1	6.23	1.58
1SD [$\mu\text{g/g}$]	535	44	11	0.7	0.31	0.12
GeoReM [$\mu\text{g/g}$]	21471	1615	342	35.0	5.90	1.69
RSF	1.03	0.92	0.96	1.00	1.06	0.94
USGS MACS-3*						
Mean [$\mu\text{g/g}$] (n = 24)	1992	175	6965	19.1	48.1	1.53
1SD [$\mu\text{g/g}$]	72	43	299	1.3	3.1	0.29
GeoReM [$\mu\text{g/g}$]	1756	104	6760	22.9	55.4	1.52
RSF	1.13	1.69	1.03	0.83	0.87	1.01

*Please note that USGS MACS-3 has no preferred values in GeoReM. Therefore, we used the compiled values from Jochum et al. (2012). ⁴³Ca was used as internal reference. The RSF (Relative Sensitivity Factor) is calculated as the ratio between the average measured mass fractions divided by the literature value.

Table A6.3: Operational parameters for LA-ICP-MS measurements at the Goethe University Frankfurt and the Johannes Gutenberg University Mainz.

Operating parameter	Goethe University Frankfurt	Johannes Gutenberg University Mainz
ICP-MS system	Thermo-Finnigan Element II	Agilent 7500ce
Laser ablation system	New Wave UP213 UV-laser	ESI NWR193 ArF Excimer laser
Isotopes used	²⁵ Mg, ³¹ P, ⁴³ Ca, ⁸⁸ Sr, ⁸⁹ Y	²⁵ Mg, ³¹ P, ⁴³ Ca, ⁸⁸ Sr, ⁸⁹ Y, ²³² Th, ²³⁸ U
Oxide rate ²³⁸ U ¹⁶ O/ ²³⁸ U	<0.5 %	<0.2 %
Calibration material	NIST SRM 610	NIST SRM 612
Spot shape	Circular	Circular
Spot size	60 μm	110 μm
Repetition rate	10 Hz	10 Hz
Transition rate	10 $\mu\text{m/s}$	10 $\mu\text{m/s}$
Fluence	3 J/cm ²	3 J/cm ²

6.9.1 Discussion of Bu2 $\delta^{18}\text{O}$ values

Under modern conditions, the $\delta^{18}\text{O}$ values of the drip water at Bunker Cave mainly reflect the $\delta^{18}\text{O}$ values of winter precipitation (Fohlmeister et al., 2012; Riechelmann et al., 2011; Riechelmann et al., 2017; Wackerbarth et al., 2010). Thus, the $\delta^{18}\text{O}$ values have been attributed to changes in the amount of winter precipitation and winter temperature, and Fohlmeister et al. (2012) concluded that higher speleothem $\delta^{18}\text{O}$ values correspond to cold and dry winters, whereas more negative $\delta^{18}\text{O}$ values indicate warmer and more humid winters. They also attributed the variability of Bunker Cave speleothem $\delta^{18}\text{O}$ values to changes in storm tracks and the source region of the water vapour. Applying this interpretation of the $\delta^{18}\text{O}$ values to our dataset, MIS 3 phase 1 would be characterised as a period of cold and dry winters, whereas phase 2 would be warmer and more humid. However, this interpretation of the $\delta^{18}\text{O}$ variability is based on modern-day and Holocene data and is in conflict with the other proxy data. Consequently, we suggest an alternative interpretation of the $\delta^{18}\text{O}_{\text{slc}}$ values of Bu2 during MIS 3.

Previous studies from Bunker Cave showed that PCP is not a major factor controlling the $\delta^{18}\text{O}$ values of the speleothems (Fohlmeister et al., 2012). Therefore, we exclude PCP as a potential driver for the observed changes in the $\delta^{18}\text{O}_{\text{slc}}$ record. The drip water has a residence time between two and five years (Kluge et al., 2010; Riechelmann et al., 2012a; Riechelmann et al., 2017), and drip water $\delta^{18}\text{O}$ values reflect the annual mean $\delta^{18}\text{O}$ value of precipitation, weighted by the monthly amount of infiltration (Riechelmann et al., 2011; Riechelmann et al., 2017). Rainwater $\delta^{18}\text{O}$ values in Central Europe vary seasonally, and summer precipitation shows higher $\delta^{18}\text{O}$ values than winter precipitation (Rozanski et al., 1982). This general trend should also hold true for MIS 3. Hence, it may be possible to attribute changes in the $\delta^{18}\text{O}_{\text{slc}}$ record of the speleothem sample to changes in the seasonality of precipitation. Today, the drip water $\delta^{18}\text{O}$ values are mainly influenced by winter precipitation (Riechelmann et al., 2017). More negative speleothem $\delta^{18}\text{O}_{\text{slc}}$ values would indicate a larger portion of winter precipitation, while more positive $\delta^{18}\text{O}_{\text{slc}}$ values would reflect an increase in the portion of summer precipitation. Pollen data from the Eifel (Sirocko et al., 2016) indicate lower summer temperatures for MIS 3 than today implying decreased evapo-transpiration above the cave. This would allow a higher proportion of summer rainfall to infiltrate the soil and result in increased speleothem $\delta^{18}\text{O}$ values. Therefore, the more positive $\delta^{18}\text{O}$ values of MIS 3 phase 1 may suggest increased summer infiltration compared to today and MIS 3 phase 2. In turn, the significantly lower $\delta^{18}\text{O}_{\text{slc}}$ values at the beginning of phase 2 may suggest a phase, when winter precipitation contributed significantly to the drip water budget. Regarding the increasing trend in $\delta^{18}\text{O}_{\text{slc}}$ during the second growth phase, a gradual change towards more summer precipitation/infiltration may be possible, besides other processes potentially affecting the $\delta^{18}\text{O}$ values. However, water availability during MIS 3 phase 2 was generally lower, as shown by the Sr isotope and Mg trace element data, as well as the lower growth rate.

Chapter 7: Manuscript V: A comparison of Holocene speleothem proxy records from Germany: Spatial variability of site-specific effects?

A comparison of Holocene speleothem proxy records from Germany: Spatial variability or site-specific effects?

Michael Weber^{1,2}, Yvonne Hinz¹, Bernd R. Schöne¹, Klaus Peter Jochum², Dirk Hoffmann³, Christoph Spötl⁴, Denis Scholz¹

¹Institute of Geosciences, Johannes Gutenberg University Mainz, J.-J.-Becher-Weg 21, 55128 Mainz, Germany

²Climate Geochemistry Department, Max Planck Institute for Chemistry (Otto Hahn Institute), P.O.B. 3060, 55020 Mainz, Germany

³Max-Planck-Institute for Evolutionary Anthropology, Department of Human Evolution, Leipzig, Germany

⁴Institute of Geology, University of Innsbruck, Innrain 52, 6020 Innsbruck, Austria

Manuscript in preparation.

7.1 Abstract

Climate variability in Central Europe during the Holocene was characterised by changes on a millennial to decadal time-scale. Speleothems provide the opportunity to study past climate variability using high resolution proxy records (e.g. stable isotopes and trace elements), and offer precise age models by U-series dating. However, the climatic significance of an individual speleothem record is still a matter of debate, and limitations in sample availability often hamper the possibility to reproduce climate patterns observed at a specific cave site or to resolve spatial climate patterns.

Here we present a palaeoclimate record based on four speleothem samples from the Hüttenbläuserschachthöhle (HBSH), western Germany, which were sampled in close proximity. Two samples cover almost the entire Holocene, with a short hiatus in between. A third sample grew between 6.1 ± 0.6 ka and 0.6 ± 0.1 ka and a fourth one grew continuously between 11.0 ± 0.4 ka and 8.2 ± 0.2 ka. Trace element and stable isotope data were analysed at high resolution and allow us to compare the results obtained by different samples and reconstruct climatic patterns during the Holocene. In addition, Sr isotopes have been investigated to further constrain soil processes and changes in weathering conditions.

The aim of this study is to evaluate the consistency of the proxy data recorded in the individual stalagmites and validate the obtained results by a multi-proxy approach. Due to the close proximity of HBSH (<1 km) to the intensively studied Bunker Cave system, this dataset also provides the unique opportunity to compare the Holocene record with a time-series from a different cave system, which should have recorded the same climate signal. While the initial growth phase after the onset of the Holocene shows similar patterns in both cave systems, an opposing trend was observed for the past 6 ka, most likely induced by a strong effect of disequilibrium isotope fractionation, resulting in a strong enrichment in $\delta^{13}\text{C}$, as well as $\delta^{18}\text{O}$. This is not visible in the stable isotope data from Bunker Cave. We were able to show this effect based on changes in the growth rate and trace element distribution, highlighting the use of a multi-proxy approach, especially if only a limited number of speleothem samples are available for palaeoclimate reconstructions.

7.2 Introduction

Today, speleothems are established terrestrial palaeoclimate archives and widely used in the reconstruction of past climate and environmental variability on different time scales (Budsky et al., 2019; Luetscher et al., 2015; Mischel et al., 2017b; Moseley et al., 2014; Wassenburg et al., 2016a; Weber et al., 2018a). One of their extraordinary features is the possibility to obtain independent, precise and accurate ages, using the U-series disequilibrium method (Richards and Dorale, 2003; Scholz and Hoffmann, 2008) and the construction of a robust age-depth relationship model. Two of the most commonly used proxies in speleothem science are stable isotopes of oxygen ($\delta^{18}\text{O}$) and carbon ($\delta^{13}\text{C}$),

as well as trace element variations (Fairchild et al., 2006; Fairchild and Treble, 2009; Lachniet, 2009; McDermott, 2004). Both can be measured in high spatial resolution and converted to a time-resolved dataset using an age-depth models (e.g. Breitenbach et al., 2012; Scholz and Hoffmann, 2011). Furthermore, additional proxies have been established for speleothems, such as the Sr isotope system, to reconstruct changes in aeolian dust transport, weathering conditions, precipitation amount and water pathways in the karst (Banner et al., 1994; Banner et al., 1996; Hori et al., 2013; Li et al., 2005; Weber et al., 2017; Weber et al., 2018a).

Although these proxies have been intensively studied, the reconstruction of past climate variability using stable isotopes can be hampered by several processes. Besides the natural variation of $\delta^{18}\text{O}$ and $\delta^{13}\text{C}$ based on climatic/environmental changes, karst and cave processes can also significantly alter the resulting proxy signal in speleothems (Deininger et al., 2012; Hansen et al., 2017; Hansen et al., 2019; Riechelmann et al., 2013). Therefore, it is important to evaluate the significance of a single speleothem stable isotope record. This is either possible by using a multi-proxy approach to support the stable isotope data, or by analysing more than one speleothem sample from the same time interval, if available. This is especially crucial for time intervals, where speleothem growth is sparse, e.g. during Marine Isotope Stage 3 in Central Europe (Fankhauser et al., 2016; McDermott, 2004; Weber et al., 2018a), and a higher number of samples covering the time interval of interest are not available. In contrast to time intervals with a low number of speleothem records, the favourable climatic conditions during the Holocene resulted in intensive speleothem growth (Mangini et al., 2007; McDermott et al., 1999), allowing to evaluate the significance of speleothem stable isotope records based on Holocene speleothem cave records.

The reconstruction of past climate variability during the Holocene is of special interest for humanity, since modern society developed during that time and climatic and environmental changes directly influenced human cultural development (Brenner et al., 2002; Dearing, 2006). Although Holocene climate variation is much smaller than on glacial/interglacial time scales (Mayewski et al., 2004; McDermott, 2004; Wanner et al., 2008), there are significant changes and events during the Holocene.

Here we present speleothem proxy data from Hüttenbläuserschachthöhle (HBSH), western Germany, covering almost the entire Holocene. In total, four samples were investigated and analysed for stable isotopes of carbon and oxygen. These records will be stacked and their significance will be evaluated by comparing our data with available datasets from the nearby Bunker cave (<1 km distance to HBSH). To further decipher our stable isotope data, we use a multi-proxy approach including trace element data and Sr isotope analysis. The aim of this study is to evaluate the significance of a speleothem record retrieved from a single cave and compare the record with a nearby Bunker Cave covering the same time intervals during the Holocene.

7.3 Site and sample description

The description of the cave environment and the speleothem samples are basic requirements for palaeoclimate reconstructions, since speleothem formation is largely dependent on the overlying host rock and the precipitation above the cave.

7.3.1 Hüttenbläuserschachthöhle

Hüttenbläuserschachthöhle (HBSH in the following) is located in the Middle- to Upper Devonian limestone of the northern Rhenish Slate Mountains (Iserlohn-Letmathe, NW Germany, Fig. 7.1), which consists of biostromal accumulations at the external shelf of the Rhenohercynian (Burchette, 1981). The cave has an elongation of about 5 km at a height difference of 46 m (Grebe, 1994), shared on three vertical levels with stable corridors. On each level, a clear main corridor has formed, which probably represents the former major karst water collector. The main corridor profiles show a clear development in the phreatic zone. The cave levels can be correlated to river terraces of the rising Rhenish Massif (Niggemann et al., 2003). Ridges and valleys in the area of Iserlohn-Letmathe usually follow the WSW-ENE strike of the rock formation (von Kamp and Ribbert, 2005). Due to the close proximity of HBSH (<1 km, Fig. 7.1) to the nearby Bunker Cave, both cave system are covered by similar vegetation and are influenced by the same climatic patterns. The vegetation cover consists of C3-plants, such as shrubs, ash and beech trees. Mean annual precipitation amounts 919 mm and the mean annual temperature in this area is 10.5°C (1988 – 2007, DWD weather station Hagen-Fley, Fig. 7.1). During a multi-annual monitoring of Bunker Cave (Riechelmann et al., 2017), the $\delta^{18}\text{O}$ values of precipitation in this area have been determined to range from -5 ‰ in summer to -13 ‰ in winter.

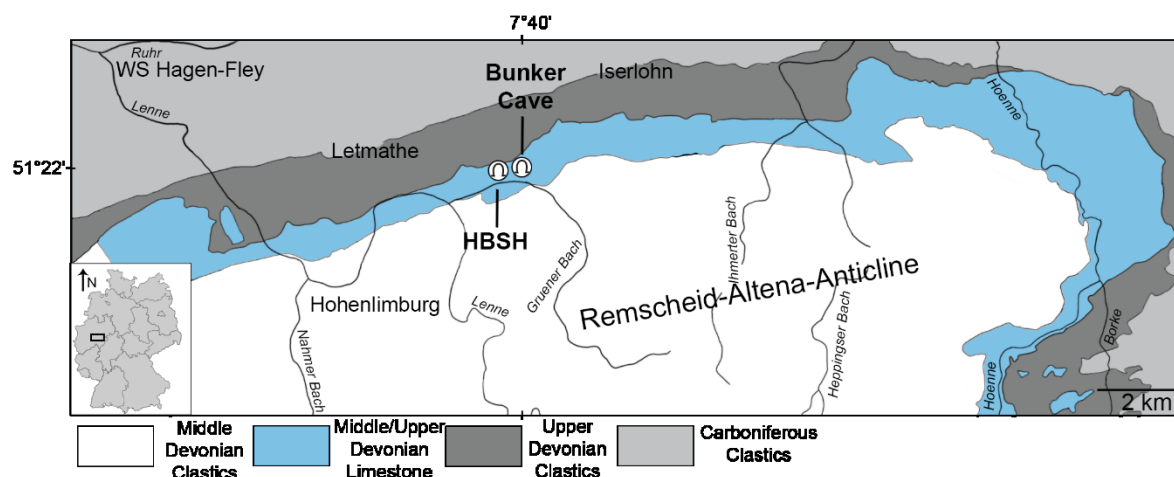


Fig. 7.1: Geological map of the cave area with Hüttenbläuserschachthöhle and Bunker Cave indicated in the Middle/Upper Devonian limestone. Weather station (WS) Hagen-Fley is indicated in the north-western part of the map. Modified after Riechelmann et al. (2011).

7.3.2 Speleothem samples

Four samples (HSBH-1, HBSH-3, HBSH-4 and HBSH-5, Fig. 7.2) have been retrieved from HBSH, covering the Holocene period. HBSH-1 is a ca. 55 cm long sample with clearly visible lamination, mainly composed of aragonite (Yang et al., 2015). For this study, we focus on an approximately 5 cm long section from the top of the stalagmite. HBSH-3 has a total length of approximately 22 cm, a bright beige colour with some darker areas and shows some lamination. In contrast to HBSH-1, the sample is composed of calcite. HBSH-4 also shows lamination in the whole sample, which has a total length of 40 cm and consists entirely out of calcite. The colour of the stalagmite is a bright beige to grey. HBSH-5 consists of calcite and has a total length of 33 cm, showing lamination and a generally darker colour than the other HBSH stalagmites. The top section covering approximately 6 cm is investigated in this study.

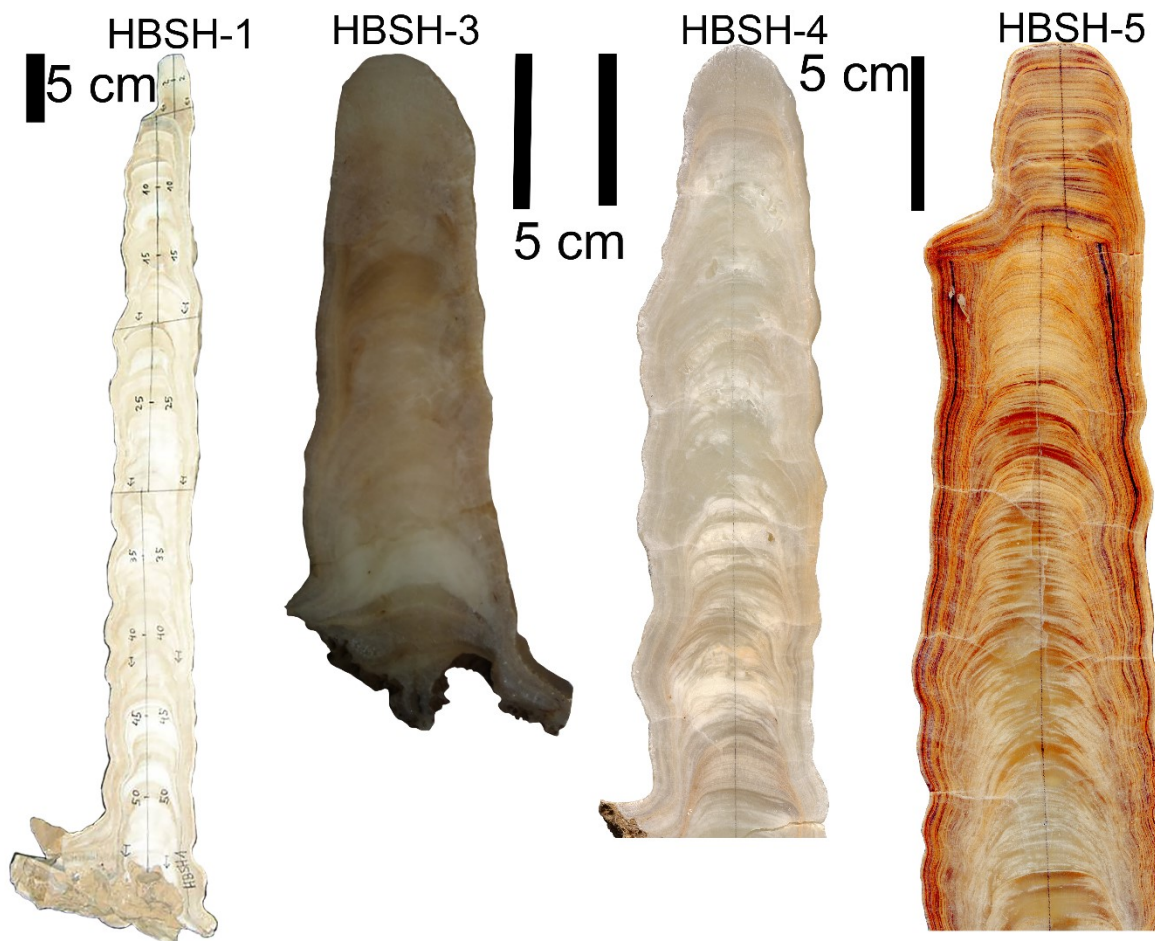


Fig. 7.2: Overview of HBSH samples HBSH-1, HBSH-3, HBSH-4, and HBSH-5 (left to right). For samples HBSH-1 and HBSH-5, only the upper parts covering the Holocene were investigated. For HBSH-3 and HBSH-4, the major parts cover the Holocene.

7.4 Analytical methods

To date and characterise the samples, several analytical methods have been applied, including MC-ICP-MS, LA-ICP-MS and IRMS, which are described in the following.

7.4.1 $^{230}\text{Th}/\text{U}$ -dating

Stalagmite samples from HBSH have been analysed using the $^{230}\text{Th}/\text{U}$ dating method by MC-ICP-MS at the Max Planck Institute for Chemistry (MPIC), Mainz, the Institute of Geosciences, Mainz, and at the School of Geographical Sciences, Bristol (HBSH-1). Samples were cut along the growth axes using a diamond wire saw. In total, 47 samples have been analysed for $^{230}\text{Th}/\text{U}$ -dating at MPIC, seven samples at the Institute of Geosciences, Mainz and five samples at the School of Geographical Sciences, Bristol (Table 7.1). Chemical separation of U and Th prior to analysis has been performed for samples HBSH-3, HBSH-4 and HBSH-5 using an ion-exchange resin (AG1-X8) at the MPIC, following the methods described in Hoffmann (2008) and Yang et al. (2015), using sample amounts of approximately 0.3 g. Chemical separation for HBSH-1 has been performed at the School of Geographical Sciences, Bristol, following the methods described in Hoffmann (2008). At MPIC, a Nu Plasma MC-ICP-MS was used to analyse U and Th in separated sessions following the protocol described in Obert et al. (2016). Details of the calibration of the U-Th-spike are presented by Gibert et al. (2016). Introduction of the samples dissolved in 0.8 mol/L HNO_3 was performed using a CETAC Aridus II desolvating nebulizer system. A daily tuning protocol was used to achieve highest signal intensities and optimised peak shapes. At Institute of Geosciences, a Neptune Plus MC-ICP-MS was coupled to a CETAC Aridus 3 desolvating nebulizer system, using the same analytical protocol as described for the Nu Plasma. Measurements at the School of Geographical Sciences have been performed using a Neptune MC-ICP-MS coupled to a CETAC Aridus desolvating system, following the methods described in Hoffmann et al. (2007). Based on the resulting ages, age-depth models (Fig. 7.3) were calculated using the algorithm StalAge (Scholz and Hoffmann, 2011).

7.4.2 Stable isotope analysis

Stable carbon and oxygen isotope values ($\delta^{13}\text{C}$ and $\delta^{18}\text{O}$) for HBSH-3, HBSH-4 and HBSH-5 were obtained at the Institute of Geosciences, Johannes Gutenberg University Mainz. Samples were drilled using a hand drill device with a spatial resolution of 500 μm . In total, 1350 samples have been analysed using a Thermo Finnigan MAT 253 continuous-flow isotope ratio mass spectrometer equipped with a Gasbench II. Stable carbon and oxygen isotope values for HBSH-1 have been obtained at the Institute of Geology, University of Innsbruck, using a Merchantek video-controlled MicroMill device with a spatial resolution of 150 μm , resulting in a total number of 301 samples. Analyses were performed using a Thermo Fisher Delta^{plus}XL isotope ratio mass spectrometer linked to a Gasbench II. Analytical

precision and accuracy on a 1 σ -level are usually better than 0.05 ‰ for the $\delta^{13}\text{C}$ and $\delta^{18}\text{O}$ measurements. All values are reported relative to V-PDB.

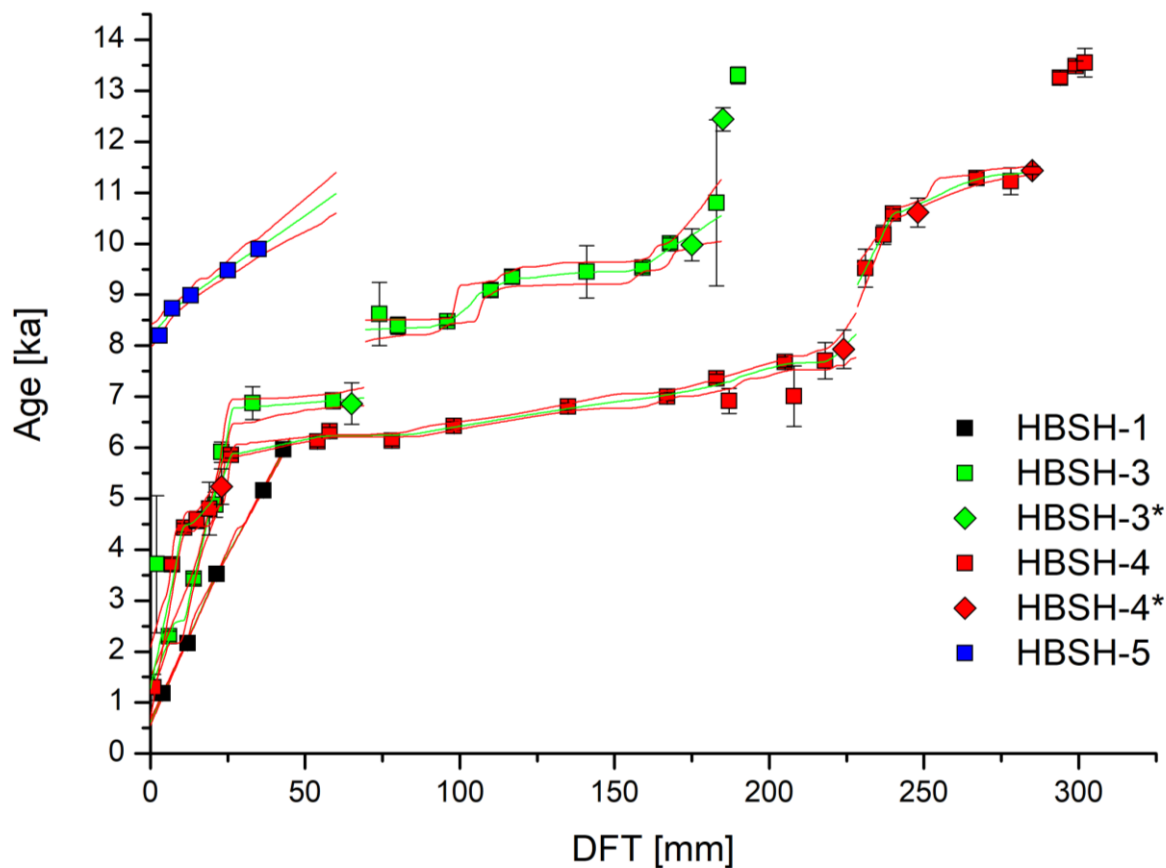


Fig. 7.3: Age-depth relationship for stalagmites HBSH-1 (black), HBSH-3 (green), HBSH-4 (red) and HBSH-5 (blue) resulting from U-series dating. Measurements performed with the Neptune Plus MC-ICP-MS at the Institut of Geosciences are marked with an asterisk or a diamond, respectively. The coloured squares/diamonds represent the resulting ^{230}Th -ages with their respective 2 SE uncertainties. Please note that some of the measurement uncertainties are smaller than the square/diamond indicating the resulting age and are therefore not visible in the figure. Detailed uncertainties are given in Table 7.1. The green lines represent the age model calculated by StalAge (Scholz and Hoffmann, 2011) with the red lines representing the corresponding age uncertainties on a 95% confidence level for each sample. For the ages before the onset of the Holocene in stalagmites HBSH-3 and HBSH-4, no age model was calculated.

7.4.3 Trace element analyses

LA-ICP-MS has been used to determine trace element mass fractions. A Thermo Finnigan Element 2 SF-ICP-MS was coupled to a New Wave UP213nm laser ablation system at the MPIC. For all samples,

the following laser parameters have been applied: spot analyses with a spot size of 100 μm , a repetition rate of 10 Hz and an energy output of 60 %, resulting in a fluence of $\sim 5 \text{ J/cm}^2$. Background signals were collected for 14 s prior to ablation and subtracted from the sample signal, followed by a wash-out time of 20 s. The following analytes have been analysed during the session: ^{24}Mg , ^{31}P , ^{88}Sr and ^{137}Ba . NIST SRM 612 was analysed for calibration purposes at the beginning, between each set and at the end of the routine. ^{43}Ca was used as internal reference to calculate trace element mass fractions.

7.4.4 Strontium isotope analyses

Strontium isotope ratios ($^{87}\text{Sr}/^{86}\text{Sr}$) were determined for speleothem samples HBSH-3 ($n = 9$), HBSH-4 ($n = 9$) and HBSH-5 ($n = 3$). The samples (2 – 7 mg) were processed at the Institute of Geosciences, Johannes Gutenberg University Mainz, using a laminar flow hood in a clean laboratory, following the methods described by Lugli et al. (2017b) and Weber et al. (2018b) for dissolution and separation of Sr using Sr-spec resin. $^{87}\text{Sr}/^{86}\text{Sr}$ ratios were determined at the MPIC using a Nu Plasma MC-ICP-MS coupled to a CITEC Aridus II desolvating nebulizing system following the methods described by Weber et al. (2017). Ion beams were simultaneously collected using seven Faraday cups covering the mass-to-charge range of 82 – 88, representing the following isotopes: ^{82}Kr , ^{83}Kr , ^{84}Sr , ^{85}Rb , ^{86}Sr , ^{87}Sr , ^{88}Sr . Strontium solution were diluted to $\sim 50 \mu\text{g/ml}$ and measured in a standard bracketing sequence, correcting for a NIST SRM 987 $^{87}\text{Sr}/^{86}\text{Sr}$ ratio of 0.710248 (McArthur et al., 2001). Correction for instrumental mass bias was performed using an exponential law, using the $^{88}\text{Sr}/^{86}\text{Sr}$ ratio of 8.375209 (Steiger and Jäger, 1977).

7.5 Results

Results obtained by the different techniques are presented in the following, separated in different chapters.

7.5.1 $^{230}\text{Th}/\text{U}$ -dating

Results of the $^{230}\text{Th}/\text{U}$ -dating are presented in Table 7.1. Resulting age-depth models of all speleothem samples are presented in Fig. 7.3 and all following ages refer to the results from StalAge (Scholz and Hoffmann, 2011). Speleothem HBSH-1 shows slow continuous growth between $6.1 \pm 0.6 \text{ ka}$ and $0.60 \pm 0.06 \text{ ka}$ with a stable growth rate of $8 \mu\text{m/a}$ (calculated based on the age-depth model) and without any growth stops. Sample HBSH-3 shows a more complex growth history. Two measurements yielded ages of $13.3 \pm 0.2 \text{ ka}$ and $12.4 \pm 0.2 \text{ ka}$ during the Bølling-Allerød and therefore before the onset of the Holocene at $11.7 \pm 0.1 \text{ ka}$ (Walker et al., 2009). Therefore, these ages were not included in the age model. The growth during the Holocene started at $10.8 \pm 1.6 \text{ ka}$ and showed continuous growth at least until $8.3 \pm 0.2 \text{ ka}$ with a fast growth rate ($>100 \mu\text{m/a}$) between 9.5 and 9.0 ka. A growth stop between

8.3 ± 0.2 ka and 7.0 ± 0.2 ka is visible and is followed by a growth phase with slow growth (6 µm/a) until the final growth cessation at 1.3 ± 0.2 ka. The growth history of speleothem HBSH-4 is similar to HBSH-3 with an initial growth phase during the Bølling-Allerød between 13.6 ± 0.3 ka and 13.2 ± 0.1 ka, followed by a growth stop until 11.4 ± 0.1 ka, representing growth inception shortly after the beginning of the Holocene at 11.7 ± 0.1 ka. The initial growth phase for HBSH-4 lasted until 9.2 ± 0.4 ka and shows a deceleration in growth rate towards the hiatus from >30 µm/a towards <10 µm/a. Growth resumed around 8.2 ± 0.4 ka and continuous fast growth (60 – 100 µm/a) is observed until ca. 5.8 ± 0.1 ka, where a significant growth deceleration (<10 µm/a) is visible, lasting until at least 3.7 ± 0.1 ka. The youngest age obtained from HBSH-4 is 1.3 ± 0.3 ka and we cannot finally constrain if the growth between the last two ²³⁰Th dating results was slow and continuous, or if there was a hiatus in between. For our age model, a continuous growth was modelled. Speleothem HBSH-5 shows continuous growth between 9.9 ± 0.3 ka and 8.2 ± 0.1 ka and a rather constant growth rate of ~20 µm/a for most of the sample. Only the youngest part shows a decelerating growth rate down towards ~10 µm/a between 8.7 ± 0.1 ka and 8.2 ± 0.1 ka.

7.5.2 Trace elements

Trace element records of Mg, P, Sr and Ba are presented in supplementary Fig. A7.1 – 7.3. To evaluate the relationship between trace element records and stable isotope data, a correlation analysis was performed using the statistical software R (R Core Team, 2013).

Since HBSH-1 consists of aragonite in comparison to the calcite speleothems HBSH-3 and HBSH-5, the trace element mass fractions can significantly differ (Wassenburg et al., 2016b). Magnesium in HBSH-1 is low (~180 µg/g) for most of the sample except for some significant spikes in mass fraction during the most recent 1000 years. Strontium mass fraction is relatively high, increasing from 500 to 800 µg/g towards younger ages until ca. 3.5 ± 0.1 ka. Afterwards, this trend is reversed. The same pattern is visible in P, while Ba is decreasing on a longer time scale towards younger ages.

HBSH-3 has a much higher Mg mass fraction between 1000 and 4500 µg/g. In general, Mg is increasing towards younger ages, especially in the second growth phase between 7.0 ± 0.2 ka and 1.3 ± 0.2 ka. Strontium and Ba show a similar trend with increasing mass fractions until the hiatus and decreasing mass fractions after growth re-inception at 7.0 ± 0.2 ka. The opposite trend is true for P. A prominent feature is the significant reduction in mass fraction for Mg, Sr and Ba around 9.5 ± 0.2 ka.

HBSH-5 does not show large trace element variation besides one significant increase in Mg, Ba and P around 8.5 ± 0.2 ka, which is contemporaneous with a decrease in Sr mass fraction. In general, all four observed trace element mass fractions decrease towards the growth cessation around 8.2 ± 0.1 ka.

Table 7.1: Uranium and Th mass fractions, activity ratios and ^{230}Th -ages for Holocene stalagmites from Hüttenbläuserschachthöhle. All uncertainties are quoted as 2 SE. All activity ratios and ages were corrected for detrital contamination, using a $^{232}\text{Th}/^{238}\text{U}$ mass ratio of 3.8 ± 1.9 , calculated from the average Th and U mass fractions of tonalities which are believed to be representative for the bulk continental crust (Wedepohl, 1995). We assumed ^{230}Th , ^{234}U and ^{238}U to be in secular equilibrium for the detritus. Activity ratios were calculated using the half-lives from Cheng et al. (2000). All measurements highlighted with an asterisk have been measured at the Institute of Geosciences with a Neptune Plus MC-ICP-MS. Sample HBSH-1 has been analysed at the School of Geographical Sciences, Bristol. BDL = below detection limit; NA = not available due to ^{232}Th mass fraction below detection limit.

Sample	DFT [mm]	^{232}Th [ng/g]	Uncertainty	^{238}U [ng/g]	Uncertainty	$(^{234}\text{U}/^{238}\text{U})$	Uncertainty	$(^{230}\text{Th}/^{238}\text{U})$	Uncertainty	$(^{230}\text{Th}/^{232}\text{Th})$	Uncertainty	Uncorrected Age [ka]	Uncertainty [ka]	Corrected Age [ka]	Uncertainty [ka]
HBSH-1-0.4	4.0	2.167	0.284	2727.52	364.02	1.965	0.003	0.0211	0.0002	81.9	0.5	1.19	0.01	1.18	0.01
HBSH-1-1.2	12.0	2.543	0.290	3427.39	392.00	2.142	0.003	0.0421	0.0002	174.3	0.9	2.18	0.01	2.17	0.01
HBSH-1-2.2	21.5	0.690	0.086	6186.75	773.74	1.891	0.003	0.0601	0.0003	1647.7	12.0	3.52	0.02	3.52	0.02
HBSH-1-3.7	36.5	4.109	0.320	4876.50	372.62	1.932	0.003	0.0895	0.0004	325.2	2.1	5.17	0.03	5.16	0.03
HBSH-1-4.3	43.0	34.837	2.624	4219.61	315.69	1.838	0.003	0.0981	0.0011	37.1	0.1	6.10	0.03	5.97	0.07
HBSH-3-0.2	2.0	0.906	0.055	38.54	0.48	1.228	0.014	0.0411	0.0145	6.1	1.9	4.27	1.33	3.72	1.34
HBSH-3-0.6	6.0	0.453	0.005	72.30	0.43	1.211	0.002	0.0253	0.0011	13.1	0.4	2.45	0.07	2.30	0.10
HBSH-3-1.4	14.0	0.066	0.001	38.05	0.25	1.208	0.002	0.0373	0.0011	66.6	2.1	3.47	0.10	3.43	0.11
HBSH-3-2.1	21.0	1.540	0.015	80.34	0.49	1.204	0.003	0.0527	0.0026	9.2	0.2	5.34	0.09	4.88	0.25
HBSH-3-2.3	23.0	0.789	0.014	99.27	0.79	1.208	0.008	0.0638	0.0021	25.3	0.8	6.10	0.18	5.91	0.20
HBSH-3-3.3	33.0	0.864	0.009	43.21	0.29	1.205	0.002	0.0737	0.0033	12.0	0.4	7.35	0.22	6.87	0.32
HBSH-3-5.9	59.0	0.413	0.005	45.97	0.31	1.212	0.002	0.0746	0.0016	26.1	0.5	7.14	0.12	6.92	0.16
HBSH-3-6.5*	65.0	6.530	0.043	87.64	0.52	1.226	0.002	0.0748	0.0044	3.8	0.1	8.62	0.15	6.86	0.41
HBSH-3-7.4	74.0	2.670	0.029	91.33	0.55	1.249	0.003	0.0951	0.0067	11.4	0.2	9.97	0.21	8.62	0.62
HBSH-3-8.0	80.0	0.096	0.001	51.95	0.35	1.249	0.002	0.0926	0.0018	153.8	3.4	8.44	0.17	8.39	0.17
HBSH-3-9.6	96.0	0.030	0.000	63.08	0.42	1.252	0.002	0.0937	0.0008	603.0	9.6	8.49	0.08	8.48	0.08
HBSH-3-11.0	110.0	0.432	0.005	109.01	0.85	1.259	0.007	0.1008	0.0013	78.5	1.1	9.18	0.13	9.09	0.13
HBSH-3-11.7	117.0	0.299	0.004	121.87	0.72	1.266	0.002	0.1041	0.0014	130.7	2.2	9.40	0.13	9.35	0.14
HBSH-3-14.1	141.0	0.111	0.005	93.56	1.96	1.278	0.026	0.1062	0.0051	273.8	17.1	9.48	0.51	9.45	0.52
HBSH-3-15.9	159.0	0.056	0.001	67.35	0.45	1.266	0.002	0.1061	0.0012	394.0	6.3	9.55	0.11	9.53	0.11
HBSH-3-16.8	168.0	0.007	0.000	52.59	0.36	1.263	0.002	0.1109	0.0012	2597.0	77.8	10.01	0.11	10.01	0.11
HBSH-3-17.5*	175.0	3.980	0.030	68.82	0.45	1.318	0.002	0.1155	0.0035	6.8	0.1	11.24	0.15	9.98	0.31
HBSH-3-18.3	183.0	13.302	0.132	88.41	0.69	1.343	0.011	0.1270	0.0182	3.3	0.1	14.07	0.26	10.80	1.63
HBSH-3-18.5*	185.0	6.838	0.048	156.76	0.99	1.369	0.001	0.1481	0.0025	11.1	0.1	13.36	0.11	12.44	0.23
HBSH-3-19.0	190.0	1.162	0.014	87.29	0.63	1.382	0.002	0.1593	0.0019	37.3	0.4	13.58	0.11	13.30	0.17

Table 7.1 (continued):

Sample	DFT [mm]	^{232}Th [ng/g]	Uncertainty	^{238}U [ng/g]	Uncertainty	$(^{234}\text{U}/^{238}\text{U})$	Uncertainty	$(^{230}\text{Th}/^{238}\text{U})$	Uncertainty	$(^{230}\text{Th}/^{232}\text{Th})$	Uncertainty	Uncorrected Age [ka]	Uncertainty [ka]	Corrected Age [ka]	Uncertainty [ka]
HBSH-4-0.1	1.0	1.859	0.019	91.22	0.52	1.209	0.002	0.0143	0.0028	2.9	0.1	1.79	0.07	1.30	0.26
HBSH-4-0.7	7.0	1.198	0.012	158.11	1.07	1.208	0.005	0.0404	0.0012	17.1	0.3	3.89	0.08	3.71	0.12
HBSH-4-1.1	11.0	1.117	0.012	192.76	1.18	1.179	0.002	0.0469	0.0009	25.5	0.3	4.57	0.05	4.43	0.08
HBSH-4-1.5	15.0	0.205	0.004	243.41	1.47	1.180	0.002	0.0486	0.0018	177.4	7.2	4.61	0.17	4.59	0.17
HBSH-4-1.9	19.0	7.369	0.073	173.13	0.98	1.181	0.002	0.0509	0.0054	4.4	0.1	5.85	0.07	4.81	0.52
HBSH-4-2.3*	23.0	8.998	0.064	143.71	0.91	1.185	0.001	0.0556	0.0037	3.5	0.0	6.77	0.09	5.24	0.35
HBSH-4-2.6	26.0	0.400	0.004	236.87	1.45	1.171	0.002	0.0612	0.0007	111.7	1.5	5.90	0.06	5.86	0.07
HBSH-4-5.4	54.0	0.131	0.002	268.41	1.57	1.132	0.002	0.0618	0.0010	386.8	7.6	6.13	0.10	6.12	0.10
HBSH-4-5.8	58.0	0.205	0.003	262.36	1.62	1.129	0.002	0.0636	0.0008	250.1	4.1	6.34	0.08	6.32	0.08
HBSH-4-7.8	78.0	0.231	0.003	288.26	1.72	1.160	0.002	0.0643	0.0010	246.3	4.8	6.23	0.10	6.13	0.10
HBSH-4-9.8	98.0	0.163	0.002	276.67	1.70	1.160	0.002	0.0664	0.0008	346.1	5.7	6.44	0.08	6.43	0.08
HBSH-4-13.5	135.0	0.093	0.001	328.15	1.89	1.157	0.002	0.0700	0.0007	758.0	10.2	6.82	0.07	6.81	0.07
HBSH-4-16.7	167.0	0.000	0.001	303.52	1.84	1.159	0.002	0.0721	0.0008	173071.5	472258.2	7.00	0.08	7.00	0.08
HBSH-4-18.3	183.0	1.506	0.015	302.81	1.75	1.138	0.002	0.0742	0.0008	46.4	0.5	7.48	0.06	7.36	0.08
HBSH-4-18.7	187.0	3.763	0.050	281.12	1.60	1.134	0.002	0.0697	0.0024	16.7	0.4	7.25	0.17	6.92	0.24
HBSH-4-20.5	205.0	1.045	0.011	296.24	2.11	1.155	0.005	0.0785	0.0009	68.8	0.9	7.77	0.09	7.68	0.10
HBSH-4-20.8	208.0	13.369	0.132	281.26	1.61	1.156	0.002	0.0720	0.0060	5.4	0.1	8.20	0.10	7.01	0.59
HBSH-4-21.8	218.0	5.615	0.055	200.84	1.14	1.155	0.002	0.0788	0.0035	9.4	0.1	8.40	0.08	7.71	0.36
HBSH-4-22.4*	224.0	12.987	0.089	191.34	1.20	1.187	0.001	0.0833	0.0038	4.5	0.0	9.59	0.08	7.93	0.38
HBSH-4-23.1	231.0	7.632	0.076	245.08	1.41	1.182	0.002	0.0989	0.0038	10.4	0.1	10.28	0.08	9.52	0.37
HBSH-4-23.7	237.0	3.146	0.032	242.88	1.47	1.155	0.003	0.1029	0.0017	25.0	0.3	10.49	0.09	10.17	0.19
HBSH-4-24.0	240.0	1.048	0.011	307.01	1.85	1.177	0.002	0.1091	0.0009	98.4	1.1	10.68	0.09	10.59	0.09
HBSH-4-24.8*	248.0	BDL	BDL	281.40	1.79	1.180	0.001	0.1096	0.0028	NA	NA	10.61	0.28	10.61	0.28
HBSH-4-26.7	267.0	2.244	0.023	306.56	1.89	1.206	0.002	0.1187	0.0012	50.3	0.5	11.46	0.09	11.29	0.12
HBSH-4-27.8	278.0	0.356	0.010	298.43	1.84	1.204	0.002	0.1180	0.0025	303.4	10.7	11.29	0.26	11.23	0.26
HBSH-4-28.5*	285.0	0.613	0.005	292.35	1.84	1.208	0.001	0.1205	0.0008	176.2	1.4	11.49	0.07	11.44	0.08
HBSH-4-29.4	294.0	0.918	0.010	291.94	1.92	1.217	0.004	0.1395	0.0011	136.4	1.5	13.32	0.11	13.25	0.12
HBSH-4-29.9	299.0	1.340	0.013	318.18	1.85	1.222	0.002	0.1425	0.0010	104.2	1.0	13.59	0.09	13.49	0.10
HBSH-4-30.2	302.0	7.717	0.076	359.05	2.08	1.228	0.002	0.1438	0.0027	21.2	0.2	14.05	0.13	13.55	0.28
HBSH-5-0.3	3.0	2.162	0.021	172.21	1.18	3.042	0.013	0.2216	0.0021	54.6	0.5	8.31	0.07	8.19	0.09
HBSH-5-0.7	7.0	5.670	0.057	205.14	1.20	3.283	0.009	0.2544	0.0032	28.7	0.3	8.97	0.06	8.73	0.12
HBSH-5-1.3	13.0	1.708	0.023	68.17	0.45	3.324	0.009	0.2650	0.0037	32.9	0.5	9.20	0.10	8.99	0.13
HBSH-5-2.5	25.0	7.054	0.114	211.18	1.30	3.320	0.014	0.2788	0.0056	26.1	0.6	9.77	0.16	9.48	0.21
HBSH-5-3.5	35.0	32.228	0.559	2196.37	16.80	3.342	0.015	0.2936	0.0055	61.8	1.5	10.06	0.19	9.90	0.25

7.5.3 Stable isotopes

Stable isotope results for $\delta^{13}\text{C}$ are presented in Fig. 7.4 [A] for all analysed speleothem samples from HBSH. Since all speleothem samples show varying and different growth rates, a centennial mean based on the age-depth model was calculated for each speleothem sample (Fig. 7.5 [A]) to focus on trends on longer time scales and smooth annual or decadal variability. Samples HBSH-3, HBSH-4 and HBSH-5 started to grow at the onset of the Holocene or shortly after. Those three samples show different absolute $\delta^{13}\text{C}$ values at their growth inception, but a generally similar trend towards more negative values after growth inception. They also reached their most negative $\delta^{13}\text{C}$ values (or at least a significant peak for HBSH-5) almost simultaneous around 9.4 ± 0.1 ka. Shortly afterwards, HBSH-4 stopped growth, while HBSH-3 and HBSH-5 continued to grow until 8.3 ± 0.2 ka and 8.2 ± 0.1 ka, respectively, and show again more positive $\delta^{13}\text{C}$ values. HBSH-4 started to grow again around 8.2 ± 0.4 ka with fluctuating $\delta^{13}\text{C}$ values between -10 and -9 ‰ with two significant negative peaks around 4.6 ± 0.2 ka and $3.8 (+0.6, -0.2)$ ka. HBSH-3 reinitiated growth at 7.0 ± 0.2 ka with a trend towards more positive $\delta^{13}\text{C}$ values, which is further intensified after 3.0 ± 0.3 ka, reaching a peak $\delta^{13}\text{C}$ value of -6.7 ‰ at 1.3 ± 0.2 ka, coherent with the final growth cessation. HBSH-1 growth during the Holocene incepted at 6.1 ± 0.6 ka with an initial decrease in $\delta^{13}\text{C}$, followed by a long-term trend towards more negative values, similar to HBSH-3. Peak negative $\delta^{13}\text{C}$ values are visible for HBSH-1 at 6.0 ± 0.1 ka, 4.6 ± 0.1 ka and 3.9 ± 0.1 ka, all coherent with peaks in $\delta^{13}\text{C}$ in HBSH-4. HBSH-1 shows the most positive $\delta^{13}\text{C}$ value of -6.5 ‰ at 1.3 ± 0.2 ka, coherent with growth cessation of speleothems HBSH-3 and HBSH-4. In contrast, HBSH-1 continued to grow with decreasing $\delta^{13}\text{C}$ values until the final growth cessation at 0.6 ± 0.1 ka.

Oxygen isotope results from all the HBSH speleothems show a general trend towards more positive $\delta^{18}\text{O}$ values to recent times. As described for the $\delta^{13}\text{C}$ values, the raw $\delta^{18}\text{O}$ values (Fig. 7.4 [B]) show a highly variable pattern on the short time scale. Therefore, we calculated a centennial mean for the $\delta^{18}\text{O}$ values (Fig. 7.5 [B]) to focus on the long-term trends in this study. In contrast to $\delta^{13}\text{C}$, the $\delta^{18}\text{O}$ values show a more coherent trend in all speleothem samples. After an initial decrease in $\delta^{18}\text{O}$ shortly after growth inception in HBSH-3, HBSH-4 and HBSH-5, those three speleothems tend to more positive values until their growth stops at 9.2 ± 0.4 ka (HBSH-4), 8.3 ± 0.2 ka (HBSH-3) and 8.2 ± 0.1 ka (HBSH-5). The most positive $\delta^{18}\text{O}$ value (-4.6 ‰) of all speleothem samples is observed in HBSH-3 around 9.6 ± 0.1 ka and is in agreement with more positive values in HBSH-4 and HBSH-5. After growth started again in HBSH-3 and HBSH-4, both speleothem samples still yield more positive $\delta^{18}\text{O}$ values, although HBSH-4 shows a significant decrease between 6.7 ± 0.3 ka and 5.8 ± 0.4 ka. Growth in HBSH-1 started at 6.1 ± 0.6 ka and tends to more positive $\delta^{18}\text{O}$ values throughout the completely Holocene part. The most prominent peak in $\delta^{18}\text{O}$ towards more positive values in HBSH-1 is observed around 5.4 ± 0.1 ka. HBSH-4 shows a coherent increase in $\delta^{18}\text{O}$ during that time, although the absolute $\delta^{18}\text{O}$ value is not significantly more positive than other peaks in this sample. All samples continue this trend towards their respective hiatus. HBSH-1 does not show any further significant peaks until its growth cessation around

0.6 ± 0.1 ka. However, HBSH-3 and HBSH-4 show a further peak towards more negative $\delta^{18}\text{O}$ values around $1.7 \pm 0.2/0.5$ ka (uncertainty depending on the sample), which cannot be observed in HBSH-1.

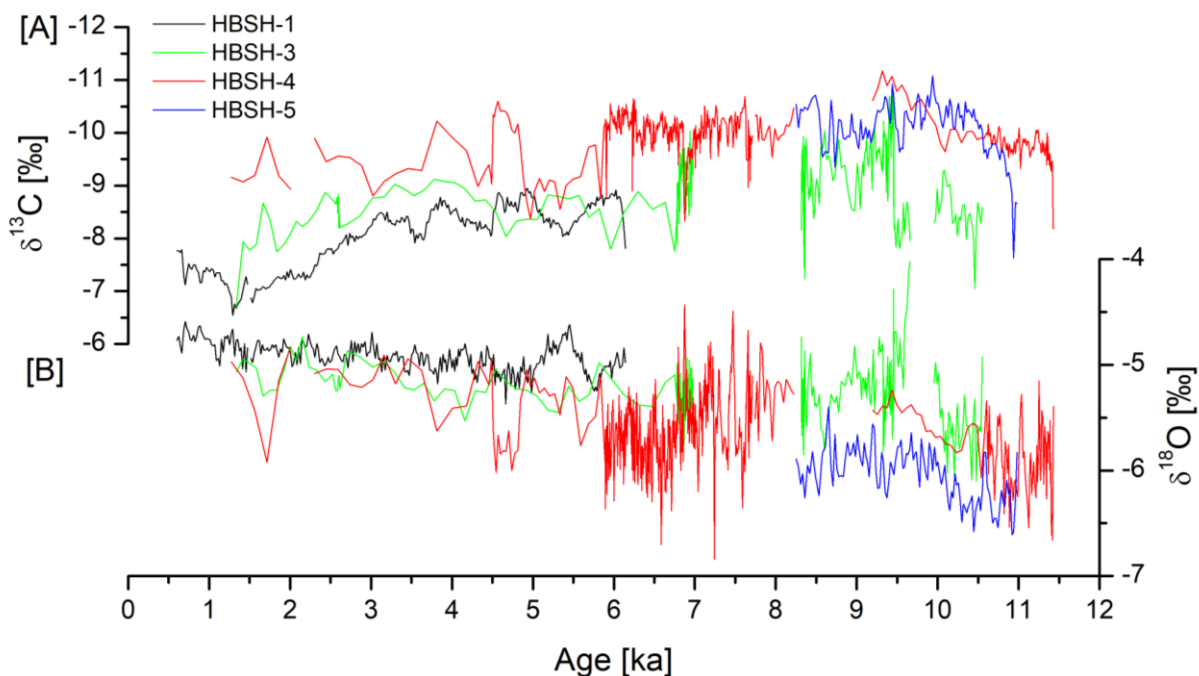


Fig. 7.4: [A] $\delta^{13}\text{C}$ and [B] $\delta^{18}\text{O}$ values for stalagmites HBSH-1 (black), HBSH-3 (green), HBSH-4 (red) and HBSH-5 (blue) based on the age-depth model. Please note the inverted axis for $\delta^{13}\text{C}$.

7.5.3.1 Processing of stable isotope data for regression analysis

All speleothem samples show high variability in growth rate, not only between each sample, but also within. Therefore, the resulting age models for the stable isotope and trace element data show a high variability in age resolution. The aim of this study is not to reconstruct climate variability on an annual or decadal time scale, but to identify common trends on a larger time scale throughout the entire Holocene. To overcome potential problems originating from differences in age resolution, we calculated centennial mean values for the stable isotope and trace element data and performed a regression analysis, where a common time scale for all data is a basic requirement. Based on the age model for each individual speleothem sample, a centennial mean value for $\delta^{13}\text{C}$, $\delta^{18}\text{O}$ and each analysed trace element was calculated. Therefore, we were able to construct stable isotope curves for each speleothem sample in the same temporal resolution (Fig. 7.5) and perform a regression analysis (see sections 7.6.3 and 7.6.4). Regression analysis was performed with the centennial stable isotope data using the statistical software R (R Core Team, 2013). In addition, we constructed a composite stack for HBSH (see section 7.6.4), using scaled stable isotope data from each speleothem to prevent the introduction of artificial steps in the final dataset from different stable isotope values between the different speleothem samples

(Fig. 7.4 and 7.5). After calculating the scaled stable isotope data for each sample, we created a composite stack using centennial means from the data of all HBSH samples. Furthermore, we calculated the number of single analyses, which were averaged for each mean value (replication). These calculations were not only performed for HBSH, but also for the stable isotope values from Bunker Cave during the same time period (Fohlmeister et al., 2012).

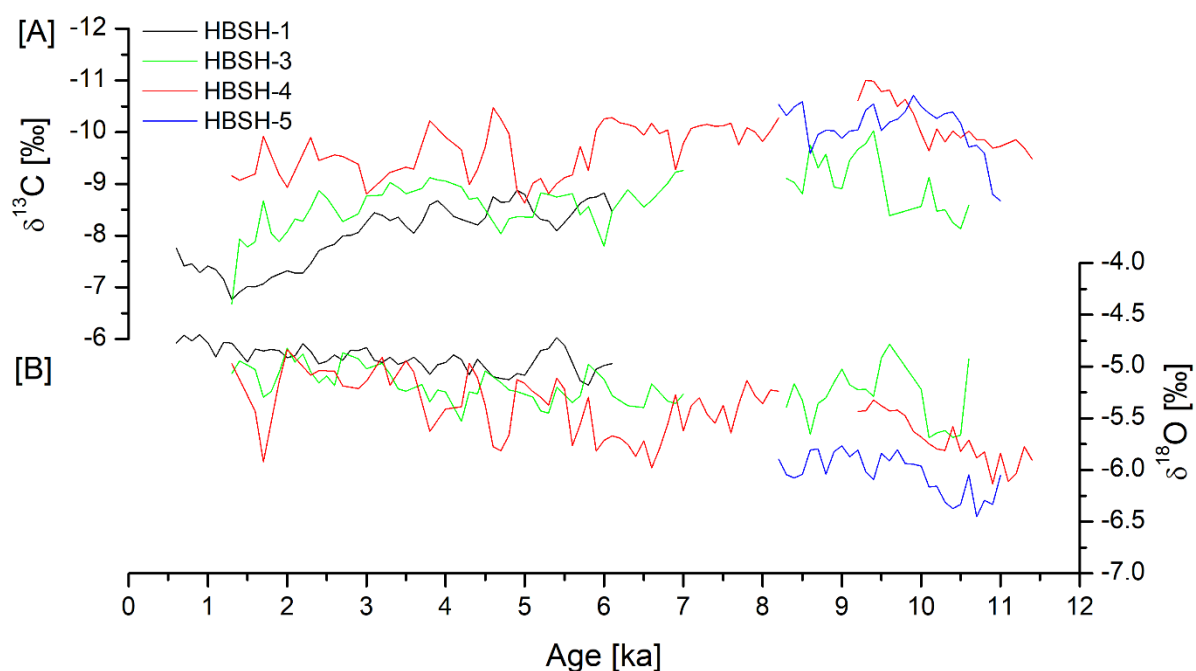


Fig. 7.5: [A] $\delta^{13}\text{C}$ and [B] $\delta^{18}\text{O}$ values averaged by a centennial mean for stalagmites HBSH-1 (black), HBSH-3 (green), HBSH-4 (red) and HBSH-5 (blue). Please note the inverted axis for $\delta^{13}\text{C}$.

7.5.4 Strontium isotopes

Strontium isotopes have been determined for samples HBSH-3, HBSH-4 and HBSH-5 (Fig. 7.6). HBSH-5 shows the least radiogenic $^{87}\text{Sr}/^{86}\text{Sr}$ ratios between 0.70899 ± 0.00002 at 9.8 ± 0.2 ka and 0.70882 ± 0.00002 at 8.8 ± 0.1 ka, showing a strong decreasing trend towards younger ages. HBSH-4 shows the same trend in the older growth section towards less radiogenic Sr isotope ratios. However, the $^{87}\text{Sr}/^{86}\text{Sr}$ ratio of HBSH-4 is overall higher radiogenic with ratios between 0.70950 ± 0.00002 and 0.70977 ± 0.00002 . The least radiogenic ratio of 0.70950 ± 0.00002 is observed at 6.5 ± 0.1 ka, followed by a significant increase towards 0.70966 ± 0.00002 at 6.0 ± 0.1 ka. Towards the final growth cessation of HBSH-4 at 1.3 ± 0.2 ka, the $^{87}\text{Sr}/^{86}\text{Sr}$ ratio gets progressively more radiogenic. HBSH-3 shows the most radiogenic Sr isotope signature, with all $^{87}\text{Sr}/^{86}\text{Sr}$ values above 0.70987 ± 0.00002 . While the first growth phase shows identical $^{87}\text{Sr}/^{86}\text{Sr}$ ratios (0.71009 ± 0.00002 and 0.71008 ± 0.00002), the second growth phase shows the least radiogenic Sr isotope ratio of 0.70987 ± 0.00002 at 7.0 ± 0.2 ka.

Afterwards, the $^{87}\text{Sr}/^{86}\text{Sr}$ increases significantly towards 0.71003 ± 0.00002 at 6.8 ± 0.2 ka and progressively becomes more radiogenic towards younger ages with a maximum $^{87}\text{Sr}/^{86}\text{Sr}$ ratio of 0.71016 ± 0.00002 at 2.2 ± 0.2 ka.

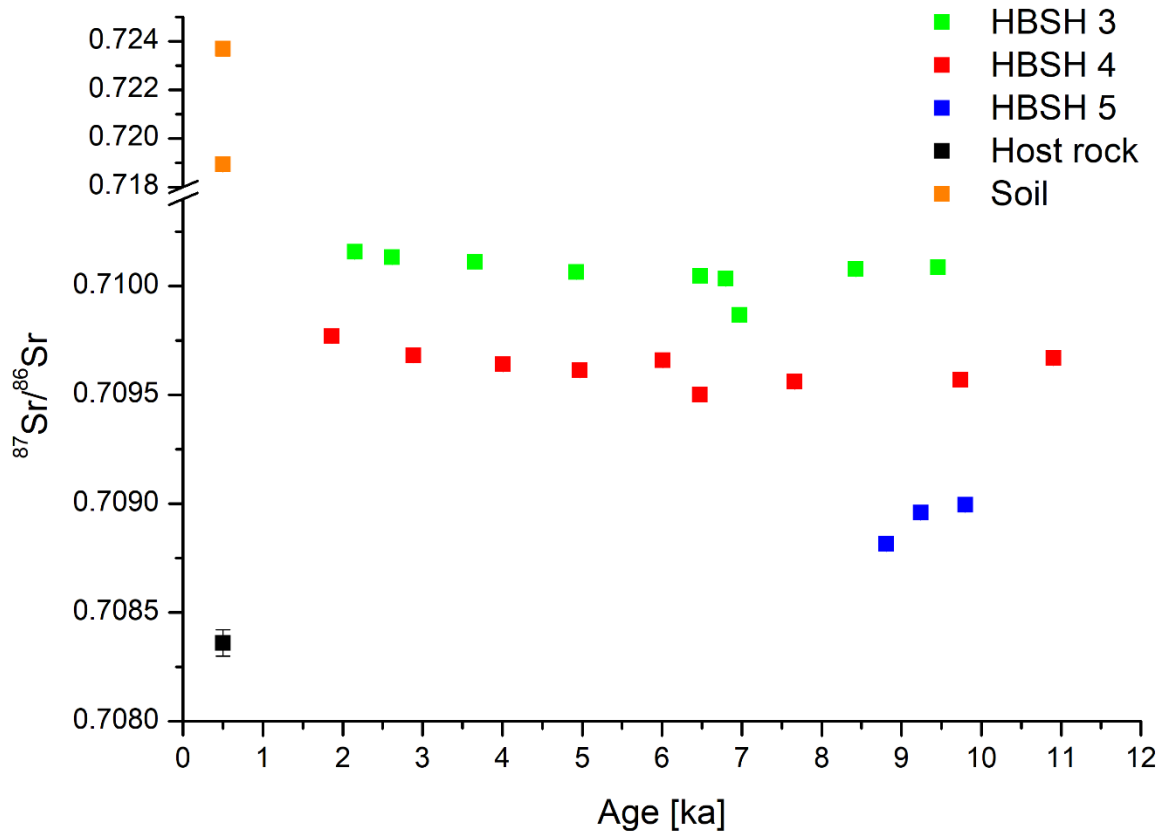


Fig. 7.6: Strontium isotope results for HBSH-3 (green), HBSH-4 (red) and HBSH-5 (blue). In addition, Sr isotope values from the host rock and overlying soil at the nearby Bunker Cave (Weber et al., 2018a) are shown (see section 7.6.2.4 for details).

7.6 Discussion

The discussion of the obtained proxy data from the HBSH speleothems is divided into several chapters, starting with the growth phases based on the U-series dating. In the following, the results from the stable isotopes are compared with the Bunker Cave record.

7.6.1 Growth phases

The four HBSH speleothem samples cover almost the entire Holocene, except the most recent 600 years. Even before the onset of the Holocene, earlier growth phases have been detected between 13.6 ± 0.3 ka and 13.3 ± 0.1 ka for HBSH-4 and at 13.3 ± 0.2 ka and 12.4 ± 0.2 ka for HBSH-3 (Table 7.1). These

initial growth phases can be related to the Bølling-Allerød warming (Köhler et al., 2011). Growth did not continue until the onset of the Holocene but was disrupted, potentially due to cooling during the Younger Dryas (Dansgaard et al., 1989). However, since we did not sample stable isotope and trace element data covering these time intervals, the interpretation of these ages is beyond the scope of this study.

Based on the age-depth model, the initial growth during the Holocene incepted at 11.4 ± 0.1 ka and is visible in HBSH-4. Growth in HBSH-5 started shortly afterwards at 11.0 ± 0.4 ka. Based on the age model, even a simultaneous growth start is plausible but cannot be resolved. The onset of growth in HBSH-3 occurred around 10.6 ± 0.6 ka, which is shortly after the onset in HBSH-4 and HBSH-5. Therefore, we expect that the climate melioration at the onset of the Holocene caused the HBSH speleothems to grow within the time period 10.6 – 11.4 ka. Between 10.6 and 9.2 ka, three speleothem samples were growing simultaneously until HBSH-4 stopped at 9.2 ± 0.4 ka. Growth rate in HBSH-4 already declined at 10.5 ± 0.2 ka and in temporal agreement with the onset of growth in HBSH-3, which grew until 8.3 ± 0.2 ka. At the same time, growth cessation is observed in HBSH-5 (8.2 ± 0.1 ka). Interestingly, by the time HBSH-3 and HBSH-5 stopped their growth, HBSH-4 again starts to grow at 8.2 ± 0.4 ka with a rapidly increasing growth rate up to $>100 \mu\text{m/a}$ (Fig. A7.4). This high growth rate is visible until around 6.0 ± 0.1 ka and declines significantly afterwards down to $<10 \mu\text{m/a}$. A similar trend is visible in the growth characteristics of HBSH-3. After growth re-inception at 7.0 ± 0.2 ka, growth rate increases rapidly, but only for a very short time frame up to $100 \mu\text{m/a}$ (Fig. A7.4). Already around 6.5 ± 0.4 ka, growth rate declined to $<10 \mu\text{m/a}$ and therefore in the same range as observed for HBSH-4. HBSH-1 growth incepted at 6.1 ± 0.6 ka and is continuous for the whole growth period until 0.6 ± 0.1 ka. However, the growth rate is very small ($<10 \mu\text{m/a}$) and agrees with the growth rates observed in HBSH-3 and HBSH-4 during the same time interval (Fig. A7.4). In general, we can divide between an initial growth phase in the first half of the Holocene where growth rate was generally higher than in a second phase. The transition between these two phases in HBSH occurred between 7 and 6 ka and is visible by a significant reduction in growth rate. Interestingly, this difference is also observed in the speleothem samples, which only grew in one of the phases (HBSH-5 in the first phase and HBSH-1 in the second phase), as well as for the two speleothem samples covering this transition phase (HBSH-3 and HBSH-4).

7.6.2 Proxy data

Results from the different proxies are discussed individually in the following chapters before compiling the obtained results towards a general interpretation for HBSH.

7.6.2.1 Stable oxygen isotopes

The $\delta^{18}\text{O}$ values of all Holocene HBSH speleothems show the same increasing trend on the longer time scale (Fig. 7.4 [B] and 7.5 [B]). At the onset of the Holocene, $\delta^{18}\text{O}$ shows the most negative values in the three coevally growing samples HBSH-3, HBSH-4 and HBSH-5, although their absolute $\delta^{18}\text{O}$ values differ. A first peak in $\delta^{18}\text{O}$ is reached around 9.4 ka, with maximum values in HBSH-3 and HBSH-4. HBSH-5 reached a stable value of ca. -5.5 ‰ at that time and remained there until the final growth cessation at 8.2 ± 0.1 ka. Until the growth stop of HBSH-3 at 8.3 ± 0.2 ka, $\delta^{18}\text{O}$ slightly decreases again. Simultaneously, HBSH-4 reinitiated growth with more positive values than before the hiatus and remained at that value (ca. -5 ‰) until 7.0 ± 0.1 ka. At that time, $\delta^{18}\text{O}$ decreases by around 1 ‰ and HBSH-3 started to grow again. From that on, $\delta^{18}\text{O}$ becomes progressively more positive until the final growth cessations in those speleothems. When HBSH-1 started to grow at 6.1 ± 0.6 ka, the $\delta^{18}\text{O}$ value also progressively increases with time until the most positive $\delta^{18}\text{O}$ value of -4.7 ‰ at 0.6 ± 0.1 ka. After 5 ka, the three growing speleothems show relatively similar $\delta^{18}\text{O}$ values within <0.5 ‰. Therefore, these were significantly affected by the same overlying signal. For $\delta^{18}\text{O}$, the major influencing factors are usually the cave temperature and precipitation above the cave. Today, the $\delta^{18}\text{O}$ of precipitation in this region varies between -5 ‰ in summer and -13 ‰ in winter (Riechelmann et al., 2017). Generally, the $\delta^{18}\text{O}$ values of all speleothems are significantly more positive than one would expect from a weighed averaged precipitation signal in this area, since speleothem deposition mainly occurs during winter times in this region (Fohlmeister et al., 2012; Lachniet, 2009; Riechelmann et al., 2017), where $\delta^{18}\text{O}$ values in precipitation are significantly more negative. Therefore, additional influencing factors need to be responsible for the more positive speleothem calcite $\delta^{18}\text{O}$ values, even after correcting for the different reference materials for calcite (V-PDB) and water samples (V-SMOW). In the nearby Bunker Cave, Holocene $\delta^{18}\text{O}$ variability is mainly attributed to changes in winter precipitation and temperature (Fohlmeister et al., 2012). In that study, more positive $\delta^{18}\text{O}$ speleothem values correspond to cold and dry winters and vice versa. This would indicate a trend towards colder and dryer winters with further progressing of the Holocene towards modern times. Besides climatic factors, isotope disequilibrium fractionation can significantly influence the $\delta^{18}\text{O}$ value of speleothem samples (Lachniet, 2009). Since we observed a significant trend towards slower growth rates towards the younger parts of the samples, these disequilibrium effects can alter the $\delta^{18}\text{O}$ values due to enhanced drip intervals on the speleothem surface (Dreybrodt et al., 2016; Hansen et al., 2019; Hendy, 1971; Lachniet, 2009), causing $\delta^{18}\text{O}$ to increase.

7.6.2.2 Stable carbon isotopes

For $\delta^{13}\text{C}$, a general division between the first part of the Holocene and the second part, starting around 7 – 6 ka is visible (Fig. 7.4 [A] and 7.5 [A]). At growth inception, $\delta^{13}\text{C}$ significantly tends towards more negative values in HBSH-4 and HBSH-5, which is most likely related to the climate melioration at the

onset of the Holocene. Increased biological activity in the newly formed soil causes the $\delta^{13}\text{C}$ values to shift to more negative values, due to the biological fractionation of carbon in the soil with increased biological activity (McDermott, 2004). This trend is less clear for HBSH-3. However, this might be related to a later onset of growth for this speleothem (see section 7.6.1), where the overlying soil and vegetation was already established. The most negative peak in $\delta^{13}\text{C}$ is reached around 9.4 ka in HBSH-3 and HBSH-4, with HBSH-5 showing a peak as well. This is coherent with a peak in $\delta^{18}\text{O}$ for these three speleothems as described in section 7.6.2.1. In general, this phase seems to be characterized by increased soil biological activity and root respiration, indicating warm and humid climate conditions during the early Holocene at HBSH. Interestingly, HBSH-4 stopped growth shortly after its most negative $\delta^{13}\text{C}$ values, while HBSH-5 remained at that $\delta^{13}\text{C}$ level and HBSH-3 showing a slight trend towards more positive values until both stopped to grow at 8.3 ± 0.2 ka and 8.2 ± 0.1 ka, respectively. Simultaneously, HBSH-4 started to grow again with $\delta^{13}\text{C}$ values around -10 ‰ and the highest growth rate of the entire sample. The negative $\delta^{13}\text{C}$ values and the high growth rate indicate further favourable climate conditions at that time, which is coherent with the Holocene climate optimum (Mayewski et al., 2004). At 7.0 ± 0.2 ka, HBSH-3 started to grow again with a high growth rate and $\delta^{13}\text{C}$ values around -9.5 ‰. However, growth rate in HBSH-3 rapidly declined after growth inception and $\delta^{13}\text{C}$ values increased towards -8 to -8.5 ‰. This pattern is also visible in HBSH-4 around 6 ka, where $\delta^{13}\text{C}$ increased more than 1 ‰ and growth rate declined to less than $10 \mu\text{m/a}$. This coherent pattern indicates a significant change in water availability inside the cave system, which can either be related to a significant climatic deterioration, or some changes in the hydrology in the epikarst system, reducing the water availability inside the cave. Shortly before the transition towards more positive $\delta^{13}\text{C}$ values and slower growth rates in HBSH-4 occurred, sample HBSH-1 started to grow at 6.1 ± 0.6 ka. The initial $\delta^{13}\text{C}$ values tend rapidly towards more negative values, before reaching their peak at 6.0 ± 0.1 ka. Further on, $\delta^{13}\text{C}$ in HBSH-1 is progressively getting more positive. The same trend is visible for HBSH-3, while the small growth rate of HBSH-4 hampers the temporal precision of individual $\delta^{13}\text{C}$ peaks. However, some coherent patterns are clearly visible. At 5 ka, HBSH-1 and HBSH-4 show a simultaneous decrease in $\delta^{13}\text{C}$ until 4.5 ka, where $\delta^{13}\text{C}$ increases in both samples. A second peak to more negative $\delta^{13}\text{C}$ values is observed in all three speleothems at 4 ka. However, the general trend in $\delta^{13}\text{C}$ is still towards more positive values, reaching its most positive peak at 1.3 ± 0.2 ka, where HBSH-3 and HBSH-4 finally stopped to grow. In contrast, HBSH-1 continued to grow with a constant growth rate and decreasing $\delta^{13}\text{C}$ towards -7.8 ‰ at 0.6 ± 0.1 ka.

Due to the significant changes in growth rate, not solely climate variability, vegetation cover and soil biological activity need to be discussed when changes in $\delta^{13}\text{C}$ are observed in speleothem samples. Besides these climatic and environmental factors affecting $\delta^{13}\text{C}$ in speleothems, fractionation effects can introduce significant bias during speleothem deposition. An increase in $\delta^{13}\text{C}$ might not only be caused by decreasing availability of soil CO_2 , but also by a decrease in drip rate, i.e. a longer residence time of the drip water on the speleothem surface, enhancing disequilibrium isotope fractionation (Deininger et

al., 2012; Mühlinghaus et al., 2009; Scholz et al., 2009). Since growth rate remarkably dropped in all speleothem samples around 7 – 6 ka, it seems likely that the typical drip interval in HBSH increased. This is a potential cause for the progressive increase in $\delta^{13}\text{C}$ in samples HBSH-1, HBSH-3 and HBSH-4, since all their growth rates are below $<10 \mu\text{m/a}$ during that time interval. In contrast, the initial phase of the Holocene in HBSH was characterized by a faster growth rate and decreasing $\delta^{13}\text{C}$ values. During that time span, isotope disequilibrium effects on the speleothem surface should have played a minor role and the decreasing trend should reflect increasing soil cover and biological activity above the cave.

7.6.2.3 Trace elements

All trace elements monitored for HBSH-5 show a decreasing trend towards the growth cessation (Fig. A7.3). At 8.5 ± 0.2 ka, significant increases in Mg, P and Ba are visible, while Sr decreases. This timing is coherent with negative peaks in $\delta^{13}\text{C}$ and $\delta^{18}\text{O}$. In general, the correlation between the four investigated trace elements is positive, with Ba and P showing the highest correlation of 0.7 (Fig. A7.5). In addition, there is a positive correlation of 0.5 between $\delta^{13}\text{C}$ and Mg. Since we attribute the decrease in $\delta^{13}\text{C}$ towards soil formation and increasing biological activity, the decrease in Mg seems to be also attributed to these influencing factors, i.e. more soil formation and wet conditions causing lower Mg mass fractions (Wassenburg et al., 2016b; Weber et al., 2018a). Furthermore, the decrease in Mg is similar as observed in the initial Holocene phase of Bunker Cave (Fohlmeister et al., 2012). The authors attributed this pattern by the deposition of Mg-rich loess during the previous glacial period and the progressive leaching of loess during the early phase of the Holocene. Due to the close proximity to Bunker Cave, the same should be true for HBSH and is an additional explanation for the Mg trend observed in HBSH-5. Since HBSH-5 only covers the initial part of the Holocene, the transition observed in the growth rate and stable isotopes cannot be monitored in this sample. However, HBSH-3 covers most parts of the Holocene besides the hiatus between 8.3 ± 0.2 ka and 7.0 ± 0.2 ka. Therefore, we can expect to see changes between the two different phases in HBSH-3. The first growth phase of HBSH-3 yielded significantly lower Mg mass fractions than the second one. In addition, $\delta^{13}\text{C}$ is significantly more negative in the first growth phase. Based on the assumption proposed for HBSH-1, we expect the first phase to be wetter and highly influenced from soil formation and biological activity. Due to the increase of Mg over time, the Mg mass fraction is positively correlated with the $\delta^{18}\text{O}$ signature (0.5, Fig. A7.6), which also increases over time. Even higher correlations are visible between Mg and Sr (0.6) and Ba and Sr (0.8), indicating the same source for Ba and Sr, most likely the overlying host rock. However, the correlation between Sr and Mg is mainly based on the first growth phase, where Ba, Sr and Mg are increasing. This is clearly visible in the correlation matrix in Fig. 7.7 [A], where only data from the first growth phase (10.6 ± 0.6 to 8.3 ± 0.2 ka) is shown. Strontium and Ba show a strong positive correlation (0.9), as well as Sr and Mg (0.7) and Ba and Mg (0.5). Magnesium, however, is slightly negatively correlated to both stable isotopes. In the second growth phase (7.0 ± 0.2 ka to $1.3 \pm$

0.2 ka), Mg mass fraction is further increasing, while Ba and Sr are decreasing. The correlation matrix for the younger part (Fig. 7.7 [B]) shows, that Mg is positively correlated with both stable isotopes during that time span. Furthermore, Mg is slightly negatively correlated to Sr (-0.1) and Ba (-0.4), while Sr and Ba still show a high positive correlation (0.9). This indicates, that there is a further mechanism during the younger part of the Holocene, which overprints the host rock signal for the trace elements and disrupts the relationship between Sr/Ba and Mg. The increase in Mg mass fraction cannot only be attributed to changes in epikarst pathways, but also to changes in the residence time of the percolating water. Prior calcite precipitation (PCP, Fairchild et al., 2000; Riechelmann et al., 2011) can influence the Mg mass fraction, with increasing PCP forcing the Mg mass fraction in the speleothem to rise (Tooth and Fairchild, 2003). This could explain increasing Mg mass fractions in the younger part and support the assumption of dryer cave conditions. In addition, differences in dissolution characteristics of calcite and dolomite (Fairchild and Treble, 2009) can cause differences in the Mg mass fraction. The host rock of HBSH is similar to the host rock above Bunker Cave, where dolomite has been observed (Grebe, 1993). During dryer conditions, the contribution of dolomite to the drip water will increase and therefore also the Mg mass fraction in the speleothem.

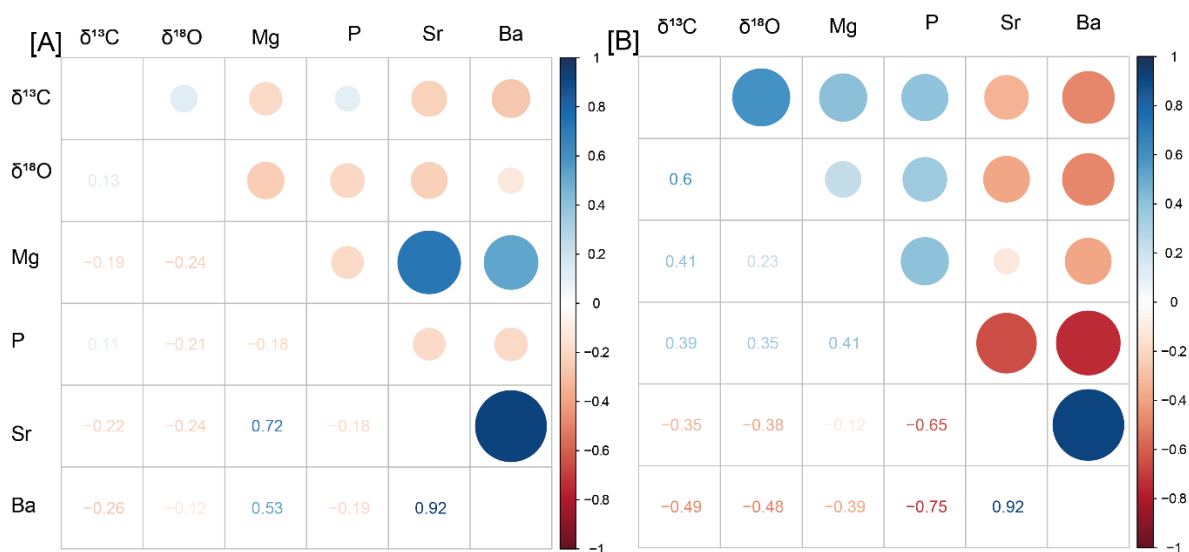


Fig. 7.7: Correlation matrix for stable carbon and oxygen isotopes and trace elements of stalagmite HBSH-3 during the early [A] and late [B] phase of the Holocene.

HBSH-1 shows some differences in the trace element mass fractions in comparison to HBSH-3 and HBSH-5, since it consists of aragonite. Magnesium mass fraction is much lower ($\sim 200 \mu\text{g/g}$) and does not significantly change within the whole section besides some peaks in the youngest 1 ka. In contrast, Sr is highly concentrated ($500 - 800 \mu\text{g/g}$) and shows negative peaks in the youngest part, where Mg is

increasing. This is most likely related to short sections consisting of calcite. In general, Ba, Sr and P show a decreasing trend towards younger ages and are positively correlated to each other (Fig. A7.7). As observed in the younger part of HBSH-3, Mg is negatively correlated to Ba, Sr and P and positively correlated to both stable isotopes. This indicates that the younger part is influenced by an additional factor as described for HBSH-3. By comparing the trace element distribution between HBSH-1 and HBSH-5, which represent only the younger and older part, respectively, the transition described for HBSH-3 is also visible. HBSH-5 shows the positive correlation between Mg and Ba/Sr. In contrast, the younger sample HBSH-1 shows the negative correlation between Mg and Ba/Sr.

7.6.2.4 Strontium isotopes

Strontium isotopes in speleothems have been successfully applied to reconstructions of water availability above the cave and differences in the relative contributions of host rock and overlying soil due to differences in the atmospheric inputs and weathering behaviours of soil components (e.g. Banner et al., 1994; Weber et al., 2018a; Zhou et al., 2009). Since HBSH is in close proximity to Bunker Cave and formed within the same Middle/Upper Devonian limestone (Grebe, 1993; Grebe, 1994), we expect them to show the same Sr isotopic signatures. Therefore, Sr isotopes ratios for host rock and overlying soil presented in Weber et al. (2018a) for Bunker Cave with values of $^{87}\text{Sr}/^{86}\text{Sr} = 0.70836 \pm 0.00006$ for the host rock, 0.71893 ± 0.00001 for soil horizon C and 0.7237 ± 0.0003 for soil horizon A are used. All $^{87}\text{Sr}/^{86}\text{Sr}$ ratios of the speleothems samples lie between these end members (Fig. 7.6) and changes in the Sr isotope composition are likely related to changes in the end-member contribution.

Similar as the changes observed for the trace elements, the Sr isotopes show a significant change in their trend between the early and the latter growth phase. While the three analysed speleothems show a trend to less radiogenic Sr isotopes ratios in the first growth phase, significant shifts are observed for HBSH-3 and HBSH-4. In HBSH-3, we observe the least radiogenic Sr isotope ratio at 6.7 ± 0.3 ka, shortly after the onset of the second growth phase. This trend towards the value of the host rock can be related to an enhanced residence time of the percolating water in the host rock during the hiatus. Therefore, the Sr isotope signature of the host rock is strongly influencing the resulting $^{87}\text{Sr}/^{86}\text{Sr}$ ratio in the speleothem. At 6.8 ± 0.3 ka, $^{87}\text{Sr}/^{86}\text{Sr}$ strongly increased towards growth cessation. The same trend is true for HBSH-4, where a strong increase in $^{87}\text{Sr}/^{86}\text{Sr}$ between 6.5 and 6.0 ka is visible, coherent with the change in growth rate in this sample. Again, $^{87}\text{Sr}/^{86}\text{Sr}$ gets more radiogenic towards younger ages. The increasing $^{87}\text{Sr}/^{86}\text{Sr}$ ratios are coherent with the reduced growth rate of the speleothems, as well as the further trend towards more positive values of $\delta^{13}\text{C}$ and $\delta^{18}\text{O}$ and the increase in Mg mass fraction. Therefore, these factors are likely influenced by the same process, i.e. a further drying of the cave within the Holocene. However, the trend in Sr isotopes with supposed further drying is contrary to the Sr isotope evolution observed in the nearby Bunker Cave during the early MIS 3 (Weber et al., 2018a). In this study, two phases during the early MIS 3 were observed with significantly different environmental conditions.

While the early phase is believed to be warm and humid with increased soil formation and a high weathering rate, the second phase is characterised by dry conditions forcing the $\delta^{13}\text{C}$ values to increase, as well as the Mg mass fraction. Strontium isotopes, however, tend towards less radiogenic values. There are several different processes potentially explaining these differences. Although both cave systems are in close proximity, the processes in the overlying epikarst can be highly variably and complex. Therefore, changes in the karst system do not necessarily affect two different caves in the same way. While for Bunker Cave, increased rainfall amounts are believed to cause an overflow systems in the karst and reducing the influence of the host rock to the Sr isotope signature and vice versa, this is not necessarily true for HBSH. The younger phase in HBSH with potential further dryness can influence the $^{87}\text{Sr}/^{86}\text{Sr}$ ratio of the samples in different ways. Although HBSH might be influenced by further dryness inside the cave, this is not necessarily true for the surface area. In Bunker Cave, no significant drying trend was observed during the Holocene (Fohlmeister et al., 2012). Therefore, it is unlikely that changes in precipitation amount are responsible for the drying observed in HBSH. In contrast, changes in hydrological pathways might be causing this trend during the younger part. Consequently, the surface conditions above the cave were still favourable and are potentially decoupled from the cave conditions. By applying this assumption to the Sr isotope signature, the increase in $^{87}\text{Sr}/^{86}\text{Sr}$ can be attributed to an increased weathering process (Capo et al., 1998; Stewart et al., 2001) due to enhanced weathering of silicate material with highly radiogenic signals as observed for Bunker Cave (Weber et al., 2018a). Besides environmental factors, the Sr isotope signature might also be influenced by fractionation effects. Although it is believed that $^{87}\text{Sr}/^{86}\text{Sr}$ is not affected by fractionation effects, these effects have been described for the stable $\delta^{88}\text{Sr}$ in the per mil range for the marine and terrestrial environment (Fietzke and Eisenhauer, 2006; Halicz et al., 2008). Due to the mass bias correction of $^{87}\text{Sr}/^{86}\text{Sr}$ with the $^{88}\text{Sr}/^{86}\text{Sr}$ ratio, a potential fractionation of that values can potentially influence the resulting $^{87}\text{Sr}/^{86}\text{Sr}$ ratio (Halicz et al., 2008). However, the underlying processes affecting the $\delta^{88}\text{Sr}$ in the soil and cave environment are still not fully understood and require further investigations. Therefore, the influence of stable Sr isotope fractionation with changes in the drip rate of speleothem samples cannot be excluded as potential influencing factor for the increase in $^{87}\text{Sr}/^{86}\text{Sr}$ during the Holocene.

7.6.3 Within cave correlation of HBSH and Bunker Cave

To evaluate the significance of a single speleothem stable isotope record within HBSH, we used the centennial means to calculate correlations between the four samples, as well as the two stacks for $\delta^{13}\text{C}$ and $\delta^{18}\text{O}$ (Fig. 7.8 [A]). In general, the correlation between both stable isotope records of the individual speleothems are highly positive correlated to their respective stack. This proves that the creation of the stack still represents the trends observed in the samples. In addition, all $\delta^{18}\text{O}$ values between all samples are positively correlated to each other, suggesting a common pattern influencing all samples. The same is true for the $\delta^{13}\text{C}$ values, where all samples are positively correlated to each other. However,

differences are observed in the comparison of $\delta^{13}\text{C}$ and $\delta^{18}\text{O}$ values within the cave. While $\delta^{18}\text{O}$ in HBSH-1 is positively correlated to all $\delta^{13}\text{C}$ values of the three remaining speleothems, the $\delta^{13}\text{C}$ values of HBSH-5 are negatively correlated to all $\delta^{18}\text{O}$ values. This trend further supports the transition within the Holocene, as described in the previous sections. Since HBSH-5 only grew in the early phase and showed the initial decrease in $\delta^{13}\text{C}$ at the onset of the Holocene, this sample does not show the transition and is negatively correlated to the similar trend observed in all $\delta^{18}\text{O}$ speleothem curves. Generally, the created stacks of $\delta^{13}\text{C}$ and $\delta^{18}\text{O}$ are slightly correlated (0.3). However, this positive correlation is mainly caused by the same trend in the youngest section, which is strongly expressed by the positive correlation between the $\delta^{13}\text{C}$ stack and the $\delta^{18}\text{O}$ of HBSH-1 (0.6) and the $\delta^{18}\text{O}$ stack and the $\delta^{13}\text{C}$ of HBSH-1 (0.7). In contrast to HBSH, the correlation matrix for Bunker Cave (Fig. 7.8 [B]) shows positive correlations between all samples and isotope curves, covering the same time interval. This indicates that these two isotope systems have been influenced by similar processes, as all individual samples show positive correlation with the created $\delta^{13}\text{C}$ and $\delta^{18}\text{O}$ stacks, both for the same, as well as for the other isotope.

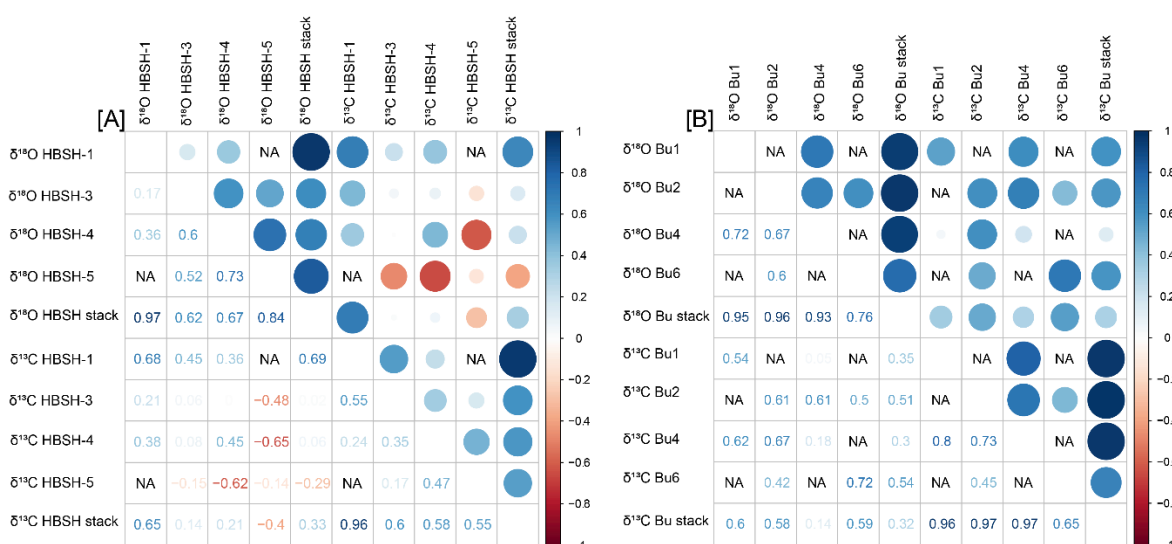


Fig. 7.8: $\delta^{18}\text{O}$ and $\delta^{13}\text{C}$ correlation matrix for [A] the four HBSH stalagmites, as well as the two HBSH stacks and [B] the four Holocene Bu stalagmites (Fohlmeister et al., 2012), as well as the two Bu stacks.

7.6.4 Inter-cave correlation between HBSH and Bunker Cave

Besides the within comparison of the individual samples and the two observed stable isotope systems, the comparison of the same stable isotope within the two nearby cave systems is of great interest. For $\delta^{18}\text{O}$, we cannot observe a significant correlation between the two created stacks for HBSH and Bunker Cave (Fig. 7.9 [A]). However, this is largely related to differences in the correlation of individual speleothem samples. While Bu2 and Bu6 show significant positive correlations to all HBSH samples covering the same time span, Bu4 does not show any correlation to HBSH and Bu1 even negative

correlations to HBSH. This indicates, that Bu does not show an overall common $\delta^{18}\text{O}$ trend as described for HBSH. However, the Bunker Cave speleothems do not overlap as much as the HBSH speleothems in their growth history. The resulting Bunker Cave stack is largely influenced by sample Bu4, which grew from 8 ka until recent times. Since Bu4 does not show any correlation with the HBSH speleothems, the lack of correlation between HBSH and Bunker Cave is plausible. Due to the lack of other longer growing speleothems samples from Bunker Cave, the $\delta^{18}\text{O}$ correlation highly relies on the Bu4 sample, although Bu2 and Bu6 correlate to HBSH, but only for short common time intervals during the early phase of the Holocene, where Bu2 and Bu6 grew. However, these findings further support the transition in HBSH during the middle Holocene. The positive correlation of Bu2 and Bu6 during the early phase of the Holocene shows that during that time, we can observe a common signal in both caves. However, since Bu4 and Bu1 started to grow around 8 and 6 ka, respectively, both samples mainly cover time periods where we expect HBSH to already be influenced by fractionation effects in $\delta^{13}\text{C}$ and potentially also $\delta^{18}\text{O}$, which hampers the potential of common signals between these two cave systems.

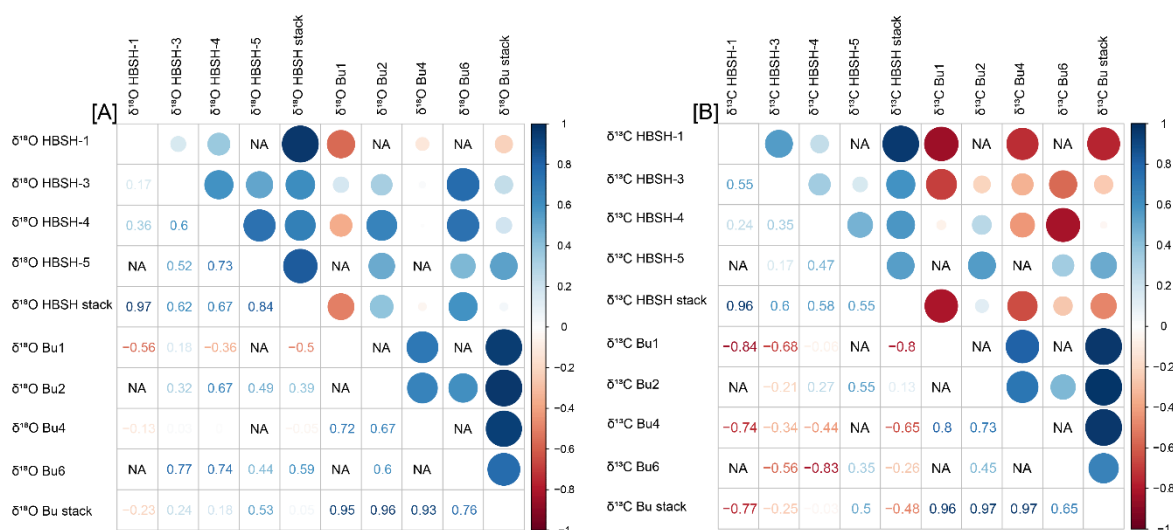


Fig. 7.9: Correlation matrix for [A] $\delta^{18}\text{O}$ of the four Bu (Fohlmeister et al., 2012) and HBSH stalagmites, as well as the two HBSH and Bu stacks and [B] $\delta^{13}\text{C}$ of the four Bu (Fohlmeister et al., 2012) and HBSH stalagmites, as well as the two HBSH and Bu stacks.

For $\delta^{13}\text{C}$ (Fig. 7.9 [B]), the comparison between the two cave systems yielded significant negative correlations. In general, the two $\delta^{13}\text{C}$ stacks show a negative correlation (-0.5). This is especially true for HBSH-1 and the simultaneously growing Bu1 and Bu4 during the younger part of the Holocene section. In addition, HBSH-3 shows negative correlations with all Bunker Cave samples, although covering large parts of the Holocene. A different pattern is visible for HBSH-4, which shows a slight positive correlation to Bu2, which grew in the early phase of the Holocene until approximately 8 ka. In

contrast, correlation with the long growing Bu4 yielded a negative correlation. Interestingly, the $\delta^{13}\text{C}$ values of HBSH-5 show a positive correlation with the simultaneously growing samples Bu2 and Bu6 in Bunker Cave during the early Holocene. This indicates, that the early Holocene signal in $\delta^{13}\text{C}$ is coherent in HBSH and Bunker Cave, while later on, the $\delta^{13}\text{C}$ trends become dispersed and yield negative correlations. This observation is in agreement with the previously observed transition in stable isotopes, trace elements and Sr isotopes.

The comparison of the resulting stable isotope stacks (Fig. 7.10) highlights the conclusions derived from the regression analysis. For $\delta^{18}\text{O}$, the first part of the Holocene shows some common features in HBSH and Bunker Cave, e.g. a peak around 9.6 ka and a general trend towards more positive values. However, this common pattern becomes negligible or even reversed in the latter parts of the Holocene stack, especially for the youngest 3 – 4 ka, where the trends are clearly opposite. Similar patterns can be observed in the $\delta^{13}\text{C}$ stack, with an initial trend towards more negative $\delta^{13}\text{C}$ in the first part until around 9.5 ka, representing the onset of the Holocene with increased soil production and biological activity. However, an even more pronounced trend towards diverging patterns is observed from around 7 – 6 ka onwards. At 6.5 ka, the $\delta^{13}\text{C}$ in Bunker Cave becomes progressively more negative, while $\delta^{13}\text{C}$ in HBSH tends towards more positive values from 6 ka on, resulting in the strong negative correlation observed in this section.

7.6.5 Implications for speleothem based palaeoclimate reconstructions

Our results show that the sole use of stable isotope for palaeoclimate reconstructions using speleothems can be highly biased by non-climatic/environmental factors. Although HBSH and Bunker Cave are located directly nearby, their stable isotope signals clearly diverge for significant parts of the Holocene. HBSH shows a clear trend towards more positive $\delta^{13}\text{C}$ values during the most recent 6 ka. This could imply a general trend towards dryer conditions, less vegetation cover and reduced biological activity, associated with a severe climate deterioration. However, by comparing these results with the Bunker Cave dataset and other well-established climate proxies from the same time interval (e.g. Mayewski et al., 2004; Wanner et al., 2008) this assumption is unlikely. By applying further proxies, such as the growth rate and the trace element composition of the speleothem samples, we were able to deduce that the increase in $\delta^{13}\text{C}$, and potentially $\delta^{18}\text{O}$, are mainly affected by disequilibrium isotope fractionation on the speleothem surface due to enhanced drip intervals. Besides these general differences between the two cave systems, we can see significant differences between samples from the same cave. For example, the relationship between $\delta^{13}\text{C}$ and $\delta^{18}\text{O}$ within one sample is different for the four HBSH speleothems. While HBSH-1 shows a strong positive correlation between these two isotopes, HBSH-5 yields a slight negative correlation. By comparing the growth phases, we were able to show that not all samples from

the same cave were growing simultaneously, although sampled in close proximity. This shows the complex interplay between the growth of speleothems and the processes in the karst system. Therefore, reconstructions based on single speleothem samples needs to be treated with caution and a multi-proxy approach should be applied to eliminate potential cave effects from environmental signals.

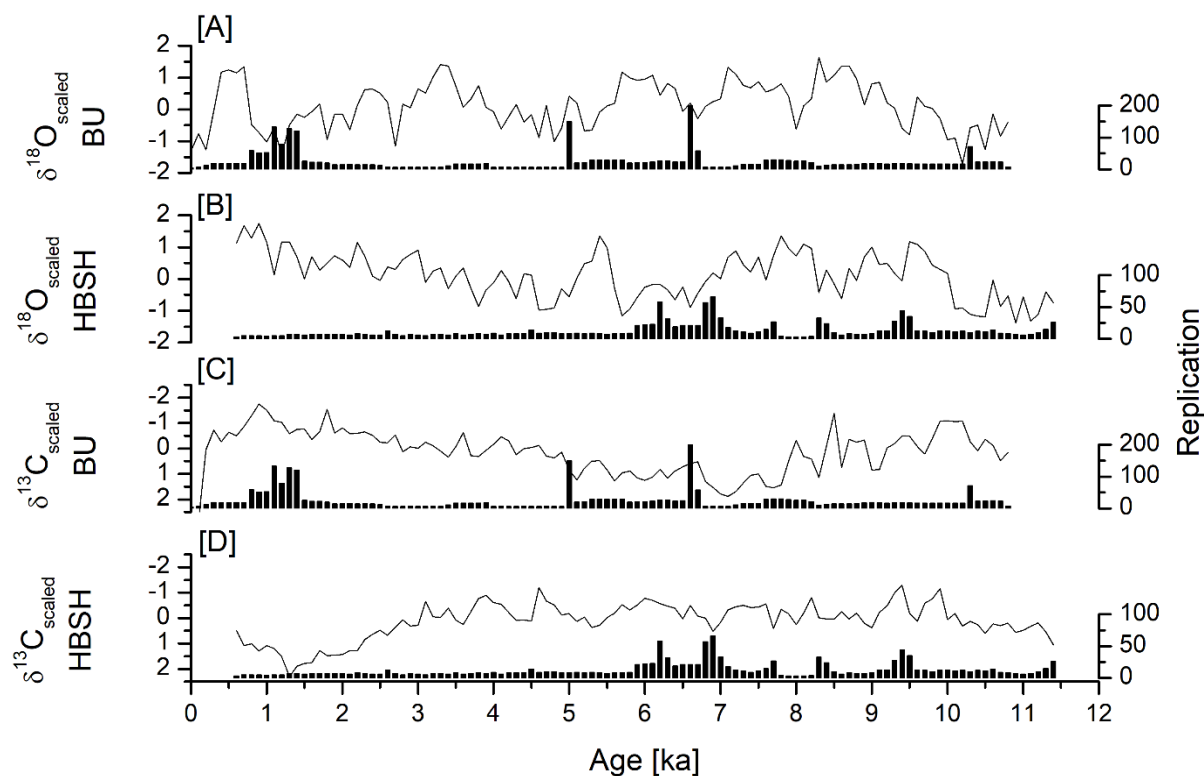


Fig. 7.10: Scaled stable isotope stacks for [A] $\delta^{18}\text{O}$ of Bunker Cave [B] $\delta^{18}\text{O}$ of HBSH [C] $\delta^{13}\text{C}$ of Bunker Cave and [D] $\delta^{13}\text{C}$ of HBSH. For all stacks, the replication indicates the number of individual stable isotope measurements averaged for the centennial mean for the specific time interval. Please note that the axes for $\delta^{13}\text{C}$ are inverted to match with the plots shown in Fig. 7.4 and 7.5.

7.7 Conclusion

Due to sampling regulations in many caves, the number of excavated speleothem samples can be restricted. Therefore, it is important to evaluate the significance of single speleothem isotope records. This is especially crucial for time periods where speleothem growth was rare. While for the Holocene, numerous samples are available for several locations, more crucial time periods might suffer from a lack of further samples and palaeoclimate reconstructions might be based on single samples. By comparing stable isotope records from HBSH and the nearby Bunker Cave, we were able to reconstruct significant changes between the two caves and even within one cave. While the initial part of the Holocene showed some similar trends in both cave systems, no common pattern was observed for the younger parts. By

using a multi-proxy approach using stable isotopes, trace elements and Sr isotopes, we were able to show that the younger part in HBSH was largely influenced by a drying in the cave, causing enrichment in $\delta^{13}\text{C}$ and $\delta^{18}\text{O}$ due to disequilibrium fractionation. This shows, that even within one sample, it is possible to have periods where the proxy data gives reliable information, while other parts can be highly influenced by disequilibrium isotope fractionation effects. Therefore, we highly encourage the application of several proxies to reconstruct past climate variability based on speleothem samples.

7.8 Acknowledgements

M. Weber, K.P. Jochum and D. Scholz are thankful to the Max Planck Graduate Center and the German Research Foundation (DFG SCHO 1274/9-1 and DFG SCHO 1274/11-1) for funding. We also thank B. Schwager, B. Stoll, U. Weis, M. Wimmer, M. Maus and M. Großkopf for assistance in the laboratory.

7.9 Supplement

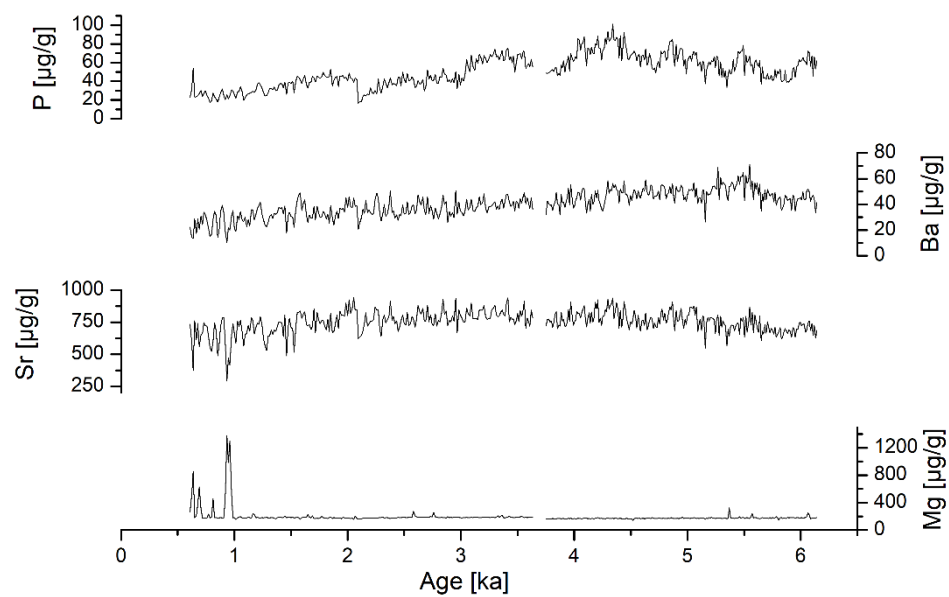


Fig. A7.1: Trace element records of P, Ba, Sr and Mg obtained from HBSH-1.

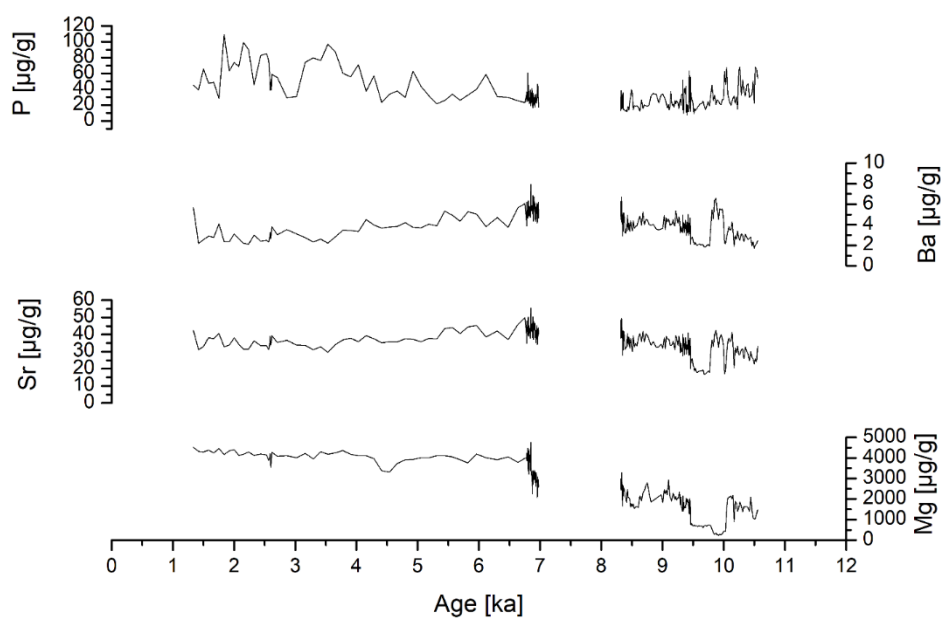


Fig. A7.2: Trace element records of P, Ba, Sr and Mg obtained from HBSH-3.

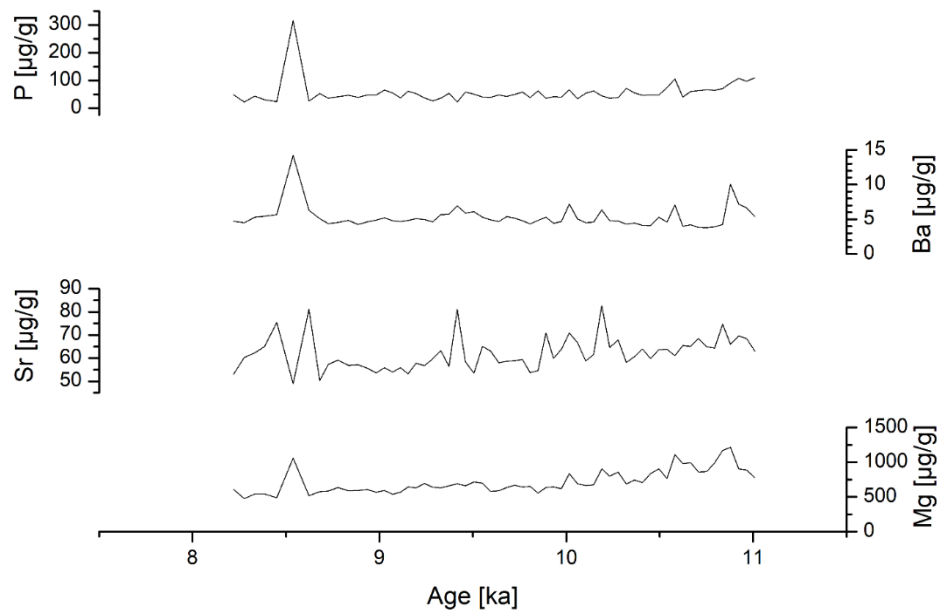


Fig. A7.3: Trace element records of P, Ba, Sr and Mg obtained from HBSH-5.

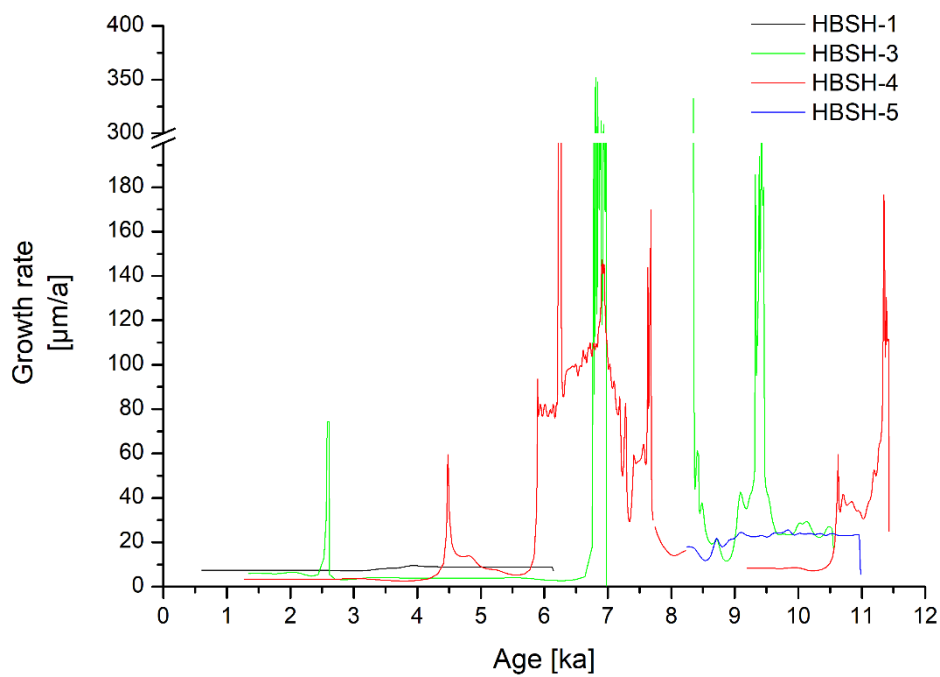


Fig. A7.4: Growth rates for speleothem samples HBSH-1, HBSH-3, HBSH-4, HBSH-5. Please note the break in the y-axis.

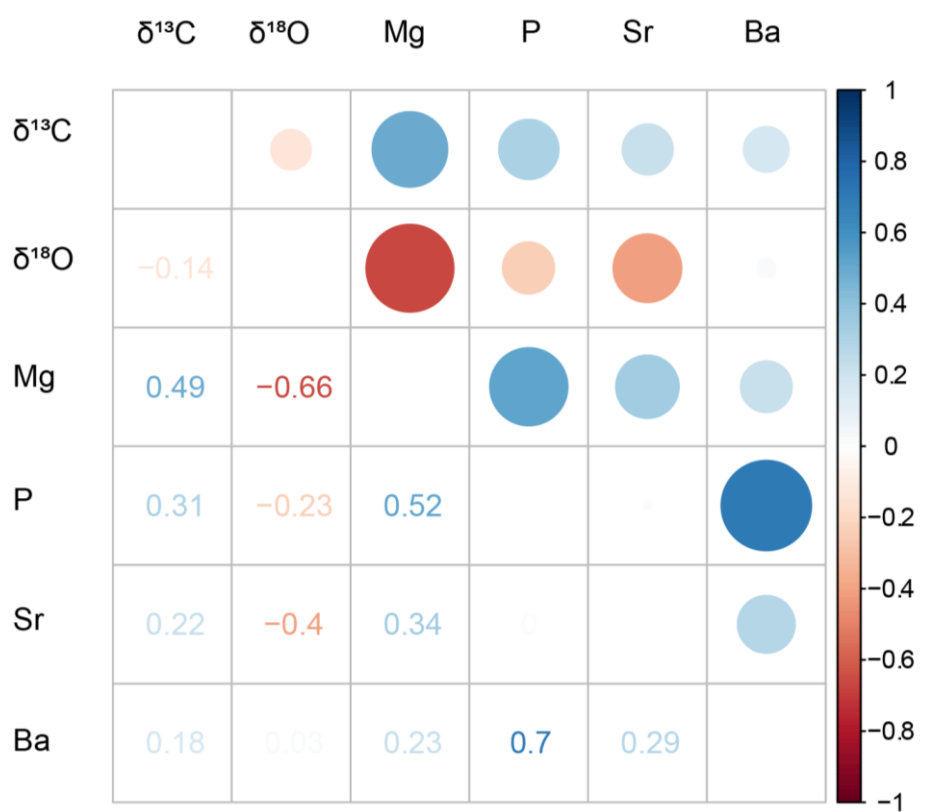


Fig. A7.5: Correlation matrix for stable isotopes and trace elements of HBSH-5.

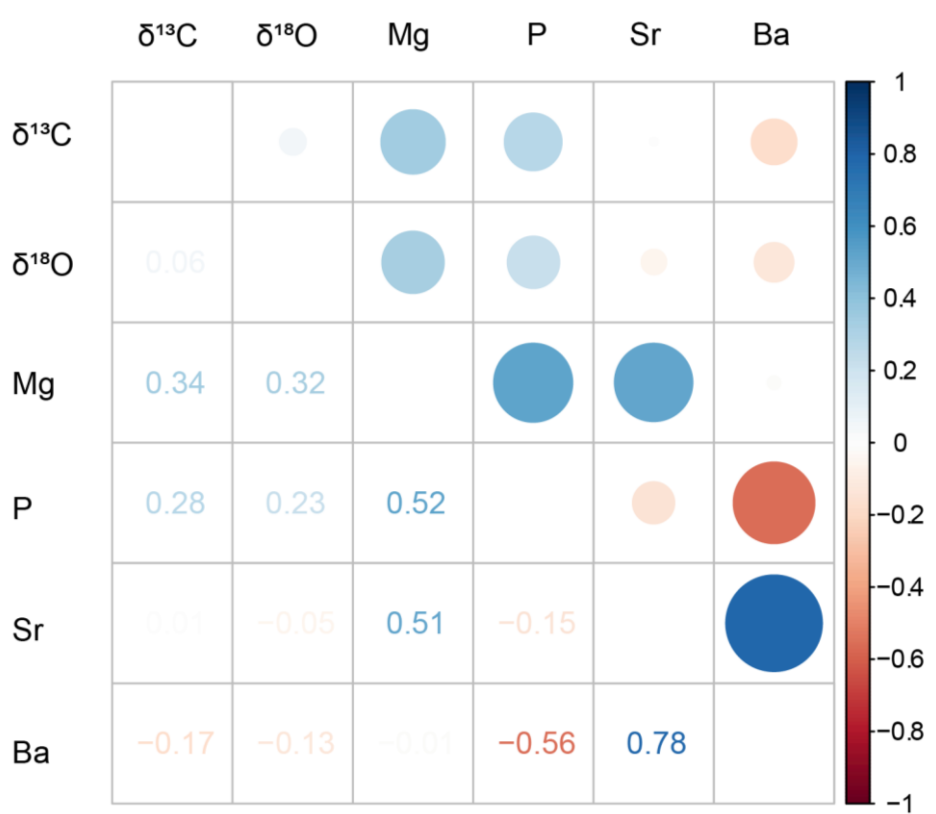


Fig. A7.6: Correlation matrix for stable isotopes and trace elements of HBSH-3.



Fig. A7.7: Correlation matrix for stable isotopes and trace elements of HBSH-1.

Chapter 8: Outlook

The analysis of Sr isotopes in speleothems allows for better understanding of the processes affecting speleothem formation and potential sources of incorporated elements. Therefore, the methodology developed and applied in the framework of this thesis has the potential to be used for different kinds of applications. Besides basic studies for reference material validation, where Sr isotope measurements by LA-MC-ICP-MS can be used as indicator for microhomogeneity, the application to speleothem samples will be further extended. So far, one of the most promising dataset consists of numerous LA-MC-ICP-MS Sr isotope analyses of a speleothem sample from Hüttenbläuserschachthöhle. While the upper Holocene part of sample HBSH-1 is investigated in the framework of this thesis in chapter 7, the remaining stalagmite grew between approximately 130 to 75 ka. Therefore, we can observe the transition from the last interglacial (MIS 5e) towards the transition from MIS 5/4. When comparing the high-resolution $\delta^{13}\text{C}$ record with the $^{87}\text{Sr}/^{86}\text{Sr}$ record (Fig. 8.1), a strong correlation is visible.

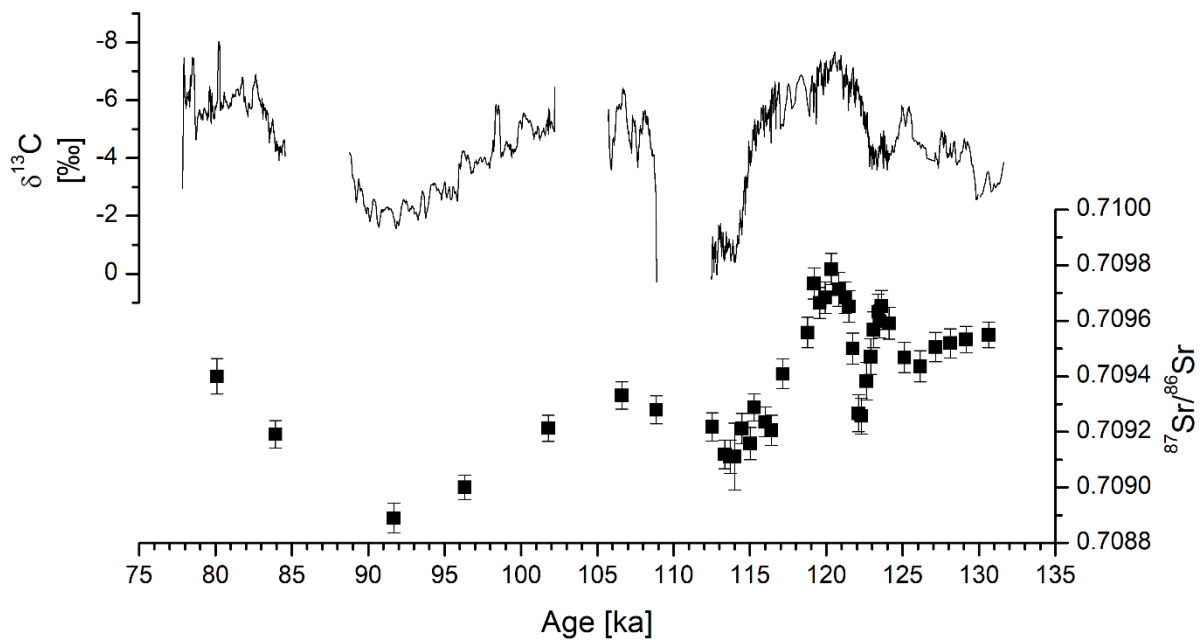


Fig. 8.1: Stable carbon (top) and Sr isotope (bottom) data obtained from stalagmite HBSH-1 from Hüttenbläuserschachthöhle. Both proxies show a similar trend on the longer time scales, covering almost the entire MIS 5. The similar pattern observed in both isotope systems suggests that the underlying mechanisms driving both proxies must be the same or closely linked, potentially related to soil development and changes in weathering above the cave.

The most radiogenic $^{87}\text{Sr}/^{86}\text{Sr}$ ratio of 0.70979 ± 0.00006 at 120.3 ka is coherent with a negative peak in $\delta^{13}\text{C}$ at the same time, potentially indicating the peak interglacial conditions during the Eemian. Furthermore, the following decrease in $^{87}\text{Sr}/^{86}\text{Sr}$ is coherent with a significant increase in $\delta^{13}\text{C}$. In

general, both curves follow the same pattern between 125 ka and 80 ka. Significant negative peaks in $\delta^{13}\text{C}$ around 107 and 80 ka are associated with more radiogenic $^{87}\text{Sr}/^{86}\text{Sr}$ ratios, as well as positive peaks of $\delta^{13}\text{C}$ at 114 ka and 92 ka are in agreement with lower radiogenic $^{87}\text{Sr}/^{86}\text{Sr}$ ratios. In general, the strong correlation between these two proxies suggests a similar underlying mechanism. Since both isotope systems are linked to soil development, the most plausible explanation for these observations are changes in the soil development in combination with changes in weathering rates, allowing different contributions of host rock and soil, influencing both, $\delta^{13}\text{C}$ and $^{87}\text{Sr}/^{86}\text{Sr}$.

In addition to the already obtained speleothem Sr isotope data, the establishment of the low-Sr carbonate reference material “NanoSr” (chapter 5) enables the analysis of speleothem samples with lower Sr mass fractions with enhanced analytical precision and accuracy. As described in chapter 3 and 4, the analysis of Sr isotopes by LA-MC-ICP-MS is mainly limited by the availability of suitable reference materials with similar Sr mass fraction as the sample of interest. By using this new reference material, it will be possible to precisely measure Sr isotopes in speleothem samples $<500\ \mu\text{g/g}$, expanding the methodology for calcite speleothem samples, which are more common in comparison to aragonitic samples. Not only does analysis of speleothems by laser ablation have a great potential, but solution MC-ICP-MS measurements can also be further applied in speleothem science. These methods allow for a higher precision, potentially revealing even small scale changes in speleothem $^{87}\text{Sr}/^{86}\text{Sr}$, not only on a millennial time scale, but also on seasonal scales, i.e. in fast growth speleothem samples, such as MAW-4 from India (chapter 3). Furthermore, with improvements in MC-ICP-MS, the analysis of stable Sr isotope ($\delta^{88}\text{Sr}$) fractionation during speleothem formation can provide additional information in the future.

Radiogenic Sr isotopes have been widely applied in archaeology and palaeontology and the high spatial resolution obtained by LA-MC-ICP-MS allows to detect changes in $^{87}\text{Sr}/^{86}\text{Sr}$ within a few tens of μm . One application of the presented LA-MC-ICP-MS methodology from this thesis is the Sr isotope analysis of dental cubes (including enamel and dentin) from an African elephant (*Loxodonta africana*) molar, which were placed in an isotopic tracer solution, enriched in ^{86}Sr at different temperatures and for varying time spans. By comparing the pristine $^{87}\text{Sr}/^{86}\text{Sr}$ and $^{84}\text{Sr}/^{86}\text{Sr}$ ratio of an unaltered dental cube with a sample, which was placed in the tracer solution at 90°C for 63 days, a significant change is visible for both monitored ratios (Fig. 8.2). While the original sample shows constant $^{87}\text{Sr}/^{86}\text{Sr}$ ratios throughout the whole sample, the altered sample shows significant decreases at the outer rims of the enamel, as well as in the whole dentin. In addition, the naturally invariant $^{84}\text{Sr}/^{86}\text{Sr}$ ratio is also influenced by the intrusion of the tracer solution, showing the same trends as $^{87}\text{Sr}/^{86}\text{Sr}$, with the whole dentin being altered, as well as the outer rim of the enamel. This application shows the high sensitivity and resolution potential of the presented LA-MC-ICP-MS methodology for Sr isotope studies, not only restricted to speleothems/carbonates, but also to samples of different matrices, such as bones and teeth.

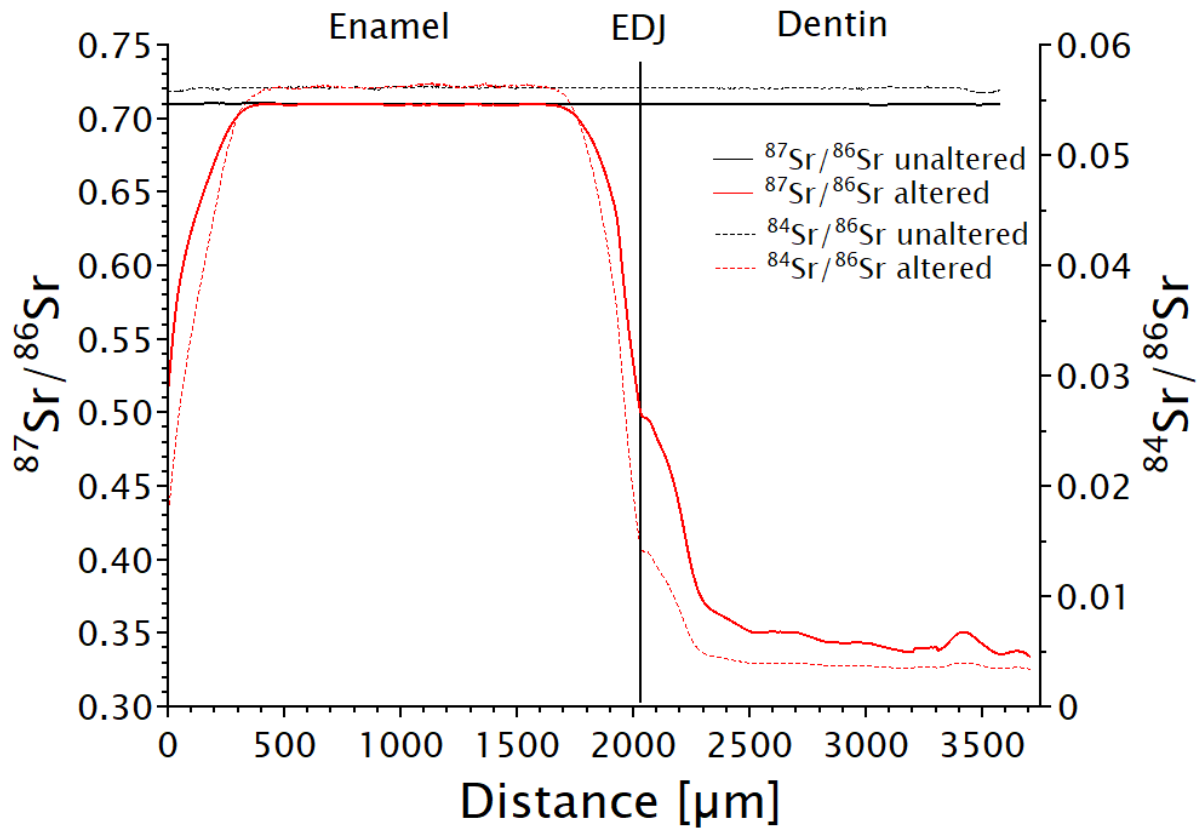


Fig. 8.2: Transect through an unaltered (black) and altered (red) dental cube consisting of enamel and dentin (EDJ = enamel dentin junction) for $^{87}\text{Sr}/^{86}\text{Sr}$ (straight line) and $^{84}\text{Sr}/^{86}\text{Sr}$ (dashed line). The unaltered sample shows constant $^{87}\text{Sr}/^{86}\text{Sr}$ ratios throughout the whole sample, without any significant changes between enamel and dentin. The invariant $^{84}\text{Sr}/^{86}\text{Sr}$ ratio is also constant for the whole sample. In contrast, the altered sample, which was placed in a ^{86}Sr -enriched solution at 90°C for 63 days shows a significant decrease in $^{87}\text{Sr}/^{86}\text{Sr}$, as well as $^{84}\text{Sr}/^{86}\text{Sr}$ in the outer rim of the enamel and the whole dentin. Only the inner part of the enamel shows pristine $^{87}\text{Sr}/^{86}\text{Sr}$ and $^{84}\text{Sr}/^{86}\text{Sr}$ ratios, with the other parts being highly overprinted.

Chapter 9: Conclusions

The methodological developments presented in this thesis allowed the application of the LA-MC-ICP-MS approach for measuring Sr isotopes in speleothems to be further improved and validated. Method robustness using solution analyses and different laser ablation systems was successfully proved using reference materials and speleothem samples. By further expanding the data availability of commonly used carbonate and phosphate reference materials, the basis for successful *in-situ* measurements of Sr isotopes was improved. Furthermore, the introduction of a customised carbonate reference material for low-Sr samples broadened the potential application of the method. Based on these fundamental requirements for successful Sr isotope analysis, the application of this isotope system to speleothem science in combination with traditional proxies, such as stable carbon and oxygen isotopes and trace elements, allows us to gain deeper insights into cave and karst processes. In order to improve palaeoclimate reconstructions based on speleothems, Sr isotopes were applied to two cave systems in Germany, the Bunker Cave and Hüttenbläuserschachthöhle. For Bunker Cave, the growth episode in the early MIS 3 was intensively investigated and Sr isotopes were used to support the $\delta^{13}\text{C}$ and trace element dataset and improve the understanding of weathering processes above the cave. The use of the multi-proxy approach allowed for the distinguishment of two different phases during early MIS 3, one warm and humid, and the second much dryer with a decreased growth rate. The Holocene stable isotope dataset of HBSH was also supplemented with Sr isotopes. By comparing the stable isotope records of four Holocene HBSH stalagmites, it was possible to show that a transition between wetter and dryer conditions in HBSH occurred around 7 – 6 ka. While the initial growth phase during the Holocene shows a good agreement with the nearby Bunker Cave, stable isotope data diverges after this transition. This is mainly attributed to isotope disequilibrium fractionation in HBSH, supported by changes in the correlation of stable isotopes and trace elements, as well as significant changes in the growth rate of all stalagmites.

This thesis highlights the importance and potential of Sr isotopes as additional proxy in speleothem palaeoclimate reconstructions. The independent $^{87}\text{Sr}/^{86}\text{Sr}$ ratio in speleothems should be increasingly used in multi-proxy approaches to support or even improve existing proxy records and exclude potential cave effects as major driver for stable isotope or trace element variations. However, the fractionation of $\delta^{88}\text{Sr}$ is still not fully understood and the potential influence of the obtained $^{87}\text{Sr}/^{86}\text{Sr}$ ratios is a matter of debate. Furthermore, the sole use of a single speleothem sample for palaeoclimate reconstructions should only be performed for time intervals with sparse speleothem growth, such as the MIS 3, and by applying a multi-proxy approach to validate single proxy datasets. This was especially highlighted in the manuscript dealing with the Holocene HBSH samples, which showed a significantly different pattern during the last 7 – 6 ka than the nearby Bunker Cave. Therefore, speleothem palaeoclimate reconstructions solely based on stable isotope records should be regarded with caution and a multi-proxy approach should be used whenever possible.

In summary, this thesis expands the existing Sr isotope methodology for speleothem science, which was used to improve multi-proxy records of speleothems from the MIS 3 and the Holocene, supporting traditional proxy datasets, such as stable carbon and oxygen isotopes and trace elements.

Chapter 10: References

- Aizawa, S., 2008. Determination of trace elements in carbonate reference samples by instrumental neutron activation analysis. *Journal of Radioanalytical and Nuclear Chemistry* 278, 349-352.
- Armstrong, J.T., 1995. CitzaF-a package of correction programs for the quantitative Electron Microbeam X-Ray-Analysis of thick polished materials, thin-films, and particles. *Microbeam Analysis* 4, 177-200.
- Armstrong, R.L., 1971. Glacial erosion and the variable isotopic composition of strontium in sea water. *Nature Physical Science* 230, 132.
- Asmerom, Y., Polyak, V.J., Burns, S.J., 2010. Variable winter moisture in the southwestern United States linked to rapid glacial climate shifts. *Nature Geoscience* 3, 114-117.
- Athanassiou, E.K., Grass, R.N., Stark, W.J., 2010. Chemical aerosol engineering as a novel tool for material science: from oxides to salt and metal nanoparticles. *Aerosol science and technology* 44, 161-172.
- Avigour, A., Magaritz, M., Issar, A., Dodson, M.H., 1990. Sr Isotope Study of Vein and Cave Calcites from Southern Israel. *Chemical Geology* 82, 69-81.
- Ayalon, A., Bar-Matthews, M., Kaufman, A., 1999. Petrography, strontium, barium and uranium concentrations, and strontium and uranium isotope ratios in speleothems as palaeoclimatic proxies: Soreq Cave, Israel. *Holocene* 9, 715-722.
- Bajo, P., Hellstrom, J., Frisia, S., Drysdale, R., Black, J., Woodhead, J., Borsato, A., Zanchetta, G., Wallace, M.W., Regattieri, E., Haese, R., 2016. "Cryptic" diagenesis and its implications for speleothem geochronologies. *Quaternary Science Reviews* 148, 17-28.
- Baker, A., Smart, P.L., Ford, D.C., 1993. Northwest European palaeoclimate as indicated by growth frequency variations of secondary calcite deposits. *Palaeogeography, Palaeoclimatology, Palaeoecology* 100, 291-301.
- Balter, V., Telouk, P., Reynard, B., Braga, J., Thackeray, F., Albarède, F., 2008. Analysis of coupled Sr/Ca and $^{87}\text{Sr}/^{86}\text{Sr}$ variations in enamel using laser-ablation tandem quadrupole-multicollector ICPMS. *Geochimica et Cosmochimica Acta* 72, 3980-3990.
- Balter, V., Braga, J., Telouk, P., Thackeray, J.F., 2012. Evidence for dietary change but not landscape use in South African early hominins. *Nature* 489, 558-560.
- Banner, J.L., Kaufman, J., 1994. The isotopic record of ocean chemistry and diagenesis preserved in non-luminescent brachiopods from Mississippian carbonate rocks, Illinois and Missouri. *Geological Society of America Bulletin* 106, 1074-1082.
- Banner, J.L., Musgrove, M., Capo, R.C., 1994. Tracing ground-water evolution in a limestone aquifer using Sr isotopes: Effects of multiple sources of dissolved ions and mineral-solution reactions. *Geology* 22, 687-690.
- Banner, J.L., Musgrove, M.L., Asmerom, Y., Edwards, R.L., Hoff, J.A., 1996. High-resolution temporal record of Holocene ground-water chemistry: Tracing links between climate and hydrology. *Geology* 24, 1049-1053.

- Banner, J.L., 2004. Radiogenic isotopes: systematics and applications to earth surface processes and chemical stratigraphy. *Earth-Science Reviews* 65, 141-194.
- Bao, Z., Chen, L., Zong, C., Yuan, H., Chen, K., Dai, M., 2017. Development of pressed sulfide powder tablets for in situ sulfur and lead isotope measurement using LA-MC-ICP-MS. *International Journal of Mass Spectrometry* 421, 255-262.
- Bar-Matthews, M., Ayalon, A., Kaufman, A., Wasserburg, G.J., 1999. The Eastern Mediterranean paleoclimate as a reflection of regional events: Soreq cave, Israel. *Earth and Planetary Science Letters* 166, 85-95.
- Barnett-Johnson, R., Ramos, F.C., Grimes, C.B., MacFarlane, R.B., 2005. Validation of Sr isotopes in otoliths by laser ablation multicollector inductively coupled plasma mass spectrometry (LA-MC-ICPMS): opening avenues in fisheries science applications. *Canadian Journal of Fisheries and Aquatic Sciences* 62, 2425-2430.
- Baskaran, M., Iliffe, T.M., 1993. Age determination of recent cave deposits using excess ^{210}Pb -A new technique. *Geophysical Research Letters* 20, 603-606.
- Baskaran, M., 2012. Dating of Biogenic and Inorganic Carbonates Using ^{210}Pb - ^{226}Ra Disequilibrium Method: A Review, *Handbook of Environmental Isotope Geochemistry*. Springer, pp. 789-809.
- Bates, S.L., Siddall, M., Waelbroeck, C., 2014a. Hydrographic variations in deep ocean temperature over the mid-Pleistocene transition. *Quaternary Science Reviews* 88, 147-158.
- Bates, S.L., Siddall, M., Waelbroeck, C., 2014b. Sea level records and deep ocean temperatures from ODP composite site 162-980/981, In supplement to: Bates, SL et al. (2014): Hydrographic variations in deep ocean temperature over the mid-Pleistocene transition. *Quaternary Science Reviews*, 88, 147-158, <https://doi.org/10.1016/j.quascirev.2014.01.020>. PANGAEA.
- Belli, R., Borsato, A., Frisia, S., Drysdale, R., Maas, R., Greig, A., 2017. Investigating the hydrological significance of stalagmite geochemistry (Mg, Sr) using Sr isotope and particulate element records across the Late Glacial-to-Holocene transition. *Geochimica et Cosmochimica Acta* 199, 247-263.
- Berglund, M., Wieser, M.E., 2011. Isotopic compositions of the elements 2009 (IUPAC Technical Report). *Pure and Applied Chemistry* 83, 397-410.
- Bizzarro, M., Simonetti, A., Stevenson, R.K., Kurszlaukis, S., 2003. In situ $^{87}\text{Sr}/^{86}\text{Sr}$ investigation of igneous apatites and carbonates using laser-ablation MC-ICP-MS. *Geochimica et Cosmochimica Acta* 67, 289-302.
- Böhm, E., Lippold, J., Gutjahr, M., Frank, M., Blaser, P., Antz, B., Fohlmeister, J., Frank, N., Andersen, M.B., Deininger, M., 2015. Strong and deep Atlantic meridional overturning circulation during the last glacial cycle. *Nature* 517, 73.
- Bolea-Fernandez, E., Van Malderen, S.J.M., Balcaen, L., Resano, M., Vanhaecke, F., 2016. Laser ablation-tandem ICP-mass spectrometry (LA-ICP-MS/MS) for direct Sr isotopic analysis of solid samples with high Rb/Sr ratios. *Journal of Analytical Atomic Spectrometry* 31, 464-472.

- Bond, G., Broecker, W., Johnsen, S., McManus, J., Labeyrie, L., Jouzel, J., Bonani, G., 1993. Correlations between climate records from North Atlantic sediments and Greenland ice. *Nature* 365, 143-147.
- Bourdon, B., Turner, S., Henderson, G.M., Lundstrom, C.C., 2003. Introduction to U-series geochemistry. *Reviews in mineralogy and geochemistry* 52, 1-21.
- Bowen, G.J., Wilkinson, B., 2002. Spatial distribution of $\delta^{18}\text{O}$ in meteoric precipitation. *Geology* 30, 315-318.
- Bowen, G.J., 2008. Spatial analysis of the intra-annual variation of precipitation isotope ratios and its climatological corollaries. *Journal of Geophysical Research: Atmospheres* 113 (5D).
- Breitenbach, S.F.M., Adkins, J.F., Meyer, H., Marwan, N., Kumar, K.K., Haug, G.H., 2010. Strong influence of water vapor source dynamics on stable isotopes in precipitation observed in Southern Meghalaya, NE India. *Earth and Planetary Science Letters* 292, 212-220.
- Breitenbach, S.F.M., Rehfeld, K., Goswami, B., Baldini, J.U.L., Ridley, H.E., Kennett, D., Prufer, K., Aquino, V.V., Asmerom, Y., Polyak, V.J., 2012. COConstructing Proxy-Record Age models (COPRA). *Climate of the past*. 8, 1765-1779.
- Breitenbach, S.F.M., Lechleitner, F.A., Meyer, H., Diengdoh, G., Matthey, D., Marwan, N., 2015. Cave ventilation and rainfall signals in dripwater in a monsoonal setting - a monitoring study from NE India. *Chemical Geology* 402, 111-124.
- Brenner, M., Rosenmeier, M.F., Hodell, D.A., Curtis, J.H., 2002. Paleolimnology of the Maya lowlands: Long-term perspectives on interactions among climate, environment, and humans. *Ancient Mesoamerica* 13, 141-157.
- Budsky, A., Scholz, D., Wassenburg, J.A., Mertz-Kraus, R., Spötl, C., Riechelmann, D.F.C., Gibert, L., Jochum, K.P., Andreae, M.O., 2019. Speleothem $\delta^{13}\text{C}$ record suggests enhanced spring/summer drought in south-eastern Spain between 9.7 and 7.8 ka—A circum-Western Mediterranean anomaly? *The Holocene*, 0959683619838021.
- Burchette, T.P., 1981. European Devonian reefs: a review of current concepts and models. *SEPM Special Publication* 30, 85 - 142.
- Burke, W.H., Denison, R.E., Hetherington, E.A., Koepnick, R.B., Nelson, H.F., Otto, J.B., 1982. Variation of seawater $^{87}\text{Sr}/^{86}\text{Sr}$ throughout Phanerozoic time. *Geology* 10, 516-519.
- Burton, J.H., Wright, L.E., 1995. Nonlinearity in the relationship between bone Sr/Ca and diet: paleodietary implications. *American journal of physical anthropology* 96, 273-282.
- Cacho, I., Grimalt, J.O., Pelejero, C., Canals, M., Sierro, F.J., Flores, J.A., Shackleton, N., 1999. Dansgaard-Oeschger and Heinrich event imprints in Alboran Sea paleotemperatures. *Paleoceanography* 14, 698-705.
- Capo, R.C., Stewart, B.W., Chadwick, O.A., 1998. Strontium isotopes as tracers of ecosystem processes: theory and methods. *Geoderma* 82, 197-225.

- Cerling, T.E., 1984. The stable isotopic composition of modern soil carbonate and its relationship to climate. *Earth and Planetary Science Letters* 71, 229-240.
- Cheng, H., Edwards, R.L., Hoff, J., Gallup, C.D., Richards, D.A., Asmerom, Y., 2000. The half-lives of uranium-234 and thorium-230. *Chemical Geology* 169, 17-33.
- Cheng, H., Edwards, R.L., Sinha, A., Spötl, C., Yi, L., Chen, S., Kelly, M., Kathayat, G., Wang, X., Li, X., 2016. The Asian monsoon over the past 640,000 years and ice age terminations. *Nature* 534, 640-646.
- Christensen, J.N., Halliday, A.N., Lee, D.C., Hall, C.M., 1995. In-Situ Sr Isotopic Analysis by Laser-Ablation. *Earth and Planetary Science Letters* 136, 79-85.
- Constantin, S., Bojar, A.-V., Lauritzen, S.-E., Lundberg, J., 2007. Holocene and Late Pleistocene climate in the sub-Mediterranean continental environment: a speleothem record from Poleva Cave (Southern Carpathians, Romania). *Palaeogeography, Palaeoclimatology, Palaeoecology* 243, 322-338.
- Copeland, S.R., Sponheimer, M., le Roux, P.J., Grimes, V., Lee-Thorp, J.A., de Ruiter, D.J., Richards, M.P., 2008. Strontium isotope ratios ($^{87}\text{Sr}/^{86}\text{Sr}$) of tooth enamel: a comparison of solution and laser ablation multicollector inductively coupled plasma mass spectrometry methods. *Rapid Commun Mass Spectrom* 22, 3187-3194.
- Copeland, S.R., Sponheimer, M., Lee-Thorp, J.A., le Roux, P.J., de Ruiter, D.J., Richards, M.P., 2010. Strontium isotope ratios in fossil teeth from South Africa: assessing laser ablation MC-ICP-MS analysis and the extent of diagenesis. *Journal of Archaeological Science* 37, 1437-1446.
- Copeland, S.R., Sponheimer, M., de Ruiter, D.J., Lee-Thorp, J.A., Codron, D., le Roux, P.J., Grimes, V., Richards, M.P., 2011. Strontium isotope evidence for landscape use by early hominins. *Nature* 474, 76-78.
- Craig, H., 1957. Isotopic standards for carbon and oxygen and correction factors for mass-spectrometric analysis of carbon dioxide. *Geochimica et Cosmochimica Acta* 12, 133-149.
- Craig, H., 1961. Standard for Reporting Concentrations of Deuterium and Oxygen-18 in Natural Waters. *Science* 133, 1833-1834.
- Cruz, F.W., Burns, S.J., Karmann, I., Sharp, W.D., Vuille, M., Cardoso, A.O., Ferrari, J.A., Dias, P.L.S., Viana, O., 2005. Insolation-driven changes in atmospheric circulation over the past 116,000 years in subtropical Brazil. *Nature* 434, 63-66.
- Dansgaard, W., White, J.W.C., Johnsen, S.J., 1989. The abrupt termination of the Younger Dryas climate event. *Nature* 339, 532.
- Dansgaard, W., Johnsen, S.J., Clausen, H.B., Dahl-Jensen, D., Gundestrup, N.S., Hammer, C.U., Hvidberg, C.S., Steffensen, J.P., Sveinbjörnsdottir, A.E., Jouzel, J., 1993. Evidence for general instability of past climate from a 250-kyr ice-core record. *Nature* 364, 218-220.
- Davidson, J., Tepley, F., Palacz, Z., Meffan-Main, S., 2001. Magma recharge, contamination and residence times revealed by in situ laser ablation isotopic analysis of feldspar in volcanic rocks. *Earth and Planetary Science Letters* 184, 427-442.

- De Jong, H.N., Foster, G.L., Hawkesworth, C.J., Pike, A.W.G., 2007. LA-MC-ICPMS $^{87}\text{Sr}/^{86}\text{Sr}$ analysis on tooth enamel - Pitfalls and problems. *Geochimica et Cosmochimica Acta* 71, A212.
- De Muynck, D., Vanhaecke, F., 2009. Development of a method based on inductively coupled plasma-dynamic reaction cell-mass spectrometry for the simultaneous determination of phosphorus, calcium and strontium in bone and dental tissue. *Spectrochimica Acta Part B: Atomic Spectroscopy* 64, 408-415.
- Dearing, J.A., 2006. Climate-human-environment interactions: resolving our past. *Climate of the past Discussions* 2, 563-604.
- Deininger, M., Fohlmeister, J., Scholz, D., Mangini, A., 2012. Isotope disequilibrium effects: The influence of evaporation and ventilation effects on the carbon and oxygen isotope composition of speleothems – A model approach. *Geochimica et Cosmochimica Acta* 96, 57-79.
- Dreybrodt, W., 2008. Evolution of the isotopic composition of carbon and oxygen in a calcite precipitating $\text{H}_2\text{O}-\text{CO}_2-\text{CaCO}_3$ solution and the related isotopic composition of calcite in stalagmites. *Geochimica et Cosmochimica Acta* 72, 4712-4724.
- Dreybrodt, W., Scholz, D., 2011. Climatic dependence of stable carbon and oxygen isotope signals recorded in speleothems: From soil water to speleothem calcite. *Geochimica et Cosmochimica Acta* 75, 734-752.
- Dreybrodt, W., Hansen, M., Scholz, D., 2016. Processes affecting the stable isotope composition of calcite during precipitation on the surface of stalagmites: laboratory experiments investigating the isotope exchange between DIC in the solution layer on top of a speleothem and the CO_2 of the cave atmosphere. *Geochimica et Cosmochimica Acta* 174, 247-262.
- Drysdale, R.N., Zanchetta, G., Hellstrom, J.C., Fallick, A.E., Zhao, J.-x., Isola, I., Bruschi, G., 2004. Palaeoclimatic implications of the growth history and stable isotope ($\delta^{18}\text{O}$ and $\delta^{13}\text{C}$) geochemistry of a Middle to Late Pleistocene stalagmite from central-western Italy. *Earth and Planetary Science Letters* 227, 215-229.
- Duplessy, J.C., Roche, D.M., Kageyama, M., 2007. The Deep Ocean During the Last Interglacial Period. *Science* 316, 89-91.
- Durante, C., Baschieri, C., Bertacchini, L., Bertelli, D., Cocchi, M., Marchetti, A., Manzini, D., Papotti, G., Sighinolfi, S., 2015. An analytical approach to Sr isotope ratio determination in Lambrusco wines for geographical traceability purposes. *Food Chemistry* 173, 557-563.
- Ehrlich, S., Gavrieli, I., Dor, L.-B., Halicz, L., 2001. Direct high-precision measurements of the $^{87}\text{Sr}/^{86}\text{Sr}$ isotope ratio in natural water, carbonates and related materials by multiple collector inductively coupled plasma mass spectrometry (MC-ICP-MS). *Journal of Analytical Atomic Spectrometry* 16, 1389-1392.
- Evans, D., Müller, W., 2018. Automated Extraction of a Five-Year LA-ICP-MS Trace Element Data Set of Ten Common Glass and Carbonate Reference Materials: Long-Term Data Quality, Optimisation and Laser Cell Homogeneity. *Geostandards and Geoanalytical Research* 42, 159-188.

- Fairchild, I.J., Borsato, A., Tooth, A.F., Frisia, S., Hawkesworth, C.J., Huang, Y., McDermott, F., Spiro, B., 2000. Controls on trace element (Sr–Mg) compositions of carbonate cave waters: implications for speleothem climatic records. *Chemical Geology* 166, 255-269.
- Fairchild, I.J., Smith, C.L., Baker, A., Fuller, L., Spotl, C., Matthey, D., McDermott, F., Eimp, 2006. Modification and preservation of environmental signals in speleothems. *Earth-Science Reviews* 75, 105-153.
- Fairchild, I.J., Treble, P.C., 2009. Trace elements in speleothems as recorders of environmental change. *Quaternary Science Reviews* 28, 449-468.
- Fairchild, I.J., Baker, A., 2012. *Speleothem Science*. John Wiley & Sons, Ltd, Chichester, 450p.
- Fankhauser, A., McDermott, F., Fleitmann, D., 2016. Episodic speleothem deposition tracks the terrestrial impact of millennial-scale last glacial climate variability in SW Ireland. *Quaternary Science Reviews* 152, 104-117.
- Faure, G., Mensing, T.M., 2005. *Isotopes: principles and applications*. John Wiley & Sons, 928p.
- Fietzke, J., Eisenhauer, A., 2006. Determination of temperature-dependent stable strontium isotope ($^{88}\text{Sr}/^{86}\text{Sr}$) fractionation via bracketing standard MC-ICP-MS. *Geochemistry, Geophysics, Geosystems* 7, Q08009.
- Fietzke, J., Liebetrau, V., Guenther, D., Gurs, K., Hametner, K., Zumholz, K., Hansteen, T.H., Eisenhauer, A., 2008. An alternative data acquisition and evaluation strategy for improved isotope ratio precision using LA-MC-ICP-MS applied to stable and radiogenic strontium isotopes in carbonates. *Journal of Analytical Atomic Spectrometry* 23, 955-961.
- Finch, A.A., Shaw, P.A., Weedon, G.P., Holmgren, K., 2001. Trace element variation in speleothem aragonite: potential for palaeoenvironmental reconstruction. *Earth and Planetary Science Letters* 186, 255-267.
- Fisher, E.C., Bar-Matthews, M., Jerardino, A., Marean, C.W., 2010. Middle and Late Pleistocene paleoscape modeling along the southern coast of South Africa. *Quaternary Science Reviews* 29, 1382-1398.
- Fleitmann, D., Cheng, H., Badertscher, S., Edwards, R.L., Mudelsee, M., Göktürk, O.M., Fankhauser, A., Pickering, R., Raible, C.C., Matter, A., Kramers, J., Tüysüz, O., 2009. Timing and climatic impact of Greenland interstadials recorded in stalagmites from northern Turkey. *Geophysical Research Letters* 36 (19).
- Fohlmeister, J., Scholz, D., Kromer, B., Mangini, A., 2011. Modelling carbon isotopes of carbonates in cave drip water. *Geochimica et Cosmochimica Acta* 75, 5219-5228.
- Fohlmeister, J., Schröder-Ritzrau, A., Scholz, D., Spötl, C., Riechelmann, D.F.C., Mudelsee, M., Wackerbarth, A., Gerdes, A., Riechelmann, S., Immenhauser, A., Richter, D.K., Mangini, A., 2012. Bunker Cave stalagmites: an archive for central European Holocene climate variability. *Climate of the Past* 8, 1751-1764.
- Ford, D., Williams, P.D., 2013. *Karst hydrogeology and geomorphology*. John Wiley & Sons, 576p.

- Frumkin, A., Stein, M., 2004. The Sahara-East Mediterranean dust and climate connection revealed by strontium and uranium isotopes in a Jerusalem speleothem. *Earth and Planetary Science Letters* 217, 451-464.
- Galiová, M.V., Fišáková, M.N., Kynický, J., Prokeš, L., Neff, H., Mason, A.Z., Gadas, P., Košler, J., Kanický, V., 2013. Elemental mapping in fossil tooth root section of *Ursus arctos* by laser ablation inductively coupled plasma mass spectrometry (LA-ICP-MS). *Talanta* 105, 235-243.
- Galler, P., Limbeck, A., Boulyga, S.F., Stingeder, G., Hirata, T., Prohaska, T., 2007. Development of an on-line flow injection Sr/matrix separation method for accurate, high-throughput determination of Sr isotope ratios by multiple collector-inductively coupled plasma-mass spectrometry. *Analytical Chemistry* 79, 5023-5029.
- Gallet, S., Jahn, B.M., Lanoe, B.V., Dia, A., Rossello, E., 1998. Loess geochemistry and its implications for particle origin and composition of the upper continental crust. *Earth and Planetary Science Letters* 156, 157-172.
- Garbe-Schönberg, D., Müller, S., 2014. Nano-particulate pressed powder tablets for LA-ICP-MS. *Journal of Analytical Atomic Spectrometry* 29, 990-1000.
- Genty, D., Massault, M., 1999. Carbon transfer dynamics from bomb-¹⁴C and δ^{13} C time series of a laminated stalagmite from SW France—modelling and comparison with other stalagmite records. *Geochimica et Cosmochimica Acta* 63, 1537-1548.
- Genty, D., Massault, M., Gilmour, M., Baker, A., Verheyden, S., Kepens, E., 1999. Calculation of past dead carbon proportion and variability by the comparison of AMS ¹⁴C and TIMS U/Th ages on two Holocene stalagmites. *Radiocarbon* 41, 251-270.
- Genty, D., Baker, A., Massault, M., Proctor, C., Gilmour, M., Pons-Branchu, E., Hamelin, B., 2001. Dead carbon in stalagmites: carbonate bedrock paleodissolution vs. ageing of soil organic matter. Implications for ¹³C variations in speleothems. *Geochimica et Cosmochimica Acta* 65, 3443-3457.
- Genty, D., Blamart, D., Ouahdi, R., Gilmour, M., Baker, A., Jouzel, J., Van-Exter, S., 2003. Precise dating of Dansgaard-Oeschger climate oscillations in western Europe from stalagmite data. *Nature* 421, 833-837.
- Genty, D., Combourieu Nebout, N., Hatté, C., Blamart, D., Ghaleb, B., Isabello, L., 2005. Rapid climatic changes of the last 90 kyr recorded on the European continent. *Comptes Rendus Geoscience* 337, 970-982.
- Genty, D., Blamart, D., Ghaleb, B., Plagnes, V., Causse, C., Bakalowicz, M., Zouari, K., Chkir, N., Hellstrom, J., Wainer, K., 2006. Timing and dynamics of the last deglaciation from European and North African δ^{13} C stalagmite profiles - comparison with Chinese and South Hemisphere stalagmites. *Quaternary Science Reviews* 25, 2118-2142.
- Genty, D., Combourieu-Nebout, N., Peyron, O., Blamart, D., Wainer, K., Mansuri, F., Ghaleb, B., Isabello, L., Dormoy, I., von Grafenstein, U., Bonelli, S., Landais, A., Brauer, A., 2010. Isotopic characterization of rapid climatic events during OIS3 and OIS4 in Villars Cave stalagmites (SW-France)

and correlation with Atlantic and Mediterranean pollen records. *Quaternary Science Reviews* 29, 2799-2820.

Gerdes, A., Zeh, A., 2006. Combined U–Pb and Hf isotope LA-(MC-)ICP-MS analyses of detrital zircons: Comparison with SHRIMP and new constraints for the provenance and age of an Armorican metasediment in Central Germany. *Earth and Planetary Science Letters* 249, 47-61.

Gibert, L., Scott, G.R., Scholz, D., Budsky, A., Ferrández, C., Ribot, F., Martin, R.A., Lería, M., 2016. Chronology for the Cueva Victoria fossil site (SE Spain): Evidence for Early Pleistocene Afro-Iberian dispersals. *Journal of Human Evolution* 90, 183-197.

Glaus, R., Kaegi, R., Krumeich, F., Gunther, D., 2010. Phenomenological studies on structure and elemental composition of nanosecond and femtosecond laser-generated aerosols with implications on laser ablation inductively coupled plasma mass spectrometry. *Spectrochim Acta B* 65, 812-822.

Goede, A., McCulloch, M., McDermott, F., Hawkesworth, C., 1998. Aeolian contribution to strontium and strontium isotope variations in a Tasmanian speleothem. *Chemical Geology* 149, 37-50.

Gordon, D., Smart, P.L., Ford, D.C., Andrews, J.N., Atkinson, T.C., Rowe, P.J., Christopher, N.S.J., 1989. Dating of late Pleistocene interglacial and interstadial periods in the United Kingdom from speleothem growth frequency. *Quaternary Research* 31, 14-26.

Grebe, W., 1993. Die Bunkerhöhle in Iserlohn-Letmathe (Sauerland). *Mitteilung des Verbands der deutschen Höhlen-und Karstforscher, München* 39, 22-23.

Grebe, W., 1994. Die Hüttenbläuserschachthöhle—eine neuentdeckte Höhle in Iserlohn-Letmathe. *Mitteilungen & Berichte Speläogruppe Letmathe* 10, 49-65.

Halicz, L., Segal, I., Fruchter, N., Stein, M., Lazar, B., 2008. Strontium stable isotopes fractionate in the soil environments? *Earth and Planetary Science Letters* 272, 406-411.

Hansen, M., Dreybrodt, W., Scholz, D., 2013. Chemical evolution of dissolved inorganic carbon species flowing in thin water films and its implications for (rapid) degassing of CO₂ during speleothem growth. *Geochimica et Cosmochimica Acta* 107, 242-251.

Hansen, M., Scholz, D., Froeschmann, M.-L., Schöne, B.R., Spötl, C., 2017. Carbon isotope exchange between gaseous CO₂ and thin solution films: Artificial cave experiments and a complete diffusion-reaction model. *Geochimica et Cosmochimica Acta* 211, 28-47.

Hansen, M., Scholz, D., Schöne, B.R., Spötl, C., 2019. Simulating speleothem growth in the laboratory: Determination of the stable isotope fractionation ($\delta^{13}\text{C}$ and $\delta^{18}\text{O}$) between H₂O, DIC and CaCO₃. *Chemical Geology* 509, 22-44.

Harris, N., 1995. Significance of weathering Himalayan metasedimentary rocks and leucogranites for the Sr isotope evolution of seawater during the early Miocene. *Geology* 23, 795-798.

Heinrich, H., 1988. Origin and Consequences of Cyclic Ice Rafting in the Northeast Atlantic Ocean During the Past 130,000 Years. *Quaternary Research* 29, 142-152.

- Hendy, C.H., 1971. The isotopic geochemistry of speleothems—I. The calculation of the effects of different modes of formation on the isotopic composition of speleothems and their applicability as palaeoclimatic indicators. *Geochimica et Cosmochimica Acta* 35, 801-824.
- Hennig, G.J., Grün, R., Brunnacker, K., 1983. Speleothems, travertines, and paleoclimates. *Quaternary Research* 20, 1-29.
- Hodge, E.J., Richards, D.A., Smart, P.L., Andreo, B., Hoffmann, D.L., Matthey, D.P., González-Ramón, A., 2008. Effective precipitation in southern Spain (~ 266 to 46 ka) based on a speleothem stable carbon isotope record. *Quaternary Research* 69, 447-457.
- Hoffmann, D.L., Prytulak, J., Richards, D.A., Elliott, T., Coath, C.D., Smart, P.L., Scholz, D., 2007. Procedures for accurate U and Th isotope measurements by high precision MC-ICPMS. *International Journal of Mass Spectrometry* 264, 97-109.
- Hoffmann, D.L., 2008. ^{230}Th isotope measurements of femtogram quantities for U-series dating using multi ion counting (MIC) MC-ICPMS. *International Journal of Mass Spectrometry* 275, 75-79.
- Hoffmann, D.L., Rogerson, M., Spötl, C., Luetscher, M., Vance, D., Osborne, A.H., Fello, N.M., Moseley, G.E., 2016. Timing and causes of North African wet phases during the last glacial period and implications for modern human migration. *Scientific reports* 6, 36367.
- Holzkämper, S., Spötl, C., Mangini, A., 2005. High-precision constraints on timing of Alpine warm periods during the middle to late Pleistocene using speleothem growth periods. *Earth and Planetary Science Letters* 236, 751-764.
- Hoogewerff, J., Papesch, W., Kralik, M., Berner, M., Vroon, P., Miesbauer, H., Gaber, O., Kunzel, K.H., Kleinjans, J., 2001. The last domicile of the Iceman from Hauslabjoch: A geochemical approach using Sr, C and O isotopes and trace element signatures. *Journal of Archaeological Science* 28, 983-989.
- Hori, M., Ishikawa, T., Nagaishi, K., Lin, K., Wang, B.-S., You, C.-F., Shen, C.-C., Kano, A., 2013. Prior calcite precipitation and source mixing process influence Sr/Ca, Ba/Ca and $^{87}\text{Sr}/^{86}\text{Sr}$ of a stalagmite developed in southwestern Japan during 18.0–4.5 ka. *Chemical Geology* 347, 190-198.
- Horn, I., von Blanckenburg, F., 2007. Investigation on elemental and isotopic fractionation during 196 nm femtosecond laser ablation multiple collector inductively coupled plasma mass spectrometry. *Spectrochim Acta B* 62, 410-422.
- Horstwood, M.S.A., Evans, J.A., Montgomery, J., 2008. Determination of Sr isotopes in calcium phosphates using laser ablation inductively coupled plasma mass spectrometry and their application to archaeological tooth enamel. *Geochimica et Cosmochimica Acta* 72, 5659-5674.
- Huber, C., Leuenberger, M., Spahni, R., Flückiger, J., Schwander, J., Stocker, T.F., Johnsen, S., Landais, A., Jouzel, J., 2006. Isotope calibrated Greenland temperature record over Marine Isotope Stage 3 and its relation to CH₄. *Earth and Planetary Science Letters* 243, 504-519.
- Immenhauser, A., Buhl, D., Richter, D., Niedermayr, A., Riechelmann, D., Dietzel, M., Schulte, U., 2010. Magnesium-isotope fractionation during low-Mg calcite precipitation in a limestone cave—Field study and experiments. *Geochimica et Cosmochimica Acta* 74, 4346-4364.

- Ingle, C.P., Sharp, B.L., Horstwood, M.S.A., Parrish, R.R., Lewis, D.J., 2003. Instrument response functions, mass bias and matrix effects in isotope ratio measurements and semi-quantitative analysis by single and multi-collector ICP-MS. *Journal of Analytical Atomic Spectrometry* 18, 219-229.
- Inoue, M., Nohara, M., Okai, T., Suzuki, A., Kawahata, H., 2004. Concentrations of trace elements in carbonate reference materials coral JCp-1 and giant clam Jct-1 by inductively coupled plasma-mass spectrometry. *Geostandards and Geoanalytical Research* 28, 411-416.
- Irrgeher, J., Galler, P., Prohaska, T., 2016. $^{87}\text{Sr}/^{86}\text{Sr}$ isotope ratio measurements by laser ablation multicollector inductively coupled plasma mass spectrometry: Reconsidering matrix interferences in bioapatites and biogenic carbonates. *Spectrochimica Acta Part B: Atomic Spectroscopy* 125, 31-42.
- Ivanovich, M., Harmon, R.S., 1992. Uranium-series disequilibrium: applications to earth, marine, and environmental sciences. 2.
- Jackson, M.G., Hart, S.R., 2006. Strontium isotopes in melt inclusions from Samoan basalts: Implications for heterogeneity in the Samoan plume. *Earth and Planetary Science Letters* 245, 260-277.
- Jochum, K.P., Nohl, L., Herwig, K., Lammel, E., Stoll, B., Hofmann, A.W., 2005. GeoReM: A new geochemical database for reference materials and isotopic standards. *Geostandards and Geoanalytical Research* 29, 333-338.
- Jochum, K.P., Nohl, U., 2008. Reference materials in geochemistry and environmental research and the GeoReM database. *Chemical Geology* 253, 50-53.
- Jochum, K.P., Stoll, B., Weis, U., Kuzmin, D.V., Sobolev, A.V., 2009. In situ Sr isotopic analysis of low Sr silicates using LA-ICP-MS. *Journal of Analytical Atomic Spectrometry* 24, 1237-1243.
- Jochum, K.P., Wilson, S.A., Abouchami, W., Amini, M., Chmeleff, J., Eisenhauer, A., Hegner, E., Iaccheri, L.M., Kieffer, B., Krause, J., McDonough, W.F., Mertz-Kraus, R., Raczek, I., Rudnick, R.L., Scholz, D., Steinhöfel, G., Stoll, B., Stracke, A., Tonarini, S., Weis, D., Weis, U., Woodhead, J.D., 2011a. GSD-1G and MPI-DING Reference Glasses for In Situ and Bulk Isotopic Determination. *Geostandards and Geoanalytical Research* 35, 193-226.
- Jochum, K.P., Weis, U., Stoll, B., Kuzmin, D., Yang, Q., Raczek, I., Jacob, D.E., Stracke, A., Birbaum, K., Frick, D.A., 2011b. Determination of reference values for NIST SRM 610–617 glasses following ISO guidelines. *Geostandards and Geoanalytical Research* 35, 397-429.
- Jochum, K.P., Scholz, D., Stoll, B., Weis, U., Wilson, S.A., Yang, Q.C., Schwalb, A., Borner, N., Jacob, D.E., Andreae, M.O., 2012. Accurate trace element analysis of speleothems and biogenic calcium carbonates by LA-ICP-MS. *Chemical Geology* 318, 31-44.
- Jochum, K.P., Stoll, B., Weis, U., Jacob, D.E., Mertz-Kraus, R., Andreae, M.O., 2014. Non-Matrix-Matched Calibration for the Multi-Element Analysis of Geological and Environmental Samples Using 200 nm Femtosecond LA-ICP-MS: A Comparison with Nanosecond Lasers. *Geostandards and Geoanalytical Research* 38, 265-292.

- Jochum, K.P., Enzweiler, J., 2014. 15.3 - Reference Materials in Geochemical and Environmental Research A2 - Holland, Heinrich D, in: Turekian, K.K. (Ed.), *Treatise on Geochemistry* (Second Edition). Elsevier, Oxford, pp. 43-70.
- Jochum, K.P., Garbe-Schönberg, D., Veter, M., Stoll, B., Weis, U., Weber, M., Lugli, F., Jentzen, A., Schiebel, R., Wassenburg, J.A., Jacob, D.E., Haug, G.H., in revision. Nano powdered calcium carbonate reference materials - a progress for microanalysis? *Geostandards and Geoanalytical Research*.
- Johnsen, S.J., Clausen, H.B., Dansgaard, W., Fuhrer, K., Gundestrup, N., Hammer, C.U., Iversen, P., Jouzel, J., Stauffer, B., 1992. Irregular glacial interstadials recorded in a new Greenland ice core. *Nature* 359, 311-313.
- Kane, J.S., Potts, P.J., Wiedenbeck, M., Carignan, J., Wilson, S., 2003. International Association of Geoanalysts' protocol for the certification of geological and environmental reference materials. *Geostandards Newsletter* 27, 227-244.
- Kelly, S., Heaton, K., Hoogewerff, J., 2005. Tracing the geographical origin of food: The application of multi-element and multi-isotope analysis. *Trends in Food Science & Technology* 16, 555-567.
- Kennett, D.J., Breitenbach, S.F.M., Aquino, V.V., Asmerom, Y., Awe, J., Baldini, J.U.L., Bartlein, P., Culleton, B.J., Ebert, C., Jazwa, C., 2012. Development and disintegration of Maya political systems in response to climate change. *Science* 338, 788-791.
- Kim, S.-T., O'Neil, J.R., 1997. Equilibrium and nonequilibrium oxygen isotope effects in synthetic carbonates. *Geochimica et Cosmochimica Acta* 61, 3461-3475.
- Kim, S.-T., Mucci, A., Taylor, B.E., 2007. Phosphoric acid fractionation factors for calcite and aragonite between 25 and 75 C: revisited. *Chemical Geology* 246, 135-146.
- Kimura, J.I., Chang, Q., 2012. Origin of the suppressed matrix effect for improved analytical performance in determination of major and trace elements in anhydrous silicate samples using 200 nm femtosecond laser ablation sector-field inductively coupled plasma mass spectrometry. *Journal of Analytical Atomic Spectrometry* 27, 1549-1559.
- Kimura, J.I., Takahashi, T., Chang, Q., 2013. A new analytical bias correction for in situ Sr isotope analysis of plagioclase crystals using laser-ablation multiple-collector inductively coupled plasma mass spectrometry. *Journal of Analytical Atomic Spectrometry* 28, 945-957.
- Kindler, P., Guillevic, M., Baumgartner, M., Schwander, J., Landais, A., Leuenberger, M., 2014. Temperature reconstruction from 10 to 120 kyr b2k from the NGRIP ice core. *Climate of the Past* 10, 887-902.
- Kluge, T., Riechelmann, D.F.C., Wieser, M., Spötl, C., Sültenfuß, J., Schröder-Ritzrau, A., Niggemann, S., Aeschbach-Hertig, W., 2010. Dating cave drip water by tritium. *Journal of Hydrology* 394, 396-406.
- Koch, J., Gunther, D., 2007. Femtosecond laser ablation inductively coupled plasma mass spectrometry: achievements and remaining problems. *Analytical and Bioanalytical Chemistry* 387, 149-153.

- Köhler, P., Knorr, G., Buiron, D., Lourdou, A., Chappellaz, J., 2011. Abrupt rise in atmospheric CO₂ at the onset of the Bølling/Allerød: in-situ ice core data versus true atmospheric signal. *Climate of the Past* 7, 473-486.
- Krabbenhöft, A., Fietzke, J., Eisenhauer, A., Liebetrau, V., Böhm, F., Vollstaedt, H., 2009. Determination of radiogenic and stable strontium isotope ratios ($^{87}\text{Sr}/^{86}\text{Sr}$; $\delta^{88}/^{86}\text{Sr}$) by thermal ionization mass spectrometry applying an $^{87}\text{Sr}/^{84}\text{Sr}$ double spike. *Journal of Analytical Atomic Spectrometry* 24, 1267-1271.
- Lachniet, M.S., 2009. Climatic and environmental controls on speleothem oxygen-isotope values. *Quaternary Science Reviews* 28, 412-432.
- Le Roux, P.J., Lee-Thorp, J.A., Copeland, S.R., Sponheimer, M., de Ruiter, D.J., 2014. Strontium isotope analysis of curved tooth enamel surfaces by laser-ablation multi-collector ICP-MS. *Palaeogeography, Palaeoclimatology, Palaeoecology* 416, 142-149.
- Lewis, J., Coath, C.D., Pike, A.W.G., 2014. An improved protocol for $^{87}\text{Sr}/^{86}\text{Sr}$ by laser ablation multi-collector inductively coupled plasma mass spectrometry using oxide reduction and a customised plasma interface. *Chemical Geology* 390, 173-181.
- Lewis, J., Pike, A.W.G., Coath, C.D., Evershed, R.P., 2017. Strontium concentration, radiogenic ($^{87}\text{Sr}/^{86}\text{Sr}$) and stable ($\delta^{88}\text{Sr}$) strontium isotope systematics in a controlled feeding study. *STAR: Science & Technology of Archaeological Research* 3, 53-65.
- Li, H.-C., Ku, T.-L., You, C.-F., Cheng, H., Edwards, R.L., Ma, Z.-B., Tsai, W.-s., Li, M.-D., 2005. $^{87}\text{Sr}/^{86}\text{Sr}$ and Sr/Ca in speleothems for paleoclimate reconstruction in Central China between 70 and 280 kyr ago. *Geochimica et Cosmochimica Acta* 69, 3933-3947.
- Lin, J., Liu, Y., Chen, H., Zhou, L., Hu, Z., Gao, S., 2015. Review of High-Precision Sr Isotope Analyses of Low-Sr Geological Samples. *Journal of Earth Science* 26, 763-774.
- Lisiecki, L.E., Raymo, M.E., 2005. A Pliocene-Pleistocene stack of 57 globally distributed benthic $\delta^{18}\text{O}$ records. *Paleoceanography* 20, 1-17.
- Luetscher, M., Boch, R., Sodemann, H., Spötl, C., Cheng, H., Edwards, R.L., Frisia, S., Hof, F., Müller, W., 2015. North Atlantic storm track changes during the Last Glacial Maximum recorded by Alpine speleothems. *Nature Communications* 6, 6344.
- Lugli, F., Cipriani, A., Arnaud, J., Arzarello, M., Peretto, C., Benazzi, S., 2017a. Suspected limited mobility of a Middle Pleistocene woman from Southern Italy: strontium isotopes of a human deciduous tooth. *Scientific Reports* 7, 8615.
- Lugli, F., Cipriani, A., Peretto, C., Mazzucchelli, M., Brunelli, D., 2017b. In situ high spatial resolution $^{87}\text{Sr}/^{86}\text{Sr}$ ratio determination of two Middle Pleistocene (c.a. 580 ka) *Stephanorhinus hundsheimensis* teeth by LA-MC-ICP-MS. *International Journal of Mass Spectrometry* 412, 38-48.
- Lugli, F., Cipriani, A., Tavaglione, V., Traversari, M., Benazzi, S., 2018. Transhumance pastoralism of Roccapelago (Modena, Italy) early-modern individuals: Inferences from Sr isotopes of hair strands. *American Journal of Physical Anthropology* 167, 470-483.

- Mangini, A., Verdes, P., Spötl, C., Scholz, D., Vollweiler, N., Kromer, B., 2007. Persistent influence of the North Atlantic hydrography on central European winter temperature during the last 9000 years. *Geophysical Research Letters* 34 (2).
- Mattey, D., Lowry, D., Duffet, J., Fisher, R., Hodge, E., Frisia, S., 2008. A 53 year seasonally resolved oxygen and carbon isotope record from a modern Gibraltar speleothem: reconstructed drip water and relationship to local precipitation. *Earth and Planetary Science Letters* 269, 80-95.
- Mattey, D.P., Atkinson, T.C., Barker, J.A., Fisher, R., Latin, J.P., Durrell, R., Ainsworth, M., 2016. Carbon dioxide, ground air and carbon cycling in Gibraltar karst. *Geochimica et Cosmochimica Acta* 184, 88-113.
- Mayewski, P.A., Rohling, E.E., Curt Stager, J., Karlén, W., Maasch, K.A., David Meeker, L., Meyerson, E.A., Gasse, F., van Kreveld, S., Holmgren, K., Lee-Thorp, J., Rosqvist, G., Rack, F., Staubwasser, M., Schneider, R.R., Steig, E.J., 2004. Holocene climate variability. *Quaternary Research* 62, 243-255.
- McArthur, J.M., Howarth, R.J., Bailey, T.R., 2001. Strontium Isotope Stratigraphy: LOWESS Version 3: Best Fit to the Marine Sr-Isotope Curve for 0–509 Ma and Accompanying Look-up Table for Deriving Numerical Age. *Journal of Geology* 109, 155-170.
- McArthur, J.M., Howarth, R.J., Shields, G.A., 2012. Strontium isotope stratigraphy. *The geologic time scale* 1, 127-144.
- McCulloch, M., Wasserburg, G.J., 1978. Sm-Nd and Rb-Sr Chronology of Continental Crust Formation. *Science* 200, 1003-1011.
- McDermott, F., Frisia, S., Huang, Y., Longinelli, A., Spiro, B., Heaton, T.H.E., Hawkesworth, C.J., Borsato, A., Keppens, E., Fairchild, I.J., 1999. Holocene climate variability in Europe: evidence from $\delta^{18}\text{O}$, textural and extension-rate variations in three speleothems. *Quaternary Science Reviews* 18, 1021-1038.
- McDermott, F., 2004. Palaeo-climate reconstruction from stable isotope variations in speleothems: a review. *Quaternary Science Reviews* 23, 901-918.
- McMillan, E.A., Fairchild, I.J., Frisia, S., Borsato, A., McDermott, F., 2005. Annual trace element cycles in calcite–aragonite speleothems: evidence of drought in the western Mediterranean 1200–1100 yr BP. *Journal of Quaternary Science* 20, 423-433.
- Mead, G.A., Hodell, D.A., 1995. Controls on the $^{87}\text{Sr}/^{86}\text{Sr}$ composition of seawater from the middle Eocene to Oligocene: Hole 689B, Maud Rise, Antarctica. *Paleoceanography* 10, 327-346.
- Miller, K.G., Feigenson, M.D., Wright, J.D., Clement, B.M., 1991. Miocene isotope reference section, Deep Sea Drilling Project Site 608: an evaluation of isotope and biostratigraphic resolution. *Paleoceanography and Paleoclimatology* 6, 33-52.
- Mischel, S.A., Mertz-Kraus, R., Jochum Klaus, P., Scholz, D., 2017a. TERMITE: An R script for fast reduction of laser ablation inductively coupled plasma mass spectrometry data and its application to trace element measurements. *Rapid Communications in Mass Spectrometry* 31, 1079-1087.

- Mischel, S.A., Scholz, D., Spötl, C., Jochum, K.P., Schröder-Ritzrau, A., Fiedler, S., 2017b. Holocene climate variability in Central Germany and a potential link to the polar North Atlantic: A replicated record from three coeval speleothems. *The Holocene* 27, 509-525.
- Montañez, I.P., Osleger, D.A., Banner, J.L., Mack, L.E., Musgrove, M., 2000. Evolution of the Sr and C isotope composition of Cambrian oceans. *GSA today* 10, 1-7.
- Mook, W.G., De Vries, J.J., 2000. Volume I, Introduction: theory methods review. *Environmental Isotopes in the Hydrological Cycle—Principles and Applications*, International Hydrological Programme (IHP-V), Technical Documents in Hydrology (IAEA/UNESCO) No 39, 75-76.
- Moseley, G.E., Spötl, C., Svensson, A., Cheng, H., Brandstätter, S., Edwards, R.L., 2014. Multi-speleothem record reveals tightly coupled climate between central Europe and Greenland during Marine Isotope Stage 3. *Geology* 42, 1043-1046.
- Mühlinghaus, C., Scholz, D., Mangini, A., 2009. Modelling fractionation of stable isotopes in stalagmites. *Geochimica et Cosmochimica Acta* 73, 7275-7289.
- Müller, W., Anczkiewicz, R., 2016. Accuracy of laser-ablation (LA)-MC-ICPMS Sr isotope analysis of (bio) apatite—a problem reassessed. *Journal of Analytical Atomic Spectrometry* 31, 259-269.
- Munksgaard, N.C., Antwertinger, Y., Parry, D.L., 2004. Laser Ablation ICP-MS Analysis of Faviidae Corals for Environmental Monitoring of a Tropical Estuary. *Environmental Chemistry* 1, 188-196.
- Neymark, L.A., Premo, W.R., Mel'nikov, N.N., Emsbo, P., 2014. Precise determination of $\delta^{88}\text{Sr}$ in rocks, minerals, and waters by double-spike TIMS: a powerful tool in the study of geological, hydrological and biological processes. *Journal of Analytical Atomic Spectrometry* 29, 65-75.
- Niggemann, S., Mangini, A., Richter, D.K., Wurth, G., 2003. A paleoclimate record of the last 17,600 years in stalagmites from the B7 cave, Sauerland, Germany. *Quaternary Science Reviews* 22, 555-567.
- Nowell, G.M., Horstwood, M.S.A., 2009. Comments on Richards et al., *Journal of Archaeological Science* 35, 2008 “Strontium isotope evidence of Neanderthal mobility at the site of Lakonis, Greece using laser-ablation PIMMS”. *Journal of Archaeological Science* 36, 1334-1341.
- Obert, J.C., Scholz, D., Felis, T., Brocas, W.M., Jochum, K.P., Andreae, M.O., 2016. $^{230}\text{Th}/\text{U}$ dating of Last Interglacial brain corals from Bonaire (southern Caribbean) using bulk and theca wall material. *Geochimica et Cosmochimica Acta* 178, 20-40.
- Ohno, T., Hirata, T., 2007. Simultaneous determination of mass-dependent isotopic fractionation and radiogenic isotope variation of strontium in geochemical samples by multiple collector-ICP-mass spectrometry. *Analytical Sciences* 23, 1275-1280.
- Okai, T., Suzuki, A., Kawahata, H., Terashima, S., Imai, N., 2002. Preparation of a New Geological Survey of Japan Geochemical Reference Material: Coral JcP-1. *Geostandards and Geoanalytical Research* 26, 95-99.
- Oster, J.L., Montañez, I.P., Guilderson, T.P., Sharp, W.D., Banner, J.L., 2010. Modeling speleothem $\delta^{13}\text{C}$ variability in a central Sierra Nevada cave using ^{14}C and $^{87}\text{Sr}/^{86}\text{Sr}$. *Geochimica et Cosmochimica Acta* 74, 5228-5242.

- Oster, J.L., Montañez, I.P., Mertz-Kraus, R., Sharp, W.D., Stock, G.M., Spero, H.J., Tinsley, J., Zachos, J.C., 2014. Millennial-scale variations in western Sierra Nevada precipitation during the last glacial cycle MIS 4/3 transition. *Quaternary Research* 82, 236-248.
- Outridge, P., Chenery, S., Babaluk, J., Reist, J., 2002. Analysis of geological Sr isotope markers in fish otoliths with subannual resolution using laser ablation-multicollector-ICP-mass spectrometry. *Environmental Geology* 42, 891-899.
- Pate, F.D., 1994. Bone chemistry and paleodiet. *Journal of Archaeological Method and Theory* 1, 161-209.
- Perrin, J., Jeannin, P.-Y., Zwahlen, F., 2003. Epikarst storage in a karst aquifer: a conceptual model based on isotopic data, Milandre test site, Switzerland. *Journal of Hydrology* 279, 106-124.
- Platzner, I., 1985. Multiple Ion Collection in Thermal Ionization Isotope Ratio Mass-Spectrometry of Strontium. *International Journal of Mass Spectrometry* 67, 129-136.
- Poitrasson, F., Mao, X., Mao, S.S., Freydier, R., Russo, R.E., 2003. Comparison of ultraviolet femtosecond and nanosecond laser ablation inductively coupled plasma mass spectrometry analysis in glass, monazite, and zircon. *Analytical Chemistry* 75, 6184-6190.
- Pons-Branchu, E., Hamelin, B., Losson, B., Jaillet, S., Brulhet, J., 2010. Speleothem evidence of warm episodes in northeast France during Marine Oxygen Isotope Stage 3 and implications for permafrost distribution in northern Europe. *Quaternary Research* 74, 246-251.
- Rachel, B.-J., Pearson, T.E., Ramos, F.C., Grimes, C.B., Bruce MacFarlane, R., 2008. Tracking natal origins of salmon using isotopes, otoliths, and landscape geology. *Limnology and Oceanography* 53, 1633-1642.
- Ramos, F.C., Wolff, J.A., Tollstrup, D.L., 2004. Measuring $^{87}\text{Sr}/^{86}\text{Sr}$ variations in minerals and groundmass from basalts using LA-MC-ICPMS. *Chemical Geology* 211, 135-158.
- Ramsey, C.B., 2008. Deposition models for chronological records. *Quaternary Science Reviews* 27, 42-60.
- Rasmussen, S.O., Bigler, M., Blockley, S.P., Blunier, T., Buchardt, S.L., Clausen, H.B., Cvijanovic, I., Dahl-Jensen, D., Johnsen, S.J., Fischer, H., 2014. A stratigraphic framework for abrupt climatic changes during the Last Glacial period based on three synchronized Greenland ice-core records: refining and extending the INTIMATE event stratigraphy. *Quaternary Science Reviews* 106, 14-28.
- Reitmaier, T., Doppler, T., Pike, A.W.G., Deschler-Erb, S., Hajdas, I., Walser, C., Gerling, C., 2017. Alpine cattle management during the Bronze Age at Ramosch-Mottata, Switzerland. *Quaternary International* 484, 19-31.
- Richards, D.A., Bottrell, S.H., Cliff, R.A., Ströhle, K., Rowe, P.J., 1998. U-Pb dating of a speleothem of Quaternary age. *Geochimica et Cosmochimica Acta* 62, 3683-3688.
- Richards, D.A., Dorale, J.A., 2003. Uranium-series Chronology and Environmental Applications of Speleothems. *Reviews in Mineralogy and Geochemistry* 52, 407-460.

- Riechelmann, D.F.C., 2010. Aktuospeläologische Untersuchungen in der Bunkerhöhle des Iserlohner Massenkalks (NRW/Deutschland): Signifikanz für kontinentale Klimaarchive. PhD, Ruhr-Universität Bochum, Germany.
- Riechelmann, D.F.C., Schröder-Ritzrau, A., Scholz, D., Fohlmeister, J., Spötl, C., Richter, D.K., Mangini, A., 2011. Monitoring Bunker Cave (NW Germany): A prerequisite to interpret geochemical proxy data of speleothems from this site. *Journal of Hydrology* 409, 682-695.
- Riechelmann, D.F.C., Deininger, M., Scholz, D., Riechelmann, S., Schröder-Ritzrau, A., Spötl, C., Richter, D.K., Mangini, A., Immenhauser, A., 2013. Disequilibrium carbon and oxygen isotope fractionation in recent cave calcite: Comparison of cave precipitates and model data. *Geochimica et Cosmochimica Acta* 103, 232-244.
- Riechelmann, S., Buhl, D., Schröder-Ritzrau, A., Spötl, C., Riechelmann, D.F.C., Richter, D.K., Kluge, T., Marx, T., Immenhauser, A., 2012a. Hydrogeochemistry and fractionation pathways of Mg isotopes in a continental weathering system: Lessons from field experiments. *Chemical Geology* 300-301, 109-122.
- Riechelmann, S., Buhl, D., Schröder-Ritzrau, A., Riechelmann, D.F.C., Richter, D.K., Vonhof, H.B., Wassenburg, J.A., Geske, A., Spötl, C., Immenhauser, A., 2012b. The magnesium isotope record of cave carbonate archives. *Climate of the Past* 8, 1849-1867.
- Riechelmann, S., Schröder-Ritzrau, A., Wassenburg, J.A., Schreuer, J., Richter, D.K., Riechelmann, D.F.C., Terente, M., Constantin, S., Mangini, A., Immenhauser, A., 2014. Physicochemical characteristics of drip waters: Influence on mineralogy and crystal morphology of recent cave carbonate precipitates. *Geochimica et Cosmochimica Acta* 145, 13-29.
- Riechelmann, S., Schröder-Ritzrau, A., Spötl, C., Riechelmann, D.F.C., Richter, D.K., Mangini, A., Frank, N., Breitenbach, S.F.M., Immenhauser, A., 2017. Sensitivity of Bunker Cave to climatic forcings highlighted through multi-annual monitoring of rain-, soil-, and dripwaters. *Chemical Geology* 449, 194-205.
- Rozanski, K., Sonntag, C., Münnich, K.O., 1982. Factors controlling stable isotope composition of European precipitation. *Tellus* 34, 142-150.
- Sánchez Goñi, M.F., Cacho, I., Turon, J.L., Guiot, J., Sierro, F.J., Peyrouquet, J.P., Grimalt, J.O., Shackleton, N.J., 2002. Synchronicity between marine and terrestrial responses to millennial scale climatic variability during the last glacial period in the Mediterranean region. *Climate Dynamics* 19, 95-105.
- Sánchez Goñi, M.F., Bard, E., Landais, A., Rossignol, L., d'Errico, F., 2013. Air-sea temperature decoupling in western Europe during the last interglacial-glacial transition. *Nature Geoscience* 6, 837-841.
- Sano, Y., Shirai, K., Takahata, N., Amakawa, H., Otake, T., 2008. Ion microprobe Sr isotope analysis of carbonates with about 5µm spatial resolution: An example from an ayu otolith. *Applied Geochemistry* 23, 2406-2413.

- Scharlotta, I., Weber, A., 2014. Mobility of middle Holocene foragers in the Cis-Baikal region, Siberia: Individual life history approach, strontium ratios, rare earth and trace elements. *Quaternary International* 348, 37-65.
- Scholz, D., Mangini, A., Felis, T., 2004. U-series dating of diagenetically altered fossil reef corals. *Earth and Planetary Science Letters* 218, 163-178.
- Scholz, D., Hoffmann, D., 2008. $^{230}\text{Th}/\text{U}$ -dating of fossil corals and speleothems. *Quaternary Science Journal* 57, 52–76.
- Scholz, D., Mühlinghaus, C., Mangini, A., 2009. Modelling $\delta^{13}\text{C}$ and $\delta^{18}\text{O}$ in the solution layer on stalagmite surfaces. *Geochimica et Cosmochimica Acta* 73, 2592-2602.
- Scholz, D., Hoffmann, D.L., 2011. StalAge—An algorithm designed for construction of speleothem age models. *Quaternary Geochronology* 6, 369-382.
- Scholz, D., Frisia, S., Borsato, A., Spötl, C., Fohlmeister, J., Mudelsee, M., Miorandi, R., Mangini, A., 2012. Holocene climate variability in north-eastern Italy: potential influence of the NAO and solar activity recorded by speleothem data. *Climate of the Past* 8, 1367-1383.
- Scholz, D., Tolzmann, J., Hoffmann, D.L., Jochum, K.P., Spötl, C., Riechelmann, D.F.C., 2014. Diagenesis of speleothems and its effect on the accuracy of $^{230}\text{Th}/\text{U}$ -ages. *Chemical Geology* 387, 74-86.
- Sforza, M.-C., Lugli, F., 2017. MapIT!: a simple and user-friendly MATLAB script to elaborate elemental distribution images from LA-ICP-MS data. *Journal of Analytical Atomic Spectrometry* 32, 1035-1043.
- Sharp, Z., 2007. Principles of stable isotope geochemistry. Pearson education Upper Saddle River, NJ.
- Simonetti, A., Buzon, M.R., Creaser, R.A., 2008. In-situ elemental and Sr isotope investigation of human tooth enamel by laser ablation-(MC)-ICP-MS: successes and pitfalls. *Archaeometry* 50, 371-385.
- Sirocko, F., Knapp, H., Dreher, F., Förster, M.W., Albert, J., Brunck, H., Veres, D., Dietrich, S., Zech, M., Hambach, U., Röhner, M., Rudert, S., Schwibus, K., Adams, C., Sigl, P., 2016. The ELSA-Vegetation-Stack: Reconstruction of Landscape Evolution Zones (LEZ) from laminated Eifel maar sediments of the last 60,000 years. *Global and Planetary Change* 142, 108-135.
- Smart, P.L., Friedrich, H., 1987. Water movement and storage in the unsaturated zone of a maturely karstified aquifer, Mendip Hills, England. National Water Well Association, pp. 57-87.
- Spötl, C., Mangini, A., 2002. Stalagmite from the Austrian Alps reveals Dansgaard–Oeschger events during isotope stage 3: Implications for the absolute chronology of Greenland ice cores. *Earth and Planetary Science Letters* 203, 507-518.
- Spötl, C., Mangini, A., Richards, D.A., 2006. Chronology and paleoenvironment of Marine Isotope Stage 3 from two high-elevation speleothems, Austrian Alps. *Quaternary Science Reviews* 25, 1127-1136.

- Starinsky, A., Bielski, M., Ecker, A., Steinitz, G., 1983. Tracing the origin of salts in groundwater by Sr isotopic composition (the crystalline complex of the southern Sinai, Egypt). *Chemical Geology* 41, 257-267.
- Steiger, R.H., Jäger, E., 1977. Subcommittee on geochronology: Convention on the use of decay constants in geo- and cosmochronology. *Earth and Planetary Science Letters* 36, 359-362.
- Stewart, B.W., Capo, R.C., Chadwick, O.A., 1998. Quantitative strontium isotope models for weathering, pedogenesis and biogeochemical cycling. *Geoderma* 82, 173-195.
- Stewart, B.W., Capo, R.C., Chadwick, O.A., 2001. Effects of rainfall on weathering rate, base cation provenance, and Sr isotope composition of Hawaiian soils. *Geochimica et Cosmochimica Acta* 65, 1087-1099.
- Svensson, A., Andersen, K.K., Bigler, M., Clausen, H.B., Dahl-Jensen, D., Davies, S.M., Johnsen, S.J., Muscheler, R., Parrenin, F., Rasmussen, S.O., 2008. A 60 000 year Greenland stratigraphic ice core chronology. *Climate of the Past* 4, 47-57.
- Tabersky, D., Luechinger, N.A., Rossier, M., Reusser, E., Hametner, K., Aeschlimann, B., Frick, D.A., Halim, S.C., Thompson, J., Danyushevsky, L., 2014. Development and characterization of custom-engineered and compacted nanoparticles as calibration materials for quantification using LA-ICP-MS. *Journal of Analytical Atomic Spectrometry* 29, 955-962.
- Taylor, S.R., McLennan, S.M., McCulloch, M.T., 1983. Geochemistry of loess, continental crustal composition and crustal model ages. *Geochimica et Cosmochimica Acta* 47, 1897-1905.
- R Core Team, 2013. R: A language and environment for statistical computing. Vienna, Austria.
- Tooth, A.F., Fairchild, I.J., 2003. Soil and karst aquifer hydrological controls on the geochemical evolution of speleothem-forming drip waters, Crag Cave, southwest Ireland. *Journal of Hydrology* 273, 51-68.
- Vanhaecke, F., Resano, M., Koch, J., McIntosh, K., Günther, D., 2010. Femtosecond laser ablation-ICP-mass spectrometry analysis of a heavy metallic matrix: Determination of platinum group metals and gold in lead fire-assay buttons as a case study. *Journal of Analytical Atomic Spectrometry* 25, 1259-1267.
- Verheyden, S., Keppens, E., Fairchild, I.J., McDermott, F., Weis, D., 2000. Mg, Sr and Sr isotope geochemistry of a Belgian Holocene speleothem: implications for paleoclimate reconstructions. *Chemical Geology* 169, 131-144.
- Voelker, A.H.L., 2002. Global distribution of centennial-scale records for Marine Isotope Stage (MIS) 3: a database. *Quaternary Science Reviews* 21, 1185-1212.
- von Kamp, H., Ribbert, K.H., 2005. Erläuterungen zu Blatt 4611 Hagen-Hohenlimburg Geologische Karte von Nordrhein-Westfalen 1: 25.000. Krefeld.
- Vroon, P.Z., van der Wagt, B., Koornneef, J.M., Davies, G.R., 2008. Problems in obtaining precise and accurate Sr isotope analysis from geological materials using laser ablation MC-ICPMS. *Analytical and Bioanalytical Chemistry* 390, 465-476.

- Wackerbarth, A., Scholz, D., Fohlmeister, J., Mangini, A., 2010. Modelling the $\delta^{18}\text{O}$ value of cave drip water and speleothem calcite. *Earth and Planetary Science Letters* 299, 387-397.
- Waight, T., Baker, J., Peate, D., 2002. Sr isotope ratio measurements by double-focusing MC-ICPMS: techniques, observations and pitfalls. *International Journal of Mass Spectrometry* 221, 229-244.
- Wainer, K., Genty, D., Blamart, D., Hoffmann, D., Couchoud, I., 2009. A new stage 3 millennial climatic variability record from a SW France speleothem. *Palaeogeography, Palaeoclimatology, Palaeoecology* 271, 130-139.
- Walker, M., Johnsen, S., Rasmussen, S.O., Popp, T., Steffensen, J.P., Gibbard, P., Hoek, W., Lowe, J., Andrews, J., Björck, S., 2009. Formal definition and dating of the GSSP (Global Stratotype Section and Point) for the base of the Holocene using the Greenland NGRIP ice core, and selected auxiliary records. *Journal of Quaternary Science: Published for the Quaternary Research Association* 24, 3-17.
- Wang, Y.-J., Cheng, H., Edwards, R.L., An, Z.S., Wu, J.Y., Shen, C.C., Dorale, J.A., 2001. A high-resolution absolute-dated late Pleistocene monsoon record from Hulu Cave, China. *Science* 294, 2345-2348.
- Wanner, H., Beer, J., Bütikofer, J., Crowley, T.J., Cubasch, U., Flückiger, J., Goosse, H., Grosjean, M., Joos, F., Kaplan, J.O., Küttel, M., Müller, S.A., Prentice, I.C., Solomina, O., Stocker, T.F., Tarasov, P., Wagner, M., Widmann, M., 2008. Mid- to Late Holocene climate change: an overview. *Quaternary Science Reviews* 27, 1791-1828.
- Wassenburg, J.A., Immenhauser, A., Richter, D.K., Jochum, K.P., Fietzke, J., Deininger, M., Goos, M., Scholz, D., Sabaoui, A., 2012. Climate and cave control on Pleistocene/Holocene calcite-to-aragonite transitions in speleothems from Morocco: Elemental and isotopic evidence. *Geochimica et Cosmochimica Acta* 92, 23-47.
- Wassenburg, J.A., Immenhauser, A., Richter, D.K., Niedermayr, A., Riechelmann, S., Fietzke, J., Scholz, D., Jochum, K.P., Fohlmeister, J., Schröder-Ritzrau, A., Sabaoui, A., Riechelmann, D.F.C., Schneider, L., Esper, J., 2013. Moroccan speleothem and tree ring records suggest a variable positive state of the North Atlantic Oscillation during the Medieval Warm Period. *Earth and Planetary Science Letters* 375, 291-302.
- Wassenburg, J.A., Dietrich, S., Fietzke, J., Fohlmeister, J., Jochum, K.P., Scholz, D., Richter, D.K., Sabaoui, A., Spotl, C., Lohmann, G., Andreae, M.O., Immenhauser, A., 2016a. Reorganization of the North Atlantic Oscillation during early Holocene deglaciation. *Nature Geoscience* 9, 602-605.
- Wassenburg, J.A., Scholz, D., Jochum, K.P., Cheng, H., Oster, J., Immenhauser, A., Richter, D.K., Hager, T., Jamieson, R.A., Baldini, J.U.L., Hoffmann, D., Breitenbach, S.F.M., 2016b. Determination of aragonite trace element distribution coefficients from speleothem calcite-aragonite transitions. *Geochimica et Cosmochimica Acta* 190, 347-367.
- Weber, M., Wassenburg, J.A., Jochum, K.P., Breitenbach, S.F.M., Oster, J., Scholz, D., 2017. Sr-isotope analysis of speleothems by LA-MC-ICP-MS: High temporal resolution and fast data acquisition. *Chemical Geology* 468, 63-74.

- Weber, M., Scholz, D., Schröder-Ritzrau, A., Deininger, M., Spötl, C., Lugli, F., Mertz-Kraus, R., Jochum, K.P., Fohlmeister, J., Stumpf, C.F., 2018a. Evidence of warm and humid interstadials in central Europe during early MIS 3 revealed by a multi-proxy speleothem record. *Quaternary Science Reviews* 200, 276-286.
- Weber, M., Lugli, F., Jochum, K.P., Cipriani, A., Scholz, D., 2018b. Calcium Carbonate and Phosphate Reference Materials for Monitoring Bulk and Microanalytical Determination of Sr Isotopes. *Geostandards and Geoanalytical Research* 42, 77-89.
- Weber, M., Lugli, F., Hattendorf, B., Scholz, D., Mertz-Kraus, R., Guinoiseau, D., Jochum, K.P., submitted. NanoSr - A new microanalytical carbonate reference material for in-situ Sr isotope analysis. *Geostandards and Geoanalytical Research*.
- Wedepohl, H.K., 1995. The composition of the continental crust. *Geochimica et Cosmochimica Acta* 59, 1217-1232.
- Wieser, M.E., Schwieters, J.B., 2005. The development of multiple collector mass spectrometry for isotope ratio measurements. *International Journal of Mass Spectrometry* 242, 97-115.
- Williams, R.A.D., Elliott, J.C., 1979. *Basic and Applied Dental Biochemistry*. Churchill Livingstone. Edinburgh-London and New York, 519p.
- Willmes, M., Kinsley, L., Moncel, M.H., Armstrong, R.A., Aubert, M., Eggins, S., Grün, R., 2016. Improvement of laser ablation in situ micro-analysis to identify diagenetic alteration and measure strontium isotope ratios in fossil human teeth. *Journal of Archaeological Science* 70, 102-116.
- Wolff, B.A., Johnson, B.M., Breton, A.R., Martinez, P.J., Winkelman, D.L., 2012. Origins of invasive piscivores determined from the strontium isotope ratio ($^{87}\text{Sr}/^{86}\text{Sr}$) of otoliths. *Canadian Journal of Fisheries and Aquatic Sciences* 69, 724-739.
- Woodhead, J., Swearer, S., Hergt, J., Maas, R., 2005. In situ Sr-isotope analysis of carbonates by LA-MC-ICP-MS: interference corrections, high spatial resolution and an example from otolith studies. *Journal of Analytical Atomic Spectrometry* 20, 22-27.
- Woodhead, J., Hellstrom, J., Maas, R., Drysdale, R., Zanchetta, G., Devine, P., Taylor, E., 2006. U-Pb geochronology of speleothems by MC-ICPMS. *Quaternary Geochronology* 1, 208-221.
- Wortham, B.E., Wong, C.I., Silva, L.C.R., McGee, D., Montañez, I.P., Rasbury, E.T., Cooper, K.M., Sharp, W.D., Glessner, J.J.G., Santos, R.V., 2017. Assessing response of local moisture conditions in central Brazil to variability in regional monsoon intensity using speleothem $^{87}\text{Sr}/^{86}\text{Sr}$ values. *Earth and Planetary Science Letters* 463, 310-322.
- Wu, S., Karius, V., Schmidt, B.C., Simon, K., Wörner, G., 2018. Comparison of Ultrafine Powder Pellet and Flux-free Fusion Glass for Bulk Analysis of Granitoids by Laser Ablation-Inductively Coupled Plasma-Mass Spectrometry. *Geostandards and Geoanalytical Research* 42, 575-591.
- Yang, Q., Scholz, D., Jochum, K.P., Hoffmann, D.L., Stoll, B., Weis, U., Schwager, B., Andreae, M.O., 2015. Lead isotope variability in speleothems—A promising new proxy for hydrological change? First results from a stalagmite from western Germany. *Chemical Geology* 396, 143-151.

- Yang, Y.H., Wu, F.Y., Yang, J.H., Chew, D.M., Xie, L.W., Chu, Z.Y., Zhang, Y.B., Huang, C., 2014. Sr and Nd isotopic compositions of apatite reference materials used in U-Th-Pb geochronology. *Chemical Geology* 385, 35-55.
- Yang, Z.P., Fryer, B.J., Longerich, H.P., Gagnon, J.E., Samson, I.M., 2011. 785 nm femtosecond laser ablation for improved precision and reduction of interferences in Sr isotope analyses using MC-ICP-MS. *Journal of Analytical Atomic Spectrometry* 26, 341-351.
- Zachos, J.C., Opdyke, B.N., Quinn, T.M., Jones, C.E., Halliday, A.N., 1999. Early Cenozoic glaciation, Antarctic weathering, and seawater $^{87}\text{Sr}/^{86}\text{Sr}$: Is there a link? *Chemical Geology* 161, 165-180.
- Zack, T., Hogmalm, K.J., 2016. Laser ablation Rb/Sr dating by online chemical separation of Rb and Sr in an oxygen-filled reaction cell. *Chemical Geology* 437, 120-133.
- Zhou, H., Feng, Y.-X., Zhao, J.-X., Shen, C.-C., You, C.-F., Lin, Y., 2009. Deglacial variations of Sr and $^{87}\text{Sr}/^{86}\text{Sr}$ ratio recorded by a stalagmite from Central China and their association with past climate and environment. *Chemical Geology* 268, 233-247.

Appendix

Curriculum Vitae

